(2)

MTL MS 89-1

AD

AD-A211 954

PROCEEDINGS OF THE ARMY SYMPOSIUM ON SOLID MECHANICS, 1989 - MECHANICS OF ENGINEERED MATERIALS AND APPLICATIONS

April 1989

Approved for public release; distribution unlimited.

US ARMY
LABORATORY COMMAND
MATERIALS TECHNOLOGY LABORATORY

TECHNOLOGY TO WIN

U.S. ARMY MATERIALS TECHNOLOGY LABORATORY
Watertown, Massachusetts 02172-0001

REPORT DOCUMENTATION PAGE

READ INSTRUCTIONS BEFORE COMPLETING FORM

1. REPORT NUMBER
MTL MS 89-1

2. GOVT ACCESSION NO.

3. RECIPIENT'S CATALOG NUMBER

4. TITLE (and Subtitle)
PROCEEDINGS OF THE ARMY SYMPOSIUM ON SOLID MECHANICS, 1989 - MECHANICS OF ENGINEERED MATERIALS AND APPLICATIONS

5. TYPE OF REPORT & PERIOD COVERED
Final Report

6. PERFORMING ORG. REPORT NUMBER

7. AUTHOR(s)

8. CONTRACT OR GRANT NUMBER(s)

9. PERFORMING ORGANIZATION NAME AND ADDRESS
U.S. Army Materials Technology Laboratory
Watertown, Massachusetts 02172-0001
ATTN: SLCMT-MRS

10. PROGRAM ELEMENT, PROJECT, TASK AREA & WORK UNIT NUMBERS

11. CONTROLLING OFFICE NAME AND ADDRESS
U.S. Army Laboratory Command
2800 Powder Mill Road
Adelphi, Maryland 20783-1145

12. REPORT DATE
April 1989

13. NUMBER OF PAGES
232

14. MONITORING AGENCY NAME & ADDRESS(if different from Controlling Office)

15. SECURITY CLASS. (of this report)
Unclassified

15a. DECLASSIFICATION/DOWNGRADING SCHEDULE

16. DISTRIBUTION STATEMENT (of this Report)

Approved for public release; distribution unlimited.

17. DISTRIBUTION STATEMENT (of the abstract entered in Block 20, if different from Report)

18. SUPPLEMENTARY NOTES

19. KEY WORDS (Continue on reverse side if necessary and identify by block number)

Ceramic materials	Impact	Shock (mechanics)	Strain rate
Composite materials	Loads (forces)	Statistical analysis	
Defects (materials)	Mechanics		

20. ABSTRACT (Continue on reverse side if necessary and identify by block number)

Proceedings of the Army Symposium on Solid Mechanics, 1989 - Mechanics of Engineered Materials and Applications, held at Newport, Rhode Island, 16-18 May 1989.

PREFACE

The 1989 Army Symposium on Solid Mechanics: "Mechanics of Engineered Materials and Applications" was the eleventh in a series of biennial symposia which has focused on solid mechanics research achievements impacting defense system needs. The Symposium had as its theme the role of solid mechanics in the development and application of advanced structural materials to meet novel and demanding performance requirements. The Symposium was held in Newport, Rhode Island during May 16-18, 1989.

The symposia series which dates back to 1966 has been sponsored by the Army Materials Technology Laboratory (Army Materials and Mechanics Research Center until 1985) in its role as the U.S. Army's lead laboratory for solid mechanics research and exploratory development.

The committee endeavored to organize a symposium which would emphasize the synergistic interplay between solid mechanics and materials science in the development and effective utilization of advanced structural materials. The plan called for papers on the wide range of advanced materials to include structural ceramics, metal matrix composites, organic matrix composites, modern metallic alloys, polymers, and hybrids. The goal was to have technical sessions comprised of contributed papers and presentations by invited researchers who have made substantial contributions to the theme area. Experimental, computer simulation, and theoretical papers were solicited which addressed state-of-the-art issues in constitutive theory, failure modes, life prediction, reliability methodology, mechanics of processing, test and evaluation of engineered materials, and structural theories for applications.

The solid mechanics research community responded to the planned Symposium with enthusiasm. Submissions were received from numerous government, industrial, and university researchers. Invitations were graciously accepted. The resulting technical program of the 1989 Symposium consisted of 54 presentations on recent developments in the mechanics of advanced structural materials. The program included a keynote lecture by Professor John Hutchinson entitled "Fracture Mechanics of Interfaces" and ten technical sessions focused on ceramic failure, composites failure, metal plasticity, experimental mechanics, micromechanics, structural applications, high strain rate behavior, composites behavior, rate dependent behavior, and penetration and impact. This document contains the abstracts of presentations which were made at the symposium. Full papers appear in an Army Symposium special issue of the research periodical Mechanics of Materials.

DOCUMENTS IN THIS SYMPOSIUM SERIES*

1968 Theme: Solid Mechanics
Proceedings: AMMRC MS 68-09, September 1968, AD 675463

1970 Theme: Lightweight Structures
Proceedings: AMMRC MS 70-05, December 1970, AD 883455L

1972 Theme: Role of Mechanics in Design - Ballistic Problems
Proceedings: AMMRC MS 73-2, September 1973, AD 772827

1974 Theme: The Role of Mechanics in Design - Structural Joints
Proceedings: AMMRC MS 74-8, September 1974, AD 786543
Work-In-Progress: AMMRC MS 74-9, September 1974, AD 786524
Bibliography: AMMRC MS 74-10, September 1974, AD 786520

1976 Theme: Composite Materials: The Influence of Mechanics of Failure on Design
Proceedings: AMMRC MS 76-2, September 1976, AD A029735
Work-In-Progress: AMMRC MS 76-3, September 1976, AD A029736

1978 Theme: Case Studies on Structural Integrity and Reliability
Proceedings: AMMRC MS 78-3, September 1978, AD A059834/2G1
Ongoing Case Studies: AMMRC MS 78-4, September 1978, AD A059605/6G1

1980 Theme: Designing for Extremes: Environment, Loading, and Structural Behavior
Proceedings: AMMRC MS 80-4, September 1980, AD A090684
Work-In-Progress: AMMRC MS 80-5, September 1980, AD A090685

1982 Theme: Critical Mechanics Problems in Systems Design
Proceedings: AMMRC MS 82-4, September 1982, AD A119510
Work-In-Progress: AMMRC MS 82-5, September 1982, AD A119497

1984 Theme: Advances in Solid Mechanics for Design and Analysis
Proceedings: AMMRC MS 84-3, October 1984, AD A150042

1986 Theme: Lightening of the Force
Proceedings: MTL MS 86-2, October 1986, AD B114635L
Work-In-Progress: MTL MS 86-3, October 1986, AD A184791

* These documents may be ordered from the National Technical Information Service, U.S. Department of Commerce, Springfield, VA 22161.

SYMPOSIUM ORGANIZATION

Co-Chairmen

Dennis M. Tracey

Shun-Chin Chou

Technical Program Committee

Roshdy S. Barsoum

Dattatraya P. Dandekar

Colin E. Freese

Arthur R. Johnson

John F. Mescall

Donald W. Oplinger

Alexander Tessler

Symposium Coordinator

Karen A. Kaloostian

Symposium Secretary

Lucy D. Ohannesian

TABLE OF CONTENTS

SESSION VII: HIGH STRAIN RATE BEHAVIOR 1530 HOURS, 17 MAY 1989

SESSION VIII: COMPOSITES BEHAVIOR 0800 HOURS, 18 MAY 1989

FRACTURE MECHANICS OF INTERFACES

by

John W. Hutchinson

Division of Applied Sciences
Harvard University
Cambridge, MA 02138

Recent developments in interfacial fracture mechanics will be reviewed with emphasis on dissimilar elastic materials joined across an interface. Interfacial fracture is often characterized by mixed mode conditions with both normal (mode I) and shear (mode II) stresses acting on the interface ahead of the crack tip. The toughness of the interface is a function of the relative amounts of the two modes, and this toughness dependence must be considered in the application of interfacial fracture mechanics. A number of examples will be discussed including bonding conditions for ensuring that a matrix crack will not penetrate a fiber in a fiber reinforced composite and various modes of decohesion for residually stressed thin films bonded to substrates. The shape of the decohesion zone for a thin film in residual tension which is cut through to the substrate (the cut test) is a strong function of the mixed mode fracture criterion. Conclusions about this criterion can be drawn by comparing computed decohesion zones with experimental observation.

MECHANICS OF CRACK-MICROCRACK INTERACTIONS

by

Mark Kachanov

Department of Mechanical Engineering
Tufts University
Medford, Massachusetts 02155

Interaction of a crack with large numbers of microcracks (in both 2-D and 3-D configurations) is considered. It is found that, contrary to the spirit of many damage models, no simple correlation between reduction of the elastic stiffness of the microcracked zone and the effect of this zone on the stress intensity factor (SIF) at the main crack tip seems to exist; therefore, modelling of the microcracked zone by a material with reduced elastic stiffness may be inadequate. This can be seen as a manifestation of a more general fact that there is no direct correlation between the fracture-related properties like SIF's (that are governed by the fluctuations of the microstructural arrangements) and the volume average properties like effective elastic moduli (that are relatively insensitive to such fluctuations).

The effects of stress shielding and stress amplification are examined (for two microcrack orientation statistics, random and normal to the maximal tensile stress, and crack densities ranging from low to relatively high). These effects fluctuate considerably from one realisation of the microcrack statistics to another realisation of the same statistics. No statistically significant effects of either shielding or amplification appear to exist (at least, for the microcrack statistics considered; the possibility that, for example, densely packed arrays of microcracks parallel to the main crack may produce shielding, is not ruled out). It is suggested that, in the cases when the effect of shielding exists, it may be produced by expending energy for the generation of the microcrack field (rather than by elastic-microcrack interactions).

The fluctuations of the crack-microcrack interaction effects are due to the fact that only several microcracks closest to the main crack tip affect the SIF and the microcracks that are farther away from the main crack tip produce virtually no effect. By the same reason, the "wake" region of microcracking is found to produce no effect, as well as the factors such as non-uniform microcrack density (decreasing with the increasing distance from the main crack tip).

Stochastic asymmetries of the microcrack field (with respect to the main crack) produce a noticeable mode II SIF on the main crack under mode I loading. This effect seems to be of importance: it may be partially responsible for kinking and irregular crack path.

Dynamic Microfracturing of Alumina

R. J. Clifton, G. Raiser, M. Ortiz, and H. Espinosa
Division of Engineering
Brown University
Providence, RI 02912

Abstract

The overall objective of this investigation is to understand and model the evolution of microcracks in ceramics. Because these microcracks often initiate, propagate, and coalesce in times that are less than the time resolution of quasi-static experiments, the experimental component of the investigation employs plate impact experiments which allow time resolution of a few nanoseconds. A so-called "soft recovery" plate impact experiment is used in which the ceramic specimen is subjected to a plane wave of short duration ($0.3\mu s$) and recovered afterwards to observe the damage induced by the known stress pulse. The rear surface motion of the target plate, monitored by means of an interferometer, provides a relatively sensitive measure of the damage that is being done by the propagating waves. The validity of proposed damage models is examined by comparing the predicted rear-surface motions based on these models with motions recorded in the experiments as well as by comparing the observed damage in the recovered specimens with that predicted by the models. The amplitude and duration of the pulse are varied to provide a data base for determining model parameters and for eliminating invalid models.

In the soft recovery experiment (See Fig. 1), a thin flyer plate impacts a target assembly consisting of a ceramic specimen backed by an impedance-matching momentum trap.

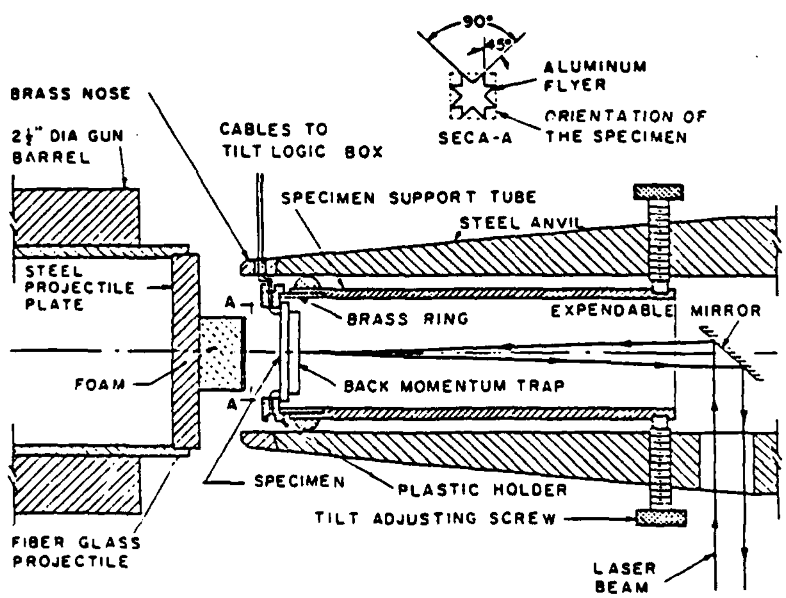

Figure 1. Experimental Configuration for Soft Recovery Experiment

A plane, square, compressive pulse is generated with a duration equal to the round-trip transit time for longitudinal waves propagating through the thickness of the flyer. Controlled tensile pulses of short duration ($20 - 60ns$) are obtained by providing a controlled gap between the specimen and the momentum trap. The duration of the reflected tensile pulse is equal to the time required to close the gap. A gap of the desired thickness is obtained by vapor deposition of thin layers of the required thickness at the corners of the interface. Once the gap is closed the compressive pulse propagates into the momentum trap and reflects from its rear surface as a tensile pulse. This tensile pulse cannot propagate back into the specimen because the momentum trap is not bonded to the specimen. Subsequent impacts by the flyer plate are prevented by the anvil which stops the projectile. Thus, the specimen is left essentially at rest and unstressed after its momentum has been transferred to the momentum trap.

Unloading waves from lateral boundaries are essentially eliminated within a central octagonal region of the specimen by making the flyer plate in the shape of an eight-pointed star. When such a flyer impacts a square specimen the cylindrical unloading waves emanating from the edges of the star are confined to corridors outside of the central octagonal region. Only spherical waves emanating from the corners of the star propagate through the central octagonal region. These waves attenuate strongly with distance of propagation and have negligible effect on the loading history at positions near the center of the specimen. Such elimination of the effects of waves reflected and diffracted from lateral boundaries allows the results of these experiments, including the induced damage, to be interpreted within the framework of one dimensional wave theory.

After the impact experiment has been performed the specimen is removed from its holder and sectioned to observe the damage induced. Thin sections are cut, both parallel to the impact face and perpendicular to the impact face. Microcracks in these thin sections are observed by transmission and scanning electron microscopy.

Such experiments have been conducted on specimens of high purity, high density Al_2O_3. Specimens have been recovered with no visible cracks up to the highest impact velocities used ($75m/s$). These impact velocities induce normal stresses (over $800MPa$) which are large relative to the tensile strength ($\approx 200MPa$) of the ceramic. Effective trapping of the longitudinal momentum and scattering of the lateral unloading waves are essential in maintaining the integrity of the specimen under these severe loading conditions.

The measured rear surface velocity for an experiment at an impact velocity of $75m/s$ is shown as a solid line in Fig. 2. The trace is obtained by automated processing of a laser displacement interferometer record, which is monitored by a LeCroy Waveform Digitizer. This Digitizer provides data points at intervals of $0.742ns$. Although the trace appears rather noisy, due in part to the numerical differentiation required to obtain the particle velocity from the recorded displacement, the main features of the velocity-time profile are evident. Nonuniformity of the rear surface motion due to the heterogeneity of microcracking appears to contribute to the lack of regularity of the recorded motion.

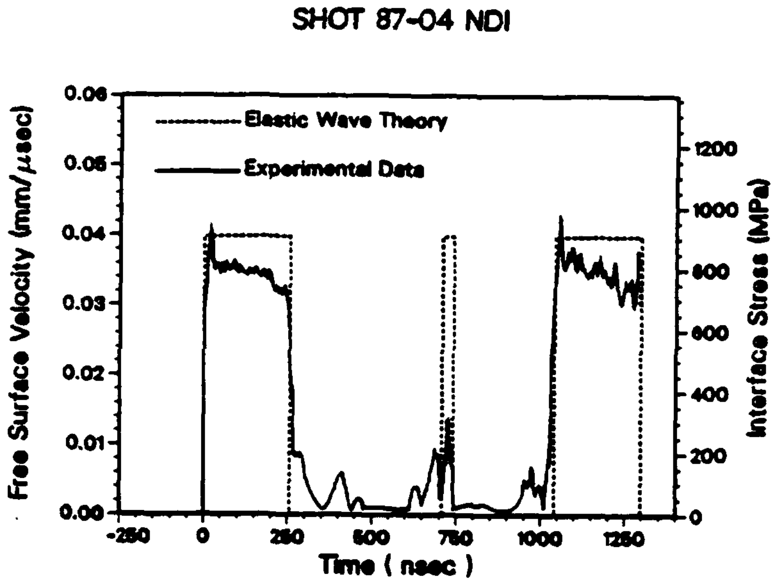

Figure 2. Velocity-Time Profile at Rear Surface of the Momentum Trap

The velocity decays during the reflection of the compressive wave from the rear surface of the momentum trap. This decay corresponds to attenuation of the incident compressive pulse due to damage which takes place in **compression**. Thus, it appears to be necessary to include the consideration of damage mechanisms which are activated by compressive longitudinal waves. The predicted velocity- time profile for fully elastic response is shown as dashed lines. The pulse with a duration of approximately $30ns$ is due to the reflected tensile pulse which arises from a small initial gap between the specimen and the momentum trap. The pulse that begins at approximately $1000ns$ is the reflected initial pulse after it has made one round-trip through the thickness of the momentum trap.

Interpretation of the experimental results has, so far, involved the use of elementary continuum damage models to predict the wave profiles of the waves transmitted to the momentum trap. These profiles are compared with those recorded in the experiments. The models include the rate dependence associated with the finite times that are required for the initiation and propagation of microcracks. Two types of analyses have been done: (i) a precursor decay analysis which gives, in closed form, the decay of the amplitude of the stress at the front of the tensile pulse and (ii) a full numerical solution of the mixed initial and boundary value problem corresponding to the conditions of the experiment. Only damage in tension has been considered. A numerical solution for the impact conditions of the experiment of Fig. 2 gives the rear surface velocity-time profile shown in Fig. 3. General features of the influence of dynamic microcracking during the tensile pulse are shown. These features include the tail on the initial compressive pulse and the strong attenuation of the second pulse. Reasonable values for such model parameters as initial crack spacing, fracture toughness, and initial crack length have been used; however, additional experiments and further development of the model are required before the model can be used to predict response under a wide range of impact conditions.

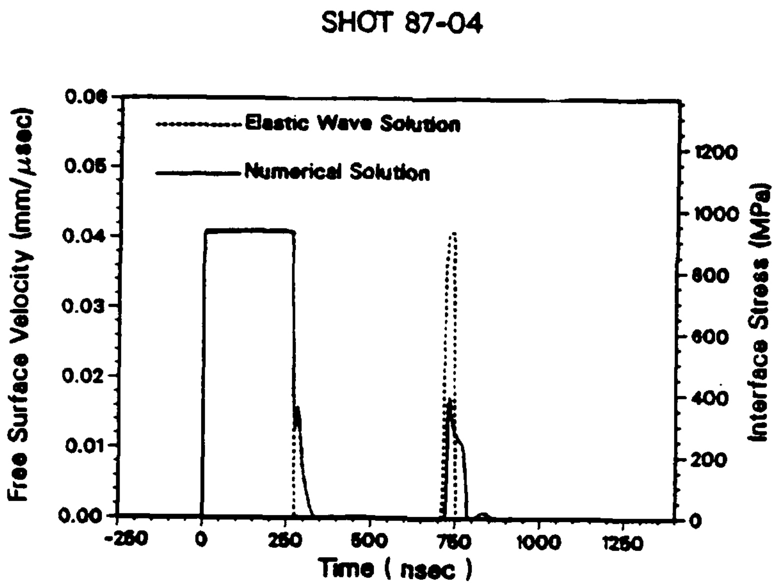

Figure 3. Computed Velocity-Time Profile at Rear Surface of the Momentum Trap

Specimens have been sectioned and thinned for transmission electron microscopy (TEM). An example of the damage observed in TEM is shown in Fig. 4, where a microcrack along a grain boundary facet appears as a thin white line. All microcracks observed lie along grain boundaries. In many cases the microcracks lie along only one facet of a grain boundary. In some cases the microcracks lie along two facets emanating from a triple point, as shown in Fig. 4. So far, insufficient data are available to establish either the densities of microcracks or any preferred orientation that they may have.

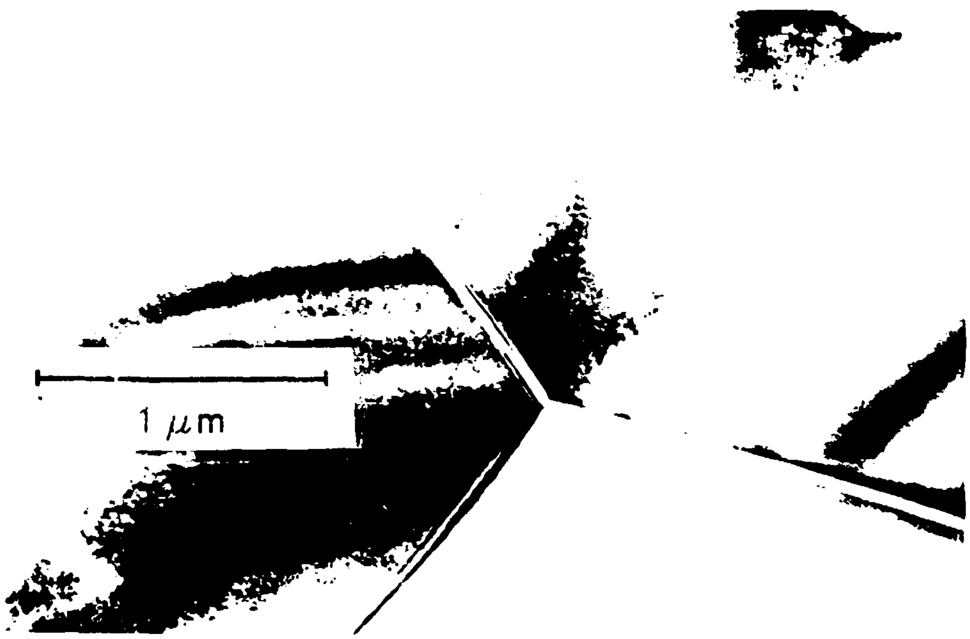

Figure 4. TEM Micrograph of Microcracks on Grain Boundary Facets

Acknowledgements

This research is supported by the Solid Mechanics Program of the National Science Foundation.

References

[1] Raiser, G., Clifton, R.J., and Ortiz, M., "A New Plate Impact Experiment for Studying Microcracking in Ceramics," (submitted for publication in the Army Symposium special issue of Mechanics of Materials)

[2] Espinosa, H., Ortiz, M., and Clifton, R.J., "Dynamic Finite Element Analysis of Stress-Wave-Induced Damage in Ceramics," (in preparation)

A New Probabilistic Model for Brittle Failure : Toughness and Reliability Evaluation

A. Chudnosky and B. Kunin
Department of Civil Engineering, Mechanics and Metallurgy
University Of Illinois at Chicago, Chicago, Illinois 60680

ABSTRACT

The significant role played by microdefects in the process of crack formation and growth is commonly recognized. We distinguish two extreme cases of the influence of defects on the fracture process; modeling of them requires essentially different formalisms.

Cooperative Fracture. The intensity of damage formed as a response to stress concentration at the tip of a propagating crack is much greater then the intensity of the pre-existing damage. The crack propagation is then inseparable from the evaluation of the accompanying damage. This strongly cooperative phenomenon allows successful modeling within the framework of Thermodynamics of Irreversible Processes (Crack Layer Theory).

Solo Crack Fracture. A crack propagates through a preexisting field of defects causing negligible changes to the field. The fluctuation of the microdefect field is directly reflected in stochastic features of fracture surfaces and also leads to scatter of experimentally observed fracture parameters, such as critical crack length, critical load, etc. A probabilistic approach is most adequate under these circumstances.

We give an outline of a recently developed probabilistic model which explains and predicts two characteristic features of brittle fracture in two-dimensional solids: (a) significant scatter of fracture parameters in identical tests (critical load, critical crack length, etc.), (b) dependence of conventional toughness parameters, (critical stress intensity factor K_{1c}, specific fracture energy 2γ, etc.) on the dimensions of the specimen ("scale effect").

Evaluations of the scatter of critical crack length, critical load, crack arrest depth, etc. are done using the concept of Crack Propagator. This is a probability $P(\underline{x},\underline{X})$ of a crack extending from a point $\underline{x}$ to a point $\underline{X}$. It is expressed as an average over all possible crack trajectories ω (connecting $\underline{x}$ and $\underline{X}$) of the conditional probability $P(\underline{x},\underline{X}|\omega)$ of the crack extending from $\underline{x}$ to $\underline{X}$ along a particular path ω. The concept of the set Ω of "all possible paths" is illustrated in Fig. 1.

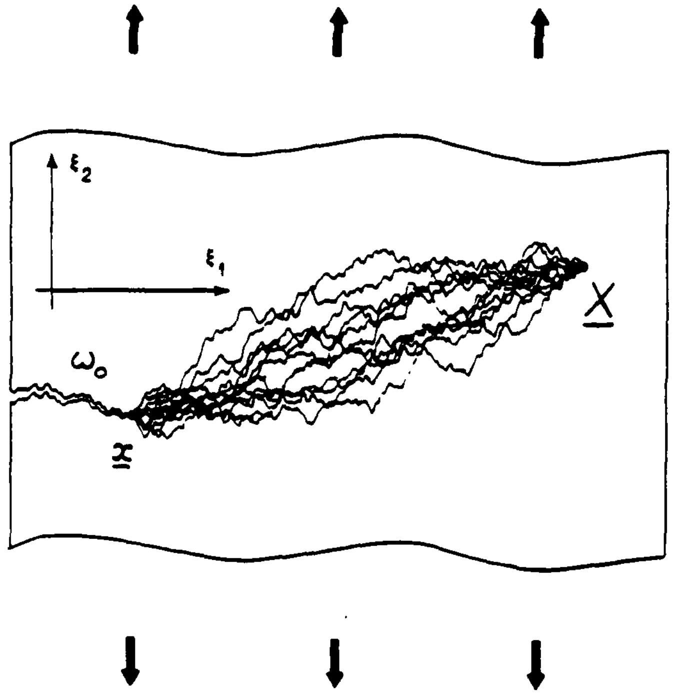

Fig. 1. A visualization of a set Ω of all possible crack trajectories extending a current crack (its tip at $\underline{x}$) and passing through another point $\underline{X}$.

Evaluation of $P(\mathfrak{x},\mathfrak{X}|\omega)$, (conditional crack propagator) is based on a Griffith type criteria of infinitestinual crack advance and certain assumptions about the fluctuating field of specific fracture energy. Evaluation of average of $P(\mathfrak{x},\mathfrak{X}|\omega)$ over Ω is reduced, in a diffusion approximation, to solving diffusion type partial differential equations. (By "diffusion approximation" we mean the assumption that crack trajectories can be modeled by Brownian paths.)

We demonstrate how the model is used to interpret successfully the data from a multiple fracture test experiment. A structural reliability parameter is suggested on the basis of the probabilistic model of brittle fracture.

Crack Stability in Simply Supported Four-Point and Three-Point Loaded Cracked Beams of Brittle Materials

by
Francis I. Baratta
and
William A. Dunlay

U.S. Army Materials Technology Laboratory
Watertown, MA 02172

ABSTRACT

Determination of fracture toughness of simple beam specimens of nonmetallic brittle materials is difficult to accomplish in an accurate manner. The techniques for introducing a sharp crack, which is required for accuracy, are not simple. In the usual situation, a ceramic specimen containing an initial blunt starter notch when loaded may sustain higher energy than the true fracture energy prior to catastrophic failure. Introduction of a sharp crack by fatigue loading at small magnitudes will fail to introduce a sharp crack, whereas an increase in loading may cause an overload at which spontaneous fracture then occurs. If this load at which fracture actually occurs is used to determine either energy-release rate or critical stress intensity, fictitiously high values may well result.

There have been successful ways of circumventing the above problems using beam specimens, but not without additional complexities associated with the starter crack geometries and the associated stress-intensity computations. This has been accomplished by introducing a 'chevron notch' as the crack starter, see for example Underwood et al.[1] Nevertheless, the use of a beam specimen of rectangular cross-section remains attractive to ceramists when determining Mode I fracture toughness (K_{Ic}) because of its simple shape and ease of loading, particularly at elevated temperatures. Such a specimen configuration has additional appeal because the stress-intensity relationship, as well as a related ASTM E399 test method[2] has already been developed and thus could be adopted to test brittle materials with some modifications.

Therefore, the first step in the attainment of a satisfactory fracture toughness test for brittle materials is to apply available theory to determine the feasibility of utilizing simple beam specimens. This then is the objective of this paper. Cracked four-point and three-point loaded beams such as those shown in Fig. 1 will be examined with regard to stable crack growth under load. This is accomplished by using crack-stability criterion already suggested[3] and developed,[4,5] but heretofore not applied in detail to exploit the use of simple through-cracked rectangular beam specimens.

Stability considerations are well presented elsewhere[4,5] and thus are not repeated here. However, Bluhm[5] noted that in no instance was there a tendency for stability throughout the range of α , where $\alpha = a/W$, under constant load for the limited through-cracked beam cases that he examined. Therefore, only the stability formulation under constant-deflection application is considered here. The applicable equation for the specific case of a cracked beam of rectangular cross-section is

$$\overline{S} = d^2\lambda_s/d\alpha^2 - (2/\lambda_t)(d\lambda_s/d\alpha)^2 \leq 0 \qquad (1)$$

note $\lambda_s = \delta_s BE/P$, $\lambda_t = \lambda_s + \lambda_m$ and $\lambda_m = \delta_m BE/P$,

where $\overline{S}$ is the stability parameter assuming constant-deflection loading or fixed-grip condition, λ_s and λ_m are the nondimensional specimen compliance and machine compliance respectively, and λ_t is the nondimensional total compliance of the test system including the testing machine and the loading fixtures.

When $\overline{S}$ becomes negative then stable crack growth (slow crack growth) is assured. Note that all that is required in Eq. (1) is the compliance of the specimen as a function of α , and the compliance of the testing machine and fixtures, etc. The nondimensional compliance of the testing machine and ancillary equipment, λ_m is usually obtained by experimental means and the compliance of the specimen can be obtained by theoretical techniques.[6]

Substituting the appropriate parameters from the compliance relationships into Eq. 1 and normalizing by $18\,(L_1/W)^2\,\alpha\,[f(\alpha)]_a^2$ and $18(S/2W)^2\alpha[f(\alpha)]_b^2$ for the four-point and three-point loaded beam, respectively, results in the following stability equations defined by $\overline{S_a}$ and $\overline{S_b}$:

$$\overline{S_a} = 2\,\frac{[f'(\alpha)]_a}{[f(\alpha)]_a} + 1/\alpha - \frac{36(L_1/W)^2\,\alpha\,[f(\alpha)]_a^2}{\lambda_s + \lambda_m} \tag{2}$$

and

$$\overline{S_b} = 2\,\frac{[f'(\alpha)]_b}{[f(\alpha)]_b} + 1/\alpha - \frac{36(S/2W)^2\,\alpha\,[f(\alpha)]_b^2}{\lambda_s + \lambda_m} \tag{3}$$

where $[f(\alpha)]_{a,b}$ is the fourth-order polynomial function included in the definition of K_I, where the subscript a represents a four-point loaded beam and b represents a three-point loaded beam; and $[f'(\alpha)]_{a,b}$ is the first derivative of $[f(\alpha)]_{a,b}$.

Machine compliance is an important consideration in the design of a stable specimen test system when attempting to determine fracture toughness of brittle nonmetallic materials. Clausing indicates that "the compliance of 1.5 is typical of very stiff loading systems, such as a bolt that directly opens the crack. The compliance of 600 is typical of a rather flexible grip system in a tension testing machine."[4] Frame stiffnesses of many present-day testing machines, ancillary transducers and fixtures within the load train can result in attainable values of in the range of 20 to 30. Therefore, Eqs. (2) and (3) were computer programmed so that the effect of machine compliance from 0 to 600 on stability with various ratios of L_1/S and S/W could readily be examined.

The four-point loaded beam with a support-span ratio of S/W = 4 is first examined, allowing the loading span L_1/S to take on the two commonly used ratios by ceramists of 1/4 and 1/3. As previously mentioned, the nondimensional machine compliance was varied from a range of 0 to 600.

These results are presented in Figs. 2(a) and 2(b). They show the stability parameter $\overline{S}_a$ for a four-point loaded beam as a function of crack-length ratio α and load-span ratios L_1/S of

1/4 and 1/3. The reader is reminded that the more negative S_a becomes, the greater the possibility that stability occurs. Therefore, as expected, as λ_m is increased, $\overline{S}_a$ becomes more positive thus becoming less stable, as shown in Figs. 2(a) and 2(b). It is also evident that $\overline{S}_a$ for the 1/3 loading-span ratio, shown in Fig. 2(b), tends to be more stable than that of 1/4, shown in Fig. 2(a) for comparable values of λ_m.

The limiting case of the four-point loaded beam is that of the three-point loaded beam, i.e., $L_1/S = 1/2$. This configuration is also examined, paying particular attention to the commonly used span ratios S/W of four and eight. Again, machine compliance was varied from 0 to 600. These results are shown in Figs. 3(a) and 3(b).

As in the case of the four-point loaded beam, as λ_m is increased, $\overline{S}_b$ becomes less stable, as shown in Figs. 3(a) and 3(b).

A comparison of the results given in Figs. 3(a) and 3(b) appears to indicate that at higher values of λ_m the three-point loaded beam having a support-span ratio of eight has greater stability than one having a support-span ratio of four. The superiority of either support-span ratio over the other is uncertain and is subsequently explored in greater detail.

Returning to Fig. 2, it seems that a larger span-loading ratio than either 1/4 or 1/3 for a four-point loaded beam might result in a more stable specimen. Therefore, L_1/S of 3/8 was arbitrarily chosen as a practical span-loading ratio while examining $\overline{S}_a$ and allowing λ_m to vary from 0 to 40 (this includes the attainable range of 20-30), and also varying S/W from three to eight. For the sake of brevity, these data are not presented, but the resulting threshold of stability parameter determined from the condition $\overline{S}_a = 0$ was calculated. These results, shown in Fig. 4(a), will subsequently be discussed.

Because of the uncertainty regarding the three-point loaded beam and the best span length to yield optimum stability, a parametric study was conducted comparable to that described above. These results are shown in Fig. 4(b). Again, λ_m between

0 and 40 was included in the study while varying the three-point loaded-beam support-span ratio from four to eight. This family of curves is approximate since the coefficients used in the polynomial function $[f(\alpha)]_{\bullet}$ describing the stress-intensity factor K_I applicable to a three-point loaded beam was obtained by interpolating between S/W of four and eight. Nevertheless, these approximate results shown in Fig. 4(b) are sufficiently accurate to portray general trends and allow one to choose an optimum specimen geometry.

Comparison of the threshold of stability parameter α_0 presented in Figs. 4(a) and 4(b) shows that the three-point loaded beam has a desirably smaller numerical value than that of the four-point loaded beam of the same compliance and support-span-length ratio.

In particular, an S/W of between five and six minimizes α_0 when λ_m is between 10 and 20 for a three-point loaded beam, see Fig. 4(b). Such a configuration results in $\alpha_0 = 0.44$ when $\lambda_m = 10$ and $\alpha_0 = 0.49$ when $\lambda_m = 20$. These configurations represent possible feasible systems for the determination of fracture-toughness for brittle materials.

On the other hand, the four-point loaded beam having a λ_m of 10 or greater does not appear to yield small enough α_0 values to insure enough stable crack growth for a usable fracture toughness test.

Experimental verification of the theoretical predictions of stability for both the four-point and three-point loaded beams was accomplished by determining and observing load-displacement curves of a quasi-brittle beam of polymethylmethacrylate (PMMA), having various initial crack length ratios α . Such beams had cross-sectional dimensions of W = 11.63mm and B = 8.13mm with a support span length of 80mm, thus S/W = 6.88. The tests were conducted in a constant deflection loading system that resulted in λ_m of 5.15 for the given beam width B and Young's Modulus of 3.17 GPa. The four-point loaded beam had a beam loading ratio L_1/S of 3/8.

Unstable and stable crack advancement was readily observed and verified via the measured load displacement plots. Unstable growth was apparent from the typical linear load-displacement plot and resulting catastrophic failure; whereas stable growth was exhibited by continuous nonlinear behavior after crack advancement.

Critical stress intensity or fracture toughness was determined as a function of α for both of the beam systems described above and by two methods: the first method entailed the knowledge of the stress intensity factor[7] as a function of α and the second utilized the energy enclosed by the load-displacemdent curve. These results for the four-point and three-point loaded beams are shown in Fig. 5(a) and Fig. 5(b), respectively. The solid vertical line in each figure indicates the experimental threshold of stability value; i.e., α_0, and for the four-point loaded beam it is approximately 0.46 as compared to the theoretically predicted result of 0.52 and α_0, the experimental value for the three-point load beam, is approximately 0.36 as compared to the theoretical prediction of 0.42. It is reasonable to expect that the experimental values of α_0 would indeed result in underestimates of the theoretical results because some plasticity will occur at the crack tips of a quasi-brittle beam material such as PMMA and thus enhance the threshold of stability and stable crack growth.

It is interesting to note that fracture toughness appears to be variable as a function of α in Fig. 5(a) and 5(b) when $\alpha \leq \alpha_0$. However, as $\alpha \geq \alpha_0$ fracture toughness approaches a constant value of approximately 1.1 $MPa/m^{1/2}$ (1.0 ksi $in.^{1/2}$) which not only agrees quite well with results in the literature[8] but indicates that crack stability is a necessary requirement for a successful candidate test system for the fracture toughness determination of brittle materials.

References

1. Underwood, J.H., Freiman, S.W. and Baratta, F.I., Chevron-Notched Specimens: Testing and Stress Analysis, ASTM Spec. Tech. Pub. 855, Amer. Soc. Test. and Mat., Philadelphia (1984).

2. ASTM Standards, Amer. Soc. for Test. and Mat., E399-83, 680-715 (1987).

3. Bluhm, J.I., "Fracture Arrest," Fracture, ed. H. Liebowitz, Academic Press, NY, 1-63 (1969).

4. Clausing, D.P., "Crack Stability in Linear Elastic Fracture Mechanics," Int. J. Fract. Mech., 5, 211-226 (1969).

5. Bluhm, J.I., "Stability Considerations in the Generalized Three Dimensional 'Work of Fracture' Specimen," Fracture 1977, 3, ICF4, Waterloo, Canada, 409-417 (1977).

6. Paris, P.C., "The Mechanics of Fracture Propagation and Solution to Fracture Arrestor Problems," Document D-2-2195, The Boeing Co., Seattle, WA (1957).

7. Brown, W.F., Jr. and Srawley, J.E., Plane Strain Crack Toughness Testing of High Strength Metallic Materials, ASTM Spec. Tech. Pub. 410, Amer. Soc. for Test. and Mat., Philadelphia, 13 (1966).

8. Margolis, R.D., Dunlap, R.W. and Markovitz, H., "Fracture Toughness Testing of Glassy Plastics," ASTM Spec. Tech. Pub. 601, Amer. Soc. for Test. and Mat., Philadelphia, 391 (1976).

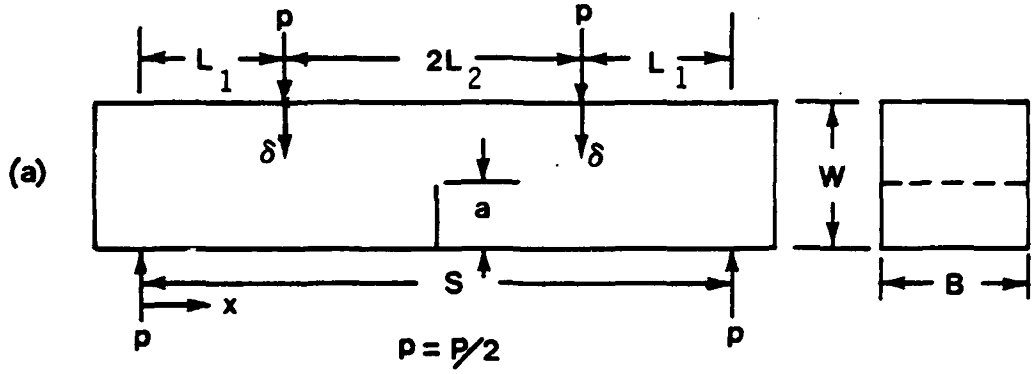

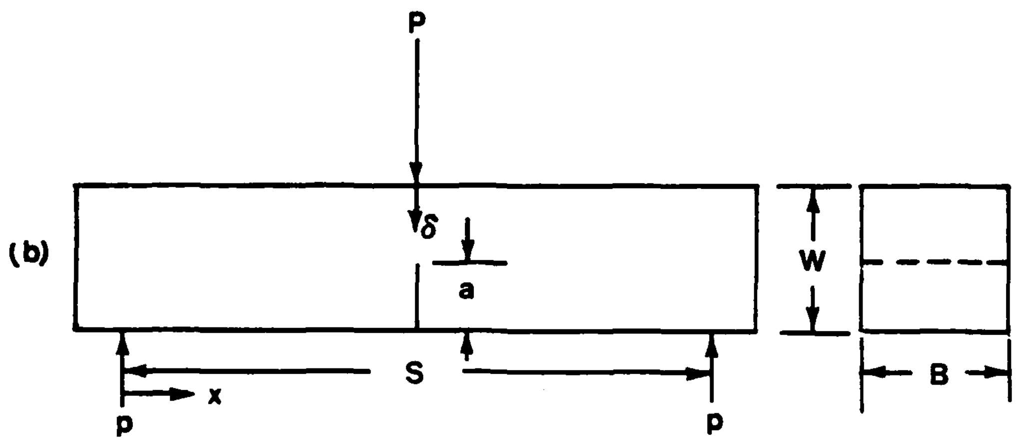

Fig. 1. Four-Point and Three-Point Beam Geometries

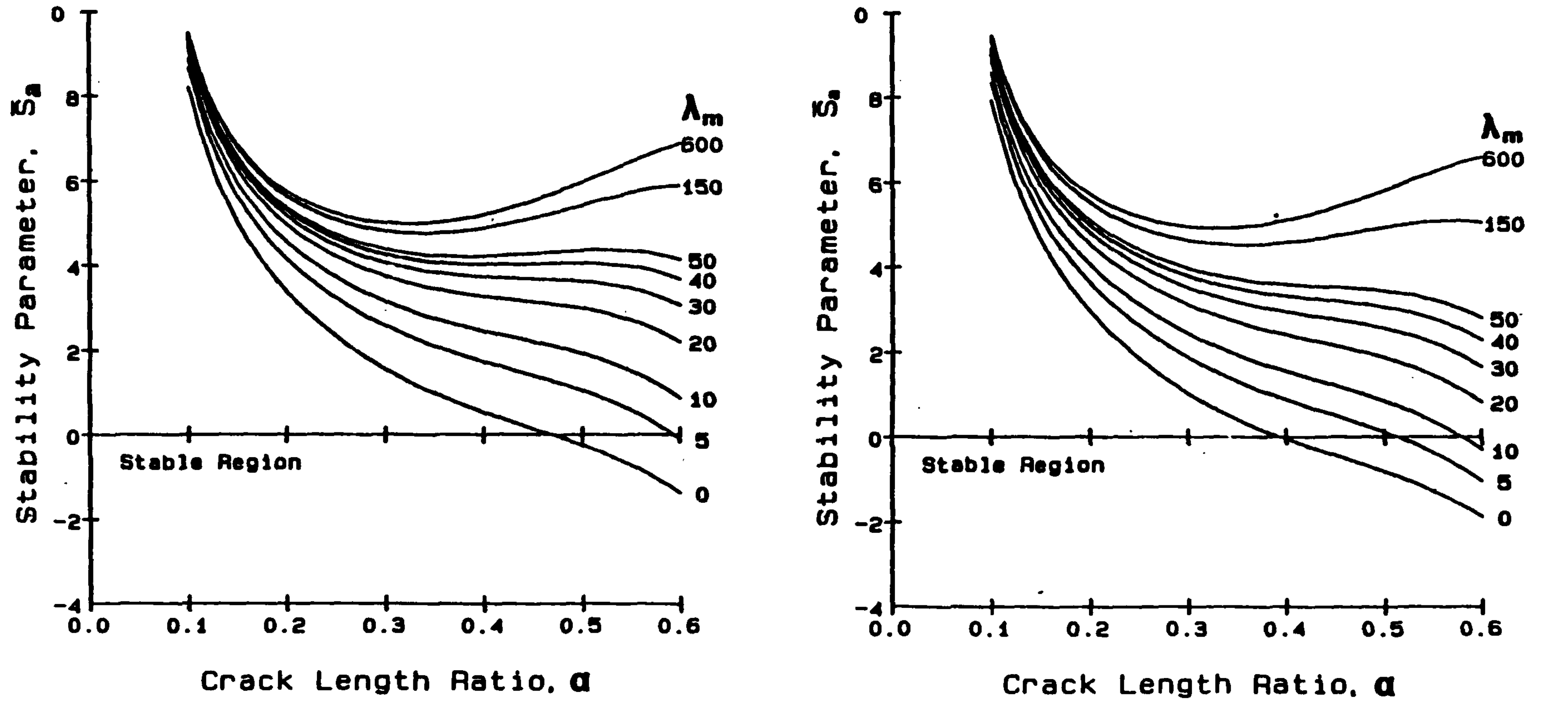

(a)

(b)

Fig. 2-Stability parameter for a four-point bend specimen with $S/W = 4$; (a) $L_1/S = 1/4$, (b) $L_1/S = 1/3$

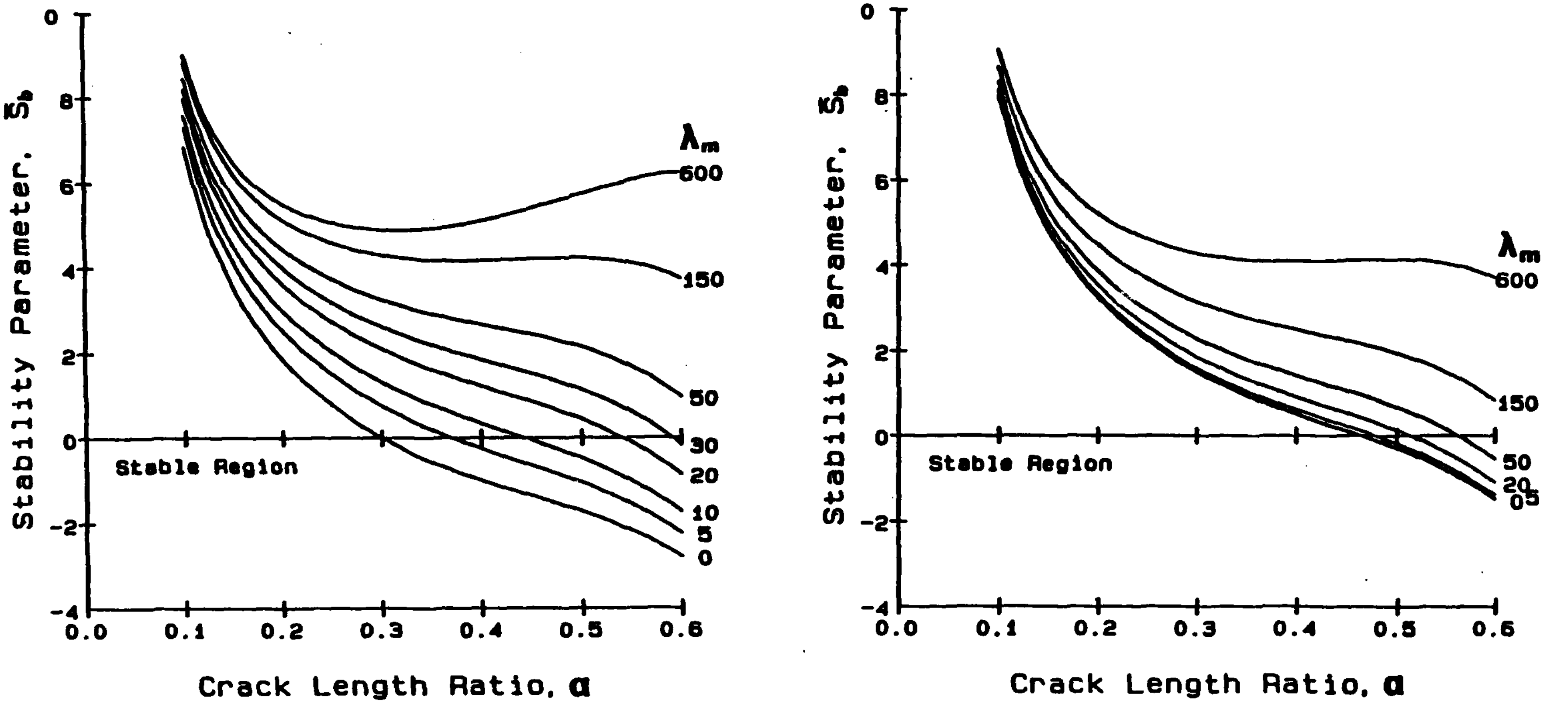

(a) (b)

Fig. 3-Stability parameter for a three-point bend specimen;
(a) S/W = 4, (b) S/W = 8

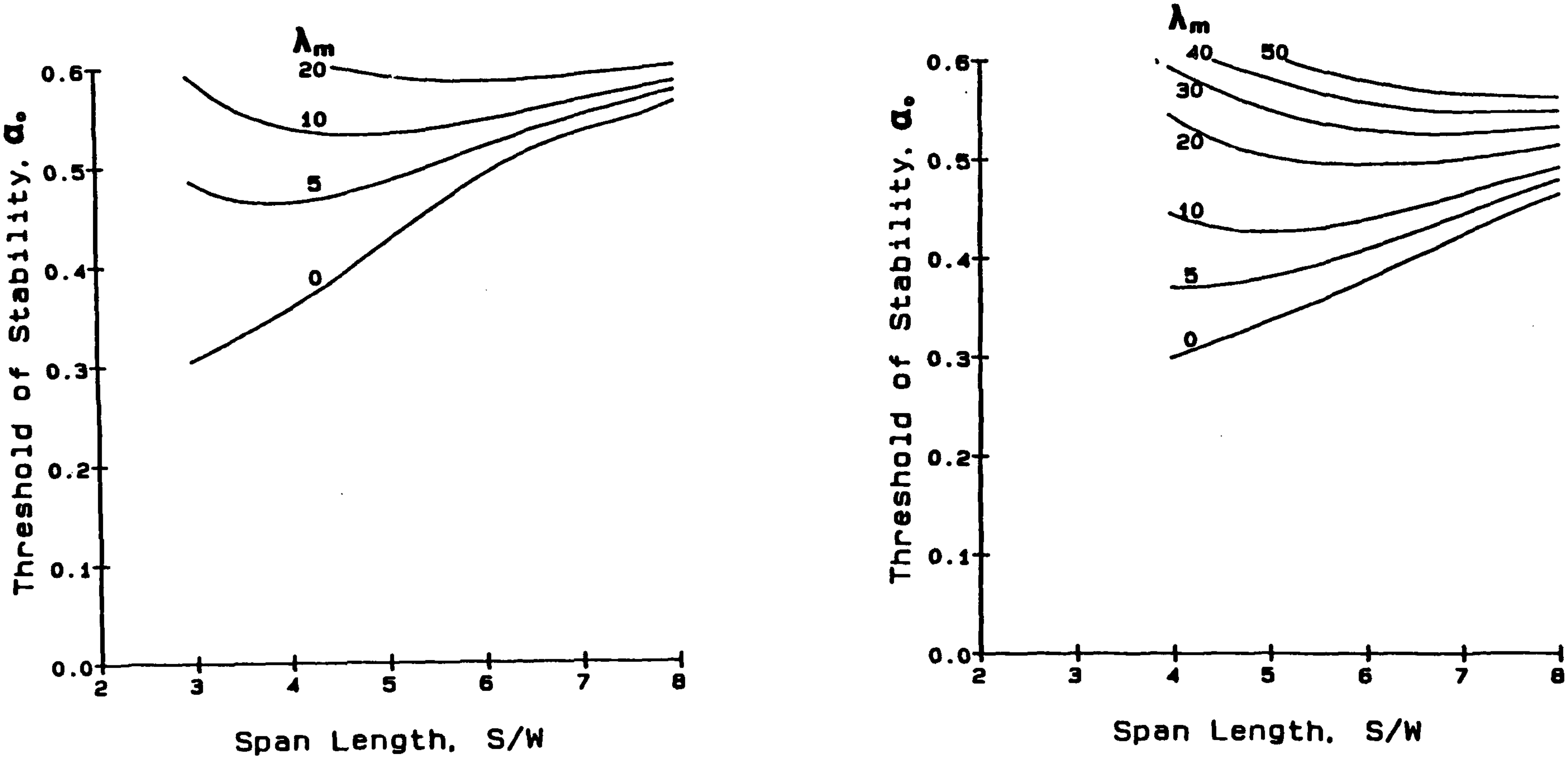

(a) (b)

Fig. 4- Threshold of stability for four-point and three-point loaded beams as a function of support-span length; (a) four-point loaded beam with L /S = 3/8, (b) three-point loaded beam

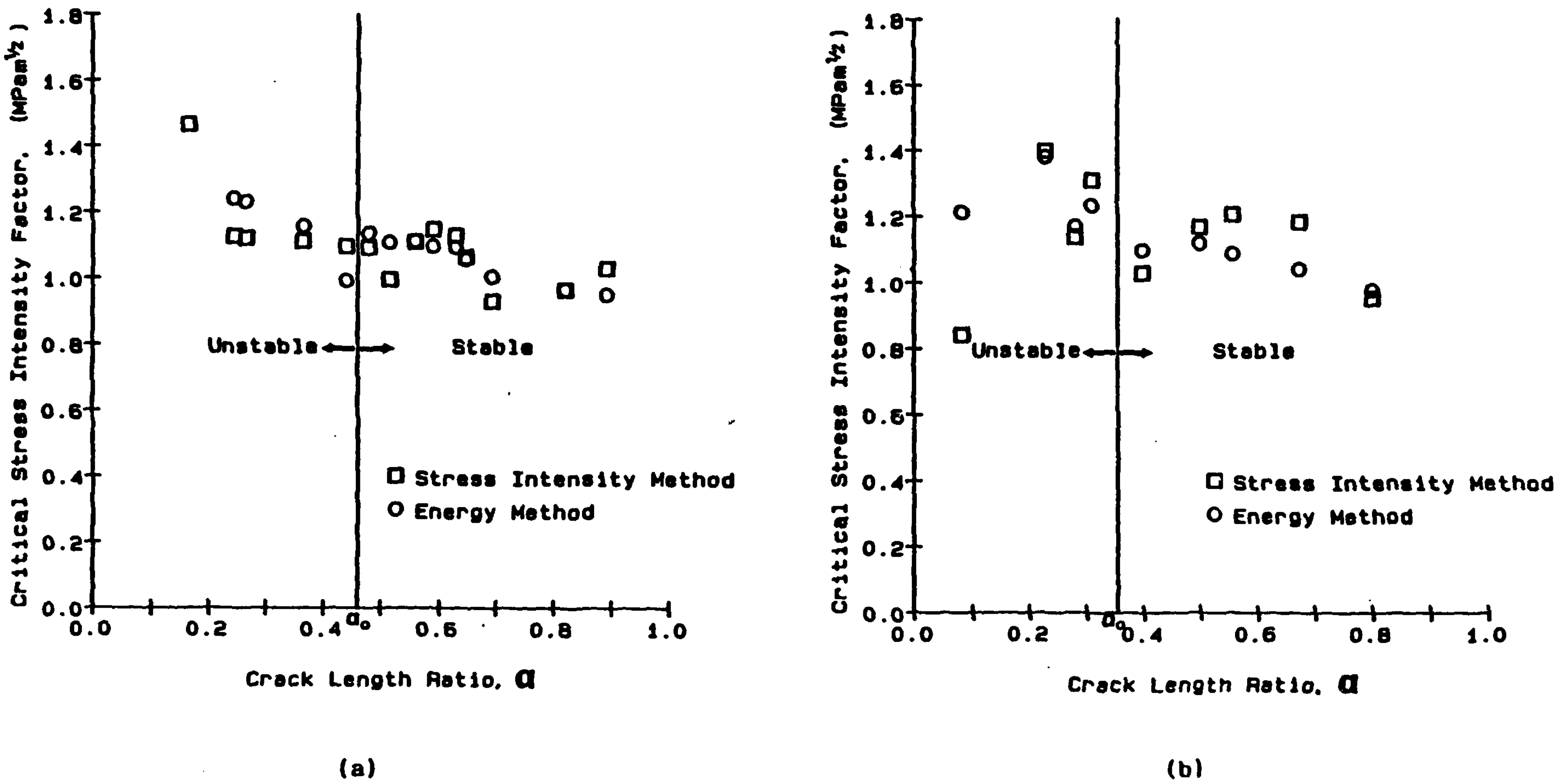

Fig. 5-Experimental threshold of stability parameter for:
(a) four-point loaded beam with $L_1/S = 3/8$, and (b) three-point loaded beam $\lambda_m = 5.15$

TIME DEPENDENT RESPONSE OF SEMIBRITTLE CERAMICS

D. Krajcinovic and A. Stojimirovic

CEMM Department
University of Illinois at Chicago, Chicago, IL 60680, USA

ABSTRACT

The paper presents a simple micromechanical model for the creep deformation of polycrystalline vitreous alumina. The inelastic strain is attributed to the grain boundary sliding and intergranular microcracks.

INTRODUCTION

As a popular refractory material ceramics are often exposed to relatively high stress levels and very high temperatures for prolonged periods of time. Consequently, the components manufactured from ceramics are especially sensitive to creep deformation and creep rupture.

The macroscopic (phenomenological) signature of the process known as creep is a gradual increase in deformation at constant stress levels. Thus, the elastic stretching of the crystalline lattice is responsible only for a fraction of the total deformation. A variety of distinctly different mechanisms of the irreversible rearrangements of the mesostructure of the solid such as: grain boundary sliding, grain boundary and bulk diffusion, nucleation and growth of voids and grain size cracks, etc. are other significant contributors to the deformation process. The relative significance of a particular mechanism varies in dependence of the crystalline structure (chemical composition, grain size, presence of the second phase, precipitates, etc.) and the temperature and stress levels.

ANALYTICAL MODEL

1.Micro-mechanism

At the considered temperature and stress level the Al_2O_3 grains remain elastic. The only source of inelastic deformation are: the grain boundary *sliding and the intergranular* microcracks propagating from the triple points. The microcracks are nucleated from very small defects at triple points as a result of the wedging action associated with the sliding over grain boundaries.

The major problem in describing the conditions leading to the propagation of the initial defect is related to deriving a believable estimate of the stress intensity factor at the tip of the wedge crack (Fig 1).

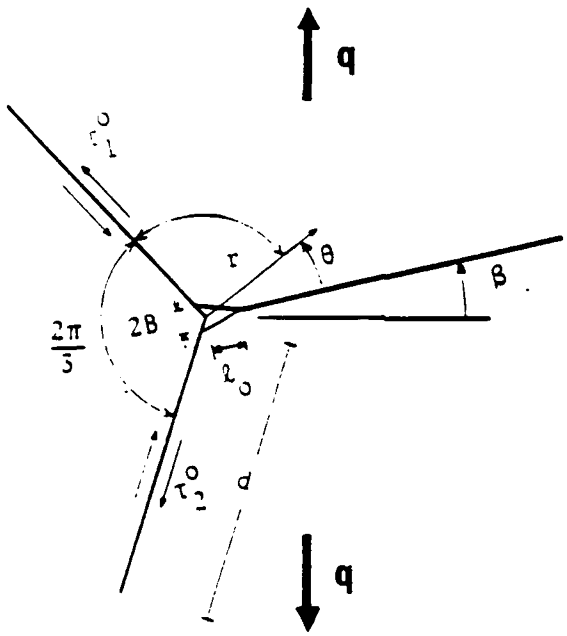

Fig.1 The geometry of triple grain junction

The actual problem, due to the crystalline anisotropy (Tvergaard and Hutchinson 1987) and the presence of the two inclined GBs is not amenable to a closed form, analytical solution. For the present purposes it appears reasonable to start with a rather rough estimate assuming the surrounding material to be isotropic. Moreover, the influence of the sliding GBs will be assessed using finite element (FE) computations. Their effect will, subsequently, be introduced as a correction of a simple formula available in the literature for a wedged crack under the influence of far field tensile stresses. The stress concentration at the far end of the crack may in that case be written (Das, Marcinkowski 1972) as a sum of two terms

$$K = C \frac{EB}{4(1-\nu^2)} (\pi a)^{-\frac{1}{2}} + \sigma_n^o (\pi a)^{\frac{1}{2}} \tag{1}$$

representing the contributions of wedging (2B being the crack opening at the TJ) and the far field tensile stresses ($\sigma_n^o = q \cos^2 \beta$) being the stress normal to the GB along which the crack propagates - assumed to be constant). Also, $2a = l_0$ is the length of the slit. The coefficient C is introduced to account for the boundary conditions along the sliding GB. Using both a semi-analytical procedure based on the superposition principle (Fig 2) and the enhanced finite elements, computations indicate that C=1 for $2a < l/3$, while for $2a=l$, C = 0.424. The residual stresses resulting from the thermal anisotropy (Evans, 1984) will be neglected hereafter.

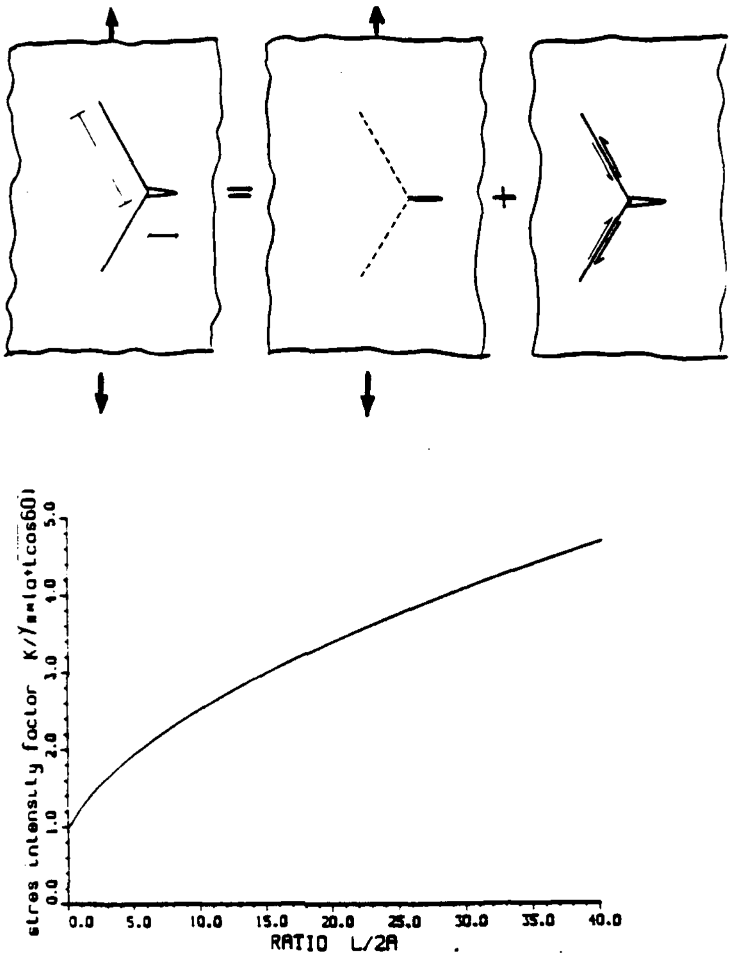

Fig.2 Superposition principle and computed SIF

The wedge opening 2B is, obviously, directly related to the amount of the shear deformation over the inclined GBs. The viscous glide of the glassy GB phase is, in general, resisted by the viscosity of the phase, irregularities of the GB, particles along the GB and keying of the grains (see Raj 1975, Riedel, 1987). Even though the keying action may have in the case of thin GB layers a rather significant effect on the sliding (see Tvergaard 1984), for simplicity, it will be assumed than for a thicker GB phase it can be neglected. Hence, the displacement discontinuity along the sliding GB can be directly related to the shear stress associated with the externally applied tensile tractions

$$u(t) = \tau^{0} / \eta \tag{2}$$

where

$$\eta = \frac{kTp^4}{8\Omega(\delta D_b + pD_v/5)\lambda^2} \tag{3}$$

is the friction coefficient depending (see Riedel 1987) on the size and distance between particles p and λ, GB and volume diffusion coefficients δD_b and D_v, atomic volume Ω and temperature T.

From (2) it is possible to determine the wedge opening as a function of the shear stresses resolved on the sliding grain boundaries, friction coefficient and time as

$$B(t) = \frac{3}{9\eta} qt \cos 2\beta \tag{4}$$

leading to the expression for the SIF at the tip of the crack in form

$$k(t) = kt + k_0 = C \frac{3 Eq \cos 2\beta}{16\pi \eta \sqrt{2a}} t + \frac{1}{2} q \sqrt{2a} \cos^2\beta \tag{5}$$

This stress is simultaneously relaxed by the process of diffusion. Modifying the Evans, Rice and Hirth model (1980), the final expression for the stress reads

$$\sigma_y(t) = 0.89 \, kt \, (\alpha t)^{-1/6} + 0.74 \, k_0 \, (\alpha t)^{-1/6} \tag{6}$$

where

$$\alpha = \frac{G\delta D_b \Omega}{2(1-\nu)\kappa T} \tag{7}$$

Equating the stress at the interactive distance b_0 computed from (6) with the ideal strength it becomes possible to derive a condition for the crack growth in the form of hypersurface

$$F(\beta, t) = \frac{k(\beta, t)}{\sqrt{b_0}} - m \left(\frac{E\gamma_s}{b_0} \right)^{1/2} = 0 \tag{8}$$

in the space of triple point geometry and time (for constant traction q). From the condition (8) it is possible to show that the growth of the crack is stable. Moreover, condition (8) leads to an algebraic relation from which the crack length can be determined as a function of time, geometry of TJ and the material parameter α (7).

The growing crack is finally arrested at the far end triple joint. At this point additional g.b. sliding is required in order to satisfy the kinking condition

$$F_k(\beta,t) = \sigma_{max}(\beta + \pi/3, t) - \sigma_{id} = 0 \tag{9}$$

where σ_{id} is the bond rupture strength defined as the second term on the right hand side of (8). In (9) σ_{max} is computed analyzing Cotterell and Rice (1980) procedure.

Consequently, assuming that the angle β is perfectly random it is possible to compute at each time the length of each straight and kinked crack. Utilizing conventional fracture mechanics procedures, in conjuction with the superposition principle shown in Fig 2, it is then possible to compute the eigenstrains (i.e. crack opening displacements) within the representative volume element.

2.Compression

In the case of compression the mechanism must be somewhat modified (Fig 3).

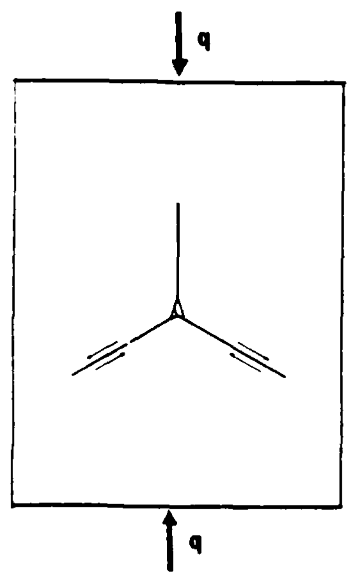

Fig.3 Triple grain junction in compression

Consequently, the second term in (1) drops out. The rest of the procedure is conceptually identical as in the preceding case.

4. Results

In computing results it is necessary to specify two material parameters η and α given by (3) and (7), respectively. These two material parameters depend, as shown, on the microstructure of the microstructure of the ceramics and will vary from one case to another. The data for the friction coefficient were taken from the literature (Riedel 1987) and the final results were compute with α as a parameter. The verification of the suggested model depends, then, on determining whether the ratio of inelastic strains in tension and compression matches those measured in experiments. While the first data we were able to locate seem to confirm our analysis we are still in process of finding experimental data for tension and compression on identical Al_2O_3 specimens. The inelastic strain is plotted as a function of time in Fig 4 with α as a parameter.

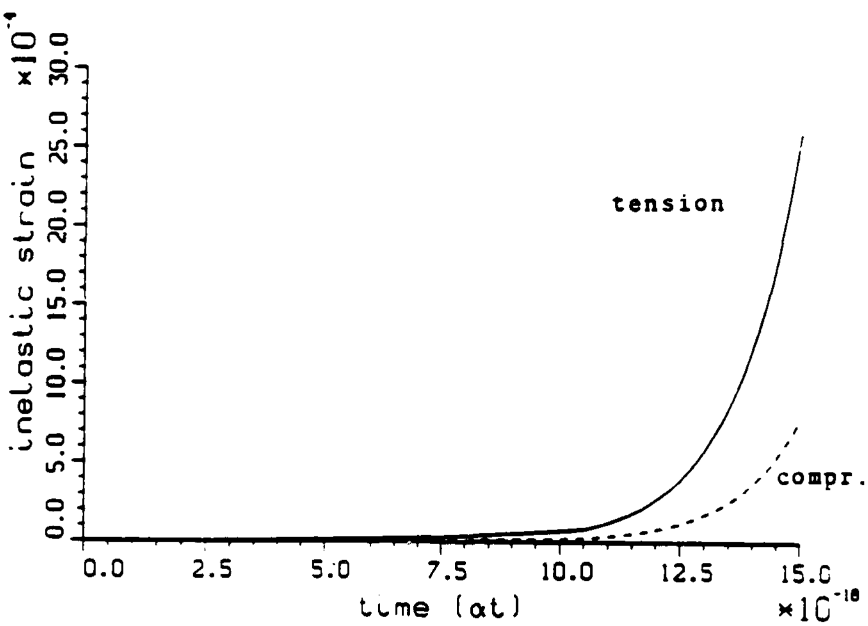

Fig.4 Macroscopic stress-strain curve for the cases of uniaxial tension (solid line) and compression

ACKNOWLEDGEMENT

The authors gratefully acknowledge the financial support rendered by the National Science Foundation, Directorate for Engineering, Solid and Geo-Mechanics Program research grant to the University of Illinois at Chicago which made this work possible.

REFERENCES

Evans, A.G., J.R. Rice and J.P. Hirth (1980). Suppression of cavity formation in ceramics: prospects for superplasticity. *J. Amer. Ceramic Soc.*, 31, 368-375.

Frost, H.J. and F.M. Ashby (1982). Deformation-Mechanism Maps. *The Plasticity and Creep of Metals and Ceramics* Pergamon Press, London, UK.

Horii, H. and S. Nemat-Nasser (1983). Overall moduli of solids with microcracks: load-induced anisotropy. *J. Mech. Phys. Solids*, 31, 155-171.

Raj, R. (1975). Transient behavior of diffusion-induced creep and creep rupture. *Metal. Trans. A*, 6A, 1499-1509.

Riedel, H. (1987). *Fracture at High Temperatures* Springer-Verlag, Berlin.

FRACTURE TOUGHNESS AND FATIGUE CRACK PROPAGATION IN CERAMICS USING THE 'DOUBLE ANVIL' GEOMETRY

I. Bar-On, J.T. Beals, C.M. Murray, and B.F. Hantz IV, Worcester Polytechnic Institute, Worcester, MA 01609

Fracture toughness and fatigue tests of ceramics are typically complicated by unstable crack growth following crack initiation. Hence the specimen geometries which are successfully used for crack initiation and propagation studies of metallic materials, cannot be adopted easily for similar studies of ceramic materials.

The double cantilever beam and double torsion specimens which have been employed for fracture testing of ceramics both use large amounts of material. Lately Nose and Fujii [1] proposed the loading geometry shown in Figure 1, which allows the controlled precracking of ceramics using a small bend bar. This loading geometry, the Double Anvil configuration, has been used in the present work for the precracking of fracture toughness specimens and for static and cyclic fatigue testing of ceramic materials.

Results of the finite element analysis of specimens loaded in the 'Double Anvil' configuration are summarized in Figure 2. These results show a strong dependence of the stress intensity on the specimen length and on the load application. Three conditions were investigated: 1) the anvils were modeled as rigid dies; 2) the load was distributed uniformly over the top die and; 3) the two different materials for die and specimen were considered explicitly. Figure 2 shows that there are large differences between the results for the rigid die and the distributed load assumptions whereas the results for the two material assumption are reasonably close to the distributed load case.

The 'Double Anvil' geometry was used for precracking of bend bars of alumina, silicon nitride and yttria stabilized zirconia. The specimens were subsequently broken in three point bending for fracture toughness determination. Good agreement was obtained between these fracture toughness values and those determined using indentation, controlled surface flaw or short bar techniques, provided the crack front was straight and the crack length was appropriate.

Static and cyclic fatigue crack propagation experiments for alumina and silicon nitride were conducted at room temperature using the double anvil configuration. The static fatigue propagation rates of alumina agree with those previously published. The static fatigue results of silicon nitride and of alumina show a load dependence.

The cyclic fatigue crack propagation rates of silicon nitride and alumina show a similar load dependence. This load dependence could be explained by increasing R-curve behavior for alumina. For silicon nitride however no R-curve behavior would be expected. For a further investigation of this question static tests of alumina bend bars in four point bending were performed and similar tests for silicon nitride are in progress. For alumina a load dependence was observed also for this test geometry.

A comparison of the fatigue crack propagation rates under static and cyclic loading shows that experiments performed at the same maximum load fall on the same line of and da/dt versus delta K (or K_{max}) graph. The crack propagation rates under static loading are lower by 1-2 orders of magnitude however.

The double anvil configuration seems to be a promising candidate for fracture toughness and fatigue crack propagation studies of ceramic materials. The results of our investigations however point at additional questions as to the fatigue crack propagation mechanism in these ceramic materials as expressed by the load dependence of the propagation rates.

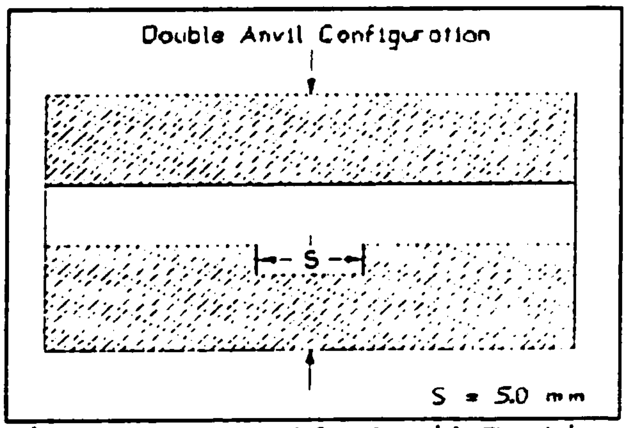

Figure 1 - Double Anvil Testing Geometry.

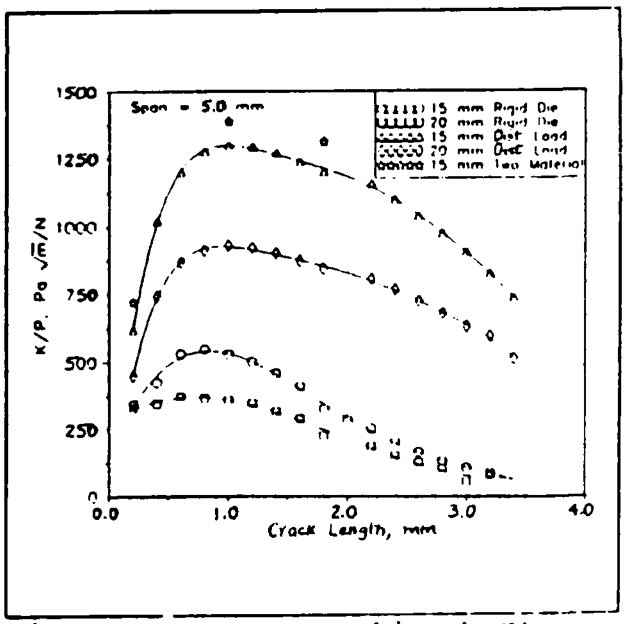

Figure 2 - Normalized Stress intensity versus crack length comparing boundary conditions.

REFERENCES

1. T. Nose, T. Fuji, "Evaluation of Fracture Toughness for Ceramic Materials by a Sinale-Edge-Precracked-Beam Method", J. Am. Cer. Soc., 71 [5] 328-333 (1988).

2. George D. Quinn, "Delayed Fracture of Commercial Vitreous Bonded Alumina", J. Mater. Sci., 22, 2309-2318 (1987).

3. B.J. Pletka, S.M. Weiderhorn, "A Comparison Failure Prdictions by Strength and Fracture Mechanics Techniques", J. Mat. Sci., 17, 1247-1268 (1982).

GENERAL OBSERVATIONS ON THE FAILURE OF COMPOSITES

by

B. W. Rosen

Materials Sciences Corporation
Spring House, Pennsylvania

Abstract was not available at time of publication.

TENSION FATIGUE ANALYSIS AND LIFE PREDICTION FOR COMPOSITSE LAMINATES

T. Kevin O'Brien
Aerostructures Directorate
U.S. Army Research and Technology Activity
Aviation Systems Command (AVSCOM)
Langley Research Center
Hampton, Virginia 23665-5225

As composite materials are considered for primary structural applications, the need to predict their fatigue behavior becomes important. For continuous fiber reinforced composites, delamination is the most commonly observed damage mechanism. Fracture mechanics analyses of delaminations have been shown to provide generic characterizations of delamination onset and growth. However, fatigue life prediction requires not only a characterization of delamination behavior, but an assessment of the consequence of fatigue damage as well. The purpose of this study was to develop a fatigue life prediction methodology for composite laminates subjected to tension fatigue loading that incorporates both the generic fracture mechanics characterization of delamination as well as the assessment of the influence of damage on laminate fatigue life.

A tension fatigue life prediction methodology for composite laminates is presented. Tension fatigue tests were conducted on quasi-isotropic and orthotropic glass epoxy, graphite epoxy, and glass/graphite epoxy hybrid laminates. Edge delamination onset data were used to generate plots of strain energy release rate as a function of cycles to delamination onset. These plots were then used along with strain energy release rate analyses of delaminations initiating at matrix cracks to predict local delamination onset.. Stiffness loss was measured experimentally to account for the accumulation of matrix cracks and for delamination growth. Fatigue failure was predicted by comparing the increase in global strain resulting from stiffness loss to the decrease in laminate failure strain resulting from delaminations forming at matrix cracks through the laminate thickness. Good agreement between measured and predicted lives (see figures) indicated that the through-thickness damage accumulation model can accurately describe fatigue failure for laminates where the delamination onset behavior in fatigue is well characterized, and stiffness loss can be monitored in real time to account for damage growth.

ACKNOWLEDGEMENT

This work was performed as part of a Memorandum of Understanding (MOU) on Helicopter Aeromechanics and Structures between the U.S. Department of the Army and the Italian Ministry of Defense.

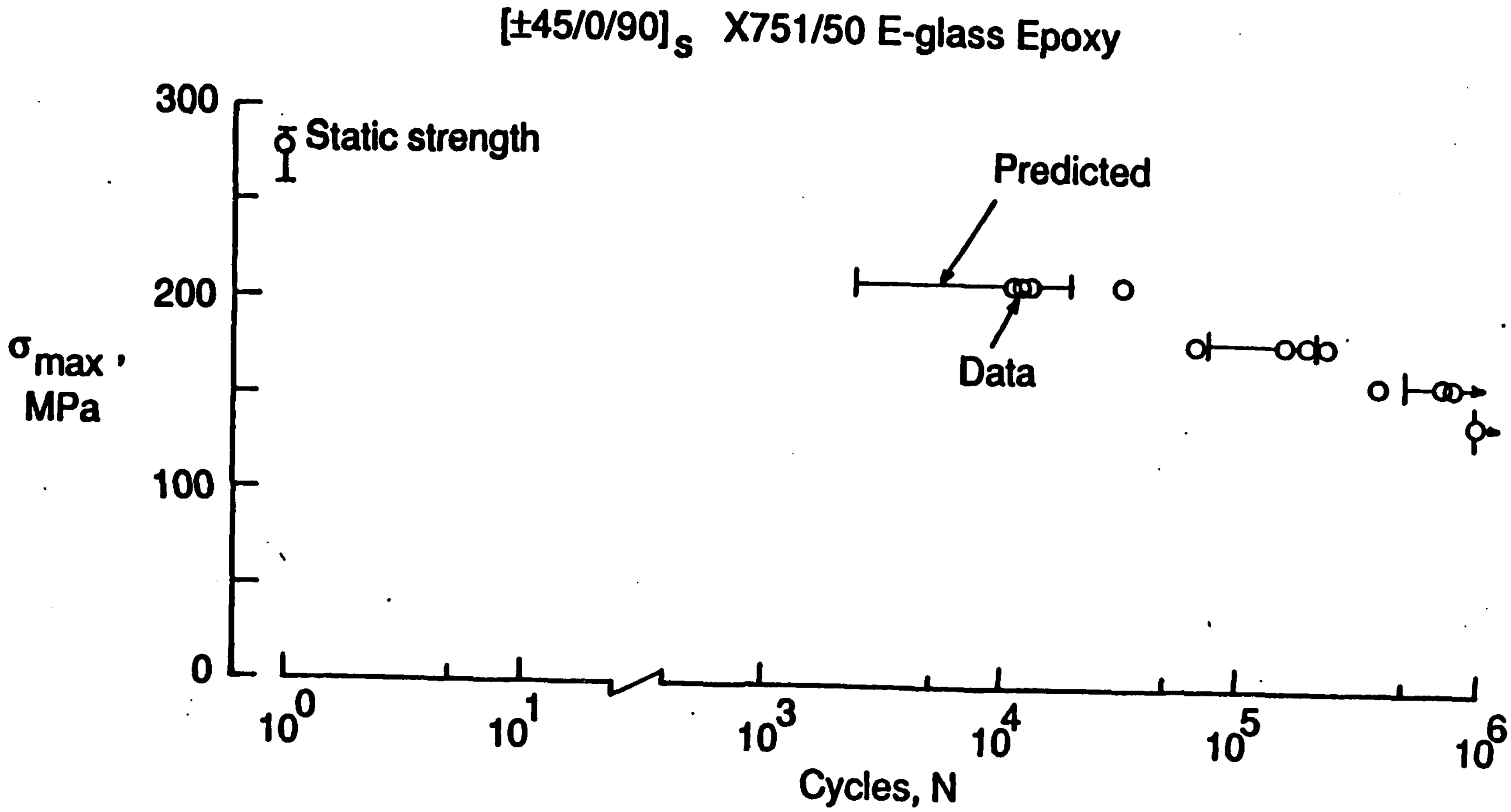

Fatigue Life Prediction Based on Local Delamination Accumulation through the Thickness for $(45/-45/0/90)_s$ E-Glass Epoxy Laminates

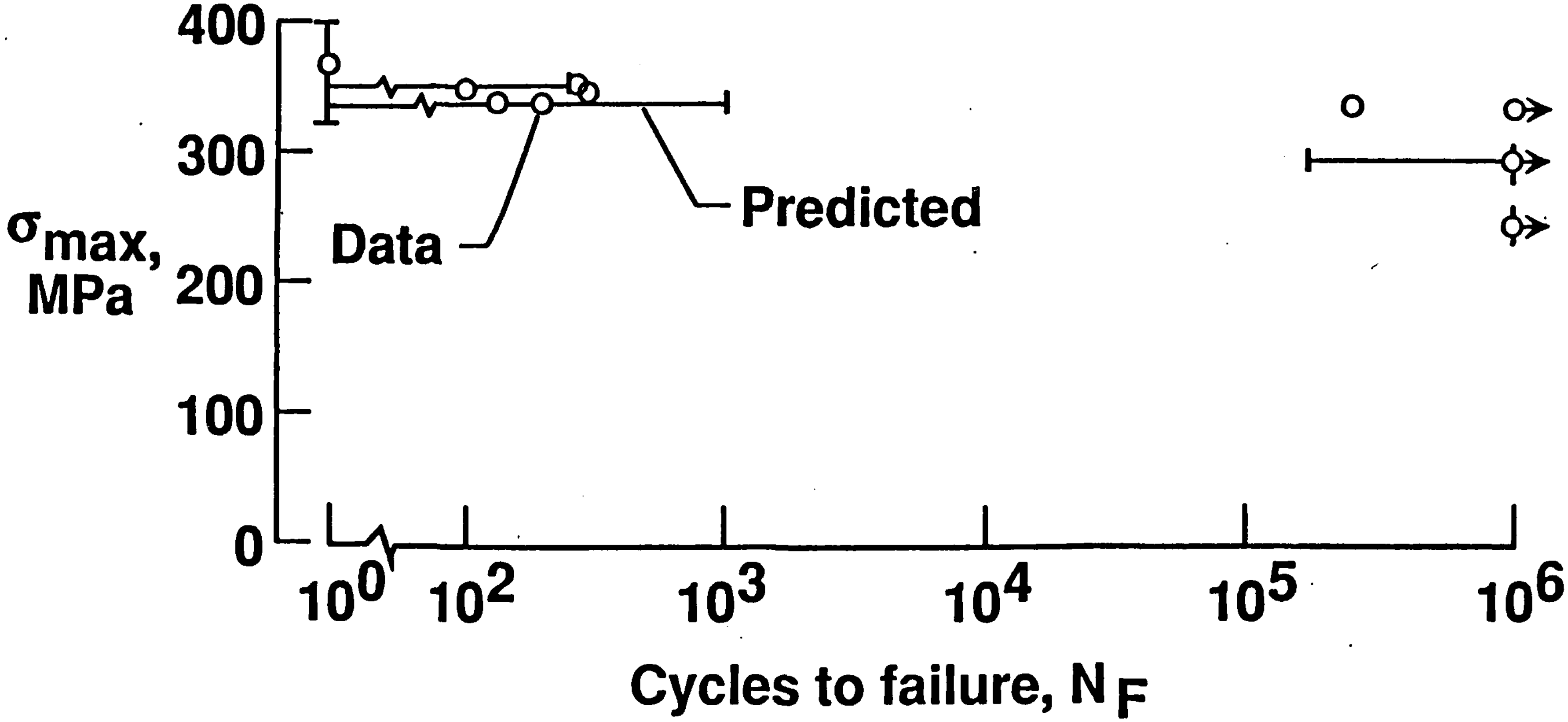

Fatigue Life Prediction for $(45/-45/0/90)_s$ Graphite/E-Glass Epoxy Hybrid Laminates

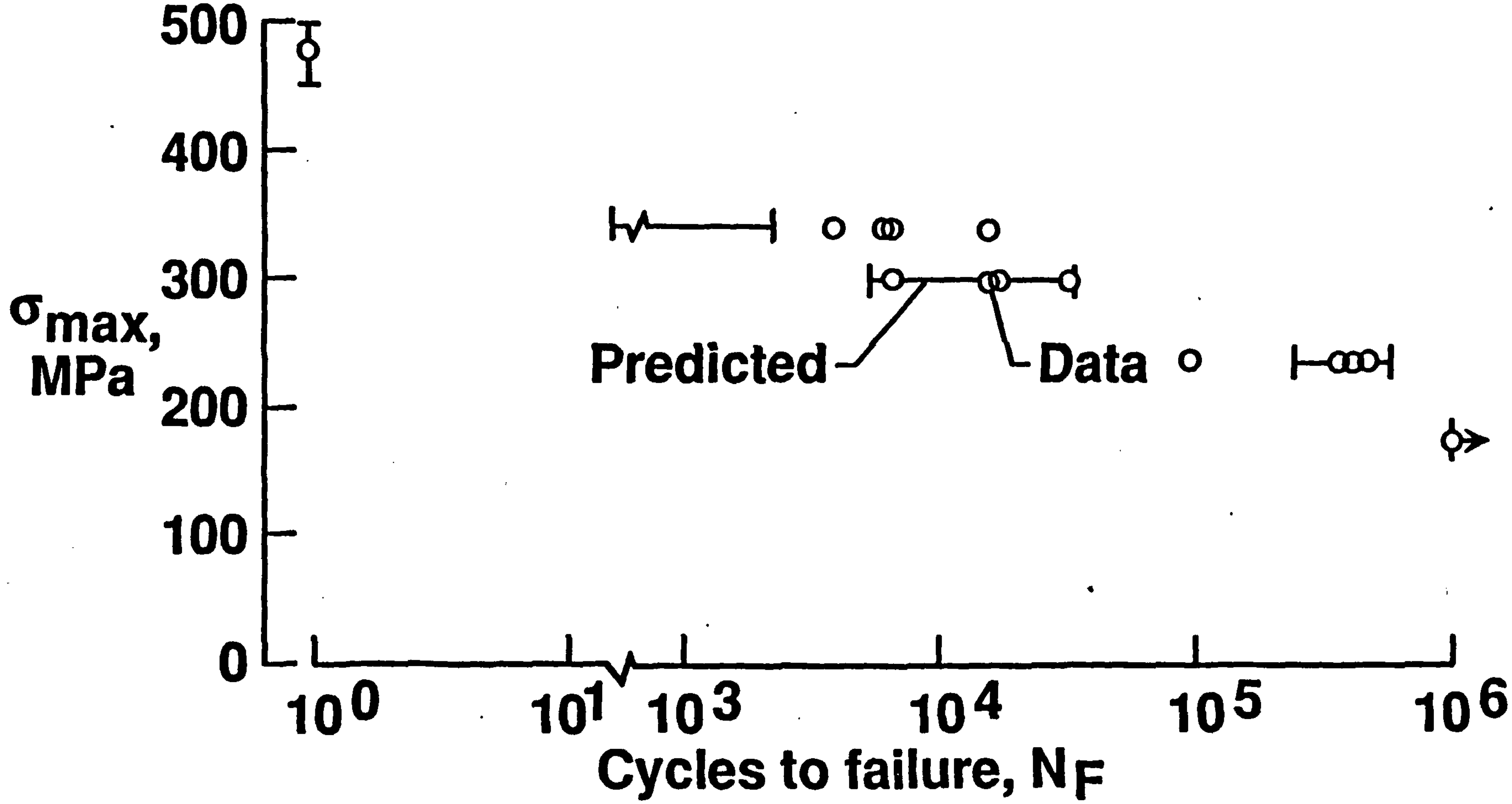

Fatigue Life Prediction for $(45/-45/0)_s$ Graphite/E-Glass Epoxy Hybrid Laminates

INVESTIGATION OF SINGULARITIES AT INTERFACES
OF ADHESIVE JOINTS

by

Roshdy S. Barsoum and Tzi-Kang Chen

U.S. Army Materials Technology Laboratory
Watertown, MA 02172-0001

Abstract

This paper presents the asymptotic singular fields associated with the fracture analysis of adhesive joints. It focuses on the behavior of interfacial singularities which arise in adhesive failure. We will discuss in detail some two and three dimensional interfacial singularity problems. The three-dimensional surface crack at the adhesive-adherend interface will be discussed in detail. The Finite Element Iterative Method (FEIM) is extended in this investigation for dealing with three-dimensional singularities and in finding multiple singularities that are important in some of the interfacial problems which are discussed here.

Fracture Mechanics of Adhesive and FEIM

The use of fracture mechanics in adhesive test analysis and design will require the evaluation of singularities and asymptotic fields encountered. Contrary to conventional fracture mechanics of homogeneous media (where the singularity is $r^{-1/2}$), the asymptotic field and the singularity are a function of the following: the adhesive and adherend properties, dimensionality of crack geometry (2-D or 3-D), and their relation to the interface. The knowledge of the asymptotic field is fundamental to development of proper fracture parameters as well as the interpretation of experimental results. For example, some of the advanced strain measurement methods such as Laser Moire interferometry rely on the availability of such analytical results.

The Finite Element Iterative Method (FEIM) was described in detail in References 1-4. Extension to three-dimensional cases is discussed here. In addition, the extension of the Method to extract multiple singularities is given.

Corner Singularity

Although properly prepared adherend surfaces are expected to lead to cohesive failure, with sharp corners, adhesive failure (interfacial cracks) may represent an initiation site for the general failure. Tests have shown that proper design of corners can increase the load carrying capacity of some adhesive joints threefold.

The problems of a rigid corner was investigated by the FEIM. In this case lower order singularities were evaluated, since they were found to be important in some loading cases. The asymptotic field is assumed to be of the form:

$$\sigma_{ij} = K_1 r^{-\alpha_1} f^1{}_{ij}(\theta) + K_2 r^{-\alpha_2} f^2{}_{ij}(\theta) + \ldots. \tag{1a}$$

$$u_i = K_1 r^{1-\alpha_1} F^1{}_i(\theta) + K_2 r^{1-\alpha_2} F^2{}_i(\theta) + \ldots. \tag{1b}$$

$$\text{where } \alpha_1 > \alpha_2 > \ldots.$$

Since α_1 is the dominant singularity, FEIM converges to $F^1{}_i(\theta)$ and α_1 as discussed in Reference 3. In order to obtain the second singular term, an orthogonalization scheme is used. The new trial vectors in this case, $\underline{W}_s$, are chosen such that they are normal to $K_1 F^1{}_i$. Therefore,

$$\underline{W}_{s+1} = \underline{V}_{s+1} - (\underline{V}_{s+1} \cdot \underline{X}_1)\underline{X}_1 \tag{2}$$

where $\underline{X}_1 = K_1 F^1{}_i(\theta)$ and $\underline{V}_s = [T]\ \underline{W}_s$, see Reference 4. Carrying out the iteration scheme, with vector $\underline{W}_s$, the method converges to the eigenfunction $F^2{}_i(\theta)$, and the corresponding singularity α_2.

Upon examination of this case it was found that it represents a symmetric loading case of zero shear about the plane of symmetry. In practice this case represents equal peal and shear loading on the corner, which may occur in some designs. Figures 1 and 2 give the results for both these cases.

Bimaterial Interfacial Surface Crack

Solutions of truly three-dimensional singularity fields are extremely difficult to obtain. The problem of surface singularity in a homogeneous material was attempted by Folias [5], Benthem [6], and Bazant and Estenssoro [7]. The analytical results of Benthem agree with the special finite element results of Bazant and Estenssoro. For comparison, FEIM was applied to this problem using the mesh configuration in Figure 3. The following table gives a comparison of the stress singularity α for mode I loading as given by Reference 6 and FEIM as a function of Poisson's ratio ν.

ν	0.0	0.15	0.30	0.40	0.48
Ref. 6 $(1-\alpha)$	0.5000	0.5164	0.5477	0.5868	0.6475
FEIM $(1-\alpha)$	0.4980	0.5133	0.5443	0.5838	0.6432

The asymptotic field for interface cracks in plane strain of two dimensional cases are more difficult to analyze because it involves the complex eigenfunctions [8]. FEIM has been applied to the two-dimensional case and excellent results were obtained [4]. As mentioned in the introduction, for the case of the bimaterial interfacial surface singularity, the resulting asymptotic field is fundamental to the interpretation of the surface measurements when using the Moire Laser Interferometry Method. The problem discussed here is for an elastic material bonded to a rigid substrate.

Figure 3 shows the geometry of the finite element used in the analysis. Figure 4 showsthe FEIM results of the displacement at the boundary of the free surface from one iteration to the next. The phase change variation indicates an oscillatory singularity as in the 2-D case. Convergence is judged by the equation:

$$A_1 \underline{V}_s + A_2 \underline{V}_{s+1} + A_3 \underline{V}_{s+2} = 0 \tag{3}$$

It is therefore possible to write the field in the form

$$\sigma_{1m} = R_e[(K_1 + iK_2)r^{-\alpha+i\epsilon}\{P_{1m}(\theta, \phi) + iT_{1m}(\theta, \phi)\}] \tag{4}$$

where $R_e[\ ]$ indicates real part and $i = \sqrt{-1}$. Both α and ϵ depend on Poisson's ratio ν. For $\nu = 0.30$ it was found that $\epsilon = 0.0$ and $(1 - \alpha) = 0.3548$ or 0.4931, depending on the mode of loading. These results indicate that the oscillatory stresses encountered in asymptotic fields of cracks at bimaterial interface of plane strain problems do not exist at the surface for some Poisson's ratios and hence may not be detectable experimentally in adhesive joints. The stress singularity α in this case also is greater than 1/2 and hence represents a super-singularity. Such a singularity is admissible in three-dimensional cases because it does not lead to infinite strain energy.

Conclusions

The applicability of the FEIM to some problems of importance to the fracture mechanics of adhesive joints was demonstrated. The method was shown to be capable of extracting lower singularities, in cases where it is essential to solve the full eigenvalue problem. The FEIM was also extended to three-dimensional cases for the solution of the problem of bimaterial interfacial surface crack. The FEIM results were compared first with Benthem's [6] theoretical results and excellent agreement was obtained. The case of elastic material bonded to rigid interface showed that the oscillatory part is equal to zero for $\nu = 0.3$, however it exhibited a super-singularity for the real part.

References

1. R. S. Barsoum, Int. J. of Fract., 32, 59-67 (1985).
2. R. S. Barsoum, Proc. 4th Int. Conf. Num. Meth. in Fract. Mech., San Antonio, TX, 23-27 March 1987.
3. R. S. Barsoum, Int. J. Num. Meth. in Eng., 25, 531-539 (1988).
4. R. S. Barsoum, Int. J. Num. Meth. in Eng., 25, 541-554 (1988).
5. E. S. Folias, Trans. ASME, J. Appl. Mech., 42, 663-674 (1975).
6. J. P. Benthem, Int. J. Solids Struct., 13, 479-492 (1979).
7. Z. P. Bazant and L. F. Estenssoro, Int. J. Solids Struct., 15, 405-426 (1979).
8. M. L. Williams, Bul. Seis. Soc. of Am., 49, 199-204 (1959).

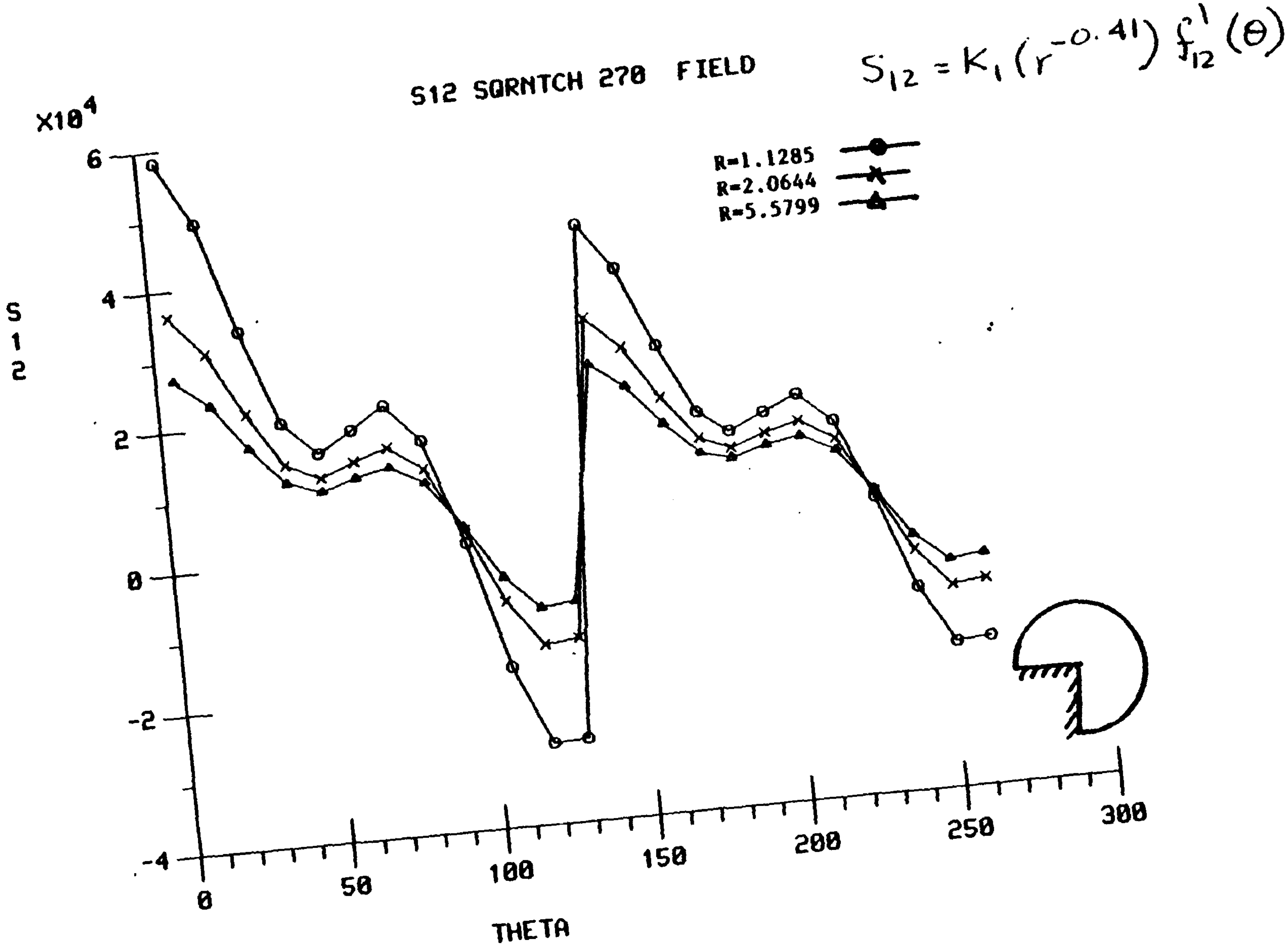

Fig.1 Stresses for corner singularity with general loading

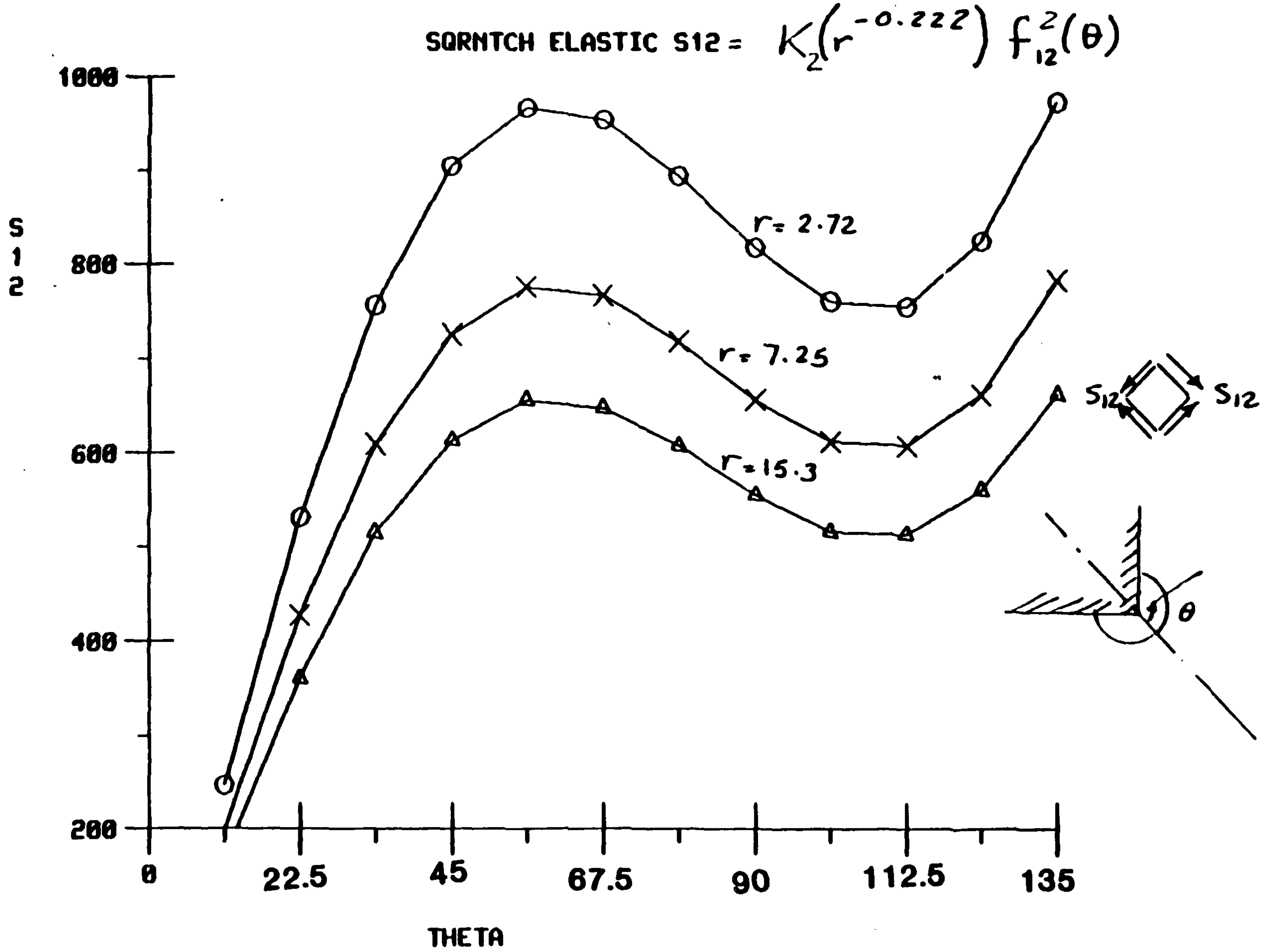

Fig.2 Stresses for corner singularity with symmetrical loading

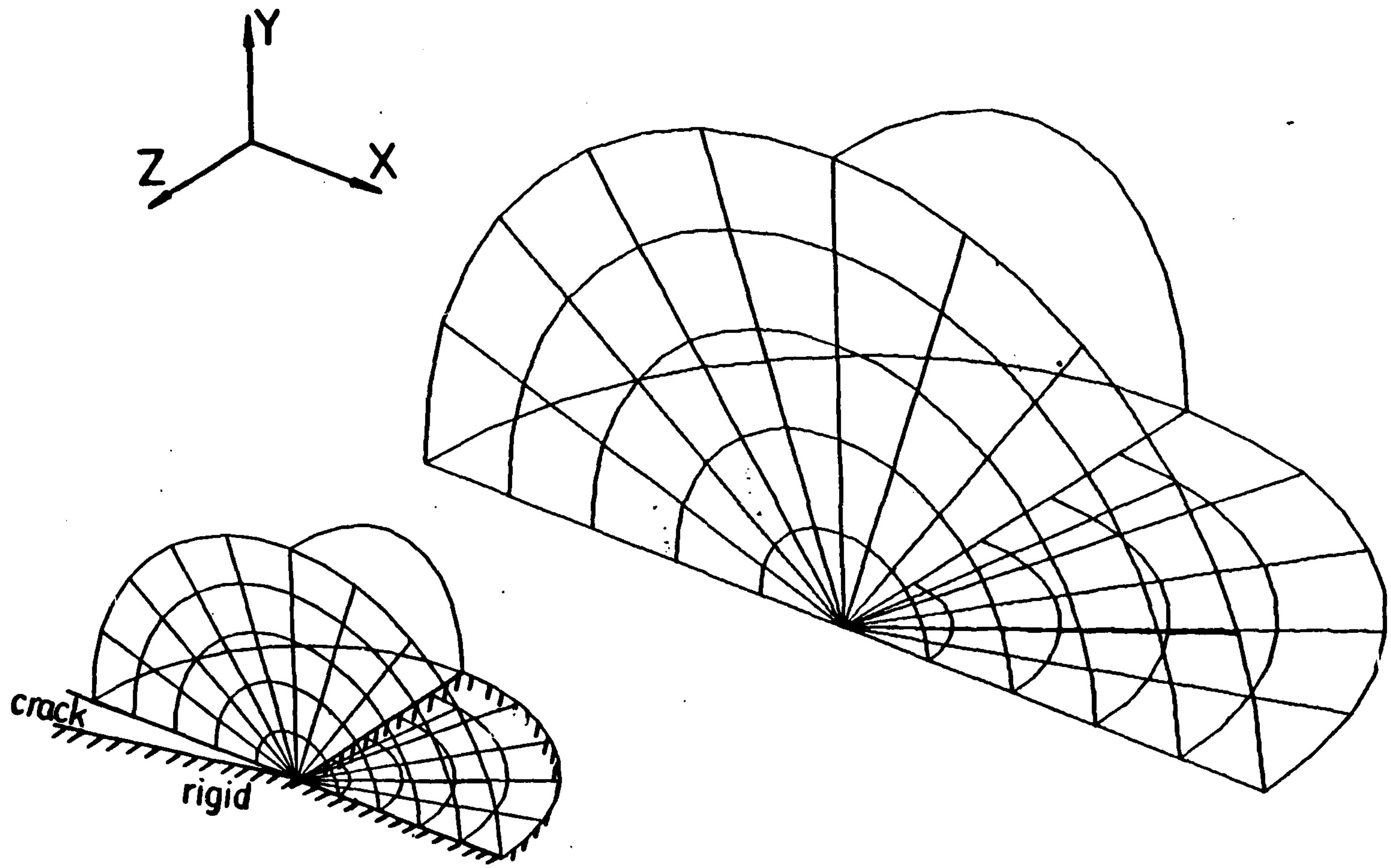

Fig.3 Finite element meshing for FEIM of surface crack

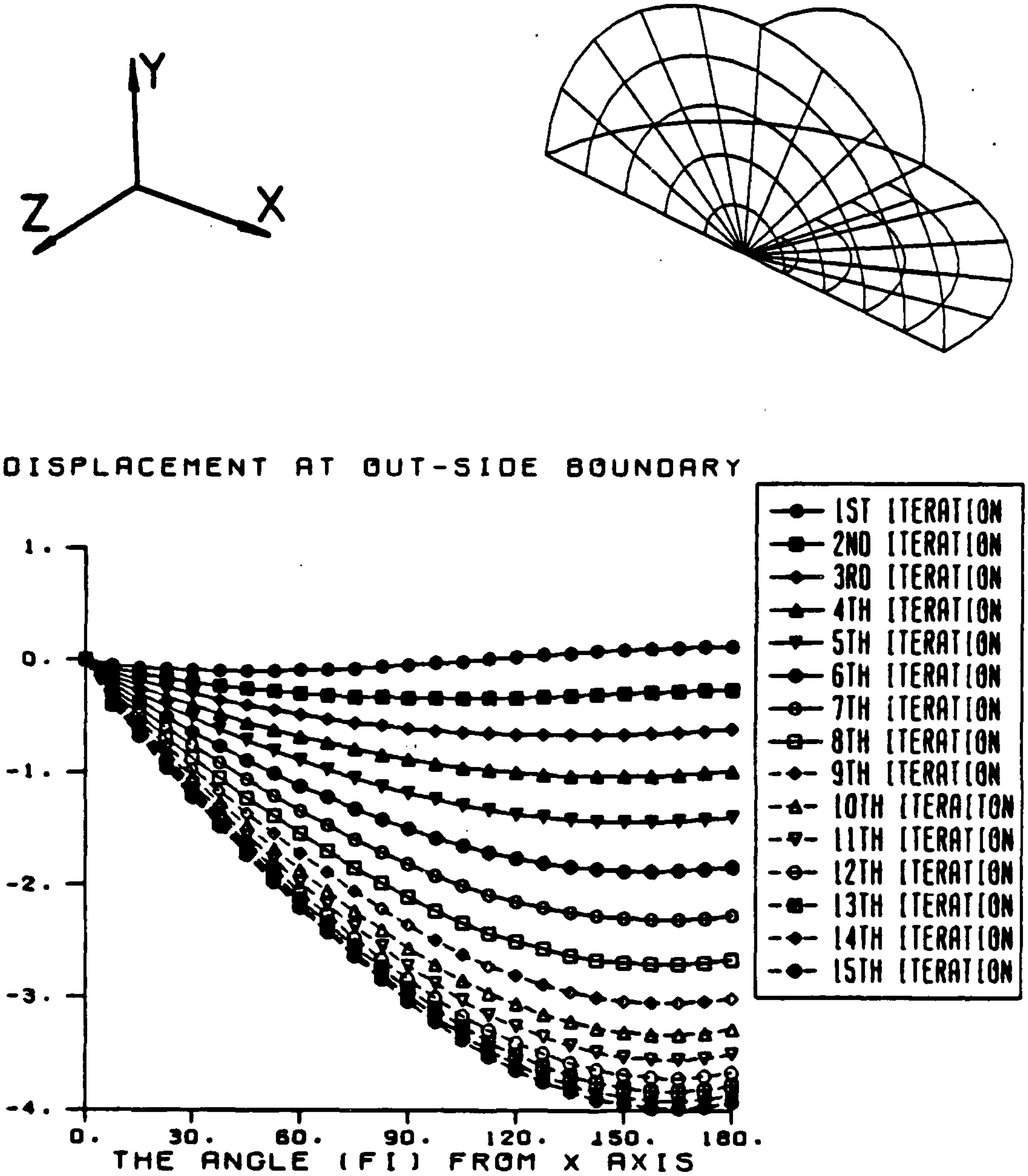

Fig.4 Convergency of iterative results for a surface crack of an elastic material bounded to a rigid substrate

FAILURE CHARACTERIZATION OF COMPOSITE MATERIALS

SCOTT E. GROVES

Composite Materials Group
Engineering Sciences Division
Mechanical Engineering Department
Lawrence Livermore National Laboratory
Livermore, California 94550

The primary objective of this research is to characterize the three-dimensional failure response of continuous fiber graphite epoxy composite materials. This effort includes the development of a new failure model, generation of the three-dimensional failure data, and an investigation of the dynamic strength behavior. This research represents a continuation of an ongoing project initiated in mid FY87. The primary effort to date has centered on the development of the necessary experimental techniques required to generate the complex failure response of these materials.

The characterization of the failure behavior for composite materials still represents an extremely challenging effort. In some cases LLNL requires structures to withstand 99 % of their catastrophic failure loads. This requires a much greater understanding of the full three-dimensional failure response of these materials. The current ability to predict this complex failure behavior is very inadequate.

What constitutes failure in a composite? Failure in a composite laminate or structure can imply many different things. One can have local failure modes in individual plies or global failure modes in the laminate. Local ply failure modes can be such that the ply has sustained a sufficient amount of damage such that it can no longer bear load or transfer load to neighboring plies. Damage can imply cracking or fiber breakage. Global failure modes can imply interlaminar delaminations, free edge delaminations, and total fiber failure or even total matrix failure. An example of global failure is shown in figure 1. This loading history was obtained by subjecting a one inch thick simply supported circular plate to a flat plate load. The peaks in the first portion of the curve correspond to the formation of delaminations within the plate. The closely spaced peaks in the later portion of the curve correspond to global fiber and matrix failure as a result of extreme out-of-plane shear stresses. In all cases the formation of failure or damage can be either cumulative or localized depending on the applied load history. Even under static loading conditions periodic arrays of cracks and delaminations can develop within a structure. Most of the damage that occurs usually initiates in subcritical elements. However, this resulting damage must redistribute the stresses in order to maintain equilibrium, and thus affects the overall structural integrity of the system -stiffness, strength, life, and thus the ultimate failure. Failure theories associated with the formation of this cumulative periodic damage are grouped into the continuum damage mechanics field and theories associated with very localized failure can be grouped into the fracture mechanics field. However, in composites one generally can not distinguish between the two fields.

There are several key factors inwhich this effort must follow. First the theoretical model must mimic the actual physics of the failure process as opposed to using non-physical empirical constants. Second, and most important, one must be able to generate the complex experimental data required to define the three-dimensional failure behavior. Because of the many failure modes possible for a composite, it is extremely necessary to generate multiaxial failure surfaces and thus perform multiaxial loading. The major uncertainty with any of the experimental testing is whether or not the test is yielding the proper constitutive and failure response desired. Because of the anisotropic nature of these materials unwanted load coupling generally prevents the desired constitutive response and therefore analytical tools such as the finite element method must be used to correct the data. Finally, the experimental test as well as specimen fabrication must be reproducable.

A continuum mechanics approach will be adhered to in developing a complete three-dimensional failure criterion. This effort will be divided into three separate modelling efforts: 1) local failure response, 2) global failure response, and 3) cumulative damage modelling.

The initial local ply failure response will be written in terms of the elastic strain invariants. This approach was previously initiated by Bill Feng [1]. For this model a second order expansion is performed about the three infinitesimal strain invariants. The leading constants in the expansion are then characterized using experimental data. In conjunction with this effort several existing failure criteria will be evaluated using the generated experimental data base.

The global modelling effort will attempt to utilzed the concepts of multipolar continuum mechanics [2,3]. Multipolar continuum mechanics can account for the local ply asymmetries in a laminate which in turn can produce local asymmetric stress-strain behavior. An example of a simple polar theory is laminated plate theory wherein the first moment of the through thickness stress field is averaged to yield a set of resultant moments. It is beleieved that by developing higher order multipolar moments one can more accurately mimic the physics of some of the complex failure mechanisms associated with global failure such as delamination that was shown in figure one.

Finally, for a complete and ultimate failure theory, one must account for the development of the internally distributed damage, ie, matrix cracking, interlaminar delaminations, fiber failure, etc. The severity of the cumulative damage is that it alters the local constitutive response of the material as well as the strength and life. Much published work is available in the literature which accounts for the changing constitutive response. A set of locally averaged history dependent constitutive equations reflecting the distributed damage was previously developed by the author [4,5]. Charaterization of these equations provides for better tracking of the local stress/strain fields for predicting failure. What still remains is to couple such equations with parts (1) and (2) and determine their impact on the failure of composite materials. This work will require a significant non-destructive evaluation study of the materials in question to document the damage which will be very time consuming. It is planned that the work on this phase of the failure modelling will not begin until the first two phases of the research are completed. Realistically this effort is several years away and for completion of failure model is mentioned here.

The development of a biaxial testing apparatus has been the focal point of the research effort to date. This system provides the capability to conduct tension/compression, torsion, and internal pressurization of 2-inch diameter flared composite tubes. These tubes can either be filament wound systems or pre-preg. The filament winding is performed on LLNL's recently acquired 6 axis winding machine.

A two-dimensional failure surface using the tension-torsion test system has been generated using T300/F263 pre-preg tape. The laminate orientation investigated was the [0,45,-45,90] quasi-isotropic sequence. These tests consisted of only combined axial and torsional loading. The results of these tests are shown in figure two. Eventhough the composite tubes utilized in this experiment were not exactly reproducable the results from figure 2 indeed indicate the asymmetric complexity of the failure behavior of this material. A major problem with these materials is that the failure modes can be path dependent. For example if one examines the shear stress at failure for the case of no tensile stress and then compares this value with the shear stress at 50% tension one can see an increase in the relative shear strength. Thus by initially applying tension to the tube one can effectively increase the available shear strength. However, the reverse is obviously not true and thus we have path dependence. Furthermore, a pre load of compression lowers the available shear strength (this is more typical of metal failure). A photograph of a biaxially failed tube is shown in figure 3. This tube was initially loaded to 22.8 ksi in tension and then catastrophically failed when the applied torsional shear stress reached 34.4 ksi. Finally, one must realize that a complete failure surface requires a superposition of the in-plane transverse stress as well as the out-of-plane stress fields. The later of which is currently not possible, ie, simultaneous full three-dimensional loading. Nevertheless, it is possible to perform some out-of-plane load coupling with in-plane loading as was the case with simply supported bending of thick plates. However, the resulting stress fields are unknown because the boundary value problem is non-homogeneous. Iteration would be required with a finite element model to assertain the critical failure stresses invovled.

The experimental techniques required to obtain the out-of-plane failure modes as well as various in-plane shear modes have also been the subject of considerable attention. Application of out-of-plane shear is extremely difficult because of the load coupling interaction. Techniques that have been investigated include the Iosipescu test, asymetric four point bending, two sizes of an opposed double notch, a compact block shear, and the the 2-inch diameter torsion tube. The compact block shear test appears from preliminary results to be the easiest to utilize for determining the out-of-plane shear modes. Nevertheless, all these test are still being evaluated. It is hoped for FY89 to obtain finite element models of each technique to better understand them. Two types of out-of-plane compression have also been developed. The first method is simple bearing compression of composite cubes. The second method is bearing compression of tapperd one inch composite cubes.

A table of the global individual directional failure strengths for the same material used in figure two is shown in table one. These results were compiled utlizing the above techniques. Most of the data was obtained for one inch thick specimens. The validity of this data is still being evaluated.

In conjunction with the failure needs of other LLNL programs the dynamic failure strengths are also being evaluated. Techniques such as the high rate MTS testing machine, the Split Hopkinson Pressure Bar, and an impacting drop tower are being utilized. The major difficulty in analyzing the test results is accounting for stray boundary value effects such as gripping problems, uniformity of load application, random propagation of stress waves, as well as stress wave reflections off of the free surfaces, and the physical limitations of acquiring accurate high speed data. Only limited data has been obtained so far. The results contain much scatter, but they do tend to indicate some increase in the compressive and shear strengths with an increase in loading rate.

In summary the failure characterization effort at LLNL is very broad in scope. This presentation will highlight the work in progress. It is hoped that as many as three of the primary high performance fiber systems currently being utilized by LLNL programs can be characterized. These include Toray 1000, Hitco 900, and IM6 which will be matrixed with a T403 resin derivative. This data will then be used to evaluate the developed failure model.

REFERENCES:

1. Feng, W. ,"A Finite Strain Elasticity Approach to Failure Modelling of Composite Materials", work in progress, LLNL 1988.

2. C. Truesdell and W. Noll, <u>The Non-Linear Field Theories of Mechanics</u>, edited by S. Flugge, Springer-Verlag, (1965).

3. W. Jaunzemis, <u>Continuum Mechanics</u>, Macmillan, (1967).

4. D. H. Allen, C.E. Harris, and S.E. Groves, "Thermomechanical Constitutive Theory for Elastic Composites with Distributed Damage--Part I: Theoretical Development," <u>Internation Journal of Solids and Structures</u>, Vol 23, (1987).

5. S.E. Groves, "A Study of Damage Mechanics in Continuous Fiber Composite Laminates with Matrix Cracking and Interply Delaminations," Dissertation, Texas A&M University, (1986).

*This work was performed under the auspices of the U.S. Department of Energy by Lawrence Livermore National Laboratory under contract No. W-7405-Eng-48.

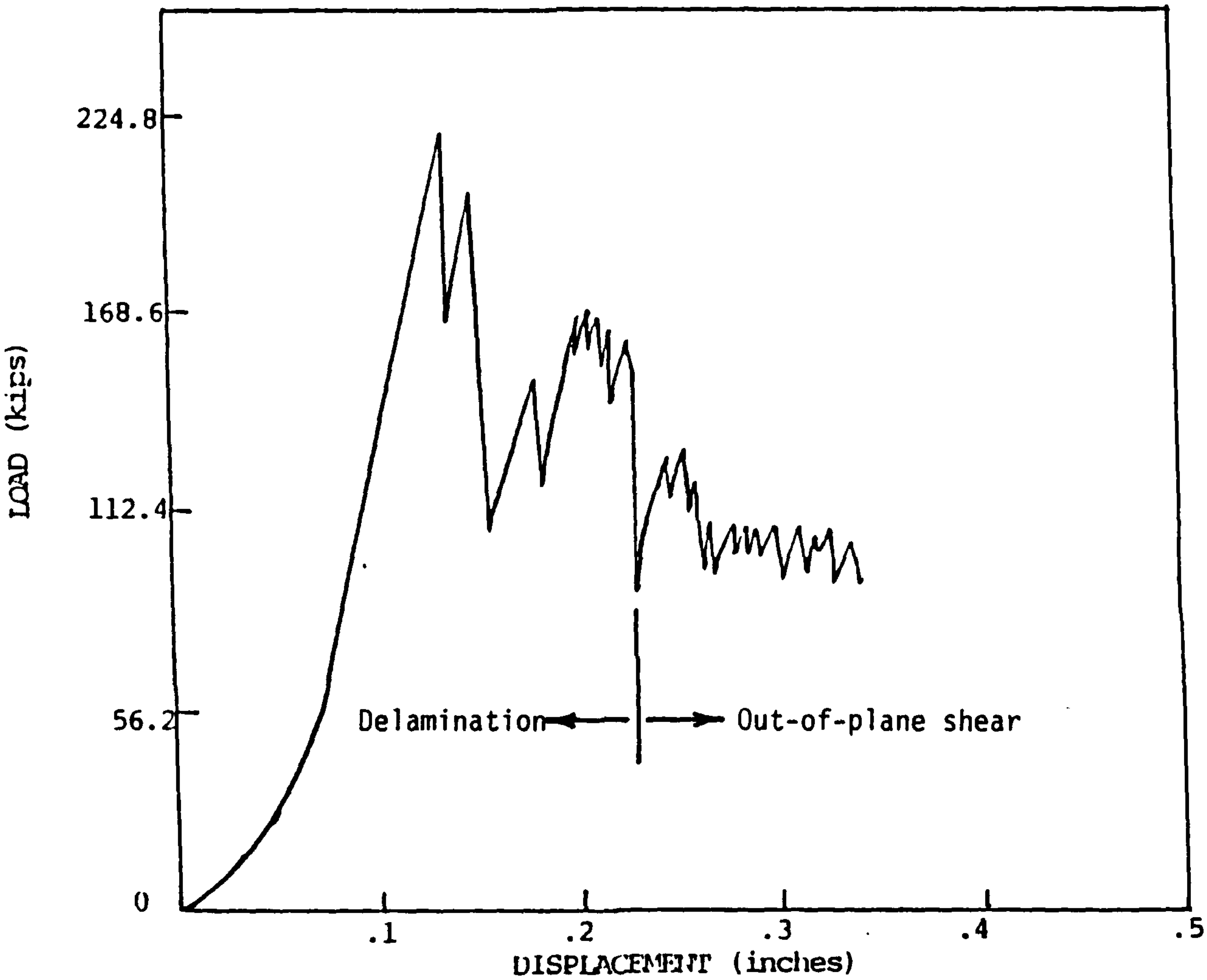

Figure 1. Failure of a simply supported one inch thick flat circular plate subjected to a flat plate loading.

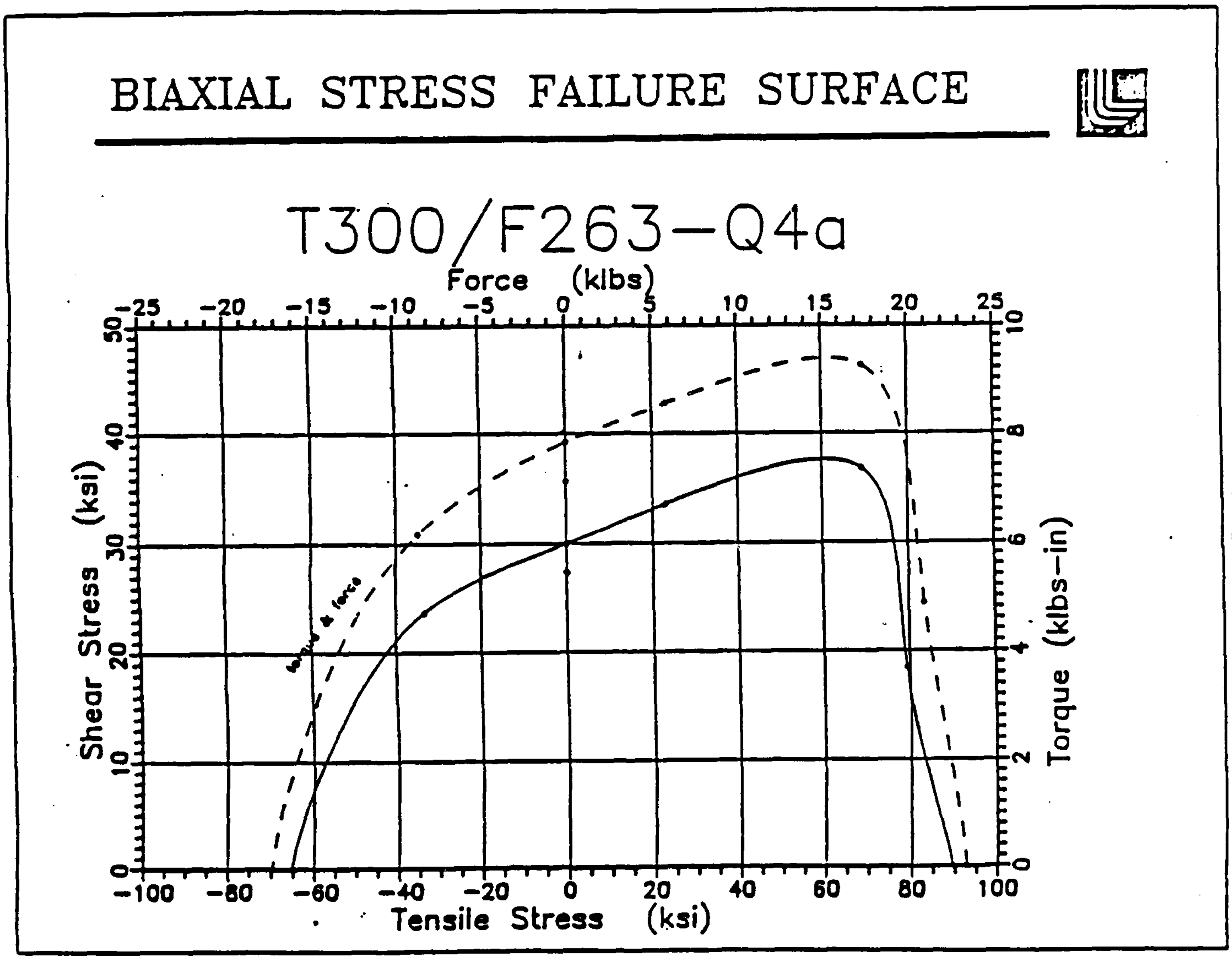

Figure 2. Biaxial stress failure surface for a $[0,45,-45,90]_s$ quasi-isotropic composite tube.

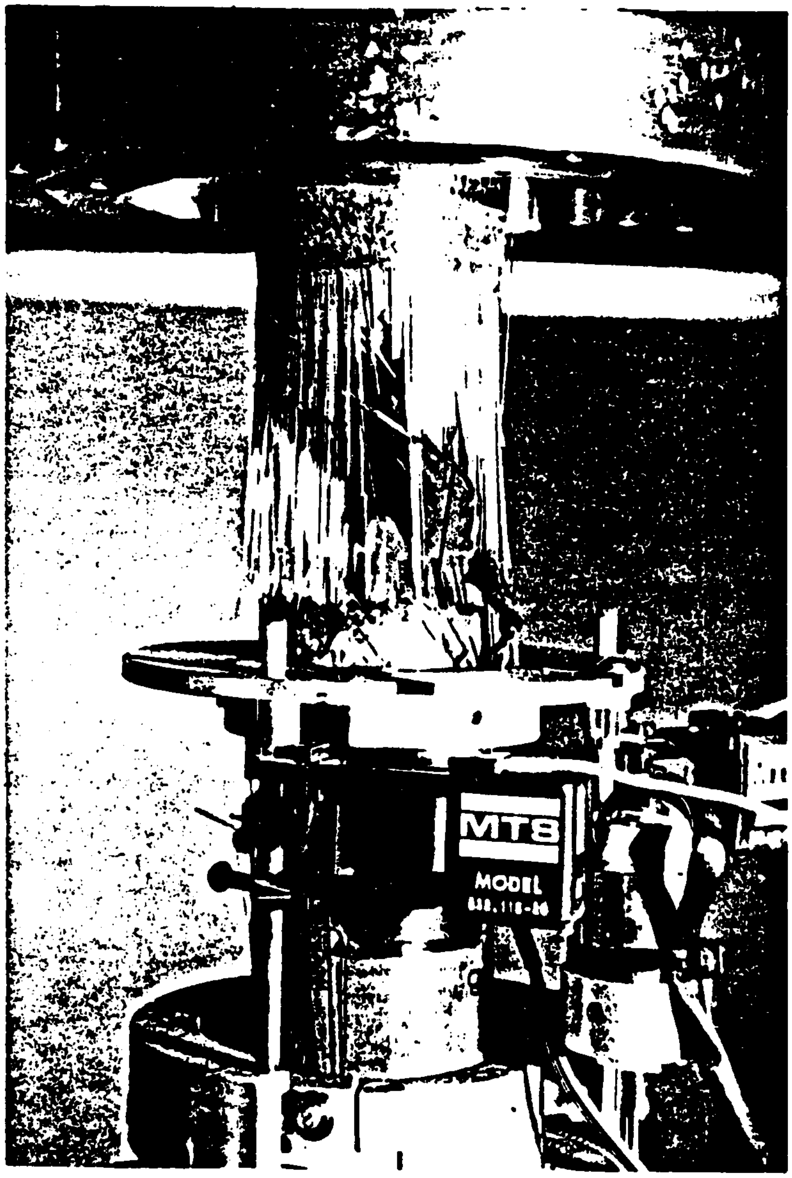

Figure 3. Biaxially failed T300/F263 $[0,45,-45,90]_s$ composite tube.
Tension = 22.8 ksi, torsional shear = 34.3 ksi.

GLOBAL STRENGTH COMPONENT	TENSION (KSI)	COMPRESSION (KSI)
X_x	89.5	65 - 80
X_y	89.5	65 - 80
X_z	11	122
X_{xy}	44	44
X_{yx}	44	44
X_{xz}	15	15
X_{yz}	15	15
X_{zx}	6.5	6.5
X_{zy}	6.5	6.5

Table 1. Global directional failure strengths for a T300/F263 graphite/epoxy $[0,45,90,-45]_{ns}$ laminate. Coordinates "x" and "y" denote the plane of the laminate and "z" is normal to the laminate plane.

ANALYSIS OF DAMAGE MODES IN FIBER COMPOSITES

by

J.N. Rossettos and S. Lin
Department of Mechanical Engineering
Northeastern University, Boston, MA 02115

Introduction

In the analysis of failure mechanisms in fiber composites, the stress concentration which occurs near fiber breaks, together with the level of matrix yielding and debonding at the fiber matrix interface, continue to be important considerations. A single broken fiber in an infinite monolayer in which the matrix adjacent to the broken fiber yields in an elastic perfectly plastic sense, or where the matrix-fiber bond fails completely when a given shear strength is reached, have been examined previously [1,2]. In the analysis, the shear lag model and an influence function approach, first introduced by Hedgepeth [3], were utilized. The shear lag model, where fibers carry only axial loads and the matrix carries only shear, continues to be useful even in cases where the matrix is relatively stiff as in metal matrix composites such as boron-aluminum. This was demonstrated in [4,5].

Although it is not clear to what extent the levels of matrix yielding and interface bond failure influence each other, an analysis of the problem where each occurs separately, provides insight into the extent of failure with increasing failure region with applied load indicates overall brittle behavior for the bond failure case in contrast to the matrix yielding case.

Analysis and Results

For purposes of describing the method, we consider the bond failure case for the finite width sheet consisting of 2q+1 fibers parallel to the x axis, which is in the load direction. The n=0 fiber is broken, and bond failure occurs over the distance

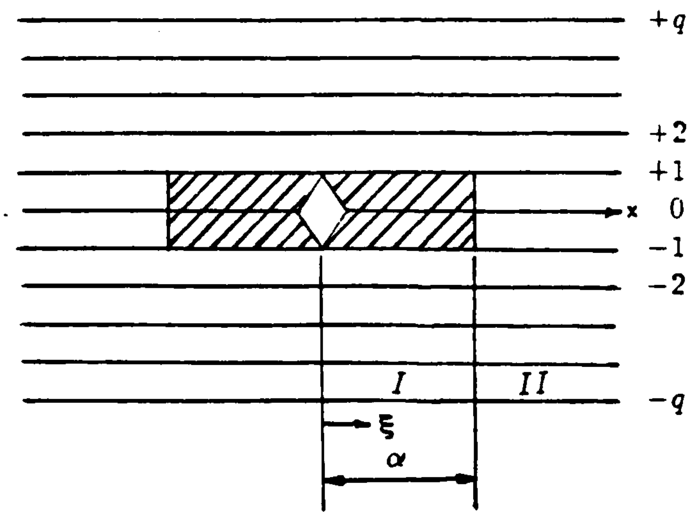

x=a. Although we discuss the symmetric case shown in the sketch, more general break configurations can be handled in similar fashion. Regions I and II are defined as shown. In region I interface bond failure occurs completely for the n=0 fiber while it occurs only on one side of the n=1 and -1 fibers. The non-dimensional equilibrium equations for fiber displacements in region I are then

$$d^2U_q/d\xi^2 + U_{q-1} - U_q = 0 \qquad (n=q) \qquad (1)$$

load, and whether the overall failure mechanism indicates a brittle or ductile response.

In the present work, the bond failure and matrix yielding problems are formulated for a finite width monolayer using the shear lag assumption. The number of fiber breaks together with the total number of fibers in the configuration used for calculation, are varied. An eigenvector expansion approach is used to solve the governing system of differential equations. The extent of the failure region as a function of applied load, and the fiber stress concentration near breaks and regions of yielding or bond failure are determined. The infinite sheet results of [1,2] are approached as the total number of fibers is increased.

The influence function approach in [1,2] leads to the necessity to solve an integral equation numerically in cases where it is possible to reduce the problem to such an integral equation. Actual composite behavior will most likely involve a combination of matrix yielding and bond failure, and mathematical complexities will be encountered in the infinite sheet approach used in [1,2,3]. The approach in the present work can handle more practical cases with less difficulty, such as multiple fiber breaks, edge cracks, two adjacent but different damage regions, and work hardening.

The results in the present paper show how matrix yielding and bond failure reduce the stress concentration near fiber breaks. Also, the manner of increase in the size of the

$$d^2U_n/d\xi^2 + U_{n+1} - 2U_n + U_{n-1} = 0 \qquad (1 < n \leq q-1) \qquad (2)$$

$$d^2U_1/d\xi^2 + U_2 - U_1 = 0 \qquad (n=1) \qquad (3)$$

$$d^2U_0/d\xi^2 = 0 \qquad (n=0) \qquad (4)$$

In region II, Eqs. (3) and (4) would not apply since these equations involve bond failure. The nondimensionalization is given by

$$(x,a) = \sqrt{EAd/Gh}\;(\xi,\alpha) \qquad (5)$$

$$p_n = pP_n \quad ; \quad u_n = p\sqrt{d/EAGh}\;U_n \qquad (6a,b)$$

where p is the fiber load at infinity (i.e., far from damage region), d is distance between fibers and h is sheet thickness. E, A, and G are fiber modulus, fiber cross-sectional area, and matrix shear modulus respectively. The nondimensional fiber load is

$$P_n = dU_n/d\xi \qquad (7)$$

Similar notation is given in Ref. (5). The boundary conditions will now be given by using subscripts I and II to refer to the solutions in those respective regions. In region I, we have at $\xi=0$

$$U_{I_n}(0) = 0 \qquad \text{unbroken fibers} \qquad (8)$$

$$P_{I_n}(0) = 0 \qquad \text{broken fibers} \qquad (9)$$

Since all fibers are continuous at $\xi = \alpha$, we have

$$U_{I_n}(\alpha) = U_{II_n}(\alpha) \quad ; \quad P_{I_n}(\alpha) = P_{II_n}(\alpha) \qquad (10a,b)$$

In addition to conditions (8)-(10), Eq. (6a) implies

$$P_{IIn}(\infty) = 1 \tag{11}$$

Eq. (4) can be solved separately giving $U_{I0}=A_0=$ constant (since $P_{I0}=dU_{I0}/d\xi=0$). Eqs. (1)-(3) are then written in matrix form for region I as

$$\underset{\sim}{U}''-\underset{\sim}{L}\underset{\sim}{U} = 0 \tag{12}$$

where $\underset{\sim}{L}$ is banded and $\underset{\sim}{U}^T=[U_q,U_{q-1},\ldots U_2,U_1]$. A solution to (12) is assumed in the form $\underset{\sim}{U}=\underset{\sim}{R}e^{\lambda\xi}$. The resulting eigenvalue problem, $(\underset{\sim}{L}-\lambda^2\underset{\sim}{I})\underset{\sim}{R}=0$, in region I leads to eigenvalues, λ_i^2, and eigenvectors, $\underset{\sim}{R}^i$, and the solution to $\underset{\sim}{U}$ can be written as the expansion,

$$\underset{\sim}{U}_I=\sum_{i=1}^{q}\underset{\sim}{R}^i(B_ie^{\lambda_i\xi}+C_ie^{-\lambda_i\xi}) \tag{13}$$

In region II, the eigenvalue problem, where now U_{II0} is included in the matrix equations, leads to eigenvalues β_i^2 and eigenvectors, Y^i. Positive β_i are discarded to satisfy the condition at ∞ given by Eq. (11), and the solution is written as

$$U_{II}=\sum_{i=1}^{q+1}D_i\underset{\sim}{Y}^ie^{-\beta_i\xi}+\underset{\sim}{U}_{PII} \tag{14}$$

where $\underset{\sim}{U}_{PII}=[\xi,\xi,\ldots\xi]$ is added to satisfy Eq. (11). The constants B_i, C_i, D_i and A_0 can be determined by using the boundary and continuity conditions already discussed. To find a relation between α and applied load, we first define a nondimensional shear load per unit width, T, by

$$T = \sqrt{EAdh/G}\,(\tau/p) = U_n-U_{n+1} \tag{15}$$

At $\xi=\alpha$, the shear stress has the critical value $\tau=\tau_c=$ constant between fibers 1 and 0, which is the value that breaks the bond.

By picking different values of α and obtaining solutions to U_n, we can determine $T = (U_{I0}-U_{I1})_{\xi=\alpha}$. The value of applied load, p, which starts bond failure ($\alpha=0^+$) is denoted by p_{limit}, with its corresponding value, T_{limit}. On using (15), with $\tau = \tau_c$, the following ratios apply

$$T_{limit}/T = p/p_{limit} = (U_{I0}-U_{I1})_{\xi=0^+} \Big/ (U_{I0}-U_{I1})_{\xi=\alpha} \tag{16}$$

Eq. (16) allows calculation of p/p_{limit} for different values of α (see Fig. 1). With minor modifications the same method can be applied to the case where the matrix yields over the range $\xi = \alpha$.

In Figs. 1 and 2 the extent of bond failure, α, is plotted against p/p_{limit}. Note that the post failure region is enlarged as the number of fibers is increased, thereby diminishing the effect of the edge and approaching the infinite sheet case. The same general behavior occurs for one and three broken fibers. Since α increases without bound for relatively small values of p/p_{limit}, the behavior can be termed "brittle". This is in contrast to the matrix yield case in Fig. 6 which shows a near linear relationship. The stress concentration which occurs at the edge of the bond failure region (Fig. 5), is seen to decrease with load ratio (Figs. 3,4). There are similar results (not shown) for the matrix yield case. It is clear that the matrix yield problem indicates more damage tolerance than the bond failure problem. The actual case may involve both matrix plasticity and bond failure, and depending on material properties, two adjacent failure regions (one of matrix plasticity, which occurs first, and one of bond failure) with matrix work hardening, provide a more realistic model. This is presently being studied.

References

1. Hedgpeth, J.M. and Van Dyke, P., "Local Stress Concentrations in Imperfect Filamentary Composite Materials," J. Composite Materials, Vol. 1 (1967) p. 294.

2. Van Dyke, P., and Hedgepeth, J.N., "Stress Concentrations for Single Filament Failures in Composite Materials," J. Textile Research, Vol. 39 (1969) p. 618.

3. Hedgepeth, J.M., "Stress Concentrations in Filamentary Structures," NASA TND-882 (1961).

4. Reedy, E.D., Jr., "Fiber Stresses in a Cracked Monolayer: Comparison of Shear Lag and 3-D Finite Element Predictions," J. Composite Materials, Vol. 18, pp. 595-607, (1984).

5. Rossettos, J.N. and Shishesaz, M., "Stress Concentration in Fiber Composite Sheets Including Matrix Extension," Trans. ASME, J. of Applied Mechanics, Vol. 54, No. 3 pp. 723-725 (1987).

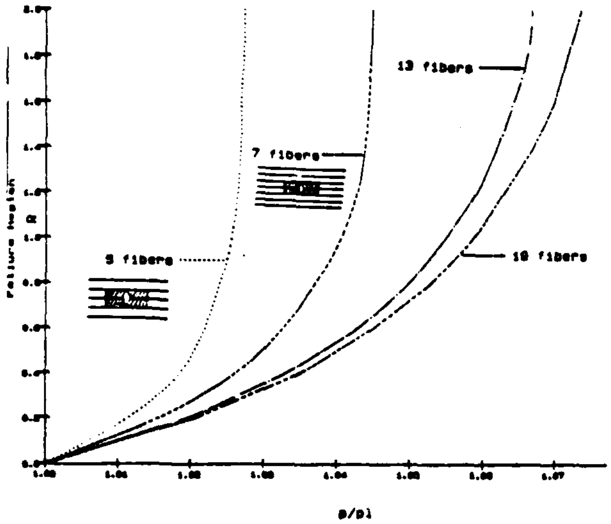

Fig. 1
Failure region vs. load ratio p/p_{limit} for different no. of total fibers; one break - center fiber.

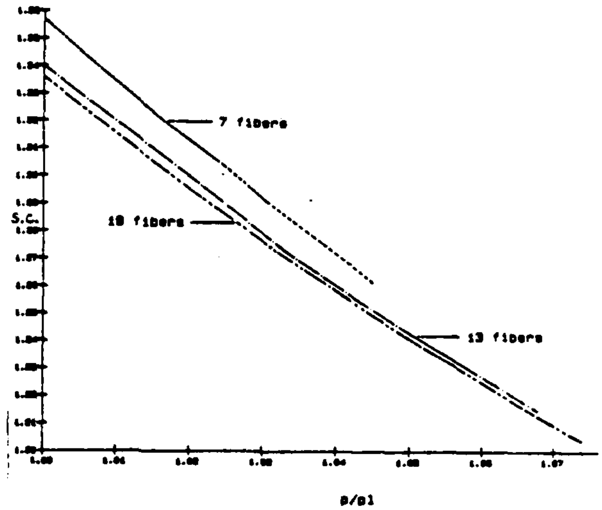

Fig. 3
Stress concentration in adjacent fiber vs. p/p_{limit} for different no. of total fibers; one break - center fiber.

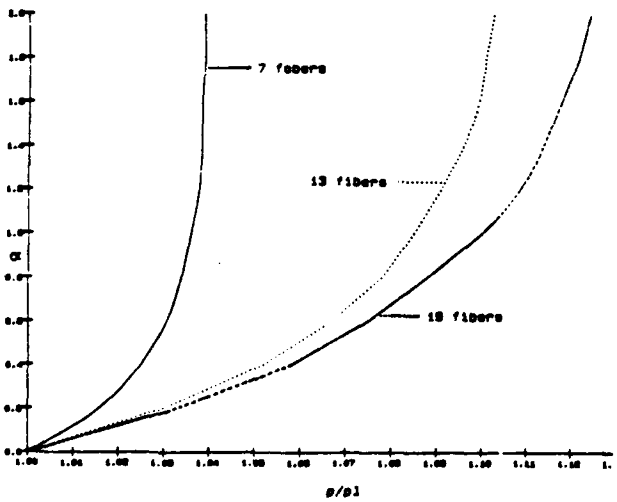

Fig. 2
Failure region vs. p/p_{limit} for different no. of total fibers; three breaks - central three fibers.

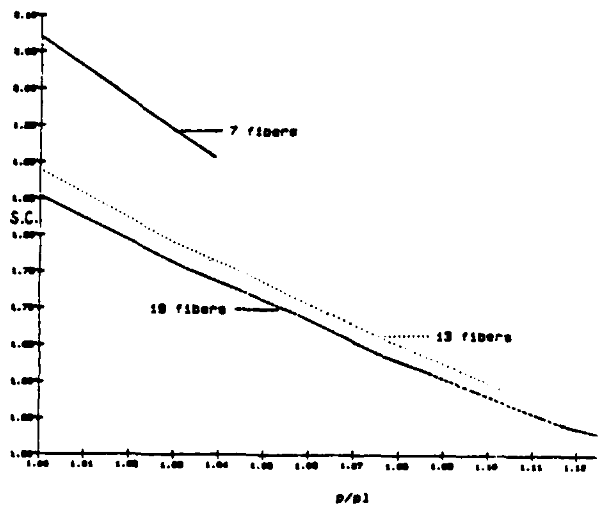

Fig. 4
Stress concentration in adjacent fiber vs. p/p_{limit} for different no. of total fibers; central three fibers broken.

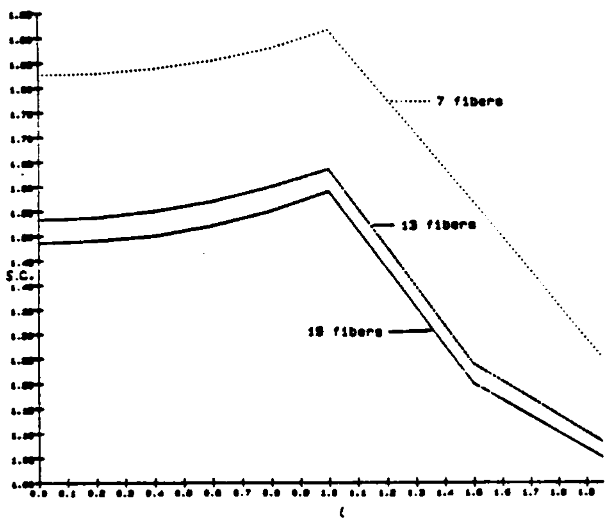

Fig. 5
Stress in adjacent unbroken fiber vs. ξ
for different no. of total fibers.
Central three fibers broken. $\alpha = 1$

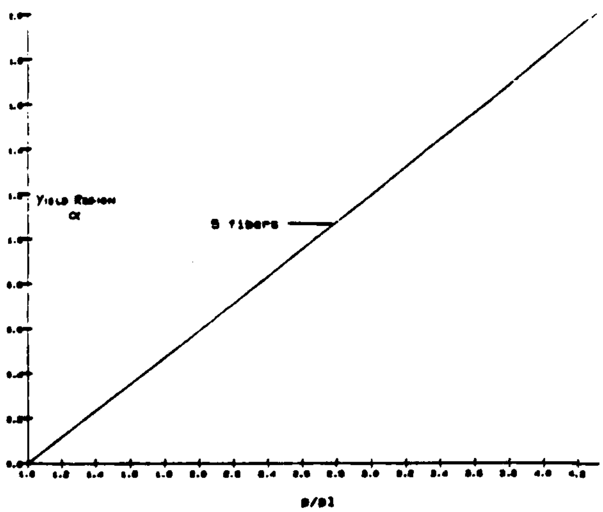

Fig. 6
Yield region, α, vs. p/p_{limit}. Five
total fibers; center fiber broken.

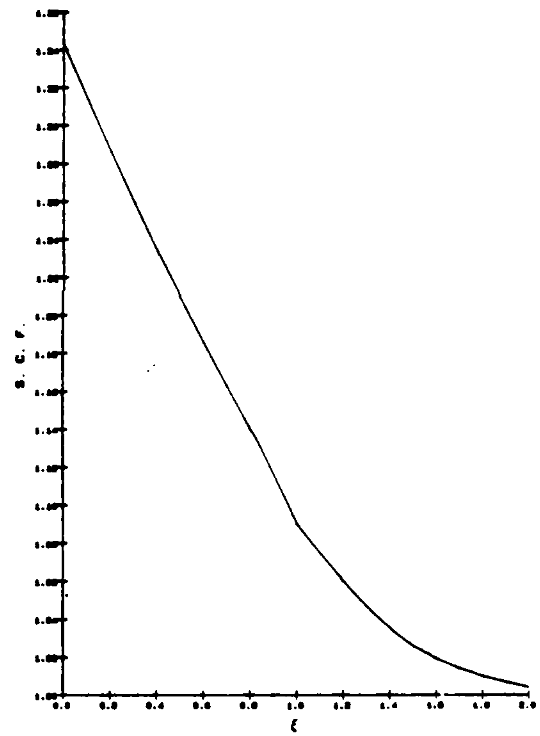

Fig. 7
Stress concentration vs. ξ . Five
total fibers; center fiber broken.
Matrix yield problem.

Models for Compressive Failure of Unidirectionally Reinforced Composite and Laminantes With Low Shear Modulus and Strength

Igor Palley
Corporate Technology
Allied-Signal, Inc.
Morristown, NJ

The paper puts into perspective the models of compressive strength of unidirectionally reinforced composites with low shear strength and/or modulus. Such composites fail through shear kinking (shear degradation) [1-3] schematically shown in Figure 1. We show that approaches in which compressive strength σ_c is expressed through the longitudinal modulus G_{13} of the composite, the longitudinal shear strength τ^* and a characteristic angle θ of fiber misalignment - rather than the mechanical parameters of the fiber and matrix - give simple and reasonable estimates for the compressive strength. It is shown also that the bending energy of the fibers does not influence the compressive strength to a large extent.

The ultimate theoretical value of compressive strength in the case of shear kinking is equal to the longitudinal shear modulus G_{13}: $\sigma_c=G_{13}$ [4]. This result corresponds to the shear microbuckling mode of failure [5] where the bifurcation takes place between the uniform compressive mode and the compressive mode which includes a band of sheared material (Figure 1). The experimentally observed (and usually much lower) values of compressive strength depend on degree of perfection of the fiber alignment. Small misalignments characterized by angle θ expose the weak fiber/matrix interface (or the interlaminar interfaces in the laminates) to shear stresses $\tau = \sigma_c \theta$, thus giving the following estimate for the compressive strength [6]:

$$\sigma_c=\tau^*/\theta \text{ for } \sigma_c \le G_{13}, \qquad (1)$$

where τ^* is the interlaminar shear strength. The relationship between σ_c and θ for three carbon fiber composites and one Kevlar fiber composite (each with an epoxy matrix) is shown by the broken lines in Figure 3. The respective mechanical properties of these composites and their constituents are given in Tables 1 and 2. Based on experimental values of compressive strength, the angles of misalignment according to (1) are small and it is reasonable to expect their presence in these composites. With such small angles, however, the deflections under the compressive load and perpendicular to the load are not negligible as compared to the misalignment deflections. This consideration leads to the non-linear models of compressive strength. There are differences in the published approaches and in the conclusions [see 7,8,9] therefore we reconsider the basic model. Figure 2 shows the shear kink with the fibers deviated from the direction of compressive load so that $v=v_0+v_1$, where v_0 is the misalignment term and v_1 is the deflection under the loading. Let $v_0=f(1-\cos\pi z/t)$; $v_1=c(1-\cos\pi z/t)$, where f,c are constants and t is the width of the kink band. First by ignoring the bending resistance of fibers the following expression for compressive strength is obtained

$$\sigma_C=\tau^*/(\theta+\tau^*/G_{13}) \qquad (2)$$

by using the moment balance expression $-\tau bdz+Qdz=0$, and expressions $Q=P(\frac{dw_o}{dz}-\frac{dw_1}{dz})$ and $\tau=\frac{dw_1}{dz}G_{13}$. Expression (2) would follow from the model discussed in ref. [7] but was not presented or used in that paper; it also differs by a factor v_f - the fiber volume content - from a similar expression in [8]. When $\theta=0$ expression (2) becomes (1). The effect of fiber misalignment on the compressive strength predicted by expression (2) is shown in Figure 3 by the solid lines. Table 2 shows the angles of misalignment corresponding to the experimental values of shear strength. Thus, the nonlinear model (2) predicts that smaller angles of misalignment are required to explain the experimentally observed shear strength. The contribution of fiber bending resistance to the general composite resistance in the process of shear kinking is evaluated by starting with the balance of moments $\frac{dM}{dz}dz-\tau bdz+Qdz=0$ (see Fig. 5) and expression $Mz=\frac{d^2v}{dz^2}EI$ in addition to the two previous ones. This approach leads to the expression

$$\sigma_C=\tau(1+\sigma_e/G_{13})/(\theta+\tau^*/G_{13}) \qquad (3)$$

where $\sigma_e=\frac{\pi^2}{12}(b/t)^2E_f$ is the Eulerian buckling stress for a single unsupported fiber with the length t. Table 3 shows the correction to the value of compressive strength given by (3) as compared to (2). As seen the correction is small. The considered misalignment models (1) - (3) (unlike the microbuckling models (10,11,12)) predict the values of compressive strength observed in experiments. Since the results are sensitive to the values of the misalignment angle, the designer should rely on the test data.

References

1. C. W. Weaver, J. G. Williams, J. Mater. Sci 10 (1975) pp 1323-1333.

2. A. G. Evans and W. F. Adler, Acta Metallurgica Vol. 26 (1978) pp. 725-738.

3. M. R. Piggott, B. Harris, J. Mater. Sci 16 (1981) 687-693.

4. O. M. Guz, FTD-HC-23-197-70, Foreign Tech. Div.:WP-AFB, Dayton, Ohio, 1970.

5. I. Palley, Proceedings, 1 Pan American Congress of Applied Mechanics, Rio de Janeiro, Brazil Jan 3-6, 1989 pp. 47-50.

6. A. S. Argon, in Treatise of Materials Science and Technology, Vol. 1 (1972) pp. 79-113.

7. A. S. D. Wang, ASME paper No. 78/Aero-1 (1978).

8. H. T. Hahn and J. C. Williams, Composite Materials: Testing and Design (Seventh Conference) ASTM STP 893, J. M. Whitney, ASTM (1988) pp 115-139

9. P. S. Steif, J. Comp. Mater. Vol 22 Sept (1988) pp. 818-827.

10. B. W. Rosen, Ch. 3 American Society for Metals, Metals Park, Ohio, (1964).

11. L. B. Greszczuk, AIAA Journal Vol. 13, No. 10, (1975) pp. 1331-1318.

12. C. C. Chamis, Reinforced Plastics/Composites Institute, The Society of Plastics Industry, Inc. Jan 16-19, (1984).

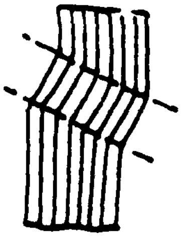

Figure 1

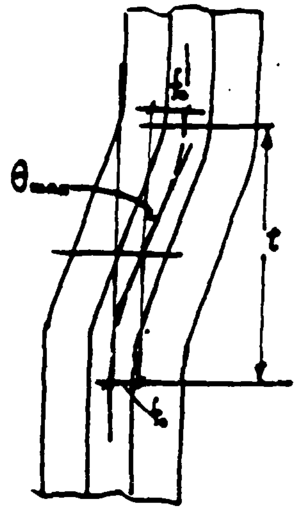

Figure 2

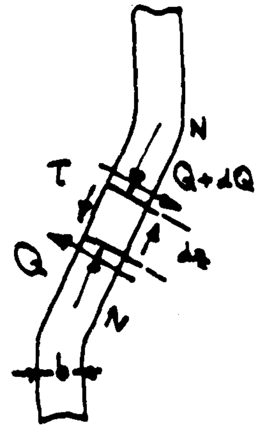

Figure 4

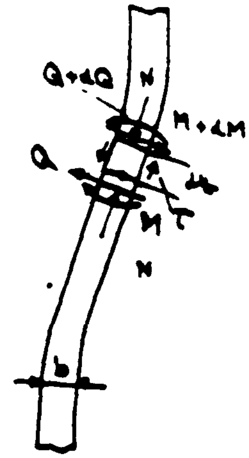

Figure 5

Effect of Fiber Misalignment
On Compressive Strength of Composites

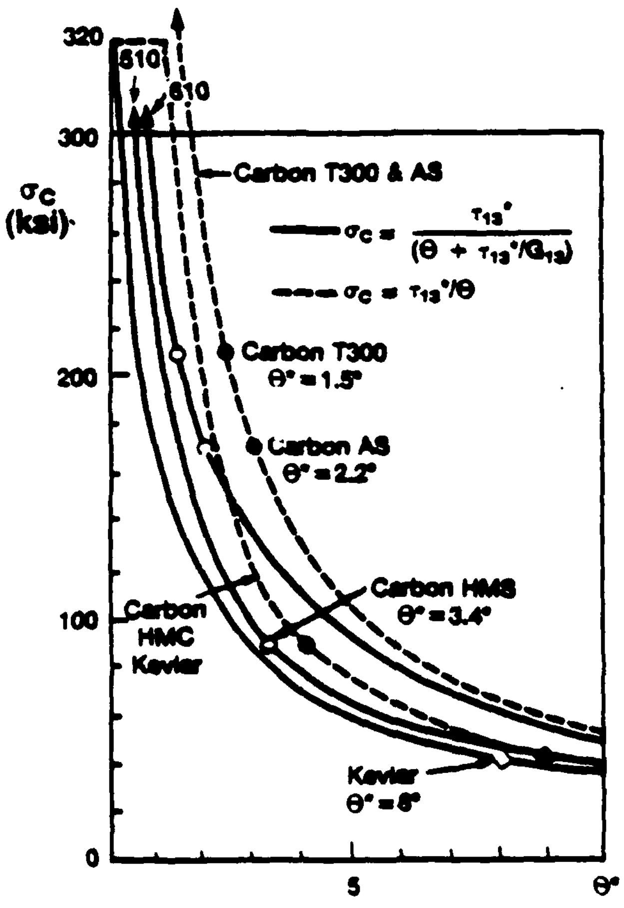

Figure 3

Table 1

Fiber Properties

Fiber	Carbon HMS	Carbon AS	Carbon T300	Kevlar
G_{f13} (ksi)	1,100	2,000	1,300	420
E_{11f} (psi)	55×10^6	31×10^6	32×10^6	22×10^6
σ_{fe} (ksi)	200	260	300	75
ϕ (in)	3×10^{-4}	3×10^{-4}	3×10^{-4}	4.6×10^{-4}

Matrix Properties

$E=0.5\times10^6$ psi $G=0.18\times10^6$ psi

Table 2

Composite Properties

Fiber	Carbon HMS	Carbon AS	Carbon T300	Kevlar
τ_{13}^*	6.5	9.0	9.0	6.5
σ_T (ksi)	120	210	210	200
σ_c (ksi)	90	170	210	40
G_{13} (ksi)	510	610	540	320
θ°	3.5	2.2	1.5	8

Table 3

Effect of fiber resistance to bending on compressive strength

Composite	HMS	AS	T300	Kevlar
E_{11f}(psi)$\times10^6$	55	31	32	22
ϕ (in)	3×10^{-4}	3×10^{-4}	3×10^{-4}	4.6×10^{-4}
t (in)	10^4 (250um)	10^{-4}	10^{-4}	1.6×10^{-2} (400um)
σ_b(ksi)	41	23	24	15
G_{13} (ksi)	510	610	540	320
correction	8%	4%	4.5%	5%

PLASTIC STRAIN INDUCED ANISOTROPY: SOME INTEGRATED EXPERIMENTAL AND THEORETICAL DEVELOPMENTS

by

S. Cheng, E. Krempl, E. H. Lee, T. L. Sham and Y. S. Suh

Department of Mechanical Engineering,
Aeronautical Engineering & Mechanics
Rensselaer Polytechnic Institute
Troy, New York

Abstract

Plastic-strain-induced anisotropy is commonly observed and can have a major effect on stress-analysis evaluations, and yet many computer programs in current use in engineering practice involving plastic deformation include the assumption of isotropic hardening. Difficulties involve both the measurement of anisotropic-hardening characteristics and the formulation of constitutive relations to incorporate such properties. The lack of validity becomes particularly severe when finite deformation is involved as in the analysis of metal-forming problems. This contribution is in the nature of a work-in-progress report on a combined experimental-analytical research program sponsored by the U.S. Army Research Office.

The experimental investigations are in support of the analytical efforts and provide the stress response to prescribed strain histories involving complex nonproportional straining and loading paths. These investigations are performed in the Mechanics of Materials Laboratory of Rensselaer Polytechnic Institute. Although multiaxial tests have been executed previously, very few have involved accompanying intermittent measurement of the changing yield surface as the straining history proceeds. One of the first tasks was to provide the capability to measure yield surfaces under nonproportional loading paths in strain or stress space. A computer controlled servohydraulic MTS axial-torsion testing machine is available for this purpose. The machine is equipped with hydraulically operated collet grips and with a biaxial extensometer. Tubular specimens of length 6.5", diameter 0.74", and a thickness-to-radius ratio of 1/6 were designed and machined from an aluminum-magnesium alloy donated by ALCOA. This material was considered to be isotropic in the as-received condition. A computer program in MTS Basic was written which permits loading the tubular specimen proportionally and nonproportionally in the axial-torsion strain space. At certain designated points yield surface probing can be performed automatically. The yield surface is defined by an offset of 10^{-4} from a least squares fit to the initial elastic line. The entire procedure is fully automatic, the digitized data are stored on floppy discs and are available for subsequent analysis. As of this writing, a whole test sequence on circular deformation in strain space has been completed. Thanks to an NSF equipment grant an internal pressurization system has been added to the testing machine which will permit the execution of triaxial strain paths.

The objective for the analytical component was to develop constitutive relations appropriate for elastic-plastic finite deformation of polycrystalline ductile metals involving strain-induced anisotropy and to apply them in stress and deformation analyses. The initial approach was to express the anisotropy through the combined-isotropic-kinematic-hardening model. Experiments have shown this to be a satisfactory model for deformations which are limited to a

restricted sector of strain-rate space. Such a restriction applies in many metal-forming processes, for example slab rolling, where, throughout the forming process, strain rates are tensile in the direction of rolling, compressive through the thickness and small laterally. As discussed on pp.36,37 of [1], the nose of the yield surface in the corresponding sector of stress-space can be adequately expressed as a circle, in, for example, tension-torsion space, which can be fitted by a combined-isotropic-kinematic-hardening model.

The basic theory of anisotropic hardening, valid for finite deformation, is given in [2]. It incorporates arbitrary rotation of the anisotropic characteristics, in this case rotation of the kinematic hardening back stress, the functional form for which will be characterized from the experimental measurements.

Our project involves extending the analysis to the development of computational procedures to evaluate stress distributions in metal forming processes. The preliminary effort in this direction was to extend the computer program developed by R. L. Mallett: IFDEPSA (Incremental Finite Deformation Elastic-Plastic Stress Analyzer) to incorporate combined isotropic-kinematic hardening which was carried out in conjunction with A. Agah-Tehrani, now with the University of Illinois at Urbana. Using the modified program, the stresses generated during extrusion were evaluated and the influence of various ratios of isotropic to kinematic hardening for the same tensile behavior were compared. As might have been expected, stresses during unloading, and in particular residual stresses, were appreciably lower as the kinematic component of the hardening increased.

As we generate more experimental data we expect to generalize the type of anisotropy which can be incorporated, including the change in shape of the yield surface, and to develop computational procedures appropriate in these cases.

References

1. E.H. Lee and A. Agah-Tehrani, "The Structure of Constitutive Relations Involving Induced Anisotropy at Finite Strain," Advances in Inelastic Analysis, Eds. S. Nakayawa, K. Willam and N. Rebelo, ASME Book G00408, AMD-Vol. 88, PED-Vol. 28, 29-40, 1987.

2. A. Agah-Tehrani, E.H. Lee, R.L. Mallett and E.T. Onat, "The Theory of Elastic-Plastic Deformation at Finite Strain with Induced Anisotropy Modeled as Combined Isotropic-Kinematic Hardening," J. Mech. Phys. Solids, 35, 519-539, 1987.

Extended Abstract

for:
Army Symposium on Solid Mechanics:
"Mechanics of Engineered Materials and Applications"

Anthony D. Rollett, U. Fred Kocks
Los Alamos National Laboratory
NM 87545

The Application of a Crystal Plasticity Model to the Prediction of Strain-Hardening and Anisotropy

Almost all metallic materials exhibit some degree of crystallographic preferred orientation and in general this leads to some degree of anisotropy. Although elastic anisotropy is of interest, the greater influence on the formability of metallic materials is their plastic anisotropy. This paper focuses on the simulation of anisotropy, both the development of crystallographic preferred orientation (texture) and its consequences for anisotropy. Software packages are described that analyze experimental textures, LAtex, and that implement a crystal plasticity model, LApp. This simulations are compared with experimental data on the strain hardening, texture and anisotropy of f.c.c. metals such as Al, Cu and Ag. The objective of modeling strain hardening is to be able to quantitatively account for the differences in strain hardening between different deformation modes such as compression and torsion. One objective of simulating anisotropy, for example, is to be able to predict r-values in rolled sheet. This work is part of a broad effort to develop constitutive models for the mechanical behavior of metallic materials in the range of ambient to low temperatures and medium to very high strain rates. One of the long-term goals of the work on texture is the development of physically-based models of anisotropy that can be applied in, e.g., finite-element models.

The crystal plasticity model (LApp) relies on the long accepted fact that slip on {111} planes and in <110> directions for face centered cubic (f.c.c.) crystals, or vice versa for b.c.c. crystals. Also there is a critical resolved shear stress (crss) for yield on any given slip system, where a slip system is defined as a particular combination of slip direction and slip plane. This permits a yield surface to be described for a single crystal or grain , which is the locus of points in stress space separating elastic from plastic behavior. The dimensionality of the stress space that must be considered is reduced to five by the insensitivity of yield to the hydrostatic stress component. Such a description of material behavior implies consideration of large strains (>5%, say) and neglect of small strain (<0.2%) effects. Also implicit is the assumption that anisotropy is only sensitive to the geometry of deformation and is not sensitive to strain rate (except for the yield surface modification described below), temperature or hardening rate.

Several modifications to the single crystal yield surface have proved to be useful. The most important of these is to introduce a mild rate sensitivity of yield, or, more generally, a stress strain-rate behavior, of each slip system. It is straight-forward to show that a crystal must have five independent slip systems in order to satisfy an arbitrary deformation imposed upon it. This is the situation of a grain in a polycrystalline metal where the assumption is made that each grain undergoes the same shape change as the macroscopic sample. This assumption is known colloquially as "compatibility first" because it means that compatibility is satisfied at the expense of stress equilibrium, i.e. that no gaps or overlaps develop between grains at large strains but that the stress state varies from grain to grain. Now the stress states required to activate a minimum of five slip systems in rate-independent cubic crystals actually activate either six or eight slip systems. This results in an ambiguity of choice as to which five slip systems are actually active. Making the single crystal yield surface mildly rate sensitive, however, eliminates the ambiguity of choice because there is then a unique stress state for any strain imposed on the crystal, Fig. 1. It is important to note that this rate sensitivity is not only convenient but is also physically correct in that pure f.c.c. metals are known to exhibit a small rate sensitivity of the yield stress. Other modifications of the single crystal yield surface are options in the simulation code that model "pencil glide" in b.c.c. metals and latent hardening.

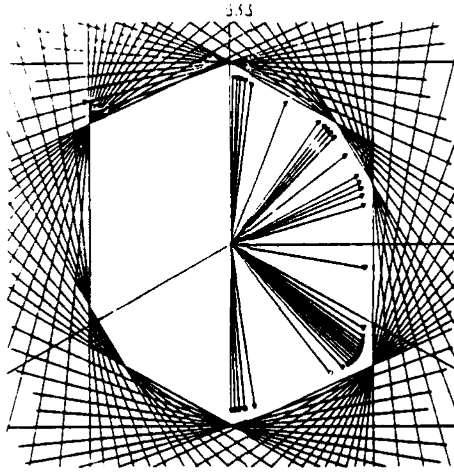

Fig. 1. The π-plane yield surface plotted for a <111> oriented single crystal, showing envelope construction for the rate-insensitive Bishop-Hill solution and stress vectors for a rate-sensitive solution with a small stress exponent (=12) that rounds the corners of the vertices.

The texture simulation code is based on applying a uniform strain to an ensemble of grains, between 200 and 1000 grains, and averaging the stress states of the individual grains to produce a stress for the ensemble. This assumption, due to Taylor, is relaxed at high strains because the grain shape in some deformation modes permits certain shears to be unconstrained. This relaxation is known as Relaxed Constraints (RC) as opposed to the Taylor uniform strain assumption which is known as Full Constraints (FC). The application of RC is important for describing more accurately the evolution of texture in rolling, for example.

The analysis of experimental textures (LAtex) is primarily for generating complete 3-D Orientation Distributions (OD's) from pole figures. The calculation of OD's from pole figures is accomplished by the Williams-Imhof-Matthies-Vinel (WIMV) method, in an implementation by Kallend, in which a discrete representation of the OD is constructed by an iterative method. The presentation of the results uses a new set of cylindrical coordinates introduced by Wenk and Kocks in which, for example, the sections of an OD are closely related to such projections of an OD as a pole figure. Experimental textures are adapted to computer simulation by generating lists of discrete orientations, "grains", in which the weight assigned to each grain is related to the intensity of the OD at that orientation.

We are currently engaged in comparing experimental with simulated in-plane anisotropy in rolled copper and aluminum. Various textures are produced by different rolling and annealing schedules, the pole figures are measured and OD's are produced by the WIMV analysis. Yield surfaces can then be calculated for any pair of stress components (or for the π-plane) and compared to experimental measurements. Another measure of anisotropy is the r-value which is the ratio of width to thickness strain rates in a tensile test. If rolled sheet is to be formed into, say, a cup, the variation of r-value with direction in the sheet is a good predictor of the earing behavior of the sheet. Simulated rolling textures have also been used to calculate r-values, Fig. 2, and the sensitivity of the variation of the r-value with direction has been investigated with respect to such features of the model as Relaxed Constraints and latent hardening. The motivation for these studies is that the r-value variation appears to be very sensitive to the nature of the experimental texture and to the assumptions of the crystal plasticity model.

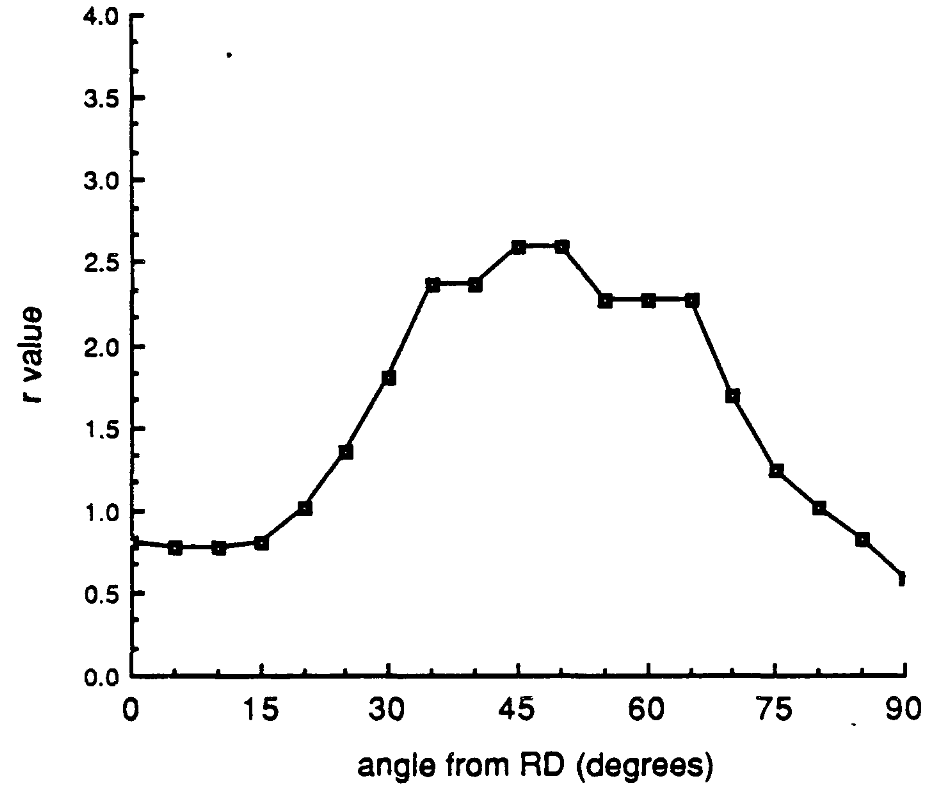

Fig. 2. Plot of r-value versus angle from the rolling direction for a simulated rolling texture.

*This work supported by the OBES office of the USDOE.

IMPROVED ISOTROPIC-KINEMATIC HARDENING MODEL FOR METAL PLASTICITY: MODEL AND EXPERIMENTS

by

C. S. White* and L. Anand**

*Materials Reliability Division
U.S. Army Materials Technology Laboratory
Watertown, Massachusetts 02172

**Department of Mechanical Engineering
Massachusetts Institute of Technology
Cambridge, Massachusetts 02139

Abstract

The need for increased accuracy in material modeling has been driven in recent years by advances in computing capability and the complexity of problems which now may be analyzed. Current material models are unable to represent many of the important multi-dimensional effects of the plastic deformation of metals to large strain. These effects can become very important at the level of deformation reached in metal processing operations, shear band formation, penetration mechanisms, and crack tip processes. A program has been conducted to examine and identify common features of various phenomena seen in metal plasticity.

An experimental program was conducted to produce a number of different types of tests on several materials. The types of tests included: tension, large strain compression, symmetric cyclic, unsymmetric cyclic, single reverse and large strain torsion. Materials tested were type 316 stainless steel and 1100-0 aluminum. These experiments represent the first collection of such a complete data base for any material. Additionally, cyclic data for three carbon steels were analyzed.

A new constitutive model for metal deformation is introduced to analyze and predict these experiments. The model contains both isotropic and kinematic hardening components but overcomes some of the shortcomings of previous such models by introducing new material functions. An important new function is the relative position of the back stress within a surface defined by its previous maximum norm. The back stress moduli are made to depend upon this relative position. This dependence implicitly defines a "reversing event" as occurring while the back stress is less than its previous magnitude.

Another important new feature is the introduction of softening of the isotropic component. During a reversing event the isotropic component initially softens. This softening is dependent upon the direction of straining and so is different than the static or dynamic softening of viscoplastic models.

The model captures key features of small strain uniaxial cyclic behavior very well. Symmetric strain cycling, unsymmetric strain cycling, unsymmetric stress cycling and the additional hardening due to nonproportional cycling in tension-torsion are all captured by the model. The predictions of the finite torsion results are not as well represented. The model predicts a monotonic increase of both shear stress and compressive normal stress toward saturation values due to the evanescent term in the back stress evolution equation. The predicted stress levels are not in good agreement with experiment. The addition of plastic spin to the model does not affect these results.

SOME THOUGHTS ON FINITE STRAIN PLASTICITY CONSTITUTIVE MODELING

Norris J. Huffington, Jr.

U.S. Army Ballistic Research Laboratory
Aberdeen Proving Ground, Maryland 21005

Recently, there have been many research publications concerned with property invariant formulations for finite deformation plasticity, and especially with respect to intermediate configurations and plastic spin. While there appears to be no consensus as to a "correct" formulation it is clear that use of the Zaremba[1]-Jaumann[2]-Noll[3] (ZJN) stress rate in large strain analyses where the principal stresses rotate leads to spurious sinusoidal stress-strain behavior. Figure 1 illustrates this for simple shear with bilinear kinematic strain hardening. In fact, sinusoidal response occurs for this problem even without plasticity. To be sure, other objective stress rate models have been advocated (Truesdell[4], Dienes[5], Onat[6], Bammann[7], Asaro[8], Anand[9], Dafalias[10], and many others). The Green-Naghdi[11] (GN) stress rate, as recommended by Bammann[7], was employed to obtain the other curve shown in Figure 1. While this result appears plausible there is a lack of quantitative verification.

In addition, there are anomalous discrepancies associated with the normal stresses accompanying simple shear, as illustrated in Figure 2. This figure compares the normal stresses σ_y associated with simple shear in an elastoplastic material with isotropic hardening for constitutive models employing the ZJN and GN stress rates, respectively, for cases in which the time histories of the shear stress σ_{yz} were the same.

The continuum codes DYNA2D[12] and DYNA3D[13], along with their pre- and post-processors, are being used as tools in an investigation of such discrepancies and for the study of other constitutive models not presently incorporated in these codes. The objective of this investigation is the establishment of an improved modeling of finite strain plasticity in continuum hydrocodes ramifications for better prediction of strain localization and rupture. Additionally, the codes cited above are being adapted to provide counterpart numerical solutions to experiments being performed by the Army Materials Technology Laboratory on Lindholm-type thin-walled torsion specimens. Results from these calculations will be incorporated in the paper.

References:

1. S. Zaremba, Sur une conception nouvelle des forces interieurs dans un fluide en mouvemount, Mem. Sci. Math. No 82 (1937).

2. G. Jaumann, Geschlossenes System physikalishcher und chemischer Differentialgesetze, Sitzbar. Akad. Wiss. Wien (IIa) 120, 385-530 (1911).

3. W. Noll, On the Continuity of the Solid and Fluid States, J. Rat'l Mech. Anal., 4, 3-81 (1955).

4. C. Truesdell, The Simplest Rate Theory of Pure Elasticity, Comm. Pure Appl. Math., 8, 123 (1955).

5. J. K. Dienes, On the Analysis of Rotation and Stress Rate in Deforming Bodies, Acta Mech., 32, 217-232 (1979).

6. E. T. Onat, Flow of Kinematically Hardening Rigid-Plastic Material, in Mechanics of Materials Behavior-D. C. Drucker Anniv. Vol., Elsevier, P. 311 (1984).

7. G. C. Johnson and D. J. Bammann, A Discussion of Stress Rates in Finite Deformation Problems, Int. J. Solids Structures, 20, 725-737 (1984).

8. R. J. Asaro and A. Needleman, Texture Development and Strain Hardening in Rate Dependent Polycrystals, Acta Metall., 33, 923 (1985).

9. L. Anand, Constitutive Equations for Hot-Working of Metals, Int. J. Plasticity, 1, 213 (1985).

10. Y. F. Dafalias, Corotational Rates for Kinematic Hardening at Large Plastic Deformations, Jour. Appl. Mech., 50, 561-565 (1983).

11. A. E. Green and P. M. Naghdi, A General Theory of an Elastic-Plastic Continuum, Arch. Rat. Mech. Anal., 18, 251-281 (1965).

12. J. O. Hallquist, User's Manual for DYNA2D - An Explicit Two-Dimensional Hydrodynamic Finite Element Code with Interactive Rezoning and Graphical Display, University of California, Lawrence Livermore National Laboratory, Rept. UCID-18756, Feb. 1987.

13. J. O. Hallquist, DYNA3D User's Manual (Nonlinear Dynamic Analysis of Structures in Three Dimensions), University of California, Lawrence Livermore National Laboratory, Rept. UCID-19592, April 1988.

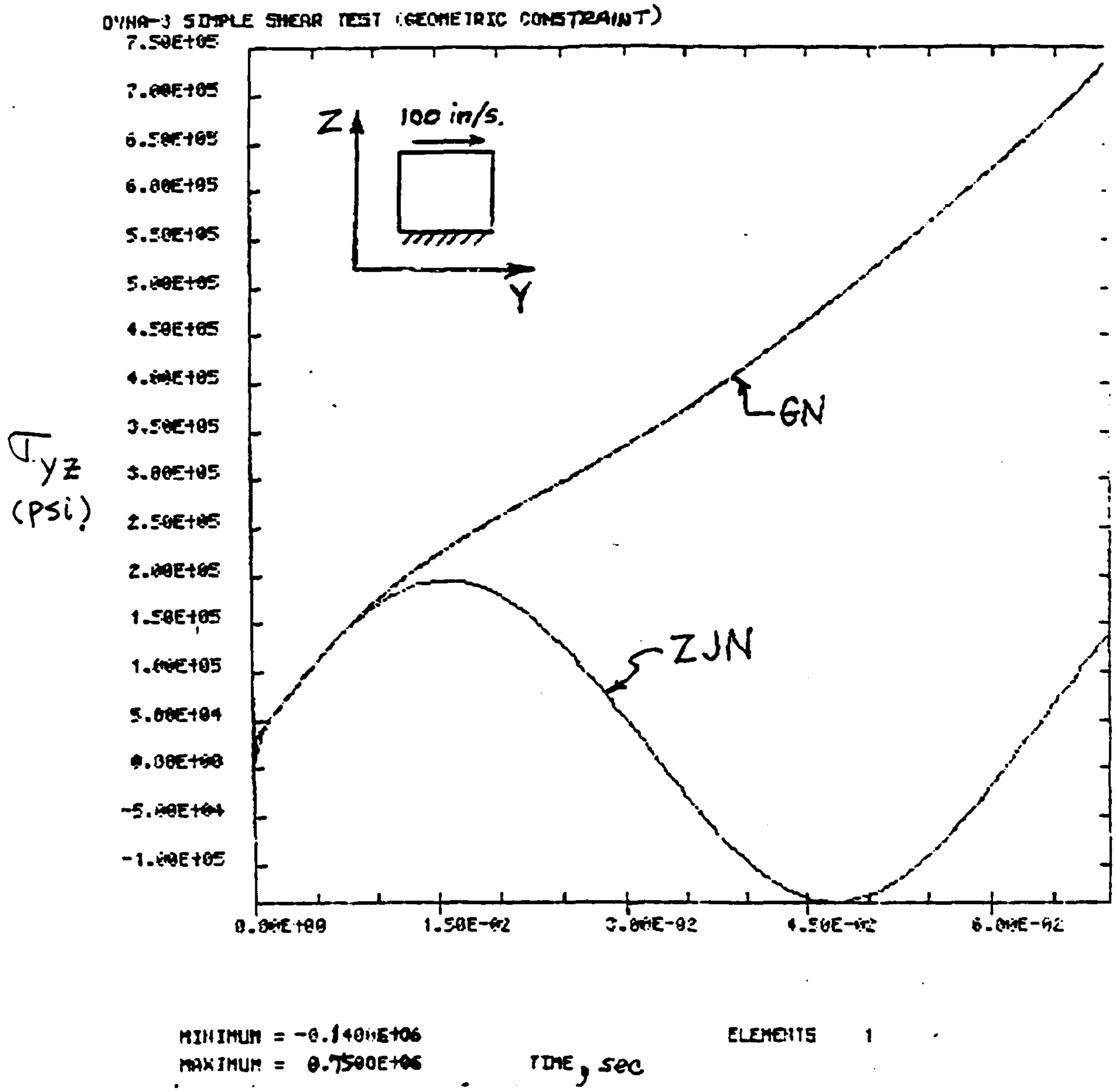

Figure 1 Comparison of shear Stress Predictions

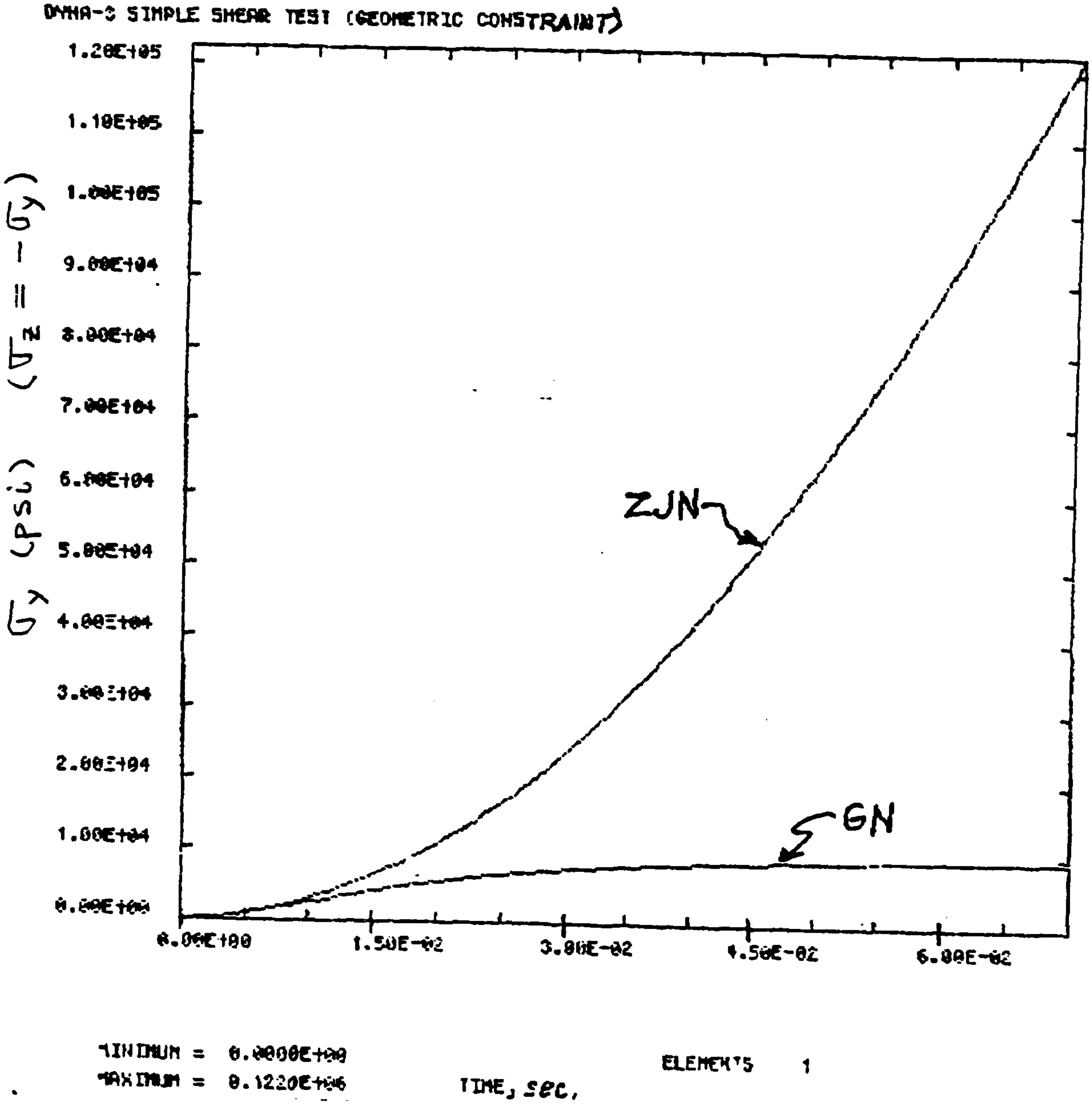

Figure 2 Comparison of Normal Stress Predictions

EXPERIMENTAL MECHANICS: NEW CHALLENGES IN MICROMECHANICS

Ulric S. Lindholm
Southwest Research Institute
San Antonio, Texas

One of the major challenges for experimental mechanics in the immediate future is the measurement of strength and damage related processes in materials at the microstructural level. The requirement is driven by the continuing development of micromechanical modeling of life controlling processes in both structural and electronic materials. For example, if we consider fatigue life, the early macroscopic approach was the measurement of S-N curves derived from bulk material specimens. The current micromechanical approach involves understanding of crack growth rates where the plastic zone size may be measured in microns and the crack length extension per cycle in angstroms. In order to verify analytical models of the latter process, we need to have experimental measurements of the displacement or strain fields at the localized crack tip with at least micron level spatial resolution. Fundamental measurements at the microscale are needed for all deformation, damage, and fracture mechanisms in materials of technical interest. Such measurements will support both the development of life prediction algorithms for technical materials and guide the synthesis of high-strength materials with damage tolerance. The evolution of nonhomogeneous or composite multiphase materials with laminar, linear fiber, or particulate phase geometries of fine scale adds emphasis to the need for micromechanical understanding; both analytical and experimental. This review will describe some recent experimental approaches which measure material strength related behavior with spatial resolution in the range from angstroms to microns.

Three examples of problems being pursued at Southwest Research Institute will be discussed in some detail. The first problem addresses the issue of mapping the in-plane displacement and, by differentiation, strain field at the tip of a propagating crack. The experimental technique used employs (1) a programmable servohydraulic loading stage mounted within a scanning electron microscope, (2) producing sequential high-resolution SEM images of the crack tip at incremental load steps, and (3) automated processing of any two photos as a stereo pair to yield a full-field, two-dimensional displacement map. The displacement field is digitized for subsequent processing in a number of formats which will be illustrated.

A second problem is the characterization of pore evolution in ceramics subject to high-temperature creep deformation or to densification during sintering or hot pressing. The primary experimental technique used is small angle neutron scattering. This technique can resolve pore sizes down to the nanometer range. The neutron scattering measurements yield cavity nucleation and growth rates and average pore size, distribution, and morphology.

The third problem to be discussed is the study of interfacial fracture and the role of surface morphology on interface bonding and fracture. A new tool for surface studies of this type is the scanning tunneling microscope (STM) which has spatial resolution down to angstrom dimensions. At the highest resolution, individual atoms can be imaged. Application of the STM to the study of interfacial fracture in a silicon fiber-reinforced titanium aluminide composite will be illustrated.

It is hoped that these examples will suggest other applications and other experimental approaches to the quantitative measurement of material behavior at the micromechanical level.

DETERMINATION OF PLASTIC STRAIN AND FATIGUE IN METAL AND METAL COMPOSITE USING LASER SPECKLES

by

F. P. Chiang
Leading Professor of Mechanical Engineering
Director, Laboratory for Experimental Mechanics Research
State University of New York at Stony Brook
Stony Brook, NY 11794-2300

Structural failure often is the result of metal fatigue. We have seen in recent years a number of aircraft disasters as a result of fatigue failure. How to detect and measure fatigue damage in metallic materials is therefore an important part of any structural integrity assurance program. It is customary in the field to do inspections visually. While this approach is definitely useful, it nevertheless is very subjective and can only be effective when the damage is substantial. In this paper we explore a non-contact and remote sensing technique using laser speckles which may someday be developed into a portable automated system for field inspection.

Speckle is the result of multiple interference of numerous waves crossing one another. When an optically rough surface is illuminated by a coherent radiation such as that from a laser beam, the reflected wavelets from each and every point mutually interfere to form a pattern of random fringes. These are the speckles, and their properties are related to the surface roughness. It is this relationship that we are exploring in our study.

It is well known that when a material experiences plastic strain, its surface roughness changes. This change can be detected by the spatial spectrum variation of its resulting laser speckle pattern. Since plastic strain precedes fatigue crack initiation, we can use it to monitor the fatigue process as well.

It has been established that by starting with a well polished specimen, its surface roughness increases (to a certain saturated level) when it experiences increased plastic strain. The path along which the plastic strain is attained is immaterial as long as the total effective strain is the same. A typical surface roughness and plastic strain relationship is shown in Figure 1.

When one illuminates a metal surface with a collimated laser beam, the reflected wavelets spread out into a spectrum depicting the spatial frequency content of the surface roughness. It can be shown that the variation of the reflected light intensity may be expressed as

$$\frac{d<I>}{<I>}|_{V=0} \approx -2g(\frac{d\sigma}{\sigma}) \tag{1}$$

along the direction of mirror reflection, and

$$\frac{d<I>}{<I>}|_{V\neq 0} \approx 2(\frac{d\sigma}{\sigma}) - \frac{1}{2}V^2T^2(\frac{dT}{T}) \tag{2}$$

along all other directions. In the above two equations <I> is the average intensity, V the direction of diffracted light, σ the standard deviation of the surface height function, T the correlation length of the surface height function, and

$$g = [\frac{2\pi}{\lambda}(1+\cos\theta)\sigma]^2 \tag{3}$$

where λ is the wavelength of the incident light and θ the incident angle. Typical diffraction patterns from a metal surface at two levels of plastic strain are shown in Figures 2 and 3.

It is seen from Equation (2) both the standard deviation σ and the correlation length T of the surface height function appear in the equation. Thus it is more advantageous to use this part of the deflected light for the characterization of surface roughness. This fact is also qualitatively obvious from the two diffraction patterns shown in Figures 2 and 3.

There are many ways that one may choose to use for extracting information from such a diffraction pattern. The one we selected is a scheme used in the discipline of pattern recognition for extracting texture of an image. We window out a portion of the higher spatial frequency domain of the diffraction spectrum, digitize it into gray levels, and then calculate the statistical contrast value of the pattern using the following formula:

$$CON = \sum(i-j)^2P(i,j) \tag{4}$$

where P(i, is the probability density function of a pair of gray levels.

We use the CON value to calibrate measured strains of an aluminum specimen (1100-H14) in tension. The result is as shown in Figure 4. We find that the CON value increases monotonically with respect to total strain until about 1.2% and plastic strain until about 0.9%. Beyond these points the CON values start to decrease with increased strain. From Figure 1 we know that the surface roughness is still increasing at this level of deformation. Apparently, the CON value is no longer sufficient to characterize it. However, we shall demonstrate in the following that the CON value nevertheless is quite effective in predicting the onset of fatigue crack initiation and propagation.

We applied the CON method to monitoring plastic strains at nine points surrounding the tip region of a saw-cut notch in an aluminum specimen under cyclic bending stress. The geometry of the specimen and configuration of the points are as shown in Figures 5 and 6, respectively.

The specimen was mounted in a fatigue machine capable of rendering cyclic bending load. At predetermined cycles the machine was stopped and a laser beam was used to illuminate the nine selected points sequentially. The resulting diffraction spectrum was received on a ground glass and a window of its high frequency region was digitized. CON value was then calculated for each of these digitized images. The result was plotted as shown in Figure 7.

It is interesting to note that along points 2, 5, and 8, which was the eventual crack propagation path, the CON value increased drastically at certain cycles of loading. On the other hand, it stayed almost stationary at all other points, which were merely 0.06 inch away from the path of eventual crack propagation. This experiment was performed on an aluminum specimen with an initial surface roughness of 0.7μm.

At the conference we shall also present results from specimens made of metal matrix composites.

Acknowledgement:

Financial support of this work provided by the Army Research Office's Engineering Science Division (Dr. R. E. Singleton, Director) through contract Number DAAL0388K0033 is gratefully acknowledged.

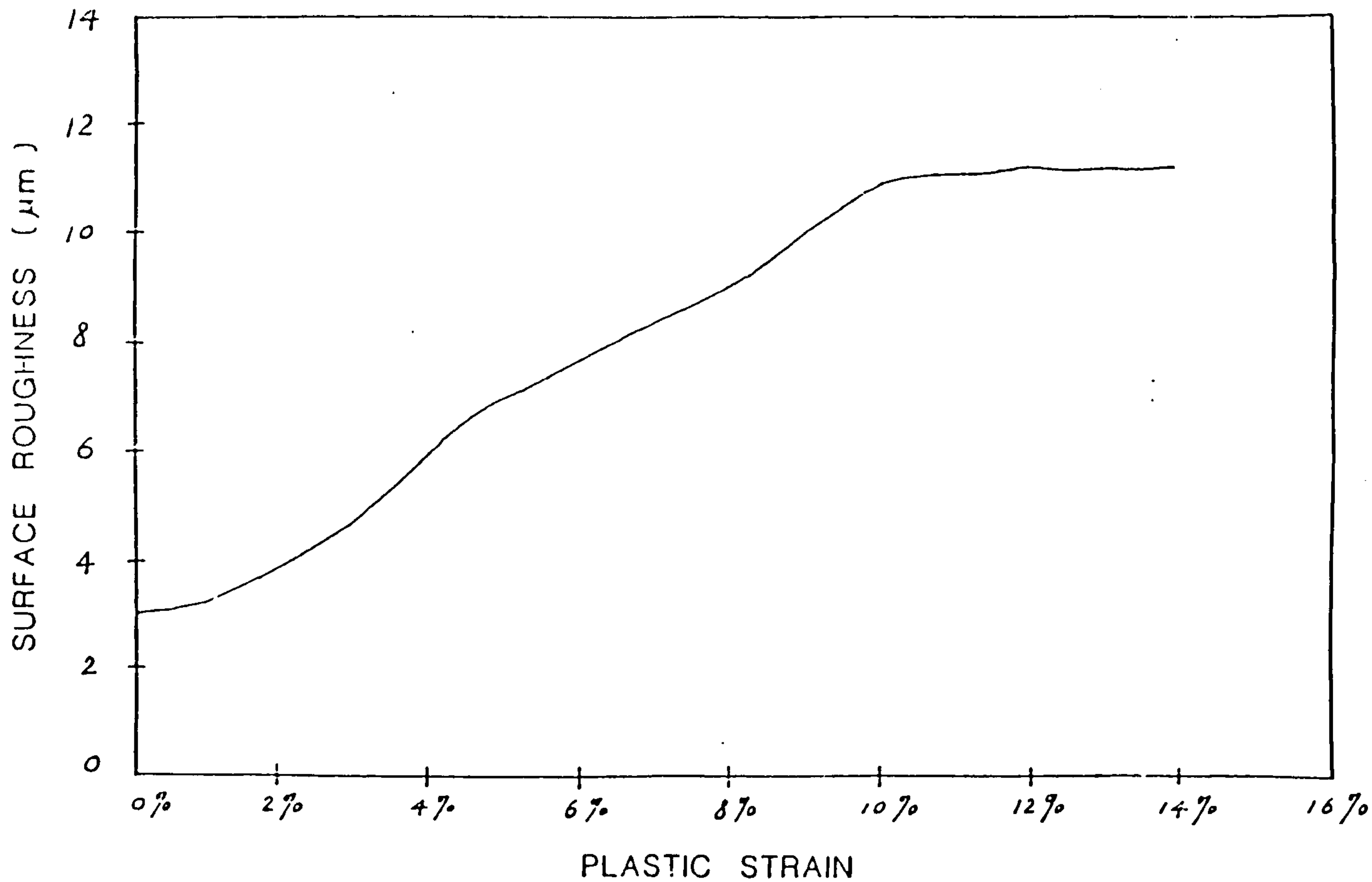

Fig. 1 Plastic strain-surface roughness curve of 1100-O AL material.

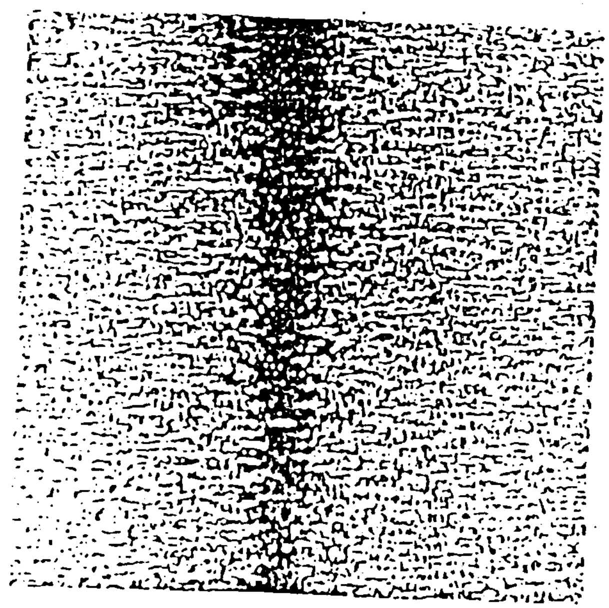

(a) Frequency spectrum.

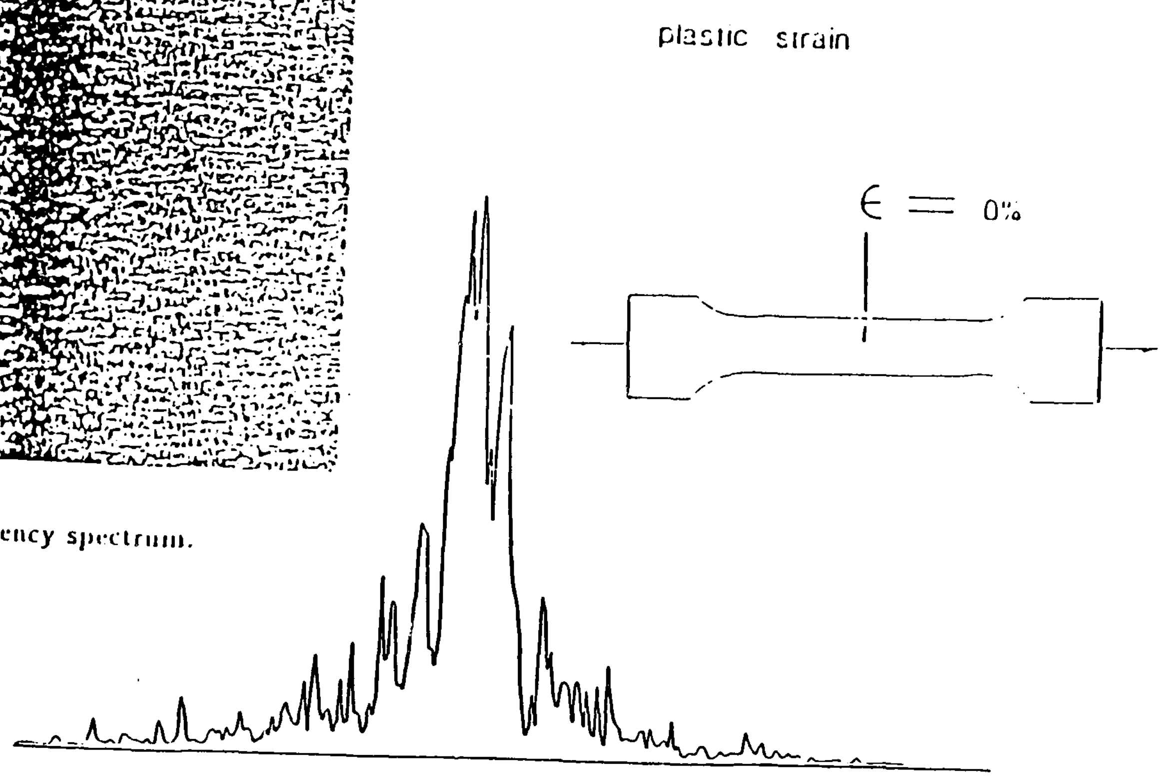

(b) Intensity profile of the frequency spectrum.

Fig. 2 Frequency spectrum from an 1100-0 AL specimen under the original (as received) state.

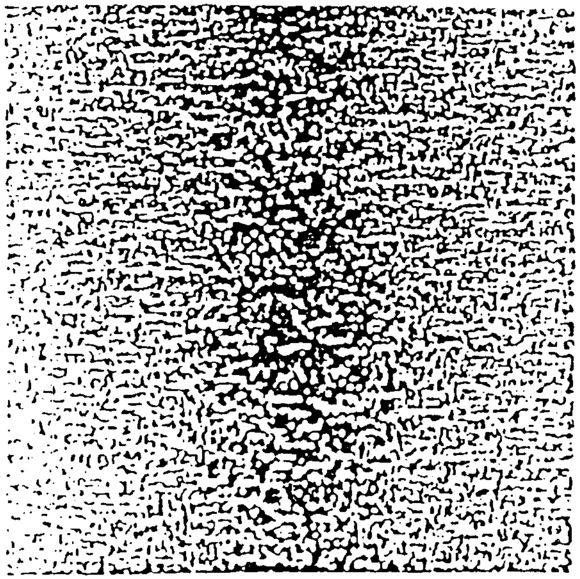

(a) Frequency spectrum.

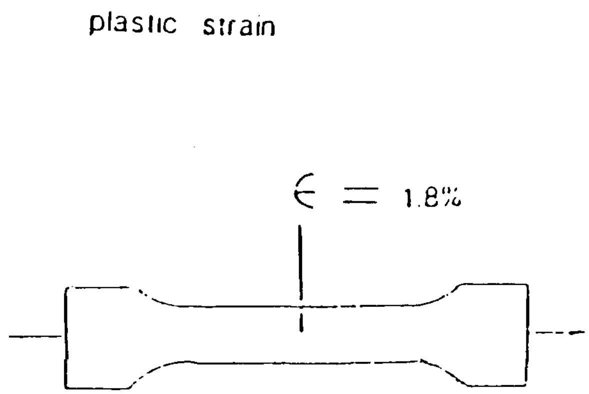

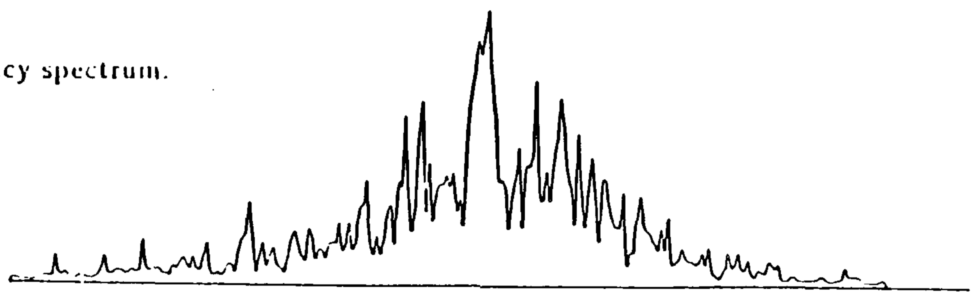

(b) Intensity profile of the frequency spectrum.

Fig. 3 Frequency spectrum from an 1100-O AL specimen under 1.8% plastic strain.

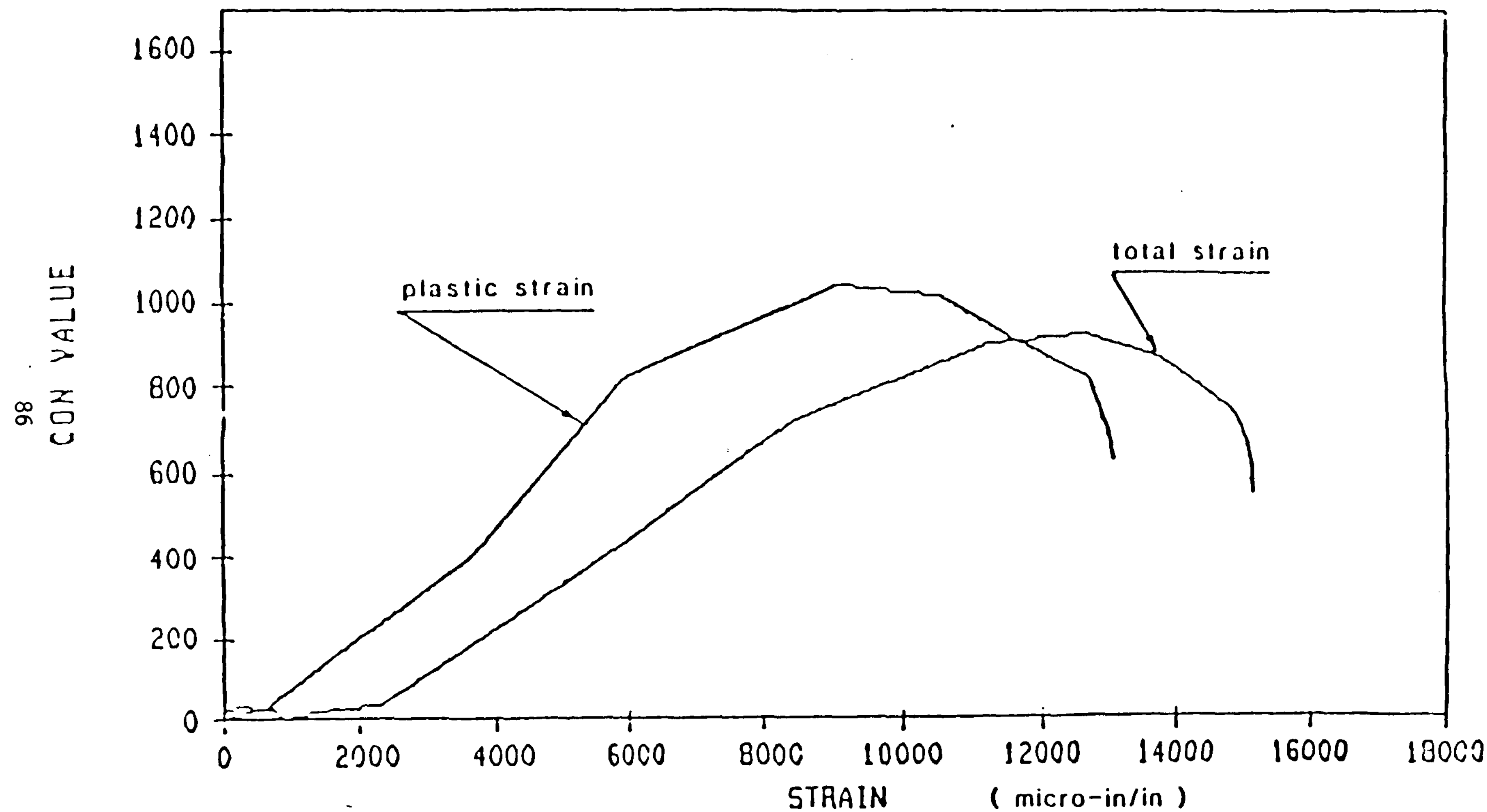

Fig. 4 Variation of strain with CON value to an 1100-H14 AL

specimen with $1\mu m$ initial surface roughness

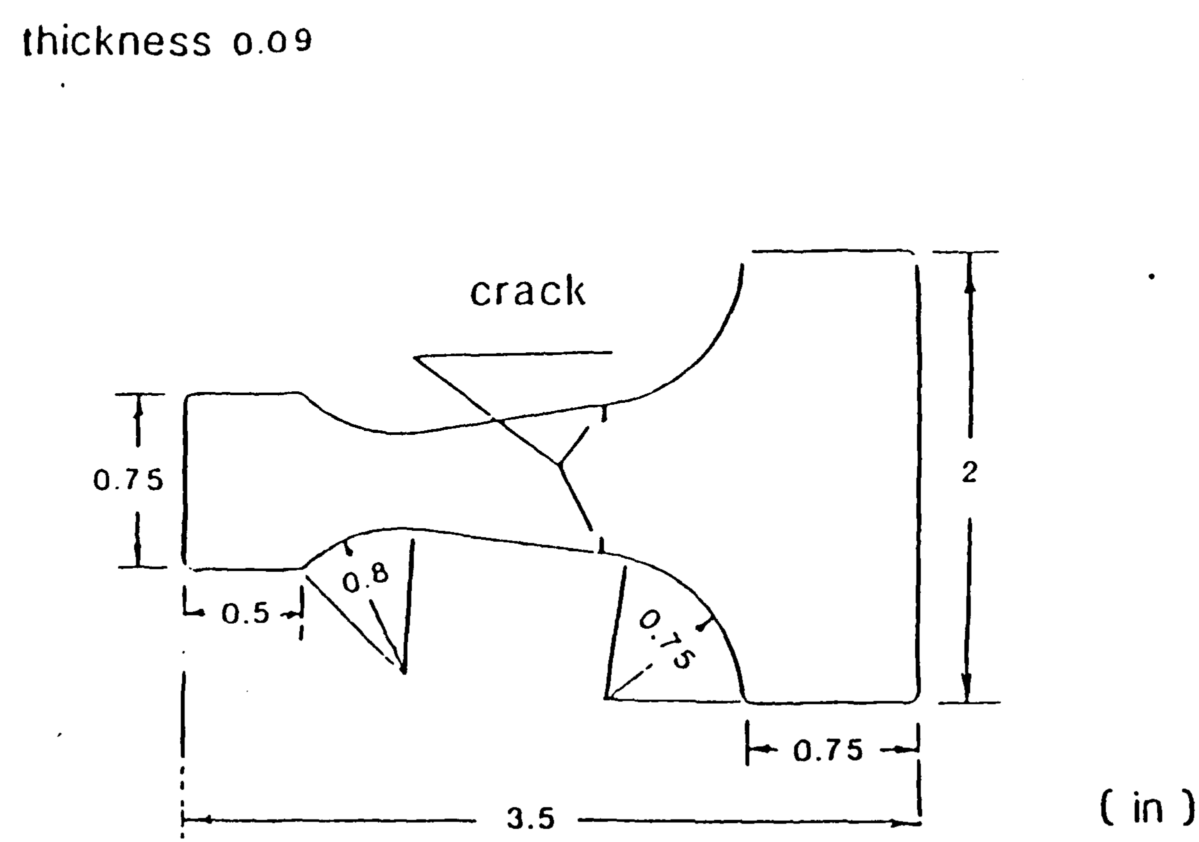

Fig. 5 Fatigue specimen made of 1100-O aluminium with cracks.

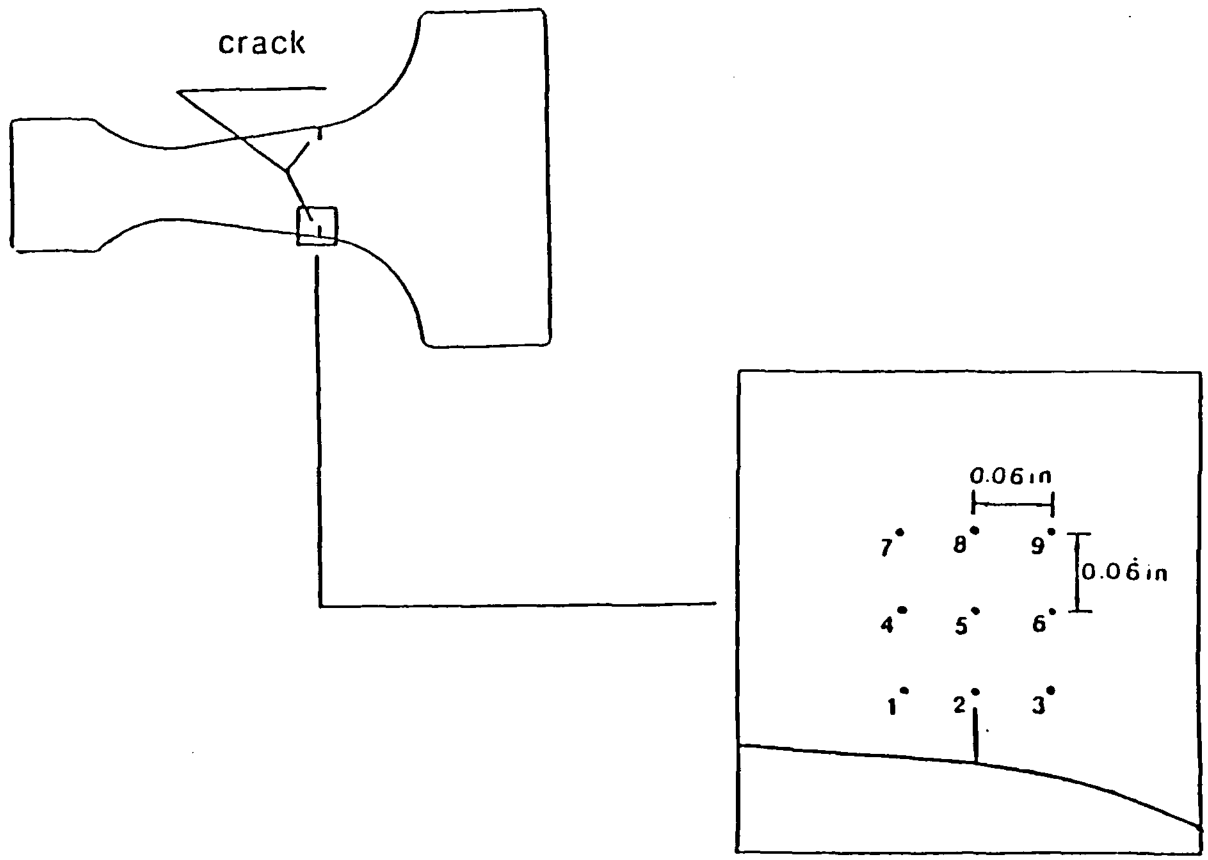

Fig. 6 Fatigue specimen with cracks and the 9 test points are arranged around the tip of a crack.

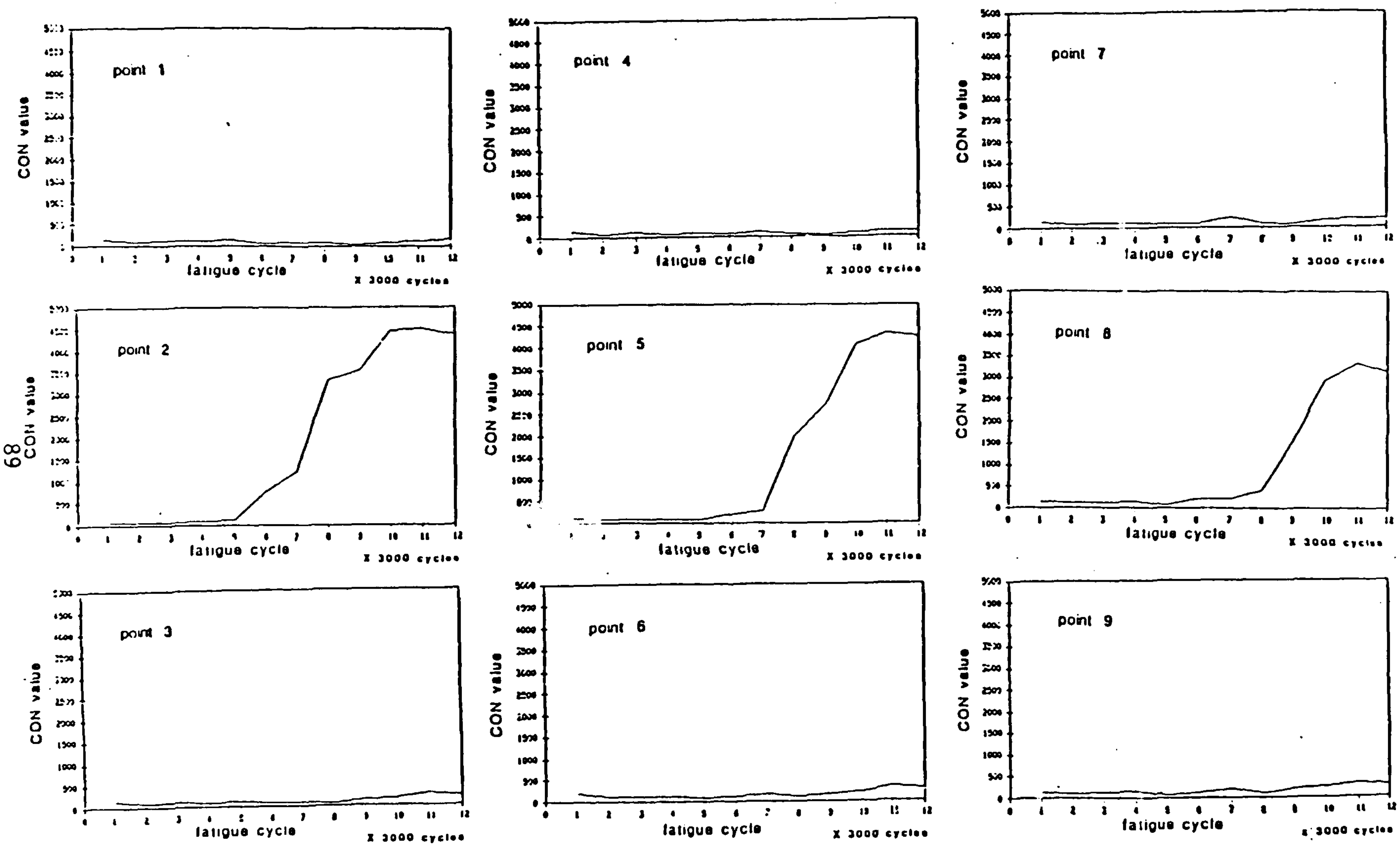

Fig. 7 Statistical contrast value (CON) of the speckle field at different points as a function of fatigue cycle.

APPLICATION OF PHOTOMECHANICS TO THE STUDY OF SOLID MECHANICS PHENOMENA AND MATERIAL PROPERTY MEASUREMENT.

J. Morton and D. Post
Virginia Polytechnic Institute and State University
Blacksburg
Virginia

ABSTRACT

Photomechanics applies optical techniques to the study of solid mechanics phenomena. Recent developments in the science have yielded moire interferometry (1), a full-field technique which provides measurement of surface in-plane displacements with very high sensitivity and spatial resolution. The principles and basic equations are shown in figure 1.

Moire interferometry has become a powerful tool for:

a. understanding physical behavior
b. discovering solid mechanics phenomena
c. measuring material properties
d. validating computer codes.

These will be illustrated through a number of examples which will include:

1. The bimaterial interface.

Moire interferometry is used to measure the coefficients of thermal expansion of brass and steel, and to study the nature of the interfacial stresses induced when these materials are bonded together at elevated temperature. The study is complemented by a finite element study of the problem. The specimen configuration and a typical fringe pattern are shown in figures 2 and 3, respectively.

2. Shear property measurement.

Moire interferometry has been used to determine the shear moduli of thick graphite epoxy composites. The Iosipescu specimen is compared with an improved specimen geometry which yields a more uniform shear strain distribution across the test section - figures 4 and 5. The improved specimen geometry has the potential to allow strength measurement, also.

3. Residual strain measurement.

Moire interferometry has been used to assess the magnitudes of residual strains present in thick composite cylinders. Under-cutting relieved manufacturing strains which were subsequently measured in the interferometer. Preliminary results, shown in figure 6, indicate the presence of very high through-thickness tensile strains together with local phenomena which coincided with major stages in the fabrication procedure.

REFERENCE

1. D. Post. "Moire interferometry", Chapter 7, Handbook of Experimental Mechanics, A.S. Kobayashi, Editor, Prentice-Hall, 1987.

$$f = \frac{2}{\lambda}\sin\alpha$$

$$U = \frac{1}{f}N_x \qquad V = \frac{1}{f}N_y$$

$$\epsilon_x = \frac{\partial U}{\partial x} = \frac{1}{f}\frac{\partial N_x}{\partial x}$$

$$\epsilon_y = \frac{\partial V}{\partial y} = \frac{1}{f}\frac{\partial N_y}{\partial y}$$

$$\gamma_{xy} = \frac{\partial U}{\partial y} + \frac{\partial V}{\partial x} = \frac{1}{f}\left[\frac{\partial N_x}{\partial y} + \frac{\partial N_y}{\partial x}\right]$$

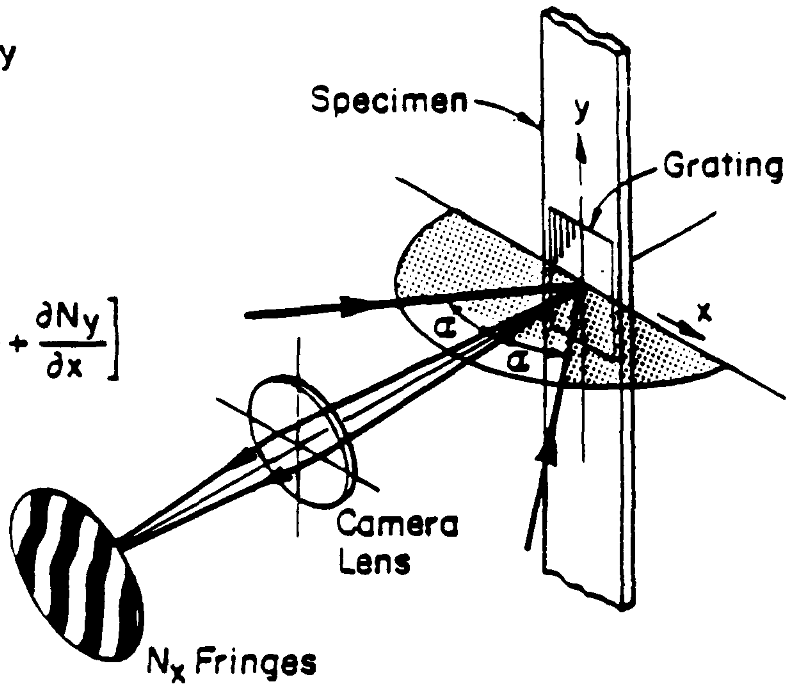

Figure 1. Moire interferometry and relevant equations.

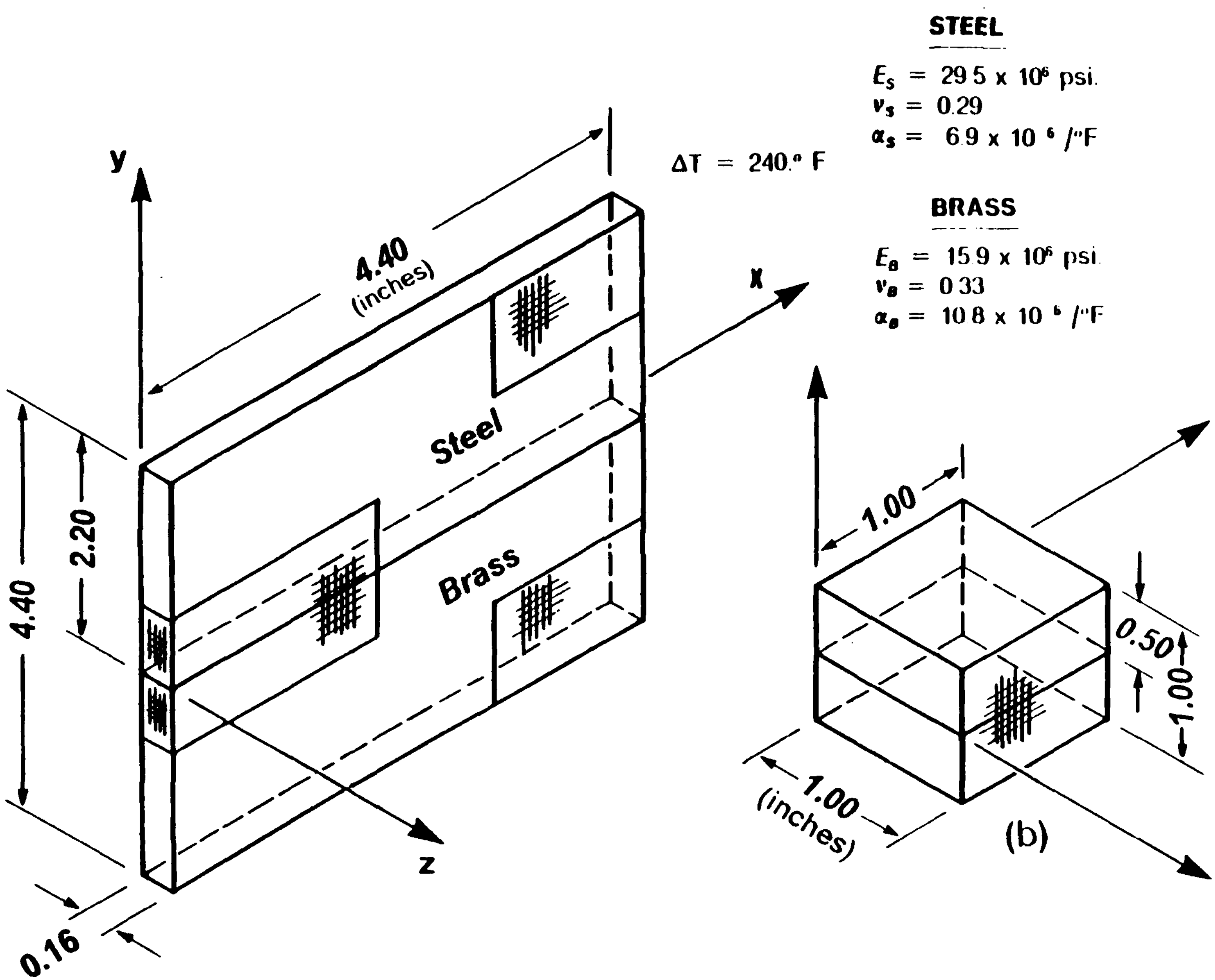

Figure 2. Specimen geometries and experimentally determined coefficients of thermal expansion for the bimaterial interface problem.

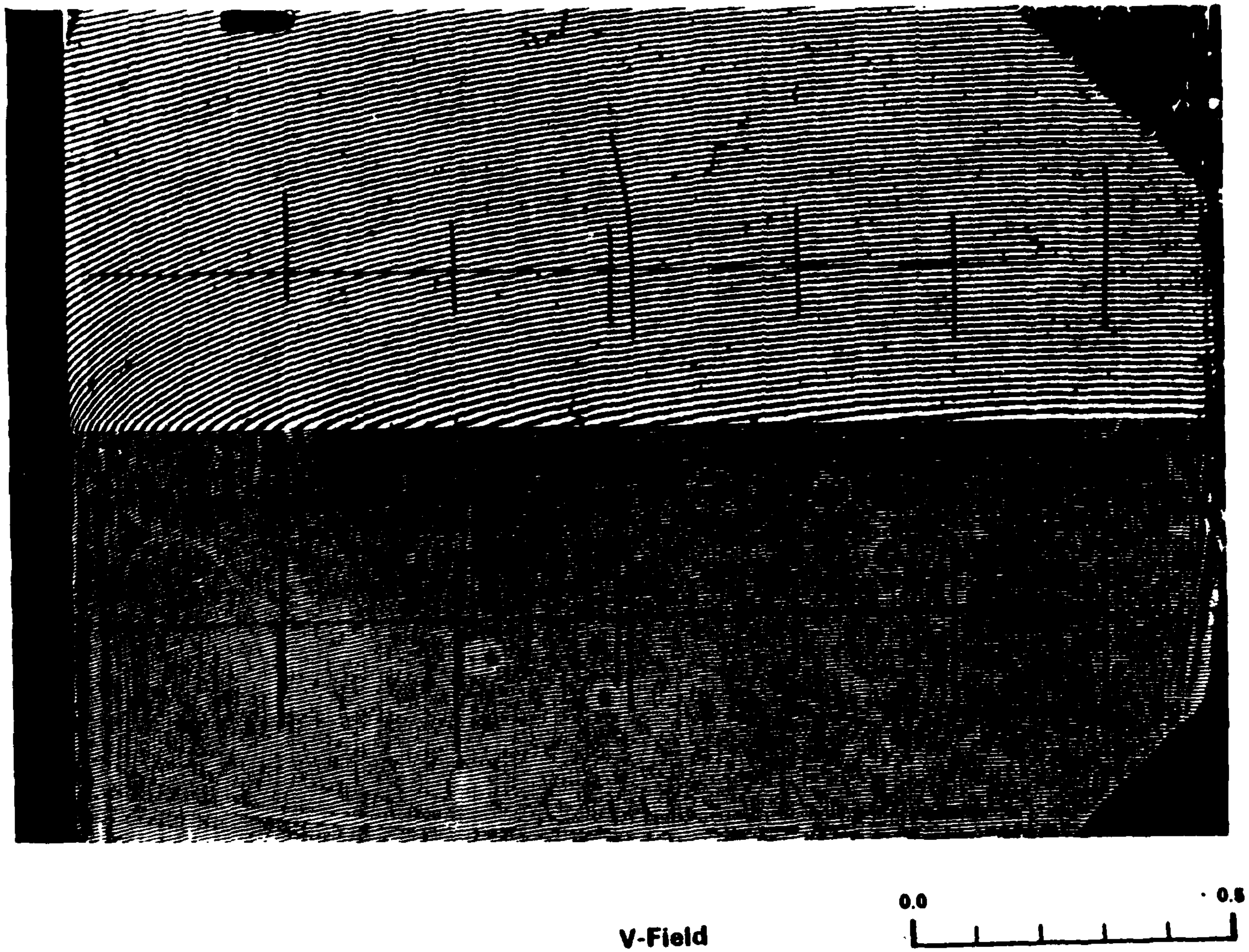

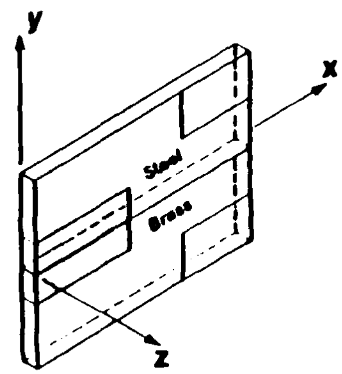

Figure 3. A typical fringe pattern (vertical V-field) near the interface at the location shown on the inset.

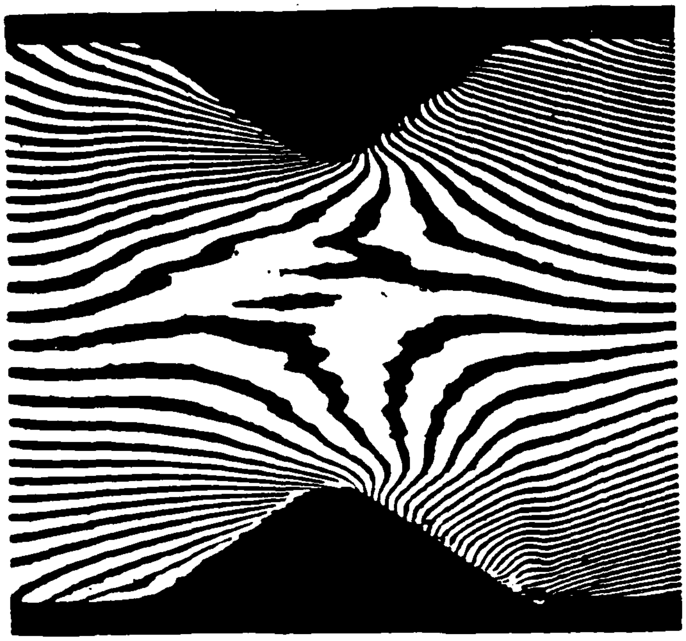

(a)

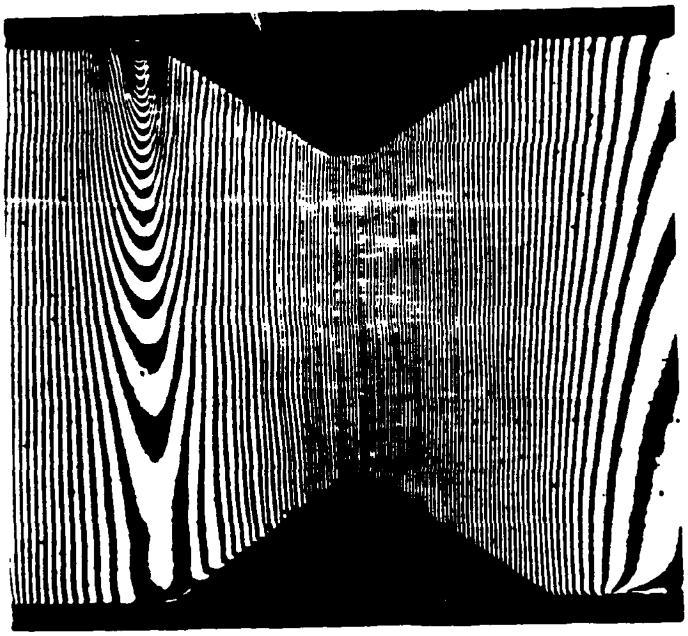

(b)

Figure 4. Moire fringe patterns for the horizontal (a) and vertical (b) displacement components in an Iosipescu specimen.

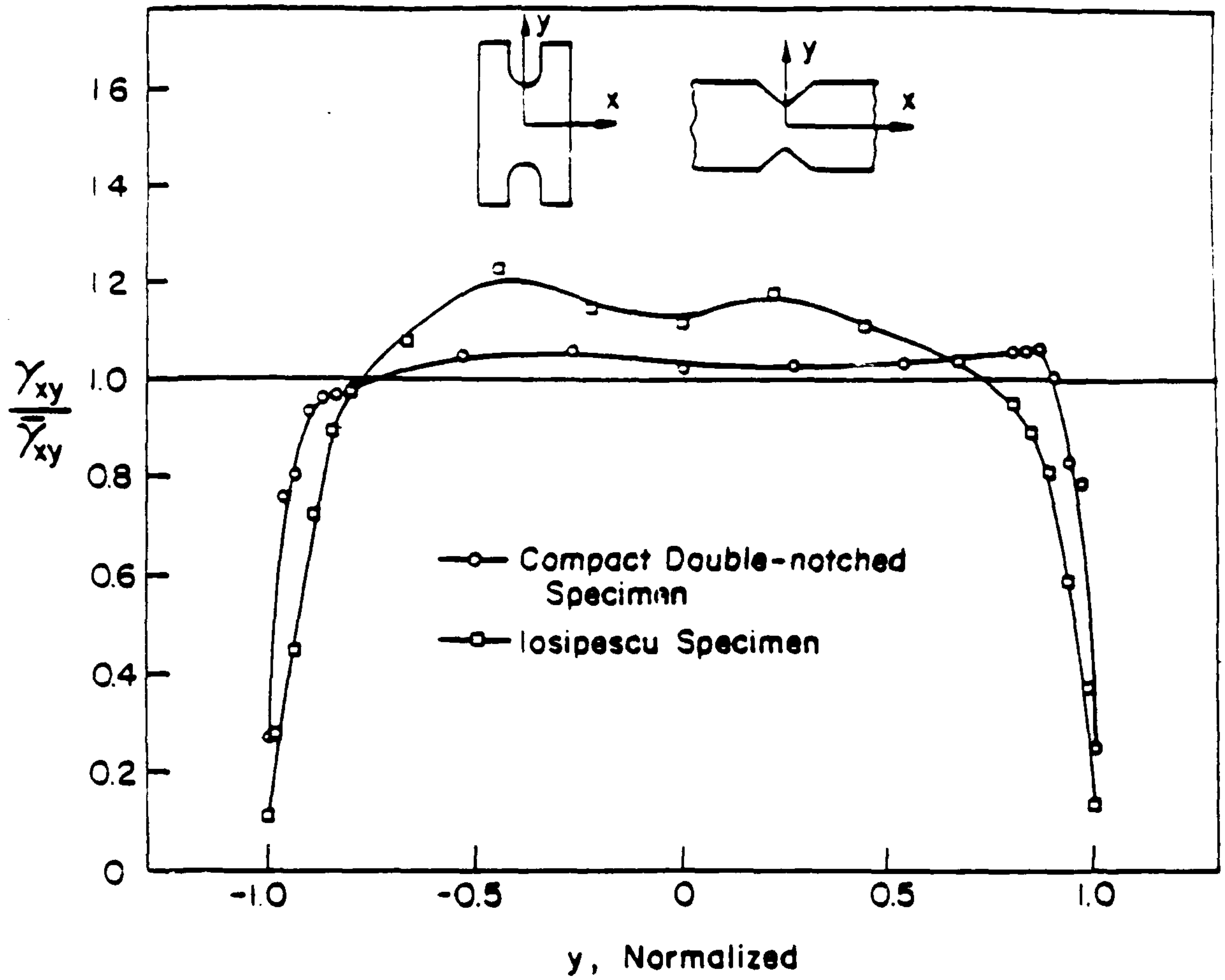

Figure 5. Shear strain distributions across the test sections of the Iosipescu and compact double - notched shear specimens.

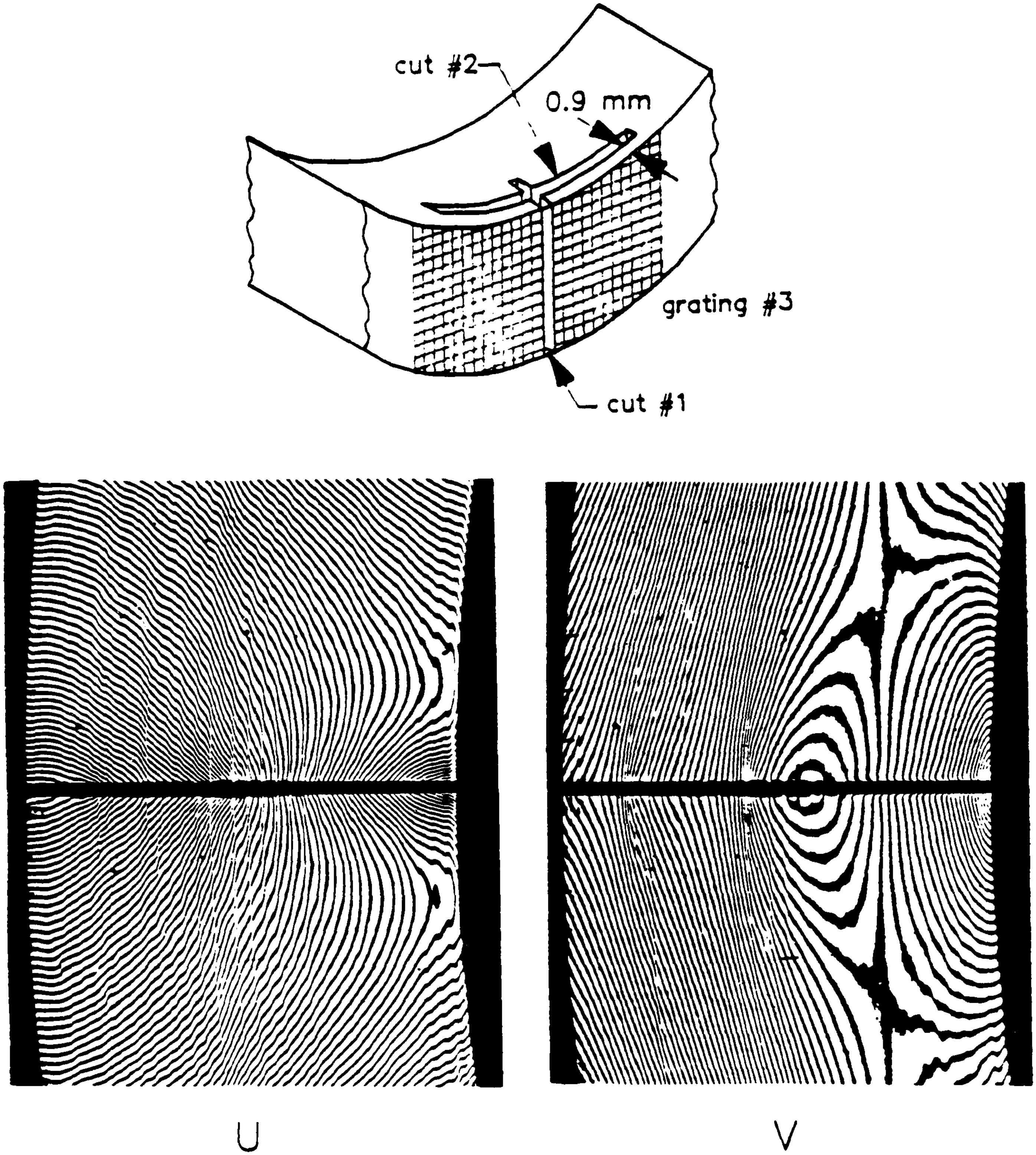

Figure 6. Fringe patterns showing displacements relieved by slicing and under-cutting a thick composite.

Temperature Fields Generated During Dynamic Crack Growth in Metals:

High Resolution Measurements by Means of High Speed Infrared Sensors

by

Alan T. Zehnder* and Ares J. Rosakis

Graduate Aeronautical Laboratories
California Institute of Technology

Temperature fields generated, due to the dissipation of plastic work, at the vicinity of dynamically growing cracks in 4340 carbon steel are studied experimentally. This non-contact measurement utilizes an eight element array of InSb high speed infrared sensors to detect the time history of temperature increase at eight discrete points, situated perpendicularly to the prospective path of a dynamically growing crack. An imaging infrared mirror system is used to focus the radiation emitted from these points on to the detector elements.

The radius of each point of measurement is approximately 0.08mm while the spacing between them is equal to 0.2mm. The high spatial resolution of the system allows us to measure temperatures well within the crack tip plastic zone to a spatial resolution of approximately $(1/10)r_p$ (r_p is the radius of the plastic zone, $r_p \sim 2$mm).

The detectors are capable of recording high frequency signals up to 300 KHz (rise time of 0.75 μ s). This rise time is below the rise time observed in the experiments which is of the order of 2μ s.

The experiments provide a complete profile of temperature variation at the near tip vicinity with maximum recorded temperature vises of approximately 450°C, closest to the crack tip, dropping to approximately 150°C at distances equal to half the plastic zone size from the tip.

The specimens used in the experiments are of the wedge loaded, double cantilever beam type. (See Figure 1.) The specimens contain an initial notch whose tip is artificially blunted. This configuration allows for the generation of of dynamically propagating sharp cracks, suddenly initiating from the blunted notch tip and propagating down the specimen with velocities ranging from 700-2000 m/s depending on the initial notch tip bluntness.

Since the path of the dynamically growing crack is known apriori, the array of infrared sensors is focussed on to eight discreet points perpendicular to the expected path at a certain distance below the notch tip. The focussing is acheived by means of a system of infrared mirrors shown in Figure 2. The sensors record temperature fields from the time of crack initiation until the crack has completely traversed the specimen.

* Current Affiliation: Department of Theoretical and Applied Mechanics, Cornell University, Ithaca, New York.

The complete crack tip velocity history is simultaneously recorded in the back of the specimen by means of a grid of conductive paint placed perpendicular to the prospective crack path by a silk screening technique. As the crack runs, the conductive strips are broken and the resistance of the whole grid is increased, providing the time history of the crack motion.

Figure 3 shows the variation of temperatures measured by channels 1-8 of the detector system as functions of time, as the crack tip approaches and passes through the detection points. It should be noted that the maximum rise times observed are of the order of 2μ s while the maximum recorded temperature increase (channel-4) is of the order of 450°C.

Figure 4 shows the contours of equal temperature distribution at the vicinity of the propagating crack. These were obtained from the temperature-time variation of Figure 3, by converting the time axis to distance from the crack tip, using the crack velocity history obtained by the conducting strips of paint placed on the back of the specimen.

The results indicate that local temperature effects might be too important to neglect in the analytical elastic-plastic modeling of crack-tip fields generated during dynamic crack growth even in moderately ductile metals. This effect may be even more important in the case of rate sensitive solids where material constitutive properties are expected to be strong functions of local temperature.

Mailing Address: Prof. A.J. Rosakis
CALTECH, 105-50
Pasadena, CA 91125

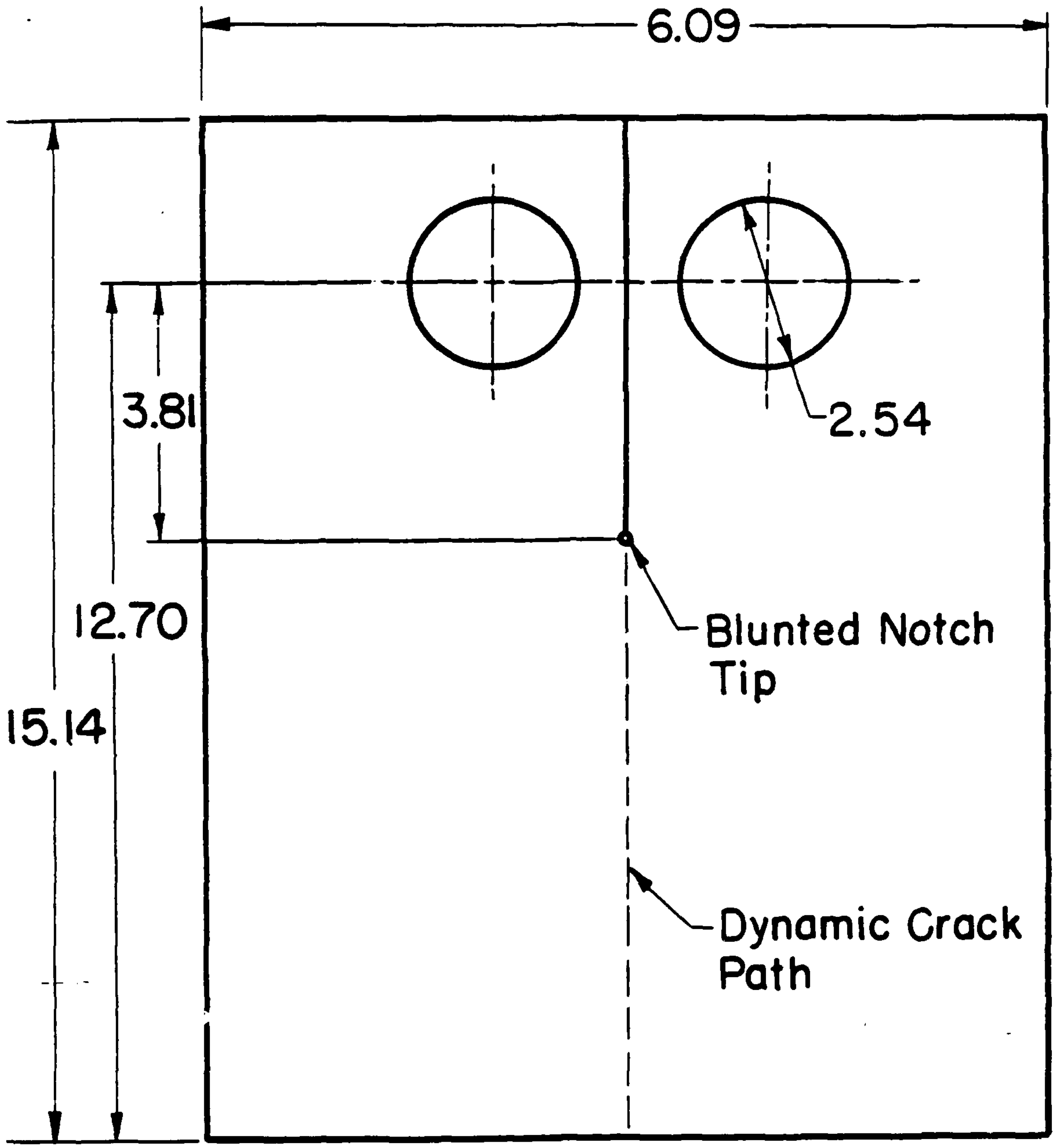

Figure 1

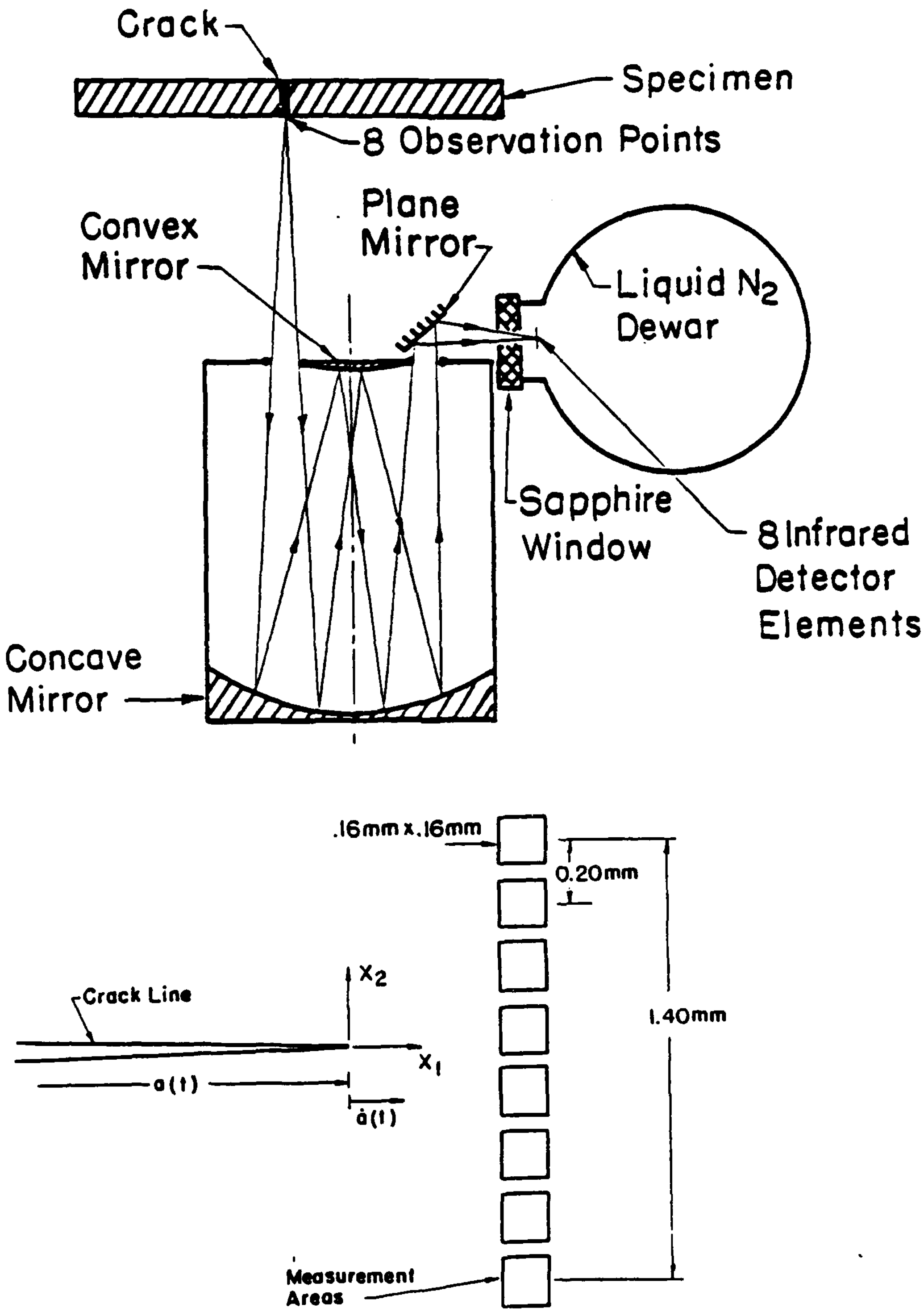
Crack
Specimen
8 Observation Points
Convex Mirror
Plane Mirror
Liquid N_2 Dewar
Sapphire Window
8 Infrared Detector Elements
Concave Mirror
.16mm x .16mm
0.20mm
1.40mm
Crack Line
x_2
x_1
a(t)
$\dot{a}$(t)
Measurement Areas

Figure 2

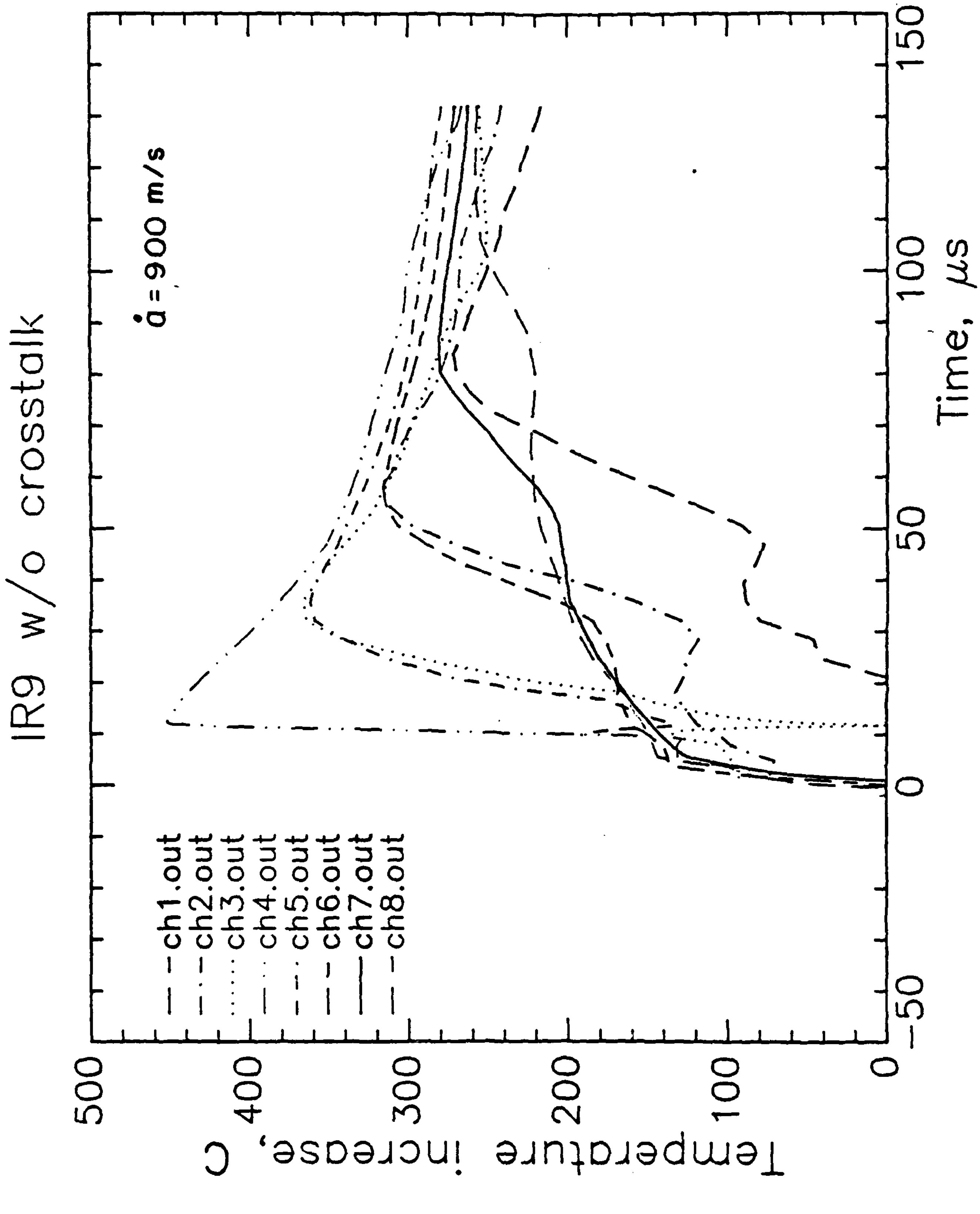
IR9 w/o crosstalk
$\dot{a}$=900 m/s
ch1.out
ch2.out
ch3.out
ch4.out
ch5.out
ch6.out
ch7.out
ch8.out
Temperature increase, C
Time, μs
0
100
200
300
400
500
−50
0
50
100
150

Figure 3

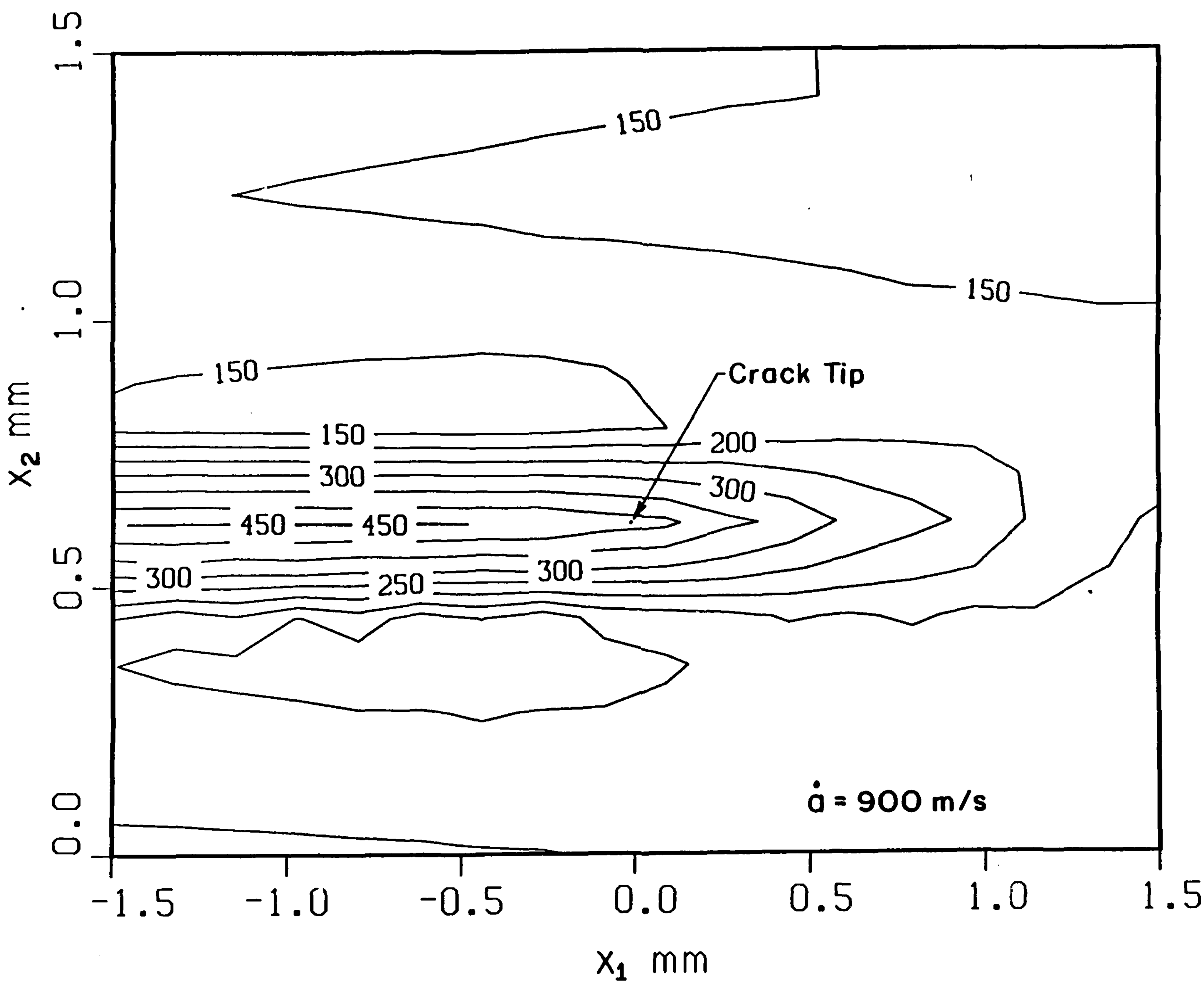

Crack Tip
150
150
150
150
200
300
300
450
450
300
250
300
ȧ = 900 m/s
1.5
1.0
0.5
0.0
-1.5
-1.0
-0.5
0.0
0.5
1.0
1.5
X2 mm
X1 mm

Figure 4

Dynamic Friction Testing of Polymers
for Materials Modeling Application *

Daniel B. Dawson
Sandia National Laboratories
Livermore, CA

To fully characterize materials behavior in analytical models of deformation processes, friction effects must often be incorporated. An important example is a polymer "friction slip clutch" that is used in some types of Army tank ammunition for 105mm rifled gun barrels. The slip clutch permits the projectile to exit the barrel at spin rates far lower than those imparted by the rifled bore.

Principal components of the slip clutch are a ring-shaped nylon 6,6 obturator that engages the rifling and seals against propellant gas leakage at the bore surface; and a polypropylene sealing band that is shrink-fitted to the projectile surface. The low coefficient of friction between the two polymer components allows the projectile and its affixed sealing band to slip relative to the spinning obturator. The spin rate of the projectile is determined by the torque transmitted through the obturator/sealing band interface, where the magnitude of the transmitted torque depends on friction and normal forces acting on this interface.

To improve our understanding of this process, Sandia is conducting a coupled analytical and experimental program in which we: (a) perform laboratory experiments to fully characterize mechanical and tribological properties of the polymer materials used in the slip clutch components; (b) develop constitutive models of deformation and tribological behavior of these polymers; (c) incorporate the materials data and constitutive models in finite element codes and structural models that we are developing to analyze performance of the slip clutch; and (d) field-test instrumented projectiles to measure critical parameters and to validate our analysis. Here we report results of the ongoing experimental program to develop the required tribology data.

Existing data on friction behavior of nylon 6,6 and polypropylene are inadequate for this purpose. Typically they do not reflect the transient nature of the slip clutch friction process and the very high slip velocities and interface pressures that apply. During passage of the projectile through the gun barrel, the slip clutch interface is subjected to time-varying normal pressures from propellant gases and rifling engagement forces that may far exceed polymer yield strength, and relative sliding velocities during slip that range from zero (initial static friction) up to hundreds of meters/sec by barrel exit. Passage through the barrel takes less than 10 ms, and the total relative slip distance between obturator and sealing band is about 1 meter. However, even in this brief period friction-induced heating of the interface is sufficient to cause surface melting of both polymers.

The slip clutch thus sees a multi-stage friction process of static friction, followed by dynamic friction between solid polymers, and finally viscous friction in a molten polymer layer. Experimental and analytical approaches are somewhat different for each of these stages:

static friction experiments to determine break-away torque for initial slip; dynamic friction experiments to determine the effects of pressure and slip velocity on friction coefficients and to define the envelope of conditions leading to surface melting; and rheological data and models to characterize viscous friction.

We report here the results of experiments that will be used to model the important middle stage of the friction process, dynamic friction between solid polymers, where the projectile acquires most of the torque transmitted from the obturator. These studies were conducted on a dual-mode servohydraulic test system configured for control of axial load and rotational displacement. The specimen configuration was the thrust washer type, consisting of a nylon 6,6 washer-shaped specimen attached to the fixed upper crosshead, bearing on a polypropylene disk specimen attached to the rotating lower ram. To simulate projectile assembly procedure, a teflon (PTFE) dry film lubricant coating was sprayed on the polypropylene disk surface.

Experiments included sliding velocities from 0.01 to 0.9 m/s and nominal interface pressures from 0.7 to 34.5 MPa (100 to 5000 psi). Our studies show that these ranges encompass the region of transition from solid to viscous friction that results from friction-induced melting of polypropylene at the slip interface. Unidirectional rotation of the lower ram was from 5 to 20 revolutions (0.5 to 2 meters total relative sliding distance). A high speed recorder monitored load, torque, and rotation signals that were used to determine dynamic friction coefficient values.

For our range of test conditions, plots of friction coefficient show substantial variation with time, sliding distance, or rotation (for example, Figures 1 and 2). Such transient effects are unimportant in most other applications, where they are typically ascribed to a wearing-in phenomenon that precedes the steady state friction process of primary interest, and ignored. In contrast, slip clutch friction is essentially a transient event throughout, and early friction behavior is important to performance. One example is surface treatment with PTFE or silicone: when applied to the friction interface, these spray lubricants have a major effect on break-away torque and early dynamic friction. However, their influence diminishes rapidly with subsequent deformation and wear of the surface.

A second example of transient effects is the influence of frictional heat. The resultant rise in interface temperature can cause an increase in friction as a result of thermal softening of the surface, as well as a subsequent decrease in friction once surface melting leads to melt lubrication. An examination of the plots for 10 cm/s and 20 cm/s in Figure 2 shows characteristic humps in the friction data at about 5 revolutions. A finite element thermal analysis of interface temperatures shows that these features are consistent with a mechanism of thermal softening and melting.

The three-dimensional plots of Figures 1 and 2 show that increases in pressure and sliding velocity both lead to decreases in friction coefficient, but that the effect of pressure is much greater. This is also shown in Figure 3, which presents friction coefficients measured at a given sliding distance, 5 revolutions. Figure 3 suggests an empirical relationship between friction coefficient, pressure, and velocity. A simple relationship of this type could be accomodated in finite element codes and structural models without great difficulty, and would be a significant improvement on the current practice of specifying a single, invariant value of friction. However, our studies lead us to conclude that a more rigorous approach, including thermal and deformation-induced transient effects, may be needed to model friction behavior of the slip clutch.

* Work supported by the U. S. Department of Energy under Contract DE-AC04-76DP0078, and a Memorandum of Understanding between the U. S. Army and the U. S. Department of Energy.

Figure 1

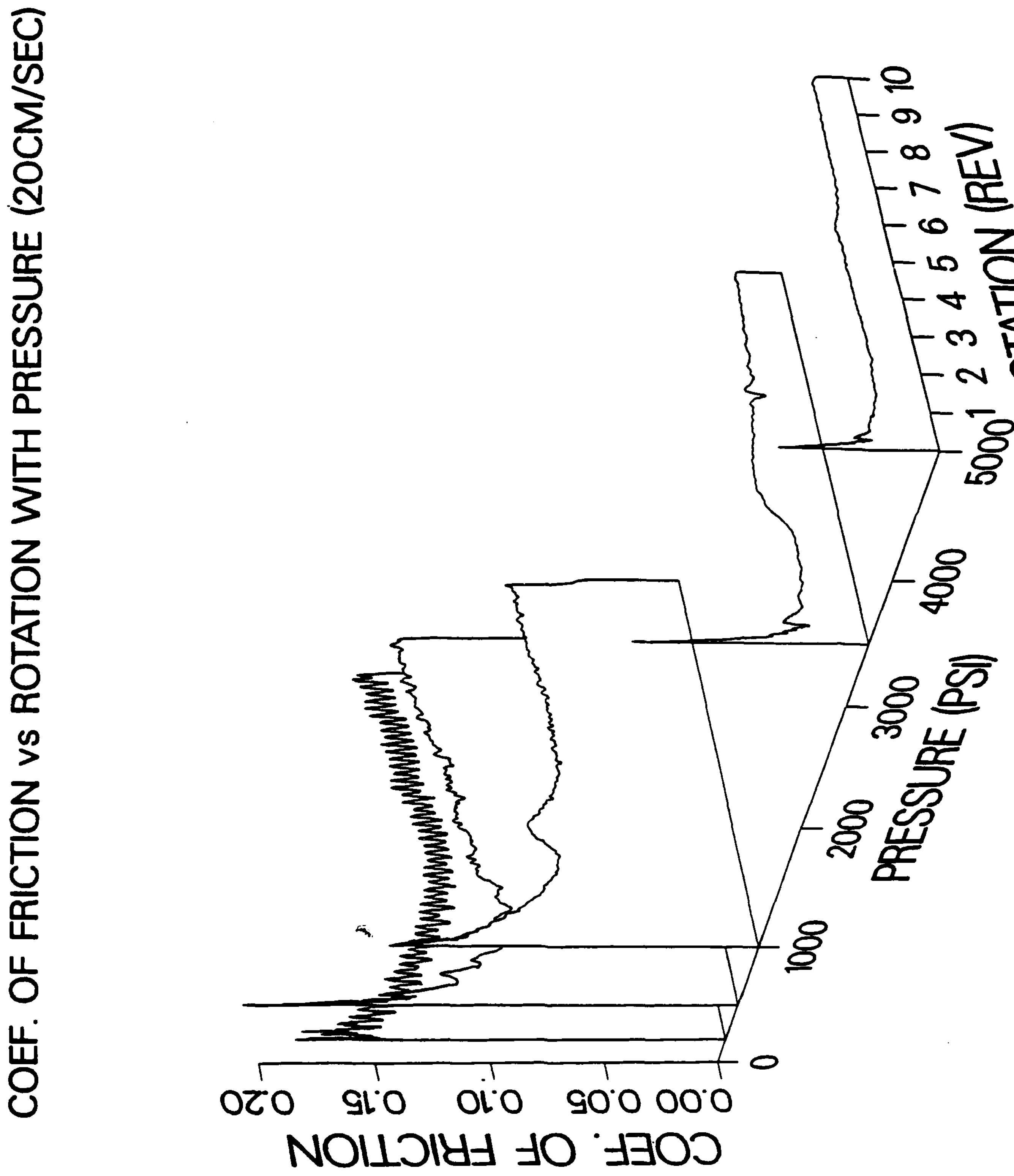
COEF. OF FRICTION vs ROTATION WITH PRESSURE (20CM/SEC)
COEF. OF FRICTION
0.00 0.05 0.10 0.15 0.20
PRESSURE (PSI)
0 1000 2000 3000 4000 5000
ROTATION (REV)
1 2 3 4 5 6 7 8 9 10

Figure 2

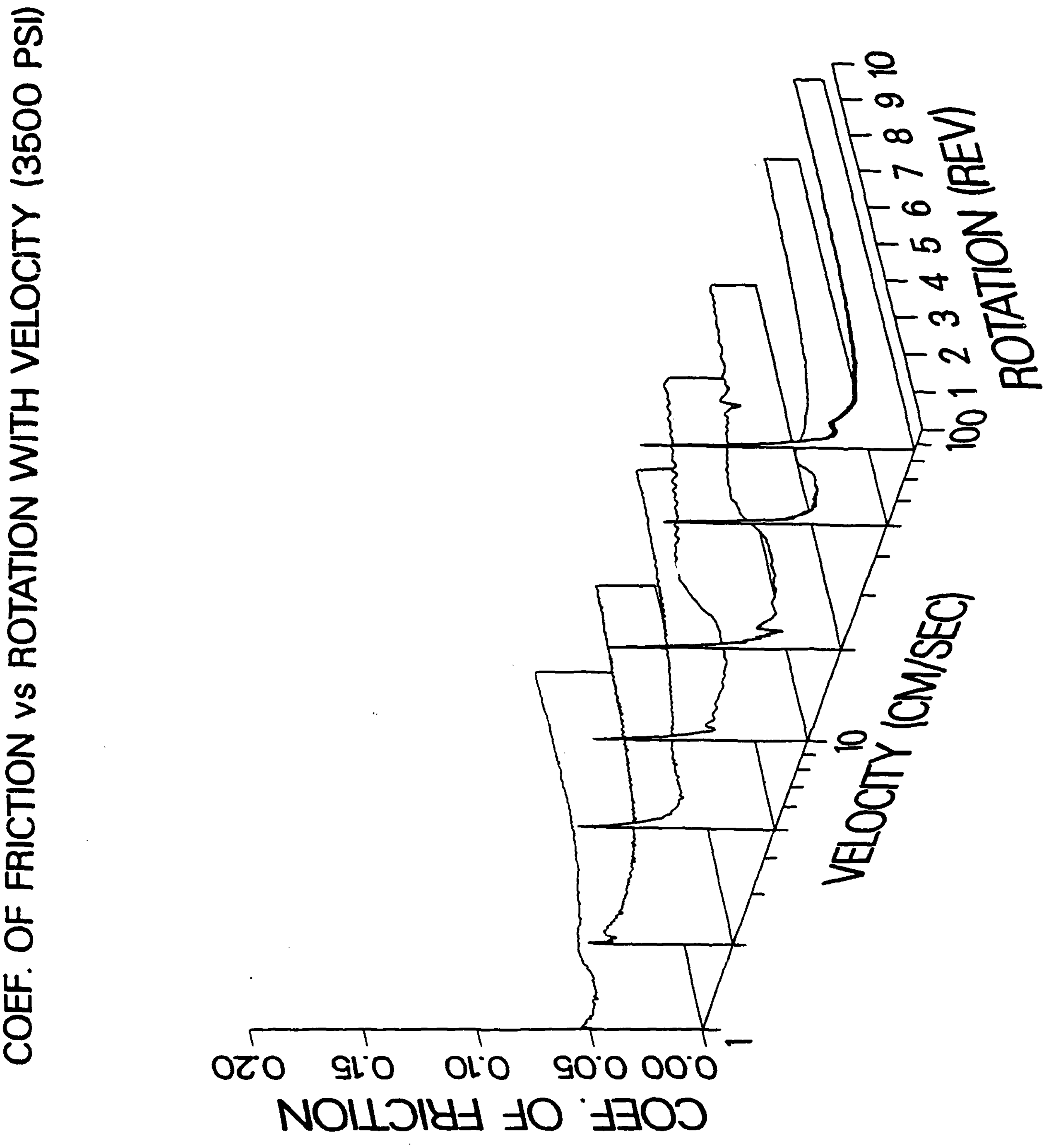
COEF. OF FRICTION vs ROTATION WITH VELOCITY (3500 PSI)
COEF. OF FRICTION
0.00 0.05 0.10 0.15 0.20
VELOCITY (CM/SEC)
1
10
100
ROTATION (REV)
0 1 2 3 4 5 6 7 8 9 10

Figure 3

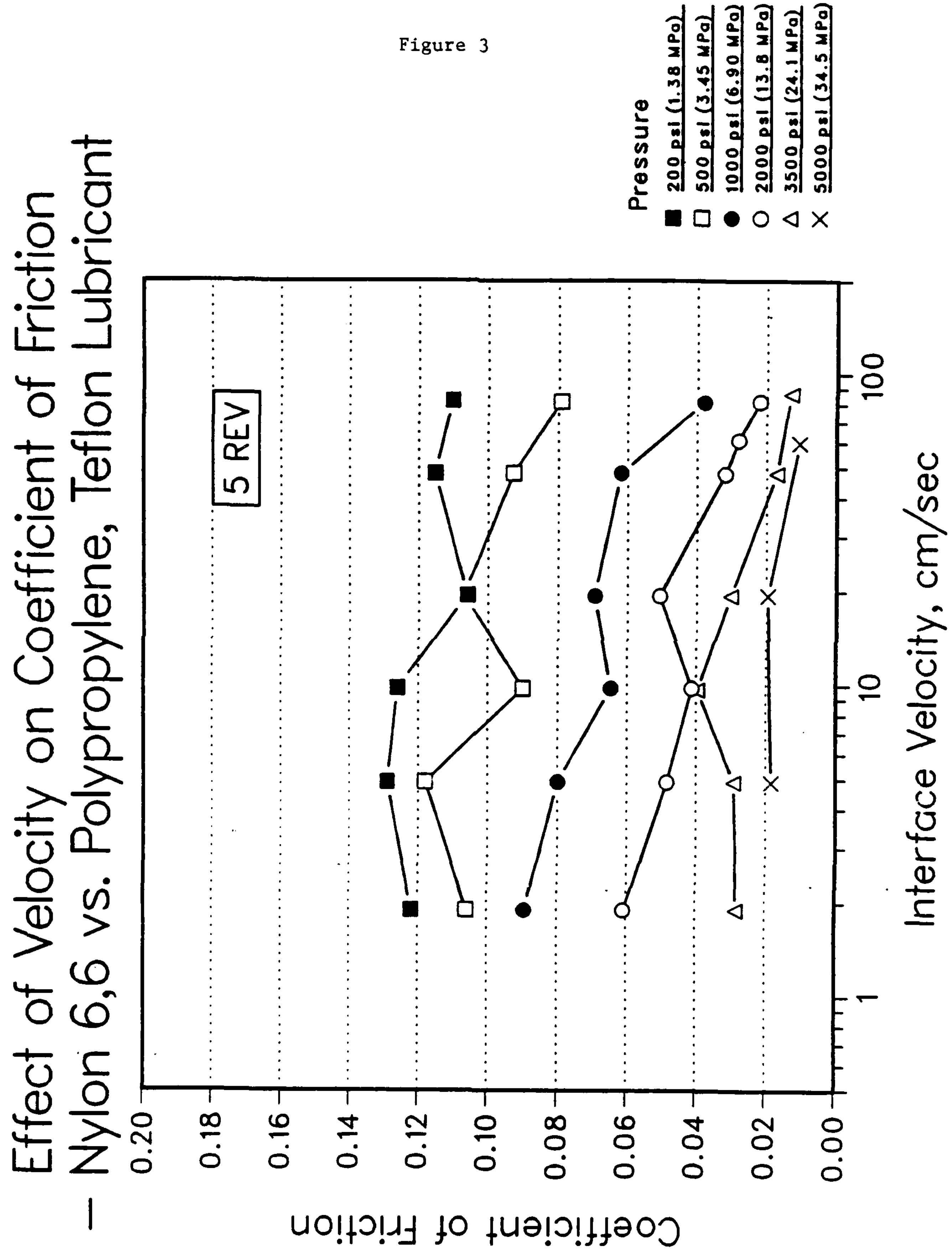

Effect of Velocity on Coefficient of Friction
— Nylon 6,6 vs. Polypropylene, Teflon Lubricant
5 REV
Coefficient of Friction
0.20
0.18
0.16
0.14
0.12
0.10
0.08
0.06
0.04
0.02
0.00
1
10
100
Interface Velocity, cm/sec
Pressure
200 psi (1.38 MPa)
500 psi (3.45 MPa)
1000 psi (6.90 MPa)
2000 psi (13.8 MPa)
3500 psi (24.1 MPa)
5000 psi (34.5 MPa)

FRACTURE OF FIBROUS METAL MATRIX COMPOSITES

George J. Dvorak and Yehia A. Bahei-El-Din

Department of Civil Engineering
Rensselaer Polytechnic Institute
Troy, New York 12180-3590

ABSTRACT

This paper presents an experimental and theoretical study of crack-tip plastic deformation fields and fracture of a unidirectionally reinforced boron-aluminum composite. In the experimental work, the deformation fields were visualized with the help of a fine bar code which was photodeposited on the surface of center-notched tension specimens so that the bars were perpendicular to the fibers and parallel to the plane of the notch. During incremental loading, the distortions of the bar code exposed the essential features of the notch-tip plastic deformation to visual observation. Discrete plastic zones were found to grow from the notch tip in the direction of the fiber. At failure, the length of these zones substantially exceeded the notch length. Evaluation of the bar code distortions indicated that the zones were typically 0.5 to 2.0 mm wide, and that the plastic shear strains in the zones were as high as 0.4. The zones effectively blunted the notch and caused a substantial stress redistribution in the specimens during loading. The fracture process was not found to be self-similar; no evidence of plastic zone formation was detected along the fracture surface.

In the theoretical part of the work, the strain and stress fields were computed for seventeen specimen geometries *during incremental loading* to failure. This was done with the ABAQUS finite element program, in a manner which was consistent with our bimodal plasticity theory of fibrous composites, and with its experimental verification. The results confirmed the existence of experimentally observed long discrete plastic zones at the tip of the notch before failure. They also give the plastic zone lengths, the magnitudes of the shear displacements across these zones which agree well with experimental measurements, notch opening displacement, and the stress distribution in the vicinity of the notch.

Experimental strength results reported by several investigators on 39 center-notched boron-aluminum specimens of many different geometries were interpreted with the help of the computed fields. The results showed that the onset of fracture in these specimens was controlled by a critical magnitude of a stress ratio between local principal stress in a small representative volume of the composite ahead of the notch tip and the corresponding off-axis strength of unnotched material. The local stresses consist of two contributions. One is the average stress in the unbroken ligaments which equilibrates the overall stresses. Another is the local stress induced into the ligament by the shear stress in the plastic zone. For a certain choice of the representative volume, the critical stress ratio at failure was found to be approximately 1.0. However, since the representative volume at the notch tip is small in comparison to typical tension specimens, the value of the stress-strength ratio may vary. If the ratio is found for a given composite system from few tests of notched specimens, it can be used to predict fracture strength of many notched specimens and structural configurations in which the plastic deformation is concentrated in long discrete zones.

A Continuum Model for Void Nucleation by Inclusion Debonding

A. Needleman
Division of Engineering
Brown University
Providence RI 02912

Abstract

A cohesive zone type model, taking full account of finite geometry changes, provides a unified framework for describing the process of void nucleation from initial debonding through complete separation. Constitutive relations are specified independently for the material and for the interface. A main feature of this model is that it permits the prediction of interfacial decohesion without the necessity of introducing some additional failure criterion. Also, since the mechanical response of the interface is specified in terms of both a critical interfacial strength and the work of separation per unit area, dimensional considerations introduce a characteristic length. For inclusions sufficiently small with respect to this characteristic length, decohesion occurs in a 'ductile' fashion, whereas for sufficiently large inclusions decohesion occurs in a 'brittle' manner. The effects of interfacial strength, inclusion size and distribution, and imposed stress state on the nucleation process are illustrated.

THE PLANAR TRANSFORMATION PROBLEM WITH INTERFACIAL DECOHESION

A.J. LEVY

SYRACUSE UNIVERSITY

Introduction

This paper will address the phenomenon of inclusion debonding through the formulation and solution of a related planar elastic problem. In particular, the problem is a variant of the standard transformation problem‡ of Eshelby [1] which seeks to determine the elastic fields within an infinite matrix and bounded inclusion which, in the absence of the matrix, would undergo a prescribed stress free change of form. In the standard problem it is implicitly assumed that the inclusion-matrix interface is coherent i.e., that the displacements (although not necessarily their gradients) are continuous at the interface. Here the transformation problem with decohesion is considered and the assumption that the displacements at the interface are continuous is discarded and replaced by the more general assumption that the inclusion interacts with the matrix through some interfacial traction which is characteristic of the interface and depends on the displacement discontinuity there. By studying the character of the displacement discontinuity at the interface for a prescribed change of form and subject to different interfacial traction laws an understanding of the nature of the decohesion process, and the physical and geometrical parameters influencing it, may be obtained.

‡ Such problems arise in metallurgy because of martensitic transformation, precipitate formation and thermal expansion.

The General Inclusion

Let a planar inclusion be embedded in an infinite matrix such that it interacts with the matrix through an interfacial traction $\mathbf{T}_I$ given by

$$\mathbf{T}_I = f_n([\mathbf{u}])\mathbf{n} + f_t([\mathbf{u}])\mathbf{t} \tag{1}$$

where **u** and **t** are unit normal and tangent vectors at the inclusion surface, and [**u**] is the displacement jump at the interface. If, in the absence of the matrix, the inclusion undergoes a prescribed stress- free strain $\mathbf{e}_T$ (eigenstrain, transformation strain) then, for the inclusion-matrix system the transformation strain $\mathbf{e}_T$ induces constrained displacements and stresses. Provided we assume infinitesimal displacements and gradients as well as Hooke's Law the displacement field within the matrix, $\mathbf{u}^+$ and inclusion, $\mathbf{u}^-$ are given by [2],

$$\mathbf{u}^- = \frac{-1}{2\pi(\lambda+\mu)}\,\sigma_T\nabla\phi - \frac{1}{4\pi\mu}\,\varepsilon\nabla[(\sigma_T\varepsilon)\cdot\nabla\nabla\psi] + \int_C f_n U^-_{Tn}\,\mathbf{n}ds + \int_C f_t U^-_{T}\ldots$$

$$\mathbf{u}^+ = -\int_C f_n U^+_{Tn}\,\mathbf{n}ds + \int_C f_t U^+_{Tt}\,\mathbf{n}ds \tag{2}$$

where σ_T is the transformation stress $(\lambda(\mathrm{tr}\mathbf{e}_T)\mathbf{I} + 2\mu\mathbf{e}_T)$, the U_T are functions of both source and field point, ε is the two dimensional alternating symbol, ϕ and ψ are, respectively, the logarithmic and biharmonic potentials of two dimensional potential theory and C represents the boundary of the inclusion. Equations (2) do not determine the displacements explicitly and cannot be solved until the displacement jump at the interface is known as a function of position along the interface. This quantity is obtained from the integral equation [2],

$$[\mathbf{u}](\mathbf{x}) = \mathbf{h}(\mathbf{x}) + \int_C f_n\left([\mathbf{u}](\xi)\right)\mathbf{k}_n(\mathbf{x},\xi)\,ds_\xi + \int_C f_t\left([\mathbf{u}](\xi)\right)\mathbf{k}_t(\mathbf{x},\xi)\,ds_\xi \tag{3}$$

where $\mathbf{x}$, ξ are respectively field and source point along the interface. The quantity $\mathbf{h}$ is generally a function of prescribed transformation strain, logarithmic and biharmonic potentials, and elastic moduli while the kernal functions $\mathbf{k}_n$, $\mathbf{k}_t$ are functions of elastic moduli. For a prescribed interfacial traction law, (3) determines $[\mathbf{u}](\mathbf{x})$ and (2) determines the displacement field everywhere. The strains follow from the strain-displacement relations and the stresses from Hooke's Law provided that account is taken of the fact that the inclusion is prestressed with uniform stress σ_T

The Circular Inclusion with Linear Interfacial Traction Law

For the case of a circular inclusion position along the interface is denoted by an angle θ (field point) or θ' (source point). Also, the biharmonic and logarithmic potentials are simply,

$$\psi = -\frac{\pi}{8} r^4$$

$$\phi = -\frac{\pi}{2} r^2$$

where r is the distance from the center of the circle to field point. If the interfacial force law is assumed to be linear, then

$$f_n = \frac{a}{\delta}\,\sigma_\delta u$$

$$f_t = \frac{a}{\delta}\,\tau_\delta v \tag{4}$$

where σ_δ, τ_δ are the normal and shear stiffnesses of the interface, δ is the characteristic length of the interface, a is the inclusion radius and u, v are respectively the normal and shear components of displacement jump at the interface. Furthermore, if it is assumed that the interface is infinitely stiff in shear then a single, linear integral equation follows from (3),

$$u(\theta) = h(\theta) + \left(\frac{a}{\delta}\right) \int_0^{2\pi} u(\theta')k(\theta-\theta')d\theta' \tag{5}$$

with

$$K(\theta-\theta') = \frac{\sigma\delta}{2\pi\mu}\left\{1 + \frac{\mu}{\lambda+\mu}\,(\theta-\theta')\sin(\theta-\theta') + \frac{\lambda+2\mu}{\lambda+\mu}\cos(\theta-\theta')\log[1-\cos(\theta-\theta')]\right\}$$

$$h(\theta) = C_1 + C_2\cos^2\theta + C_3\sin^2\theta + C_4\sin\theta\cos\theta \tag{6}$$

$$C_1 = -\frac{1}{2}\,\frac{\lambda}{\lambda+\mu}\,(e_x+e_y), \qquad C_2 = -\frac{1}{2}\,\frac{\lambda+3\mu}{\lambda+\mu}\,e_x + \frac{1}{2}\,e_y$$

$$C_3 = -\frac{1}{2}\,\frac{\lambda+3\mu}{\lambda+\mu}\,e_y + \frac{1}{2}\,e_x, \qquad C_4 = -\frac{2(\lambda+2\mu)}{\lambda+\mu}\,e_{xy}$$

Equation (5) is the standard Fredholm integral equation with a symmetric, weakly singular kernal [2]. Such equations may be treated within the framework of the Hilbert-Schmidt theory for Fredholm integral equations with a symmetric and quadratically integrable kernal [3,4]. In particular, it is possible to show that the eigenvalues λ_n of the homogeneous equation,

$$u_n(\theta) = \lambda_n \int_0^{2\pi} u_n(\theta')k(\theta-\theta')d\theta' \tag{7}$$

are all negative and therefore, because the difference of two solutions to (5) must satisfy (7), a unique solution for the displacement jump will exist for all positive values of $\frac{a}{\delta}$. Hence, for the case of linear interfacial tractions the phenomenon of "brittle" decohesion [5], does not occur and we expect the existence of equilibrium solutions for all positive values of $\frac{a}{\delta}$. A more general interfacial traction law,

$$f_n = \frac{a}{\delta}\sigma_\delta \hat{f}(u) \tag{7}$$

will lead to an integral equation which is nonlinear and therefore to the possibility of bifurcation points i.e., values of $\frac{a}{\delta}$ at which uniqueness breaks down (brittle decohesion). A necessary condition for $\frac{a}{\delta}$ to be a bifurcation point is for the linear, homogeneous integral equation,

$$\begin{aligned} \delta u(\theta) &= \lambda \int_0^{2\pi} K^*(\theta,\theta')\delta u(\theta')d\theta' \\ K^* &= -[\partial_u \hat{f}](\theta')\ k(\theta-\theta') \end{aligned} \tag{8}$$

to have positive eigenvalues. The eigenfunctions $\delta u(\theta)$ corresponding to these eigenvalues are the mode shapes for brittle decohesion. By studying the interplay between interfacial traction laws and prescribed transformation strain an understanding of the mechanics of the decohesion process may be obtained.

1. Eshelby, J. D.; The Determination of the Elastic Field of an Elipsoidal Inclusion and Related Problems; Proc. Roy. Soc., A241, p. 376, 1957.

2. Levy, A. J.; The Planar Transformation Problem with Inclusion Debonding; U.S. Army Report DAAL03-86-D-0001, 1988.

3. Mikhlin, S. G.; Integral Equations, 1964.

4. Tricomi, F. G.; Integral Equations; 1957.

5. Needleman, A.; A Continuum Model for Void Nucleation by Inclusion Debonding; Nat. Sci. Found. Report MSM-8419338/2, 1986.

ELASTIC MODULI CALCULATED BY THE AVERAGE FIELD METHOD AND DETERMINATION OF THE BOUNDS

T. Mura and S. C. Lin
Department of Civil Engineering
Northwestern University
Evanston, Illinois 60208, U.S.A.

T. Mori and K. Wakashima
Department of Materials Science and Engineering
Tokyo Institute of Technology
4259 Nagatsuta
Midori-ku, Yokohama 227, Japan

Abstract

The concept of the average field in an elastically homogeneous but inclusions bearing body is used to examine the elastic state of an elastically inhomogeneous body. First is discussed the physical base on which the disturbances in stress and strain due to inhomogeneities in the inhomogeneous body are simulated by the internal stress and strain in the equivalent body: The equivalent body contains elastically homogeneous inclusions with proper eigenstrains. Next, the average of the stress and strain disturbances are determined and approximate average elastic moduli of the inhomogeneous body are calculated. Finally, using these quantities, an upper and a lower bound of the average elastic moduli of an inhomogeneous body are proposed on the basis of the variational principles.

Shear Band Development in Dynamic Plane
Strain Compression of a Viscoplastic Material

R. C. Batra and De-Shin Liu
Department of Mechanical and Aerospace Engr.
and Engineering Mechanics
University of Missouri-Rolla
Rolla, MO 65401-0249

Adiabatic shear banding is the name given to a localization phenomenon that occurs during high-rate plastic deformation. Practical interest in the phenomenon derives from the fact that once a shear band has formed, subsequent deformations of the body occur in this narrow region with the rest of the body undergoing very little deformations. Thus shear bands are often precursors to shear fractures.

Earlier work [1-3] on the adiabatic shear banding problem involved analyzing the simple shearing deformations of a viscoplastic body. Recently Needleman [4] and Batra and Liu [5] have studied the initiation and growth of shear bands in plane strain deformations of a softening material. Needleman [4] analyzed a purely mechanical problem, approximated the effect of thermal softening by assuming the existence of a peak in the stress-strain curve and modeled a material inhomogeneity/flaw by presuming that the flow stress for a small amount of material near the center of the block was less than that of the surrounding material. Batra and Liu [5] studied the coupled thermomechanical deformations of a thermally softening viscoplastic solid and modeled the material inhomogeneity by introducing a temperature bump at the center of the block whose boundaries were taken to be perfectly insulated. Two different loadings namely those corresponding to simple shearing and simple compression of the block were considered. Here we examine the effect of (a) modeling the material inhomogeneity in two different ways, namely introducing a temperature perturbation and assuming the existence of a weak material, (b) introducing two defects place symmetrically on the vertical axis of the block, (c) varying the reduction in the flow stress of the weak material, and (d) two different sets of initial conditions.

Fig. 1a is a sketch of the undeformed and homogeneously deformed shape of the block. In terms of non-dimensional variables, the governing equations are:

$$\dot{\rho} + \rho\, v_{i,i} = 0\ ,$$

$$\delta\tilde{\rho}\, \dot{v}_i = T_{i\alpha,\alpha}\ ,$$

$$\tilde{\rho}\dot{\theta} = \beta\, \theta_{,\alpha\alpha} + (\tilde{\rho}/\rho_r)\ [1/(\sqrt{3}\ I)]\ (1+bI)^m(1-\nu\theta)D_{ij}\ D_{ij}\ ,$$

$$\sigma_{ij} = -B(\rho - 1)\ \delta_{ij} + [1/(\sqrt{3}I)]\ (1+bI)^m(1-\nu\theta)D_{ij},$$

$$T_{i\alpha} = \tilde{\rho}/\rho\ X_{\alpha,j}\ \sigma_{ij},\ 2D_{ij} = v_{i,j} + v_{j,i},$$

$$2I^2 = \tilde{D}_{ij}\ \tilde{D}_{ij},\ \tilde{D}_{ij} = D_{ij} - \frac{1}{3} D_{kk}\ \delta_{ij}$$

Here ρ is the present mass density, v_i the velocity of a material particle, $\tilde{\rho} = \rho_o/\rho_r$, $\delta = \rho_r v_o^2/\sigma_o$, ρ_r is the mass density in the stress-free reference configuration, ρ_o is the mass density in the reference configuration, σ_o is the yield stress in a quasistatic simple tension or compression test, σ_{ij} is the Cauchy stress tensor, θ is the temperature change, and β, m and ν are material parameters. These equations are written in terms of rectangular cartesian coordinates, a comma followed by i or α implies partial differentiation with respect to x_i or X_α, and a repeated index implies summation over the range of the index.

We study only those deformations that remain symmetric about the horizontal and vertical planes passing through the center of the block. Thus, we analyze the deformations of the material in the first quadrant. The use of the Galerkin method and the lumped mass matrix reduces the governing equations to a set of coupled nonlinear ordinary differential equations which are integrated by using the IMSL subroutine LSODE. We use the 9-noded quadrilateral element and do not a priori align the sides of the elements so that they are along the direction of the maximum shearing at the instant of the initiation of a shear band.

Figure 1b depicts the stress-strain curve for plane strain uniform compression of the block deformed at a nominal strain rate of 5,000 per sec. Because of the rather high value assumed for the coefficient ν of thermal softening the material softening caused by the heating of the material exceeds the hardening due to strain-rate effects right from the beginning.

Fig. 2 shows the contours of the second invariant I of the deviatoric strain-rate tensor at successively higher values of the average strain γ_{avg} when the material defect is modeled by introducing a temperature perturbation centered around the point P (0.0, 0.375). In each case, the peak value I_{max} of I occurs at the point P where the temperature is maximum. At an average strain of 0.04, $I_{max} = 11.44$ implying thereby that the material surrounding it is deforming at a strain-rate greater than 50,000 sec^{-1}. For $\gamma_{avg} = 0.04$, $\theta_{max} = 0.341$ occurs at P and equals 68.2 percent of the presumed melting temperature of the material. The contours of I originate at the point P and then fan out along the direction of maximum shearing. There appear to be sources of energy building up at the point P and three other points on the boundary where the parallelogram through P with adjacent sides making angles of $\pm 45^o$ with the horizontal axis intersect it. When there is sufficient energy built up at these points contours of successively higher values of I originate from these points and propagate along the direction of maximum shearing. Also as the deformation of the block progresses, these contours become narrower implying thereby that severe deformations are localizing into thin bands.

Similar results are obtained for the other cases. Thus, irrespective of the way a material inhomogeneity is modeled, a shear band initiates from the site of the defect and propagates in the direction of maximum shearing. The value of the average strain at the instant of the initiation of the band depends upon the strength of the material defect introduced. Once the shear band reaches the boundaries of the block it is reflected back, the angle of reflection being nearly equal to the angle of incidence.

Acknowledgements: This work was supported by the U. S. Army Research Office Contract DAAL03-88K-0184 to the University of Missouri-Rolla.

References:

1. R. J. Clifton, Adiabatic Shear in Material Response to Ultrahigh Loading Rates, U. S. NRC National Material Advisory Board Report NMAB-356, (W. Herrman, ed.), 1980.

2. R. C. Batra, The Initiation and Growth of, and the Interaction Among Adiabatic Shear Bands in Simple and Dipolar Materials, Int. J. Plasticity, 3, 75-89, 1987.

3. T. W. Wright and J. Walter, On Stress Collapse in Adiabatic Shear Bands, J. Mech. Phys. Sol., 35, 701-716, 1988.

4. A. Needleman, Dynamic Shear Band Development in Plane Strain, J. Appl. Mech. (in press).

5. R. C. Batra and De-Shin Liu, Adiabatic Shear Banding in Plane Strain Problems, J. Appl. Mech. (accepted).

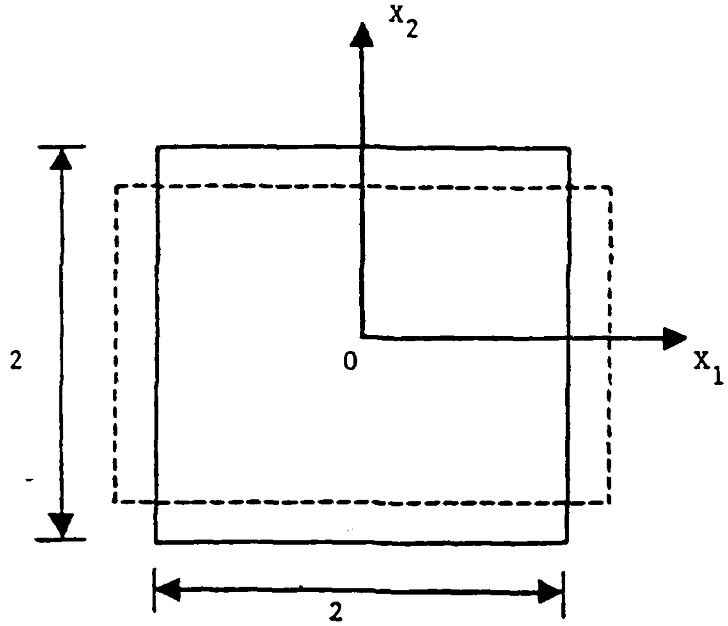

(a) The problem studied.

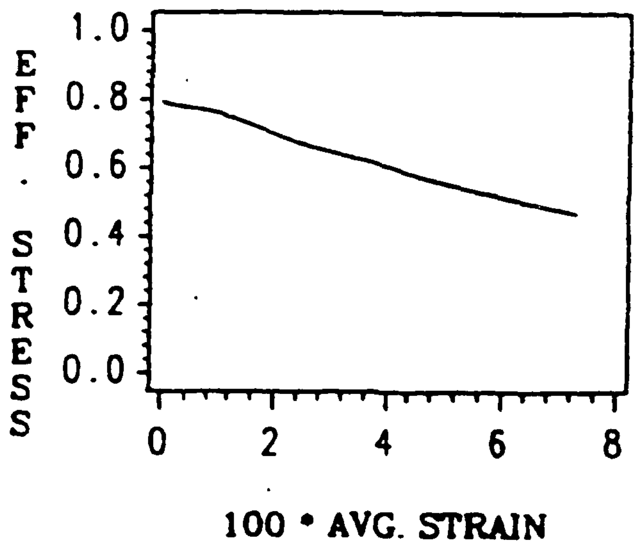

(b) Stress-strain curve in simple compression for the material studied.

Figure 1

Figure 2

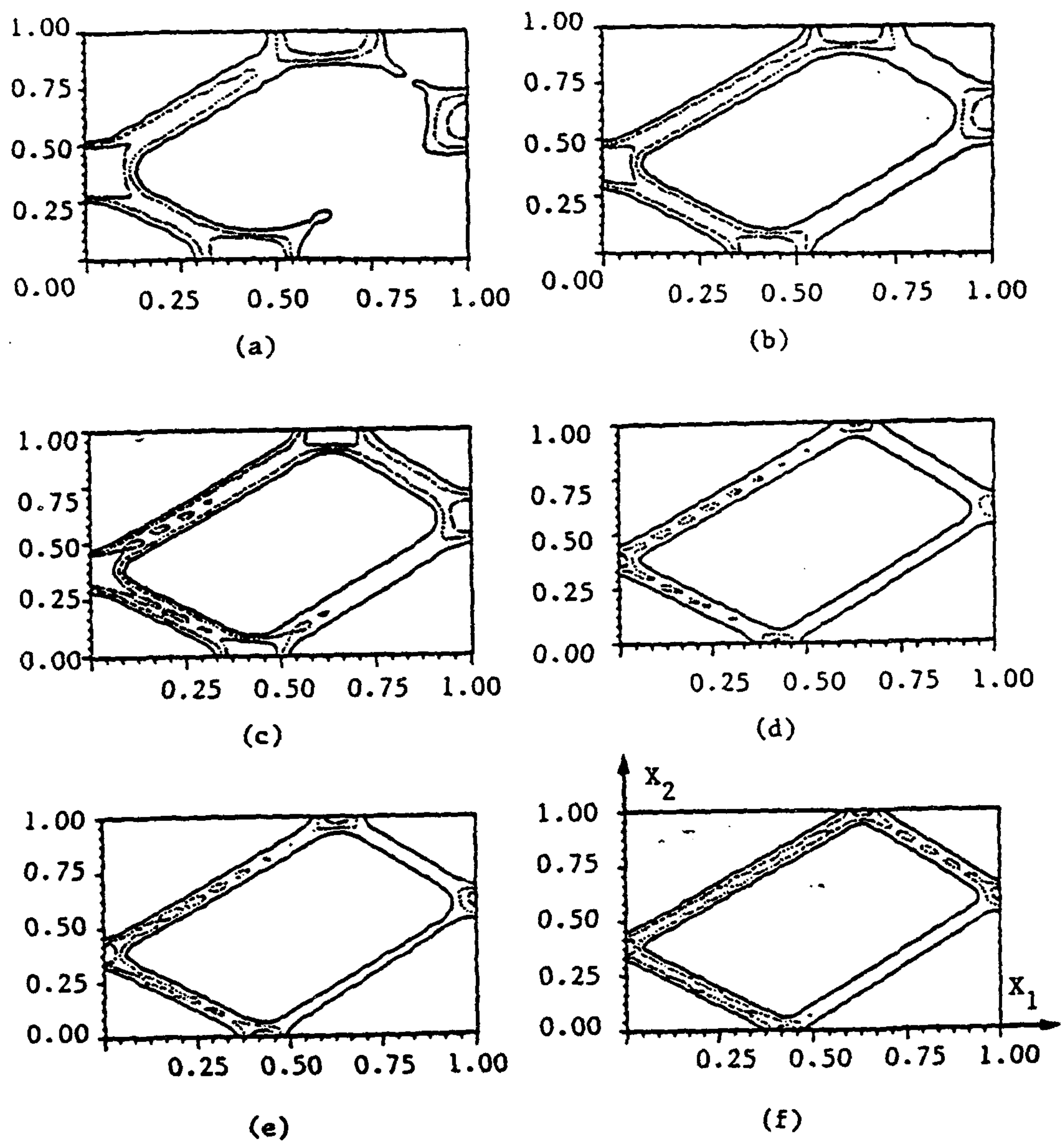

Contours of the second invariant I of the deviatoric strain-rate tensor at different values of the average strain when the material defect is modeled by a temperature perturbation.

(a) $\gamma_{avg} = 0.02$, $I_{max} = 3.5$; ____ 1.50, ... 1.75, —·—·—· 2.0.

(b) $\gamma_{avg} = 0.025$, $I_{max} = 4.51$; ____ 1.50, ... 2.0, —·—·—· 2.5.

(c) $\gamma_{avg} = 0.030$, $I_{max} = 4.83$; ____ 1.50, ... 2.0, —·—·—· 2.5.

(d) $\gamma_{avg} = 0.035$, $I_{max} = 7.91$; ____ 2.50, ... 3.75, —·—·—· 5.0.

(e) $\gamma_{avg} = 0.0375$, $I_{max} = 10.51$; ____ 2.50, ... 5.0, —·—·—· 7.5.

(f) $\gamma_{avg} = 0.040$, $I_{max} = 11.44$; ____ 2.50, ... 5.0, —·—·—· 7.5.

FIBER REINFORCED PLASTIC INFANTRY FIGHTING VEHICLE TECHNOLOGY DEVELOPMENT

BY
D. ERICH WEERTH

Two fundamental barriers have explained the slow acceptance of polymer composites in the military combat vehicle market place, namely, a lack of material data/design experience and the need for new manufacturing technology and facilities. The benefits of using these more expensive fiber reinforced plastic (FRP) materials, in overall cost and performance, are becoming more pronounced as mission requirements become more difficult to satisfy. This attitude is born out in surve··s performed by Arthur D. Little, Inc. and SRI International, where significant growth is projected in structural laminate and ballistic laminate applications of polymer composites to non-aerospace military markets. It is anticipated that by 1995 armored vehicles, submarine hulls and ship superstructure will be mass produced using fiber reinforced plastics as a substitute for steel and aluminum. Drivers generating increased attention toward the military application of polymer composites are:

- o weight reduction
- o reduced noise & vibration
- o improved ballistic performance
- o enhanced survivability
- o reduced life cycle costs
- o reduced production costs
- o reduced signature
- o improved mass distribution and lowered center of gravity

through planned research and development over the past five years, great strides have been made in the design, analysis, prototyping and field testing of thick ballistic laminate ground combat vehicle hulls and turrets.

The utillization of FRP materials for structural applications has been perfected by numerous aerospace companies. The designs are driven by the need to develop high quality load bearing structural laminates which have high fiber/resin bond strengths. FRP laminates for military vehicle applications are required to be structural and capable of resisting impact due to ballistic projectiles. Previous research and development programs have demonstrated that FRP laminates, with intentionally degraded interfacial bond strengths, ballistically out-perform laminates with high fiber/resin bond strengths.

Therefore, the design challenge here involves the tuning of laminate properties to simultaneously satisfy both structural and ballistic requirements. The fabrication and processing challenge is to consistently reproduce the afore-mentioned properties such that part quality and mechanical property scatter is minimized, resulting in consistently reproducible composite laminates. These topics will be addressed in more detail by describing the evolutionary development of the FMC/AMTL Composite Infantry Fighting Vehicle Program.

COMPOSITE MATERIALS SELECTION AND EVALUATION FOR ADVANCED TOWBARS

by

G. Samavedam and T. G. Campbell

Foster-Miller, Inc.
Waltham, Massachusetts 02254

Current heavy duty towbars, as shown in Figure 1, capable of recovering disabled M1 tanks are of steel construction and are extremely heavy, requiring three troops to attach. Application of composite materials to lighten the towbars has been a challenge to the material engineer due to large static and dynamic loads developed in these structures during recovery operations. Previous attempts to develop a composite towbar were not successful. This paper identifies significant structural problems involved in the selection of the materials, optimization of the geometry and the weight, and the problems of load transfer and the resulting complex stress distribution in the end fittings. Analyses of these problems to arrive at an optimum design rationale will be presented in this paper.

Service Load Analysis

The first part of the paper identifies static and dynamic loads developed in the towbars during the recovery operations.

Static analyses were conducted for various maneuvers and ground conditions to determine the limit towbar load. A dynamic model was developed to predict the steady and transient loads on the towbar as a function of towing speed, towbar stiffness and play in the attachment joints. Previously obtained field test results have been used for model correlation. The model was then used to determine the peak tensile and compressive loads of each composite tube arm of the towbar.

Material Selection and Analyses

Several criteria have been used in the choice of a basic material system for the tubular towbar arm. The primary criteria of high strength and stiffness at low weight and reasonable cost yielded organic composites as prime candidates. The material must sustain the sudden load applications indicative of the sharp peak loads exhibited in field testing. Another criterion used is the inherently high strain-to-failure and energy storage capacity required in both tension and compression. The resulting fibers of choice are T-40 graphite and S2 fiberglass.

The above fibers are combined in a hybrid construction using an epoxy matrix. Environmental effects are accounted for in property determination. Material ratios and orientations have been optimized subject to requirements on tension and compression strength, column buckling, shell buckling, handling loads and damage tolerance. A typical trade-off analysis is graphically presented in Figure 2. The resulting hybrid construction is expected to meet the stringent design criteria for the towbar. External Kevlar overwraps provide additional damage tolerance in a hybrid design utilizing three different fibers for optimum performance and durability.

Optimized End Fitting Design and Analysis

Although the use of trapped tapered end fittings have been in common use for som· time, their optimal design requires an advanced analysis. The distribution of contact pressure at the interface between the tapered fitting and the composite is critical to the design. A special finite element analyses has been used to determine the distribution, taking into account the effects of interface friction. An analysis of a multilayered thick-walled orthotropic cylinder under internal pressure has been carried out to optimize the ply orientation for hoop and radial stresses. The resulting end fitting design yields the most efficient material usage and low weight.

Subsequent Work

The composite tube design discussed above will be fabricated and tested in both tension and compression. The design corroboration will be conducted at the Materials Technology Laboratory. The proven design will then be incorporated into complete towbars and field tested at the Aberdeen Proving Grounds.

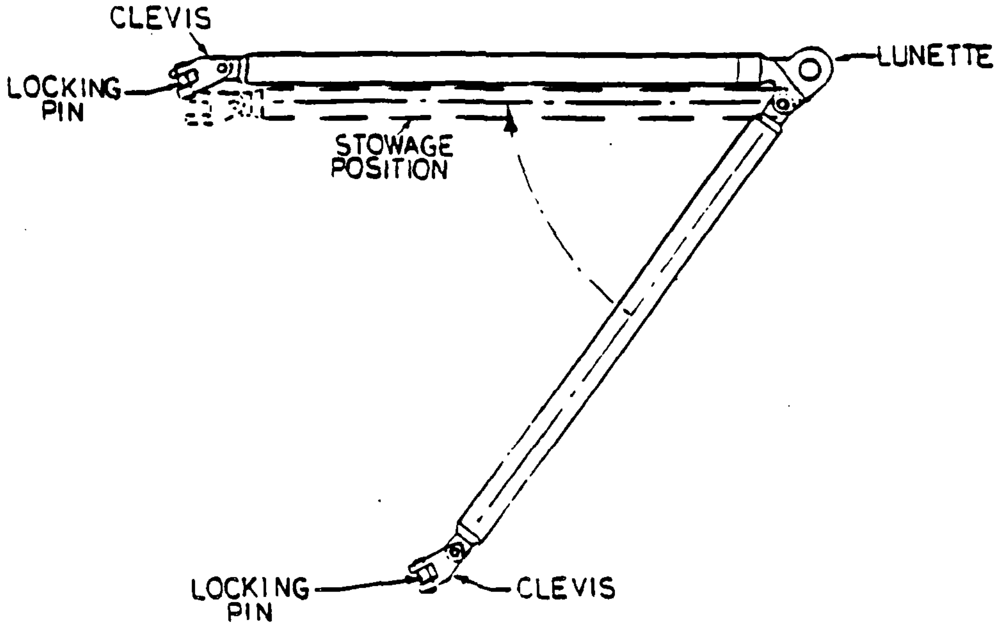

Figure 1. Heavy Duty V-Type Towbar

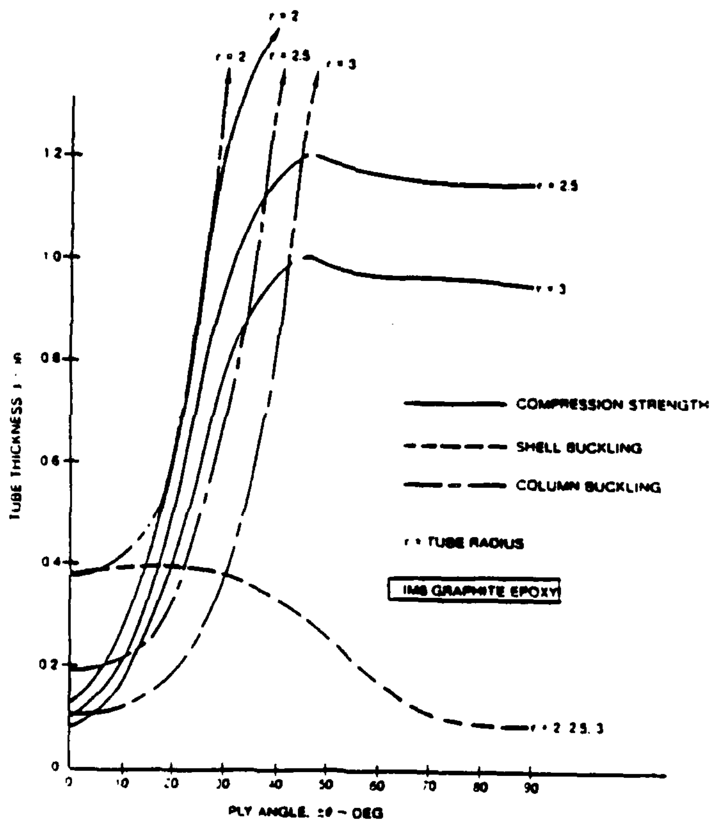

Figure 2. Typical Composite Tube Analysis

A GENERALIZED STRUCTURAL INTEGRITY ASSURANCE PROGRAM: APPLICATION TO ARMY MATERIEL SYSTEMS

WILLIAM T. MATTHEWS
MATERIEL DURABILITY BRANCH
ARMY MATERIALS TECHNOLOGY LABORATORY
WATERTOWN, MA 02172-0001

This program addresses the application of solid mechanics methods, failure modes and life prediction to a generalized structural integrity assurance (SIA) program which includes use of advanced materials. Except for some notable exceptions, structural integrity assurance is typically addressed by ad hoc analyses, tests and perhaps in-service structural maintenance measures for each structural system. In-service usage may differ substantially from initial design estimates but no formalized program may exist to assess the implications of such changes. The success of such ad hoc methods is largely dependent upon the experience base of previous design and usage. However with increasing application of emerging materials the prior experience base derived primarily from metallic structures is of diminished value. A generalized structural integrity assurance program would deal with a wide variety of structural systems.

The Army has no formalized SIA program, although interest has been shown recently at the top command level of Army Materiel Command. Army materiel systems involve many types of structures where structural integrity assurance is of critical importantance, for example: helicopter and fixed wing aircraft, missiles, gun tubes and projectiles, bridging, large scale antennas, vehicle track and suspension systems and gun mounts.

In the development of systems with critical structural components, structural integrity assurance concerns are inseparable from associated issues of performance, downtime or readiness, cost and scheduling. In view of the integrated nature of SIA with other system issues of major importance, structural integrity issues cannot be resolved by structural specialists only. Resolution of structural integrity assurance issues are major system decisions which must be made with the support of an integrated staff of specialists. In the Army decisions related to specific materiel systems are the responsibility of individual Major Subordinate Command: Aviation Command, Missile Command, etc.

In view of this relationship of SIA to system development, the Generalized Structural Integrity Program must be expressed in the form of a framework of issues which must be addressed, resolved and specified. The Generalized Program does not specify the outcome of the development within its framework. In the application to Army materiel systems, the Generalized Program requires the development of Specific Structural Integrity Assurance programs by each Major Subordinate Command for specific classes of materiel within the Generalized Program framework.

The Generalized Program, figure 1, consists of five major tasks (cradle to grave); design information, design analysis / material characterization, design development testing, qualification testing/documentation and force management. The program tasks are adapted from the specific Air Force Structural Integrity Programs for airframes and engines. The tasks are modified for use in a generalized program. The Generalized Program defines five structural integrity parameters to characterize the structural integrity of structural systems for maximum load resistance and service life including limited duration service life conditions related to in-service damage. For Army materiel systems the primary concern for limited duration service life is related to battle damage and survivability. The Generalized Program addresses the issues of characterizing service life both in terms of nominal life and by considering extreme case conditions. The definition of SI Parameters permits extensive flexibility in devising SIA methods for both nomimal and extreme design conditions. For example, either flaw based (damage tolerant) or non flaw based (safe life) methods may be applied to service life analysis and qualification tests. The program focuses attention on critical components only. Development of predictive mechanics models is required which are applied and interpreted in a consistent fashion throughout all of the major tasks. Analyses must be documented and maintained in up-to-date status throughout the program. All analyses must be validated by appropriate testing. A system is required for in-service monitoring of critical SIA parameters for service usage and damage detection which includes feedback to design/analysis functions in order to maintain realistic prediction of SIA Parameters. Design with emerging, advanced materials is included in the framework through the "Building Block" approach: a series of tests for effects of loading, geometric compexity, environment and material variability of increasing complexity. Careful documentation of the basis and supporting rationale for the application of the Building Block approach to a structural system is required in order to promote understanding of the interpretation and limitations of the associated SI information. The Generalized SIA Program requires careful documentation of basis and supporting rationale for modeling methods, failure criteria, factor of safety, service life scatter or fatigue factors, statistical bases for material properties, treatment of environmental, dynamic load and size effects in general, and interpretation of qualification tests including the significance of local damage.

It is recognized that completely satisfactory technical methods may not be immediately available for detailed quantitative strength, stiffness and fatigue analyses of designs using a wide variety of advanced materials. It is important to document in a formalized way the limitations of interim methods which are based on limited empirical foundations in order to understand the limitations of application. Adoption of a formalized program would clearly document technical gaps and justify technical investigations.

A formalized, disciplined program would be expected to aid in the early discovery of SI problems in materiel system development and to lead to design, directly related to SI parameters, which takes advantage of appropriate material properties. The standarized program would promote SIA technology transfer among Army Commands and improve communication between the Army and its contractors, within contractor organizations and within major contractor partnerships.

GENERALIZED STRUCTURAL INTEGRITY ASSURANCE PROGRAM

TASK I DESIGN INFORMATION	TASK II DESIGN ANALYSES AND MATERIAL CHARACTERIZATION	TASK III DESIGN DEVELOPMENT TESTING	TASK IV QUALIFICATION TESTS AND DOCUMENTATION	TASK V FORCE MANAGEMENT
A. SIA PLAN	A. MAX LOAD ANALYSIS	A. SERVICE LOAD AND ENVIRONMENTAL	A. MAX LOADING RESISTANCE	A. OPERATION ENVELOPE IMPLEMENTATION
B. SI CHARACTERIZATION o MAX LOADING RESISTANCE o SERVICE LIFE BASE LINE DESIGN SUFFERANCE o LIMITED DURATION SERVICE LIFE	B. SERVICE LOAD ANALYSES	B. JOINTS-MECHANICAL TESTS	B. SERVICE LIFE o BASE LINE o DESIGN SUFFERANCE	B. FORCE SIA MAINTENANCE IMPLEMENTATION
C. DESIGN FOR SIA	C. CHEMICAL/THERMAL ENVIRONMENT	C. BUILDING BLOCK: ADVANCE MATERIAL TESTING	C. LIMITED DURATION SERVICE LIFE	C. IN-SERVICE USAGE MONITORING
D. SERVICE LIFE SIA PLAN	D. MECHANICAL PROPERTIES CHARACTERIZATION	D. MAX LOADING RESISTANCE	D. SIA EVALUATION	D. IN-SERVICE SIA DATABANK: FEEDBACK TO ANALYSIS SUMMARY
E. DESIGN SERVICE LIFE AND DESIGN USAGE	E. MECHANICS ANALYSES	E. SERVICE LIFE o BASE LINE o DESIGN SUFFERANCE	E. FORCE MANAGEMENT o SIA ANALYSIS SUMMARY o OPERATIONAL ENVELOPE o FORCE SIA MAINTENANCE PLAN o IN-SERVICE MONITORING PLAN	
F. MATERIALS, PROCESSES, JOINING METHODS SELECTION	F. SIA ANALYSES AT MAX LOADING	F. LIMITED DURATION SERVICE LIFE		
	G. SERVICE LIFE ANALYSES o BASE LINE o DESIGN SUFFERANCE	G. MANUFACTURING QUALITY CONTROL SUMMARY		
	H. LIMITED DURATION SERVICE LIFE ANALYSES/SUVIVABILITY	G. MANUFACTURING QUALITY CONTROL SUMMARY		

Structural Testing of Metal/Composite Conical Structures With Holes

by
William J. Tedeschi, Rodney A. May,
Albino C. Bustamante, Eric W. Reece, and D. Neill Benton
Sandia National Laboratories
Albuquerque, NM 87185

Conical structures containing holes were tested for the purpose of determining their structural load carrying capacity. The conical structures were composed of an aluminum substructure with an outer layer of composite material. Holes were machined into all but one of the structures, the holes ranged in circumferential size from 15 to 35 percent of removed structure at the maximum hole diameter. The structures were quasi-statically loaded in tension, compression, and bending until structural failure occurred. The structural failure modes for each shell were analyzed. Supporting analyses used a finite element structural response code to model the elastic-plastic response of the loaded structures, including structure failure.

TEST STRUCTURES, FIXTURES, AND LOADING CONFIGURATIONS

The tested conical structures consisted of an aluminum substructure with a composite overcoat. Between the two conical layers was a bond. Figure 1 shows a schematic of the compression test structure. The tension and bending test structures were similar.

Special fixtures were designed to allow the structures to be tested in existing axial test machines at Sandia National Laboratories and in a specially designed bending test machine, which will be described later. Three criteria were established for the test fixtures. First, the fixtures should be used for all three loading configurations. Second, the fixtures should apply the loads as equally as possible between the substructure and the composite overcoat. Finally, the fixtures should apply the loads in such a manner that a failure would not take place at the structure-fixture interface due to a stress concentration or point load caused by the fixture. A fixture was designed that not only bolted to the aluminum substructure, but used a tapered clamping ring to allow loads to be transmitted to the composite overcoat. Figure 2 shows the axial compression and tension fixtures used to transmit applied axial loads into the test structures.

All tests were conducted in the Sandia National Laboratories Structural Mechanics Laboratory. The test specimen without a hole was tested in compression on a Tinius-Olson, universal testing machine capable of applying 600,000 pounds of force. All other axial tension and compression tests were accomplished on a 220,000 pound MTS servo-hydraulic testing machine. All these tests were conducted using the fixtures shown in Figure 2. Pure bending tests were done using the Sandia designed and fabricated test fixture shown in Figure 3. It has the capability of applying 600,000 in-lb of pure moment to the conical test structure.

The tests were conducted in a displacement controlled mode so that structure failure was gradual rather than catastrophic and could therefore be observed. Displacements were applied to the ends of the conical structures in order to produce either axial loads or bending moments. The loading was interrupted at equal load increments to obtain data. Strain gage and displacement data were taken during the tests using an existing computer-based data acquisition system. Strain gage data were obtained from both axial and rosette (triaxial) strain gages.

TEST MATRIX

A total of thirteen structural response tests were conducted, nine axial and four bending. The test matrix and measured failure loads are shown in Figure 4. Four loading configurations were used: axial compression, axial tension, bending - hole in tension, and bending - hole in compression. In addition to the conical structure with no hole, three types of hole configurations were tested; circular, elliptical, and diamond. The hole sizes varied from 15 to 35 percent. Hole size is defined as the percentage of circumference removed at the maximum hole diameter.

TEST RESULTS

Six compression tests were conducted. Figure 5 is a plot of measured failure load versus hole size for the compression tests. As expected, the failure load decreases with increasing hole size. In general for the compression tests, increasing load failed the composite overcoat first by fracturing in shear, followed by substructure buckling. Failure always initiated locally near the maximum hole diameter. Figure 6 shows the test results for the 35 percent hole size test structure.

Two of the conical structures were tested in compression with diamond-shaped holes (see Figure 5). The purpose for these two hole configurations was to introduce a different stress concentration at the maximum hole diameter and see if this affected the results for a fixed hole size. The results indicate that introducing this stress concentration did not significantly affect the failure load.

Three axial tension tests were conducted; two tests with 25 percent hole sizes and one test at 35 percent hole size. Similar failure modes were observed in all three tests. Tensile fracture of the outer composite layer occurred first, followed by a ductile tearing of the substructure. Failure always initiated locally at the maximum hole diameter. Figure 7 shows the measured applied load versus strain (deflection) and a photograph of the 25 percent hole size test results. The load - strain curve indicates that the structure's response was elastic in nature before composite fracture, followed by a plastic response until substructure failure occurred. This response is explained by the fact that the composite material is very brittle compared to the aluminum substructure and is also thicker. The strain response of the conical structure is dominated by the composite, until the composite fractures, and then the strain response is governed by the relatively ductile substructure.

Finally, four pure moment tests were conducted; two with the hole in tension and two with the hole in compression. Two hole sizes were tested: 15 and 35 percent. Structure failure in these tests initiated in the local region around the maximum hole diameter. The observed failure characteristics were somewhat similar to those observed in the axial tests for the same tension or compression loading local to the hole. Figure 8 is a photograph of the 15 percent hole size, hole in tension, post-test results. Brittle fracture of the composite overcoat near the hole is apparent. Note also that the substructure buckled on the opposite side of the shell near strain gage number eight. This was due to the loading configuration. The side of the structure opposite the hole is in compression, even though the hole side is in tension. The loading opposite the hole was great enough to cause local substructure buckling.

Material properties for the aluminum substructure, the composite overcoat, and the bond in between were generated for use in a finite element code. It was found that the composite overcoat was anisotropic in nature, unlike the aluminum substructure.

SUPPORTING ANALYSES

Supporting analyses were used to: design the conical test structures and fixtures, make pre-test calculations, and interpret the observed and measured test results. The ABAQUS finite-element code was used for these purposes.

Preliminary calculations indicated that the structure/fixture design was such that the applied loads would be transmitted into the structure test section uniformly and without edge effects. This was verified by measured data from the compression test with no hole in the test structure.

An example of one of the pre-test calculations is the one done for the 15 percent hole size bending test - hole in compression. The test structure was predicted to fail at an applied bending moment of 390,000 in-lbf. The measured failure load for the shell was 340,800 in-lbf. A comparison of calculated versus measured strains is shown in Figure 9. The predicted sequence of failure was that the composite overcoat would fracture first, followed by substructure buckling. The pre-test calculation agreed very well qualitatively with the test results. The buckled substructure observed in the test results was similar to the predicted buckled substructure shape shown in Figure 10.

SUMMARY

Thirteen structural response tests of conical structures with hole configurations were conducted to study how they would fail with increasing applied load. The structures consisted of an aluminum substructure with a composite overcoat. The test structures were loaded in three different ways: axial tension and compression and pure bending. The observed test results and measured data have been used to understand how structure failure occurred. Analytical calculations using the ABAQUS finite element code helped in the design of the test structure and fixtures and in interpreting the test results. The test results and analytical calculations have allowed us to understand the complex interaction of the composite overcoat with the metal substructure under different loading conditions.

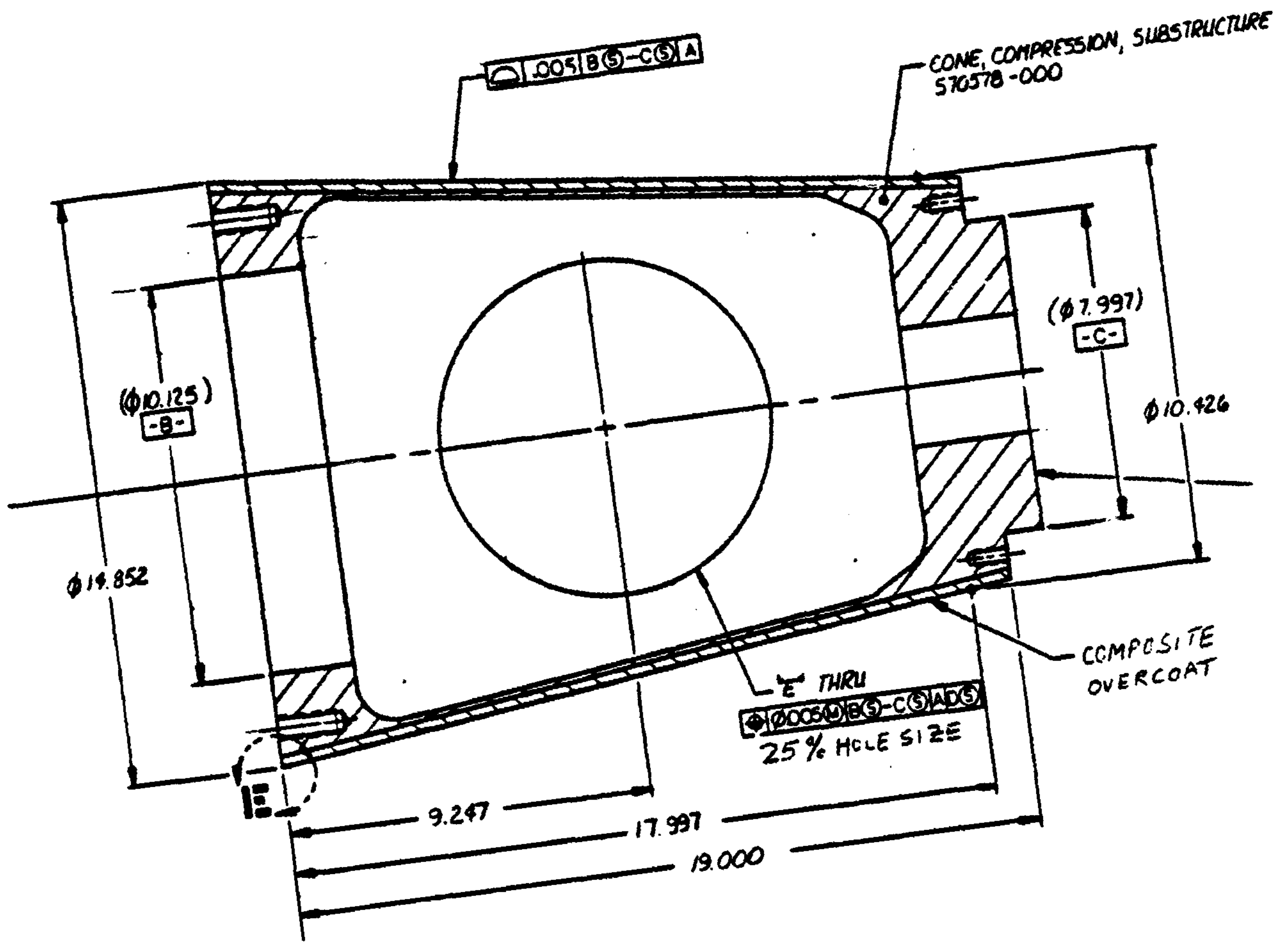

FIGURE 1. Conical test structure used for compresion tests.

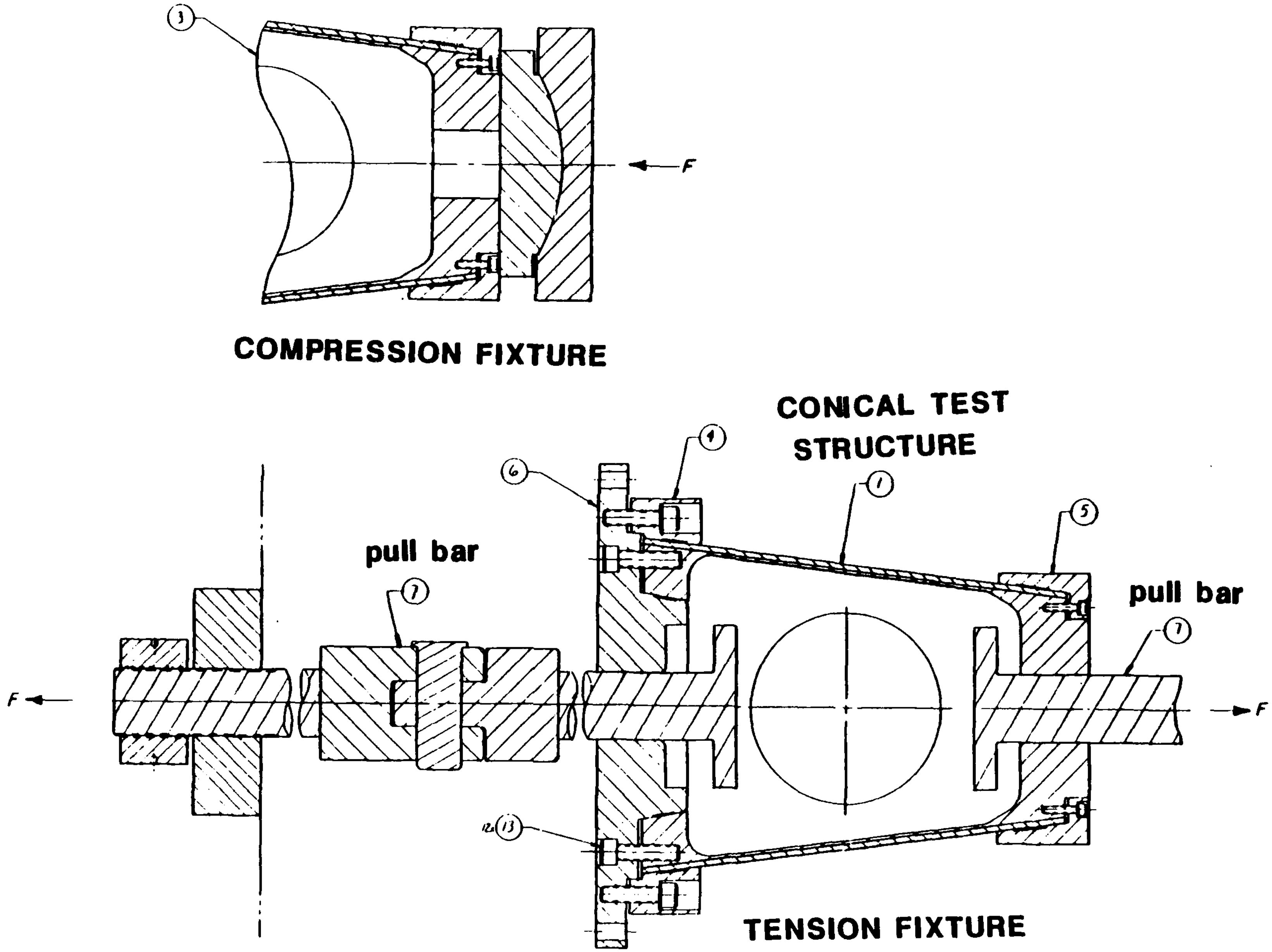

FIGURE 2. Axial compression and tension test fixtures.

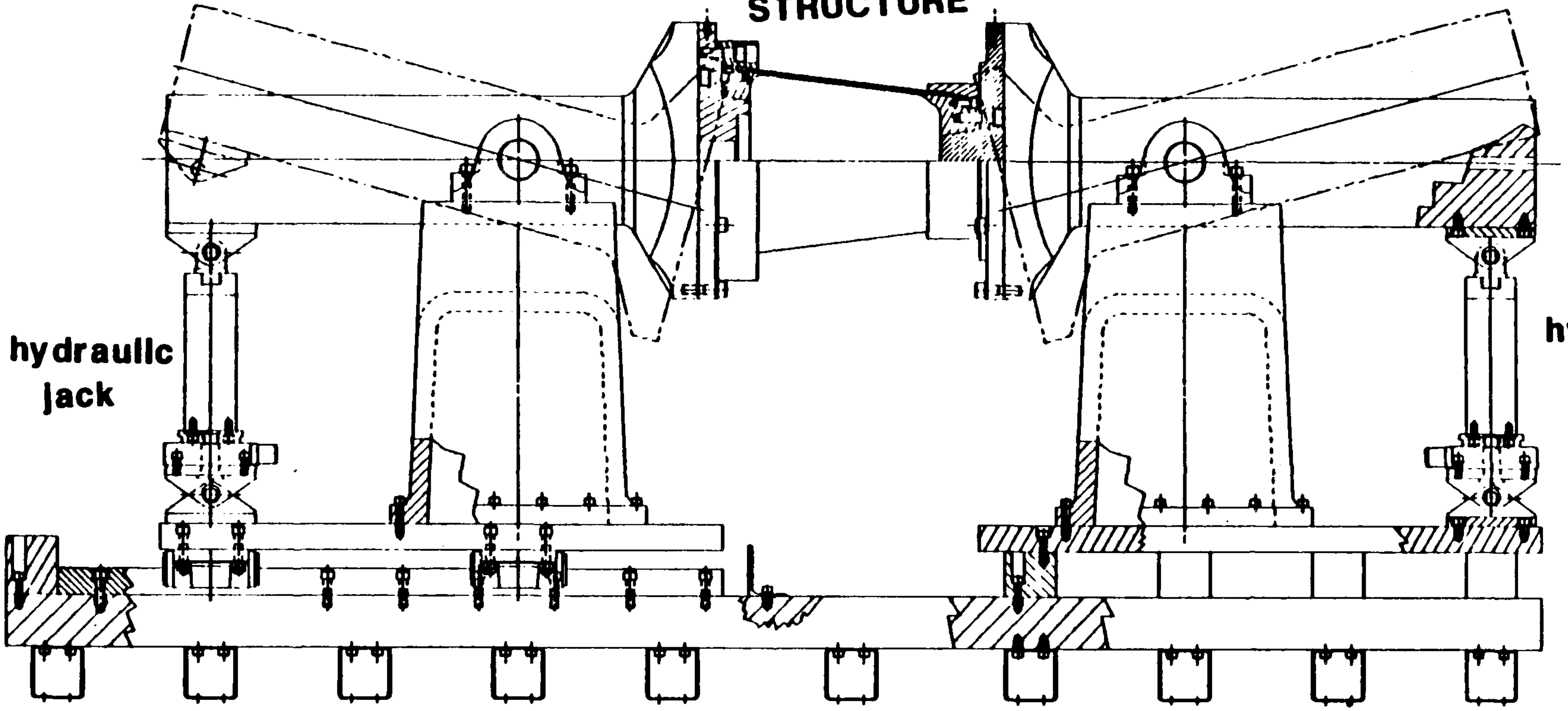

FIGURE 3. Pure moment test fixture.

FY87-88 STRUCTURAL RESPONSE TEST MATRIX

TEST NO	DATE	TYPE	HOLE CONFIGURATION SHAPE	HOLE CONFIGURATION LEVEL	MAX LOAD
1	10/15/86	COMPRESSION	NO HOLE	0%	250,000 LB
2	11/11/86	TENSION	1 CIRCULAR	25%	85,000 LB
3	12/5/86	COMPRESSION	1 CIRCULAR	25%	78,000 LB
4	1/9/87	TENSION	1 CIRCULAR	25%	100,590 LB
5	3/3/87	COMPRESSION	1 CIRCULAR	15%	114,410 LB
6	4/6/87	COMPRESSION	1 DIAMOND	25%	84,700 LB
7	5/22/87	COMPRESSION	1 CIRCULAR	35%	49,000 LB
8	6/8/87	TENSION	1 CIRCULAR	35%	40,570 LB
9	6/26/87	COMPRESSION	1 DIAMOND	35%	53,300 LB
10	3/22/88	MOMENT-T	1 CIRCULAR	15%	420,000 IN-LB
11	6/13/88	MOMENT-C	1 CIRCULAR	15%	340,800 IN-LB
12	8/25/88	MOMENT-C	1 CIRCULAR	35%	168,000 IN-LB
13	9/27/88	MOMENT-T	1 CIRCULAR	35%	198,000 IN-LB

FIGURE 4. Structural response test matrix and measured failure loads.

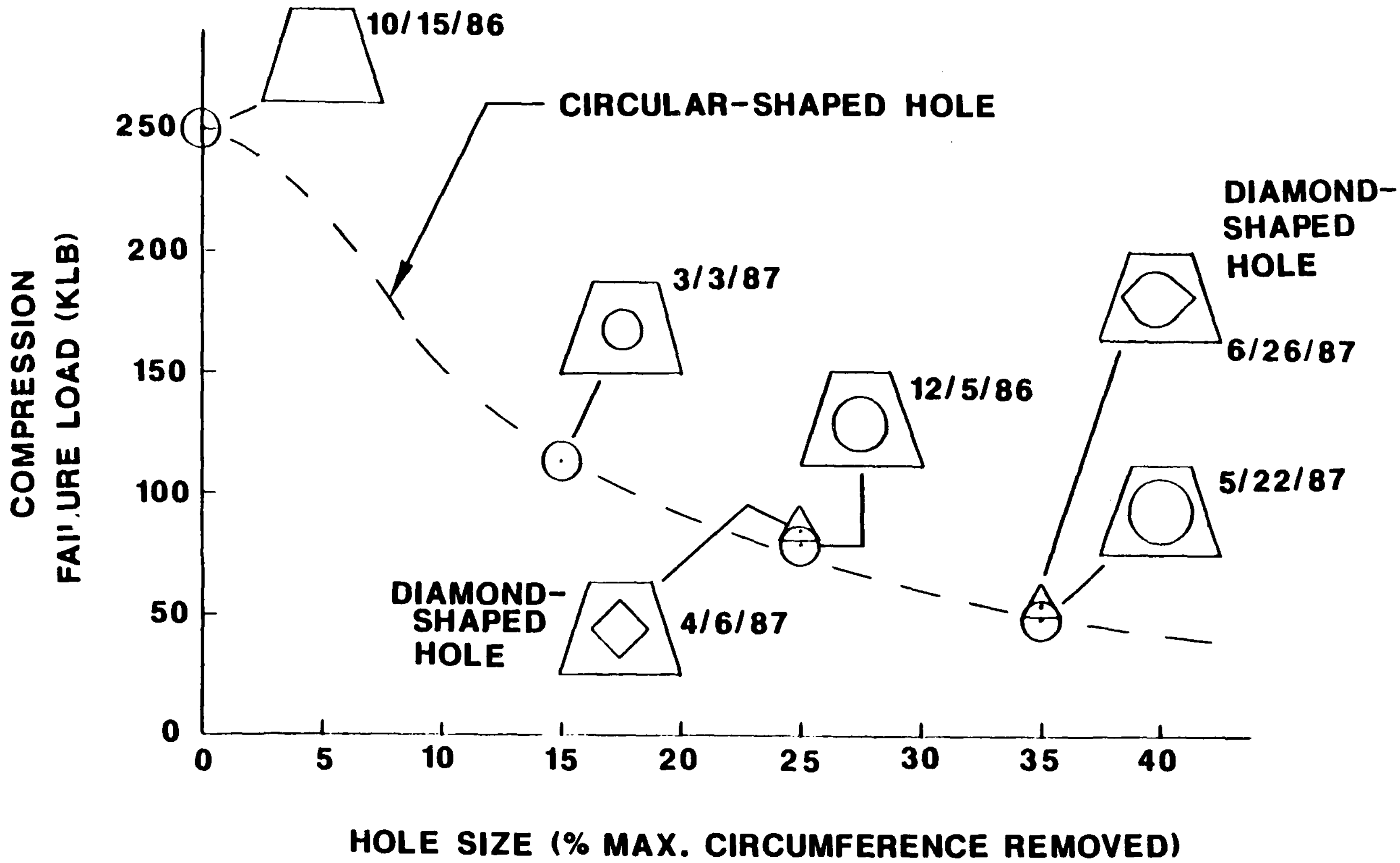

FIGURE 5. Summary of compression test data.

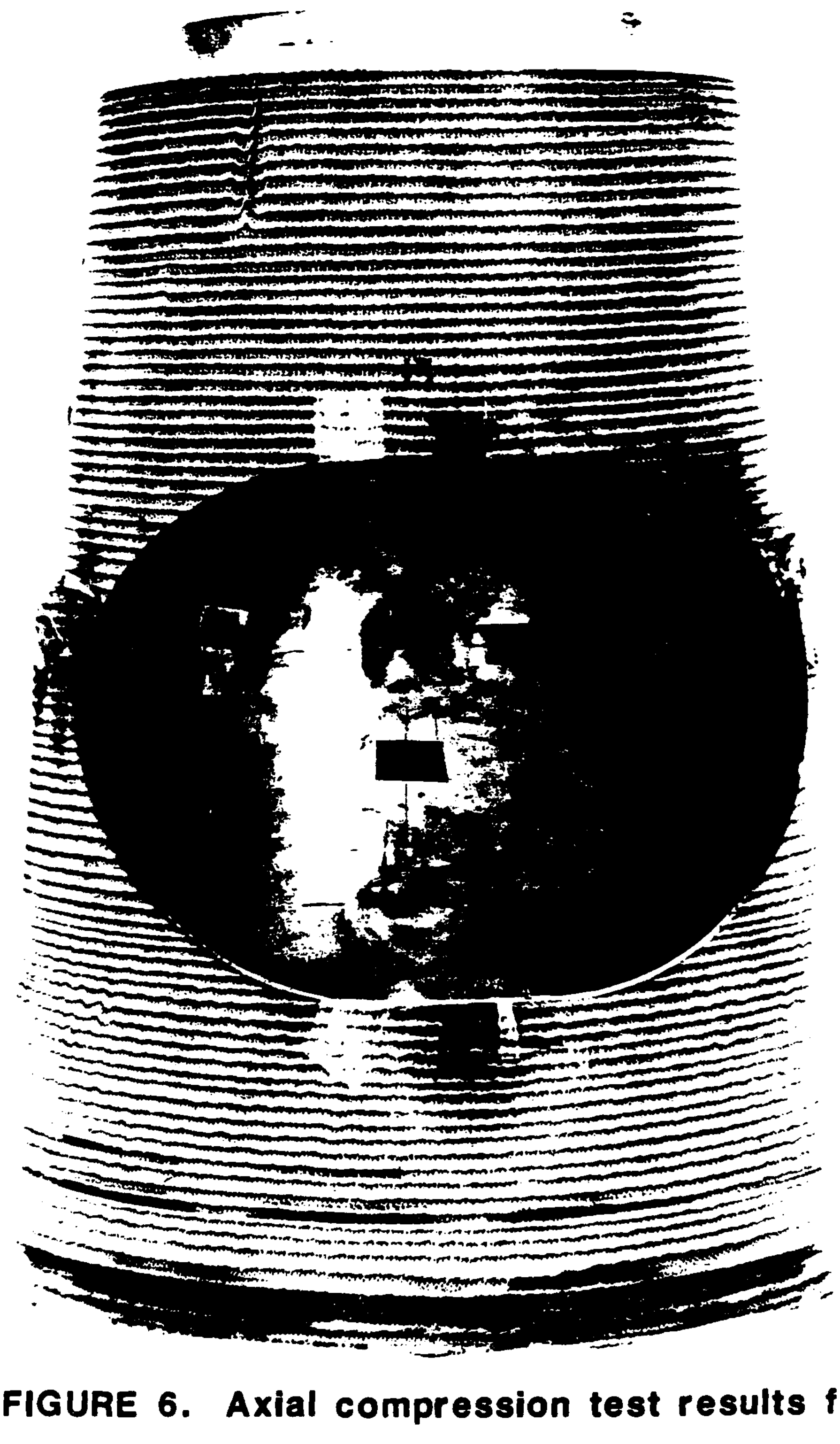

FIGURE 6. Axial compression test results for conic structure with 35 % hole.

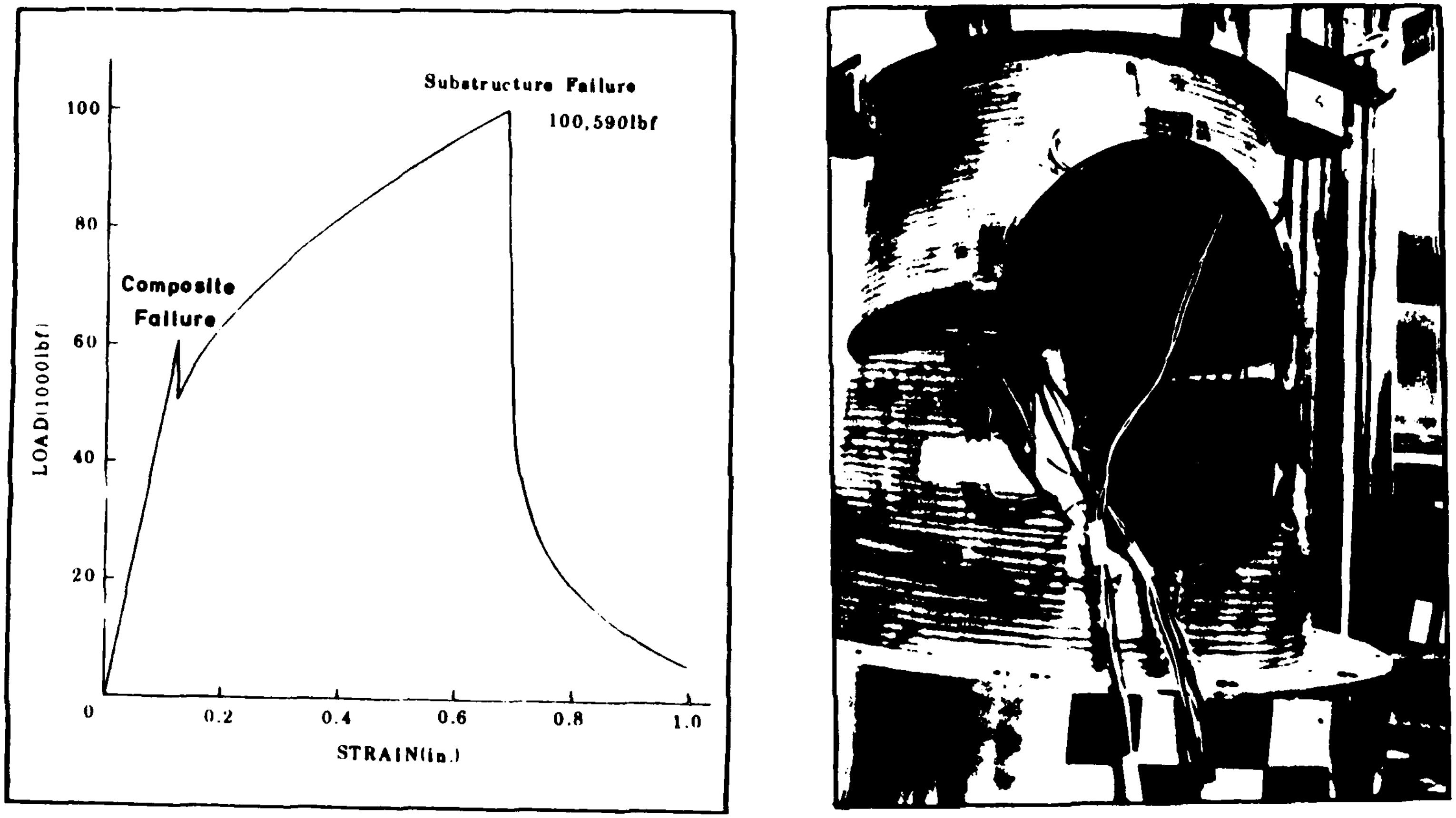

FIGURE 7. Measured applied load versus strain and photograph of axial tension test with 25% hole.

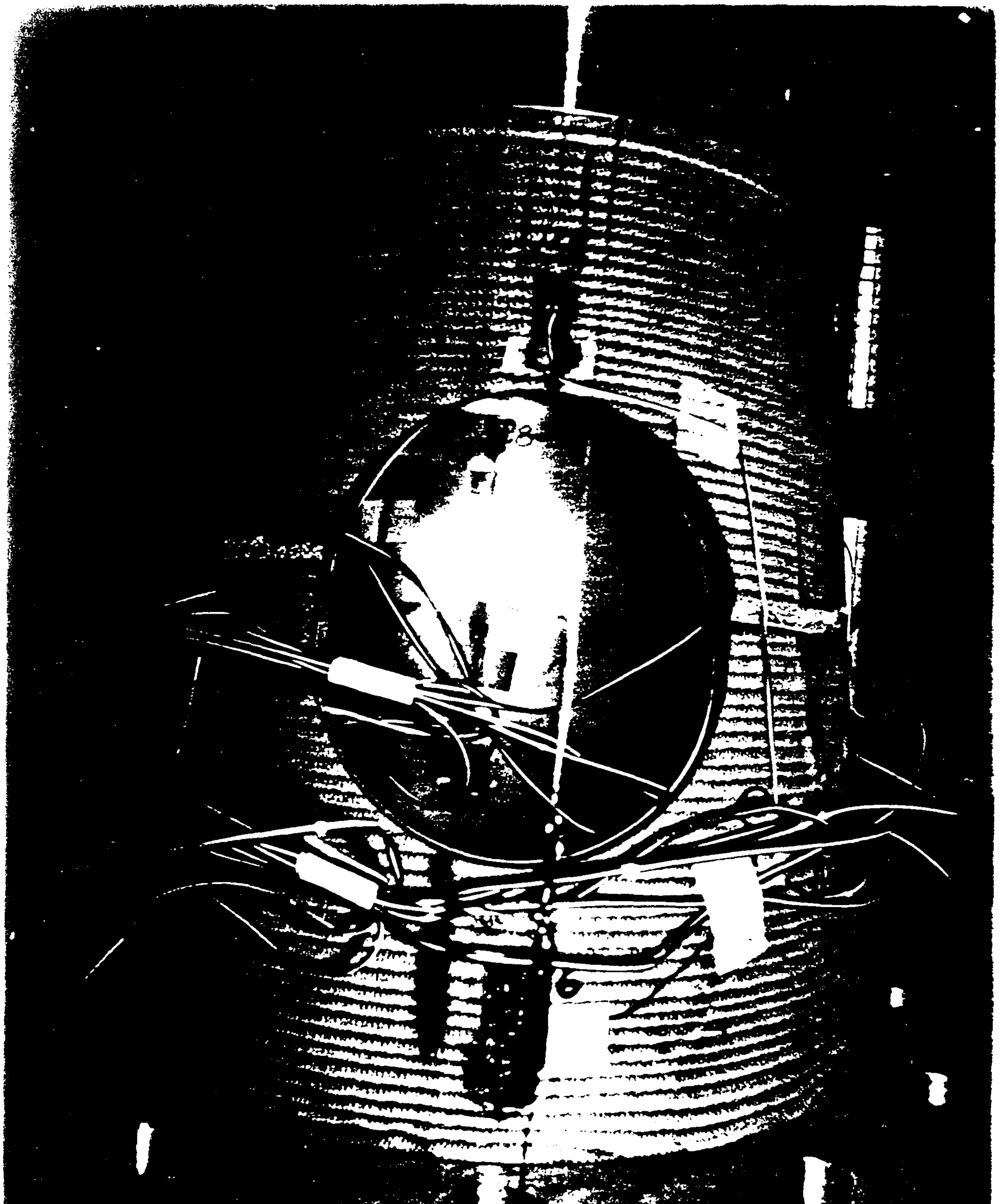

[illegible] ... results hole in tension

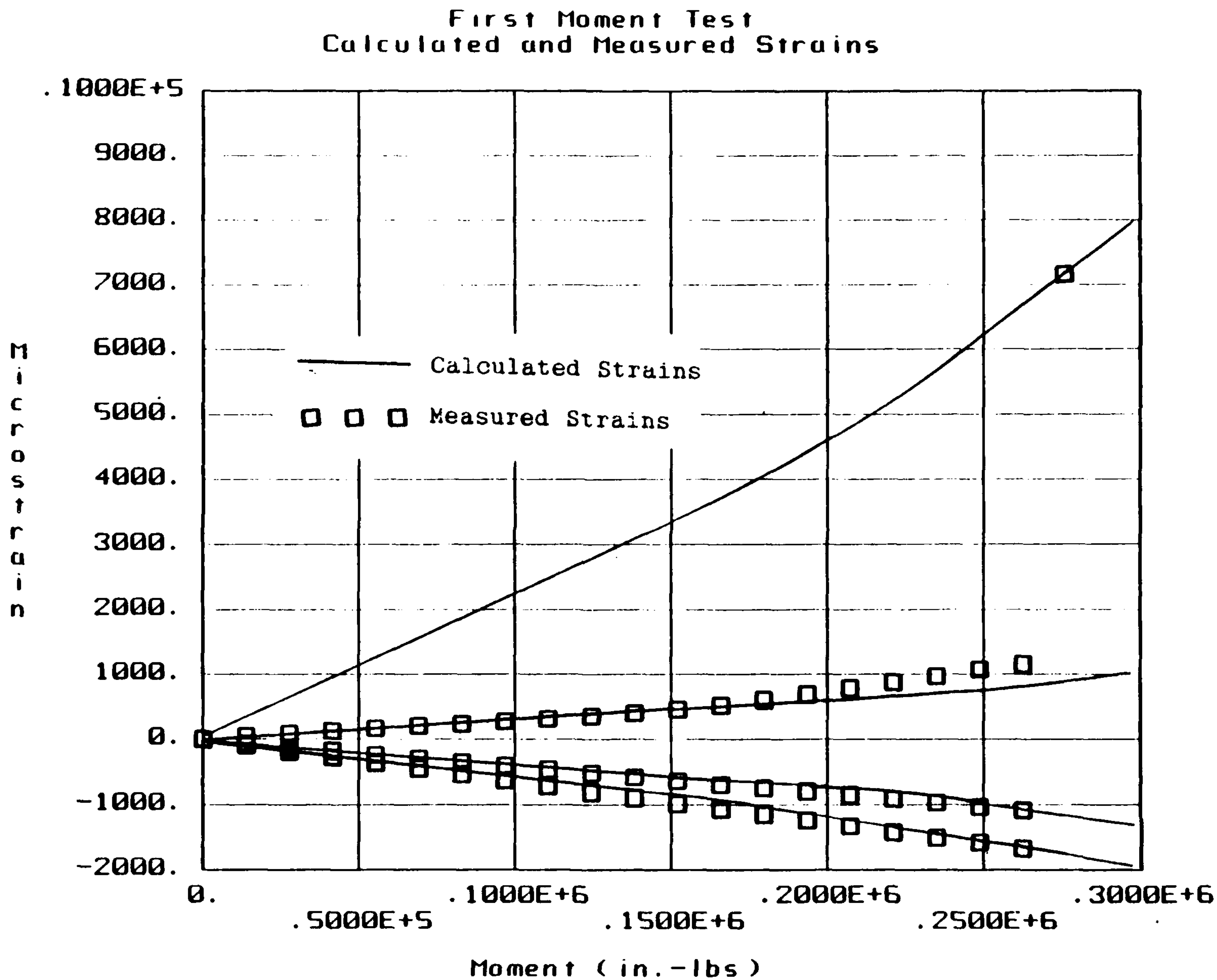

FIGURE 9. Comparison of calculated and measured strains for pure moment test (hole in compression) with 15% hole size.

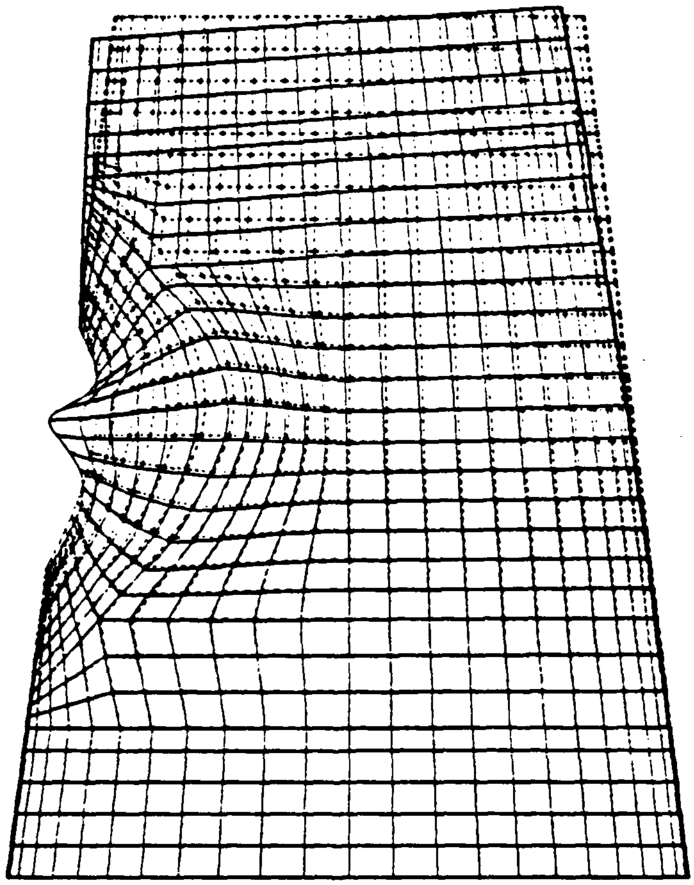

FIGURE 10. Predicted substructure deformation for pure moment test, hole in compression.

EFFICIENT FINITE ELEMENT MODELING OF THICK COMPOSITES BASED ON HIGHER-ORDER PLATE THEORY

Alexander TESSLER and Erik SAETHER

Mechanics and Structures Branch
U.S. Army Laboratory Command
Materials Technology Laboratory
Watertown, Massachusetts 02172-0001

ABSTRACT

Army's considerable interest in adopting advanced composite materials for its next generation of combat vehicles, aircraft, and weapon systems necessitate improved computational mechanics methods, particularly those dealing with thick-section composite laminates and structures. One example of a thick-composite technology is a composite IFV (Infantry Fighting Vehicle), currently being developed by FMC with a supporting effort from MTL. In this application, both the turret and hull structures are made of a glass-fiber polyester resin system, with the thickness ranging from 1 to 3 inches.

What makes the mechanical behavior of "thick" composites different from their "thin" counterparts are the through-thickness strain effects, both due to transverse shear and transverse normal modes of deformation. Whereas in thin laminates these effects are often neglected due to the smallness of their contribution to deformation as compared to the normal strains; in thick laminates, the transverse straining may be rather pronounced and, therefore, cannot be ignored. Amplifying the significance of the transverse effects in the state of stress and deformation are the relatively low material compliancy and strength in the transverse direction. Thus, from the analytic standpoint, to adequately model the thick-composite laminate behavior, an accurate bending/stretching theory should used, which includes both transverse shear and transverse normal effects. From the perspective of the large-scale response simulation of thick-composite plate and shell structures, there exists a need for efficient and robust plate and shell finite elements, incorporating the aforementioned transverse deformation modes. It is the latter aspect which motivated the present investigation and development of a higher-order laminate plate theory.

The scope of the present paper is twofold; first, the recently developed higher-order displacement theory for homogeneous elastic plates [1] will be extended to laminated composites within a variational framework, in which the deformations due to inplane, transverse shear and transverse normal straining are accounted; second, guidelines for developing efficient plate finite elements based upon the higher-order analytic theory will be presented. Our further goal, although it goes beyond the scope of this paper, is to fully develop and explore these new types of finite elements that will enable efficient large-scale analysis of

general composite plate and shell structures ranging from thin to truly thick that may be subject to a wide range of loading regimes.

Displacement Expansions. The present displacement plate theory is derived from three-dimensional elasticity via the principle of virtual work by expanding the displacement components with respect to the thickness coordinate (z) by means of Legendre polynomials.[1] These include linear (in z) inplane displacements, and a special form for a parabolically varying transverse displacement. The displacement expansions appear as:

$$
\begin{aligned}
u_x(x,y,z) &= u(x,y) + hP_1(\xi)\theta_y(x,y), \\
u_y(x,y,z) &= v(x,y) + hP_1(\xi)\theta_x(x,y), \qquad (1)\\
u_z(x,y,z) &= w(x,y) + P_1(\xi)w_1(x,y) + [P_0(\xi)/5+P_2(\xi)]w_2(x,y),
\end{aligned}
$$

where $P_n(\xi)$ denote Legendre polynomials:

$$P_n(\xi) = \frac{1}{2^n\, n!}\, d^n[(\xi^2-1)^n]/d\xi^n, \quad P_n(1)=1,$$

(i.e., $P_0 = 1$, $P_1 = \xi$, $P_2 = (3\xi^2-1)/2$, $P_3 = \xi(5\xi^2-3)/2$)

($\xi = z/h \in [-1,1]$, where 2h denotes the total plate thickness.)

The five kinematic variables u, v, w, θ_x, and θ_y in (1) are Reissner-Mindlin type [2-4] weighted average displacements:

$$u = \frac{1}{2h}\int_{-h}^{h} u_x dz, \quad v = \frac{1}{2h}\int_{-h}^{h} u_y dz, \quad w = \frac{1}{2h}\int_{-h}^{h} u_z(P_0 - P_2)\, dz,$$

$$\theta_x = \frac{3}{2h^3}\int_{-h}^{h} u_y z\, dz, \quad \theta_y = \frac{3}{2h^3}\int_{-h}^{h} u_x z\, dz, \qquad (2)$$

where u and v represent the midplane displacements in the x and y coordinate directions, respectively, and θ_x and θ_y denote the normal rotations about the x and y axes, respectively. Note that while w is a weighted average value of u_z (and not the midplane displacement), w_1 and w_2 are the higher-order displacement components of the parabolically distributed u_z displacement. As will be seen subsequently, the special form of u_z leads to important simplifications in the theory.

---

[1] The use of Legendre polynomials is carried over from the homogeneous plate formulation [1] where their orthogonal nature allows simplified integration across the plate thickness. In the present context, however, their use is strictly to maintain notational compatibility with the homogeneous case.

Transverse Shear Field-Consistency. As in some previous efforts (e.g., refer to [5,6]), this order of displacement expansions leads to **field-inconsistent** transverse shear strains [1]. The field-inconsistency manifests itself in distinctly different z-distributions of the displacement gradients in the transverse shear strains:

$$\gamma_{iz} = u_{i,z} + u_{z,i} \quad (i=x,y). \tag{3}$$

Note that $u_{i,z}$ are uniform across the thickness whereas $u_{z,i}$ vary parabolically. The direct implication of this type of field inconsistency is that conditions of shear-traction free plate faces cannot be satisfied and, moreover, an ad hoc specification of a shear correction factor is necessary to achieve agreement with Kirchhoff theory for the class of thin plate problems [6]. Naturally, the field-consistency implies identical z-distributions of these displacement gradients.

One way to ensure field-consistency is to adopt complete cubic z-distributions for u_x and u_y (as in [7]), instead of the linear expansions in (1). This, however, gives rise to yet a higher-order theory, possessing four more displacement variables. Alternatively, field-consistency can be effectively realized with the assumptions in (1), following the procedure developed in [1]:

(a) $u_{i,z}$ are replaced in (3) with the field-consistent 'substitute gradients', $u^*_{i,z}$, which have a parabolic z-distribution across the thickness:

$$u^*_{i,z} = \sum_{k=0}^{2} a_{ik}(x,y)\, P_k(\xi) \quad (i=x,y) \tag{4}$$

where the relationship between a_{ik} and plate displacement variables are determined via:

(a.1) shear traction-free boundary conditions at the top and bottom plate faces:

$$\tau_{iz}(\xi=\pm 1) = 0 \quad (i=x,y)$$

giving rise to

$$\gamma_{iz}(\xi=\pm 1) = \{u^*_{i,z} + u_{z,i}\}\big|_{\xi=\pm 1} = 0 \quad (i=x,y), \tag{5}$$

(a.2) equivalence of $u^*_{i,z}$ and $u_{i,z}$ in the mean:

$$\min \int_{-h}^{h} (u^*_{i,z} - u_{i,z})^2\, dz \quad (i=x,y). \tag{6}$$

Then, the field-consistent shear strains evolve as:

$$\gamma_{xz} = k^2(P_0 - P_2)(w,_x + \theta_y)$$
$$\gamma_{yz} = k^2(P_0 - P_2)(w,_y + \theta_x) \tag{7}$$

in which the factor $k^2=5/6$, resulting from the derivation, is coincident with Reissner's shear correction factor. The shear strains in (7) are same expressions as their counterparts for the homogeneous orthotropic plate [1].

Transverse Normal Field-Consistency. There still remains another field-inconsistency which is inherent in the third equilibrium equation:

$$\tau_{xz,x} + \tau_{yz,y} + \sigma_{zz,z} = 0 \quad \text{(ignoring the body force)} \tag{8}$$

Here, owing to the parabolic z-distribution of τ_{iz} $(i=x,y)$, σ_{zz} must be cubic in z; however, assumptions (1) can only yield σ_{zz} which is linear in z. To remedy this situation, the approach developed in [1] is undertaken:

(b) $u_{z,z}$ is replaced with the field-consistent 'substitute gradient', $u^*_{z,z}$, having a cubic z-distribution across the thickness:

$$u^*_{z,z} = \sum_{k=0}^{3} b_k(x,y)\, P_k(\xi) \tag{9}$$

and b_k is determined from the constraint equations:

(b.1) stress boundary condition on $\sigma_{z,z}$ for the top and bottom plate faces:

$$\frac{\partial}{\partial z}(\sigma_{zz})\Big|_{\xi=\pm1} = 0, \tag{10}$$

which results from (8), taking into account shear-traction free conditions at the top and bottom plate faces.

(b.2) equivalence of $u^*_{z,z}$ and $u_{z,z}$ in the mean:

$$\min \int_{-h}^{h} (u^*_{z,z} - u_{z,z})^2\, dz \tag{11}$$

In (10), the transverse normal stresses, $\sigma_{zz}^{(k)}$, for the top and bottom plies of the laminated plate (k=top and k=bottom), are determined from the 3-D anisotropic Hooke's law:

$$\sigma^{(k)} = C^{(k)} \varepsilon, \tag{12}$$

in which the stress vector $\sigma^{(k)}$, the strain vector ε, and the elastic modulus tensor $C^{(k)}$ are respectively expressed as

$$\begin{aligned} \sigma^{(k)T} &= \{\sigma_{xx}, \sigma_{yy}, \sigma_{zz}, \tau_{yz}, \tau_{xz}, \tau_{xy}\}^{(k)}, \\ \varepsilon^{T} &= \{\varepsilon_{xx}, \varepsilon_{yy}, \varepsilon_{zz}, \gamma_{yz}, \gamma_{xz}, \gamma_{xy}\}, \\ C^{(k)} &= [C_{ij}^{(k)}], \text{ in which } C_{i4}^{(k)} = C_{i5}^{(k)} = C_{46}^{(k)} = C_{56}^{(k)} = 0 \quad (i=1,2,3), \end{aligned} \tag{13}$$

where the elastic stiffness coefficients $C_{ij}^{(k)}$ are obtained using the usual strain-tensor transformation from the material directions to the laminate ones, starting out with the orthotropic properties for each ply and taking advantage of the strain energy density invariance. The resulting form of the transverse normal strain $\varepsilon_{zz} = u^*_{z,z}$ is:

$$\varepsilon_{zz} = u^*_{z,z} = \varepsilon_{z_0} + \sum_{j=1,2,3,6} \phi(\xi)_j \, \kappa_j \,, \tag{14}$$

where

$$\varepsilon_{z_0} = w_1/h,$$

$$(\kappa_1, \kappa_2, \kappa_3, \kappa_6) = (\theta_{y,x}, \theta_{x,y}, w_2/h, \theta_{x,x} + \theta_{y,y}),$$

$$\phi(\xi)_i = \frac{h}{6} \{P_2(\xi)\, r_i - [P_1(\xi)/14 + P_3(\xi)]\, k_3^2\, s_i\},$$

$$\phi(\xi)_3 = k_3^2\, [6P_1(\xi) - P_3(\xi)], \quad k_3^2 = 42/85,$$

$$r_i = (C_{3i}/C_{33})^{\text{bottom}} - (C_{3i}/C_{33})^{\text{top}},$$

$$s_i = (C_{3i}/C_{33})^{\text{bottom}} + (C_{3i}/C_{33})^{\text{top}} \quad (i=1,2,6).$$

For the case of a homogeneous orthotropic material, (14) takes the form derived in [1].

Governing Equations. The remainder of the derivation of the laminated theory follows the variational formulation of [1], where the equations of equilibrium together with natural boundary conditions are obtained from the principle of virtual work, which includes all strain and stress components:

$$\iiint_V (\sigma_{xx}\delta\varepsilon_{xx} + \sigma_{yy}\delta\varepsilon_{yy} + \sigma_{zz}\delta\varepsilon_{zz} + \tau_{xy}\delta\gamma_{xy} + \tau_{xz}\delta\gamma_{xz} + \tau_{yz}\delta\gamma_{yz}) \, dxdydz$$

$$- \iint_{S^+} q^+ \delta u_z dxdy - \iint_{S^-} q^- \delta u_z dxdy - \iint_{S_\sigma} (\bar{T}_x \delta u_x + \bar{T}_y \delta u_y + \bar{T}_z \delta u_z)\, dsdz = 0 \tag{15}$$

where q^+ and q^- are the prescribed transverse normal tractions at the top (S^+) and bottom (S^-) plate faces, respectively, and $\bar{T}_i$ (i=x,y,z) denote the prescribed tractions on the part of the edge boundary S_σ. Integrating (15) across the plate thickness yields the statement of virtual work for the plate:

$$\iint_{S_m} \Big\{ N_x \delta u,_x + N_y \delta v,_y + N_z \delta(w_1/h) + N_{xy}(\delta u,_y + \delta v,_x)$$

$$+ M_x \delta\theta_{y,x} + M_y \delta\theta_{x,y} + M_z \delta(w_2/h) + M_{xy}(\delta\theta_{x,x} + \delta\theta_{y,y})$$

$$+ Q_x(\delta w,_x + \delta\theta_y) + Q_y(\delta w,_y + \delta\theta_x) - q_1(\delta w + \delta w_2/k^2) - q_2 \delta w_1 \Big\} dxdy$$

$$- \oint_{C_\sigma} \Big\{ \bar{N}_{xn} \delta u + \bar{N}_{yn} \delta v + \bar{M}_{xn} \delta\theta_y + \bar{M}_{yn} \delta\theta_x + \bar{Q}_{zn} \delta w$$

$$+ \bar{Q}_{z_1} \delta w_1 + \bar{Q}_{z_2} \delta w_2 \Big\} ds = 0 \tag{16a}$$

Integrating by parts results in:

$$\iint_{S_m} \Big\{ -[N_{x,x} + N_{xy,y}]\, \delta u - [N_{y,y} + N_{xy,x}]\, \delta v$$

$$+ [- M_{x,x} - M_{xy,y} + Q_x]\, \delta\theta_y + [- M_{y,y} - M_{xy,x} + Q_y]\, \delta\theta_x$$

$$- [Q_{x,x} + Q_{y,y} + q_1]\, \delta w + [N_z/h - q_2]\, \delta w_1$$

$$+ [M_z/h - q_1/k^2]\, \delta w_2 \Big\} dxdy$$

$$+ \oint_{C_\sigma} \Big\{ (N_{xn} - \bar{N}_{xn})\, \delta u + (N_{yn} - \bar{N}_{yn})\, \delta v + (M_{xn} - \bar{M}_{xn})\, \delta\theta_y + (M_{yn} - \bar{M}_{yn})\, \delta\theta_x$$

$$+ (Q_{zn} - \bar{Q}_{zn})\, \delta w + \bar{Q}_{z_1} \delta w_1 + \bar{Q}_{z_2} \delta w_2 \Big\} ds$$

$$+ \oint_{C_u} \Big\{ N_{xn} \delta u + N_{yn} \delta v + M_{xn} \delta\theta_y + M_{yn} \delta\theta_x + Q_{zn} \delta w \Big\} ds = 0 \tag{16b}$$

where C_σ and C_u are parts of the boundary surrounding the middle surface S_m where the tractions and displacements are prescribed, respectively, and n is an outward normal to the boundary of S_m. The stress resultants are defined as:

$$q_1 = q^+ - q^-, \quad q_2 = q^+ + q^-,$$

$$(N_x, N_y, N_z, N_{xy}) = \sum_{k=1}^{N} \int_{h_{k-1}}^{h_k} (\sigma_{xx}, \sigma_{yy}, \sigma_{zz}, \sigma_{xy})\, dz,$$

$$(M_x, M_y, M_z, M_{xy}) = \sum_{k=1}^{N} \int_{h_{k-1}}^{h_k} [(z\sigma_{xx} + \phi_1\sigma_{zz}), (z\sigma_{yy} + \phi_2\sigma_{zz}),$$

$$(\phi_3\sigma_{zz}), (z\tau_{xy} + \phi_6\sigma_{zz})]\, dz,$$

$$(Q_x, Q_y) = \sum_{k=1}^{N} \int_{h_{k-1}}^{h_k} k^2(P_0 - P_2)(\tau_{xz}, \tau_{yz})\, dz,$$

$$(\bar{N}_{xn}, \bar{N}_{yn}) = \sum_{k=1}^{N} \int_{h_{k-1}}^{h_k} (\bar{T}_x, \bar{T}_y)\, dz, \tag{17}$$

$$(\bar{M}_{xn}, \bar{M}_{yn}) = \sum_{k=1}^{N} \int_{h_{k-1}}^{h_k} (\bar{T}_x, \bar{T}_y)\, z\, dz,$$

$$(\bar{Q}_{zn}, \bar{Q}_{z_1}, \bar{Q}_{z_2}) = \sum_{k=1}^{N} \int_{h_{k-1}}^{h_k} \bar{T}_z(1, P_1, P_0/5 + P_2)\, dz,$$

$$N_{xn} = N_x\ell + N_{xy}m, \quad N_{yn} = N_{xy}\ell + N_y m,$$

$$M_{xn} = M_x\ell + M_{xy}m, \quad M_{yn} = M_{xy}\ell + M_y m, \quad Q_{zn} = Q_x\ell + Q_y m,$$

$$\ell = \cos(x,n), \quad m = \cos(y,n),$$

where N denotes the total number of plies in the composite laminate.

Thus, the principle of virtual work provides seven equations of equilibrium:

$$
\begin{aligned}
&(\delta u): && N_{x},_{x} + N_{xy},_{y} && = 0 \\
&(\delta v): && N_{xy},_{x} + N_{y},_{y} && = 0 \\
&(\delta\theta_{y}): && M_{x},_{x} + M_{xy},_{y} - Q_{x} && = 0 \\
&(\delta\theta_{x}): && M_{xy},_{x} + M_{y},_{y} - Q_{y} && = 0 \qquad (18)\\
&(\delta w): && Q_{x},_{x} + Q_{y},_{y} + q_{1} && = 0 \\
&(\delta w_{1}) && -N_{z}/h + q_{2} && = 0 \\
&(\delta w_{2}): && -M_{z}/h + q_{1}/k^{2} && = 0
\end{aligned}
$$

five Poisson-type (physically desirable) stress boundary conditions on C_{σ}:

$$N_{xn} = \bar{N}_{xn}, \quad N_{yn} = \bar{N}_{yn}, \quad M_{xn} = \bar{M}_{xn}, \quad M_{yn} = \bar{M}_{yn}, \quad Q_{zn} = \bar{Q}_{zn}, \qquad (19)$$

two vanishing conditions on the higher-order shear resultants:

$$\bar{Q}_{z_1} = \bar{Q}_{z_2} = 0 \qquad (20)$$

and five displacement boundary conditions on C_{u}:

$$u = \bar{u}, \quad v = \bar{v}, \quad \theta_{y} = \bar{\theta}_{y}, \quad \theta_{x} = \bar{\theta}_{x}, \quad w = \bar{w}. \qquad (21)$$

where the superior bar denotes prescribed quantities. Note that (20) signifies, as for the homogeneous plate [1], a parabolic through-thickness distribution for the prescribed shear traction, i.e.,

$$\bar{T}_{z} = (P_{0} - P_{2})\, \bar{T}_{z_0}(s). \qquad (22)$$

Further steps in the theory development involve: (i) Obtaining the plate constitutive equations by introducing Hooke's law (12) into the stress resultants (17), and performing the requisite through-thickness integrations; (ii) Expressing the equilibrium equations (18) in terms of displacement variables by invoking the plate constitutive relations from (i) into (18). The resulting equilibrium equations in terms of the plate displacement variables can be written in operational form as:

$$\mathbf{Q}\,\mathbf{L}_{2}\mathbf{u} = \mathbf{L}_{1}\mathbf{q}, \qquad (23)$$

$$\mathbf{w} = \mathbf{R}\,\mathbf{M}_{1}\mathbf{u} + \mathbf{S}\,\mathbf{q}, \qquad (24)$$

where **Q**, **R**, and **S** are matrices containing various plate stiffness coefficients; $\mathbf{L}_1$ and $\mathbf{M}_1$ are first order linear differential operators; and $\mathbf{L}_2$ is a second order linear differential operator, with

$$\mathbf{q}^T = \{q_1, q_2\}, \tag{25}$$

$$\mathbf{u}^T = \{u, v, w, \theta_x, \theta_y\}, \tag{26}$$

$$\mathbf{w}^T = \{w_1, w_2\}. \tag{27}$$

Equations (23) contain five coupled second-order partial differential equations of equilibrium in terms of five weighted average displacements (26); equations (24) are zero order in terms of **w** (27).

The solution procedure for a plate boundary-value problem is then as follows: (i) solve (23) for **u** subject to boundary conditions (19)-(21); (ii) solve (24) for **w** with the use of the solution from (i). Once the displacement variables (26)-(27) are determined, computations for stress resultants and stresses are performed using the plate constitutive equations and Hooke's law.

Assessment of Theory. A qualitative evaluation of the laminate plate theory will be carried out for the problem of an infinite plate in equilibrium loaded at the top surface by a sinusoidal pressure of the form:

$$q^+ = q_0 \sin(\pi x/L) \quad \text{on } S^+ \qquad (q^- = 0 \text{ on } S^-)$$

where L is a half wavelength of the loading pattern. The exact solutions obtained with the present theory will be compared with the available exact elasticity [10] and a 22nd order theory [7] solutions.

Aspects of Finite Element Approximation. A particularly attractive feature of this higher-order theory is its ideal applicability within the framework of displacement finite element approximations. In fact, the simplicity and efficiency of such elements will be virtually identical to comparable elements derived from Mindlin theory [4]; however, the elements derived from the present theory will be more accurate and have a wider range of applicability.

To highlight the pertinent aspects of finite element approximations based on the present theory, consider first the virtual work statement for plates (16a). It is evident that, as in Reissner [2-3] and Mindlin [4] theories, the weighted average kinematic variables in (2) need only be C^0-continuous[2] since their highest spatial derivatives in (16a) are of order one. Further, the two higher-order displacements, w_1 and w_2, do not possess spatial derivatives in (16a); hence, they need only be C^{-1}-continuous (i.e., interelement discontinuous). This latter aspect has significant implications as far as deriving finite elements whose simplicity and

---

[2] C^0-continuous functions are continuous at element boundaries, however, their derivatives are discontinuous at those boundaries.

efficiency are nearly identical to elements based on refined theories [8,9]. For instance, by taking w_1 and w_2 to be uniform across the element domain (i.e., C^{-1} continuous) will only produce two degrees of freedom (dof) in excess of the weighted average variable dof. These w_1 and w_2 dof can then be condensed out statically at the element level ((24) may be regarded as an analytic analogue of this procedure), giving rise to the element stiffness equations involving only the weighted average variable dof (the same as in the case of refined plate elements). Thus, the implication of such an approximation strategy is clear; at the same cost of a refined (low order) theory finite element solution we will obtain more accurate results afforded by this higher-order displacement theory. Efforts are currently underway to implement these ideas in conjunction with some previously explored refined-element methods [8].

REFERENCES

1. Tessler, A., "Higher-Order Displacement Theory for Orthotropic Plates," Journal of Applied Mechanics (in review).

2. Reissner, E., "On the Theory of Bending of Elastic Plates," Journal of Mathematics and Physics, 23, 1944, pp. 184-191.

3. Reissner, E., "On a variational theorem in elasticity," Journal of Mathematics and Physics, v. 28-29, 1950, pp. 90-95.

4. Mindlin, R. D., "Influence of Rotatory Inertia and Shear on Flexural Motions of Isotropic, Elastic Plates," Journal of Applied Mechanics, 18, 1951, pp. 31-38.

5. Hildebrand, F. B., Reissner, E. and Thomas, G. B., "Notes on the foundations of the theory of small displacements of orthotropic shells," NACA T.N. no.1833, 1949.

6. Whitney, J. M. and Sun, C. T., "A Refined Theory for Laminated Anisotropic, Cylindrical Shells," Journal of Applied Mechanics, 41, 1974, pp. 471-476.

7. Lo, K. H., Christensen, R. M., and Wu, E, M., "A Higher-Order Theory of Plate Deformation, Part 1: Homogeneous Plates and Part 2: Laminated Plates, Journal of Applied Mechanics, 44, 1977, pp. 663-676.

8. Tessler, A., "Shear-deformable bending elements with penalty relaxation," in Finite Element Methods for Plate and Shell Structures, Vol. 1: Element Technology, (eds. T.J.R. Hughes and E. Hinton), Pineridge Press, Swansea, U.K., 1986, pp. 266-290.

9. Hughes, T.J.R., The Finite Element Method: Linear Static and Dynamic Finite Element Analysis, Chapter 5, Prentice-Hall, Englewood Cliffs, NJ, 1987.

10. Pagano, N.J., "Influence of Shear Coupling in Cylindrical Bending of Anisotropic Laminates," Journal Comp. Mats., 4, 1970, pp.330-343.

STUDY ON ELASTIC COMPLIANCE AND LIMITING LOAD OF A 3-D LAYERED CONTACT WITH SOFT SUBSTRATE

by Y. P. Chiu
Torrington Company, Torrington, CT 06790

INTRODUCTION

The application of hard coating on soft substrate can result in higher wear resistance , load capacity and changes in contact compliance. It is of interest to know under what conditions the variation in coating thickness can have strong effect on the stress and deflection of the layered contact system. Although stress analyses of layered solid in contact have been recently published using finite element technique (e.g. Komvopolous,et.al. 1985), the solutions are limited to two dimensional cases only. For 3-D contact problem, the computation time to conduct parametric analysis may be inhibitive. An alternative approach is to use a numerical solution, developed by Chiu et.al.(1983). The solution is applicable to a layered half space indented by an elastic indenter of any surface profile without friction (see Chiu,1986). The method does not require the discretization of the solids into finite elements, but only the loaded surface area into rectangular cells. The contact pressure is solved from a system of simultaneous linear equations using the Gauss-Siedel method (see Hartnett, 1980). The coefficients in the equations are the influences coefficients calculated based on analytical solution for a layered half space under a single rectangular surface load . By applying this method to layered contact with second order surface, the extension of Hertz theory to layered half space has been achieved (Fig.1).

Based on the modified Boussinesq solution for a layered half space (Burmister,1945 and Muki et. al. 1981), the governing equation of the contact of a layered half space and a half space with a gap described by g(x,y) between the undeformed surfaces and under a known load Q is given by

$$\frac{(1-v^2)}{\pi E}\iint_A p(x',y')\bar{w}(r')dx'dy' + \frac{(1-v''^2)}{\pi E''}\iint_A p(x',y')/r'dx'dy' = D-g(x,y)$$

and

$$\iint_A p(x',y')dx'dy' = Q \quad \text{, the load.}$$

with

$$\bar{w} = \int_0^\infty F(sh)J_0(sr')ds \qquad F(t) = \frac{1-4kt\exp(-2t)-kt\exp(-4t)}{1-(\lambda+k+4kt^2)\cdot\exp(-2t)+k\lambda\exp(-4t)}$$

$$\beta = \frac{E/(1-v^2)}{E''/(1-v''^2)} \qquad k = \frac{\omega-1}{\omega+3-4v} \qquad \lambda = \frac{(3-4v')\omega-3+4v}{(3-4v')\omega+1} \qquad \omega = \frac{E(1+v')}{E'(1+v)}$$

and $$r' = \{(x-x')^2+(y-y')^2\}^{\frac{1}{2}}$$

$$g(x,y) = x^2/2R_x + y^2/2R_y, \text{ for second order surfaces.}$$

where p is the pressure, D the approach, h the layer thickness, Rx,Ry the principal radius of curvature, E,v the Young's modulus and Poisson ratio of the layer, E',v' are for the substrate and E",v" are for the indenter (see Fig.1).

Examination of the basic governing equation for this contact problem reveals that the following non-dimensional parameters are involved in addition to the Poisson ratios v,v'.

$$Rx/Ry\ ,\ \omega\ ,\ \beta\ ,\ \bar{p} = pRy/(Eh)\ ,\ \bar{Q} = QRy/Eh^3 \text{ and } \bar{D} = DRy/h^2$$

where $\bar{p}$, $\bar{Q}$ and $\bar{D}$ are respectively the dimensionless pressure, load and deflection. Parametric study has been conducted with many computer runs for Rx/Ry=1,37,800 and several combinations of material parameters shown below;

Table 1

Code	E"/E	E'/E	v,v"	v'	β	ω
AL	1.0	.344	.29	.34	1.0	.331
MG	1.0	.217	.29	.35	1.0	.207
PL	1.0	.100	.29	.29	1.0	.100

Note that for the special case that the layer is of steel material, the codes AL,MG,PL are for substrate material of aluminum, magnesium and plastics respectively.

FINDINGS

A typical variation of the dimensionless approach $\bar{D}$ with the dimensionless load $\bar{Q}$ for different material types for Rx/Ry=37 is shown in Fig.2.

The results show that the degree of deviation from the Hertz solution with infinite layer thickness is controlled by either dimensionless Q or D . Note that Q is proportional to the cubic of the semi- Hertz contact width b* (assuming h approaches infinity) , the dimensionless $\bar{Q}$ varies with (b*/h) . Figs.3 and 4 plot the variations of the dimensionsionless ratio D/D* (for approach) and pm/pm* (for maximum pressure) with the ratio b*/h where D* and pm* are the approach and maximum contact pressure respectively for the limiting case h=∞.

It is shown that the pressure distribution in the layered contact can be considered as Hertzian without taking into account the substrate , if b*/h<0.8 for circular contact and b*/h<0.10 for Rx/Ry>37. Also, the layer can be considered to to be absent if b*/h>6 for circular contact and >4 for Rx/Ry>37. For the maximum approaches, it is found that the substrate material can be neglected if b*/h<0.05 for Rx/Ry=1 and b*/h<0.01 for Rx/Ry>37. The layer material may be neglected if b*/h>7 for Rx/Ry=1 and b*/h>4 for Rx/Ry>37.

An approximate formula can be obtained as follows for the deflection D of the layered contact in terms of the ratio b*/h , the Hertzian deflections D* (for h=∞) and D** (for h=0);

$$D = (D^*)^{\alpha}(D^{**})^{1-\alpha} \quad \text{with} \quad \alpha = \exp(-f)$$

where f can be obtained from the calculated values of D and its limiting Hertzian deflections D* (for $h=\infty$) and D** (for h=0). Fig.5 plots the value of f calculated from the above equation versus b*/h for two values of Rx/Ry and differnet material combinations. The plot shows that f increases monotonically with b*/h and Rx/Ry. It is also shown that f is a weak function of materials.

LIMITING LOADS

Based on the stresses in the substrate formulated for a rectangular surface load (Chiu, 1983), the stresses in the substrate under the previously determined contact pressure on layer surface are calculated using method of superposition. In all the cases calculated, the maximum effective stress in the substrate under the contact loads is found to lie on the layer-substrate interface.

The limiting load is defined as the load corrsponding to the initial yield in the substrate. First the dimensionless maximum effective stress has been obtained in term of the dimensionless load Q. Calculation has been made for the ratio of the limiting load for a layered solid to that without the layer. This ratio may be considered as a measure of effectiveness of hard coating in achieving higher load carrying capacity.

DISCUSSION

Most of the engineering surfaces are not perfectly smooth. The load is the sum of the loads carried by the asperities of certain height distribution. The stress field is the sum of the stresses caused by each asperity penetration. The result of compliance in this paper may be applicable to analyze the microcontacts of asperity on layered solid and the onset of plastic yielding of rough surfaces in contact, if the interaction among the asperities can be neglected.

Under high contact load, plastic flow can occur in the soft substrate, which may alter the compliance of the contact and produces residual stresses in the substrate as well as the layer. The onset of the plasic flow in the substrate can be influenced by the friction force on the surface. The knowledge of the contact compliance in the plastic regime is needed to determine the state of asperity contacts of rough surfaces.

REFERENCES

Burmister, D.M., J. App. Physics, Vol.16, 1945, pp.89-94.

Chiu,Y.P. and Hartnett,M., 1983,Trans.ASME, J.Lubr. Tech.,105, pp.585-590.

Chiu,Y. P. 1986, Trans.SAE,Paper No.861217.

Hartnett,M.J., 1980, ASME AMD-Vol.39, Solid Contact and Lubrication, edited by Cheng and Keer, p.51

Komvopolous,K.,Saka,N. and Suh.N., 1985, ASME J. Tribology,109, p.223-231.

Muki, R. and Dong, S., ASME J. App. Mechanics, Vol.47, 1980, pp. 504-512.

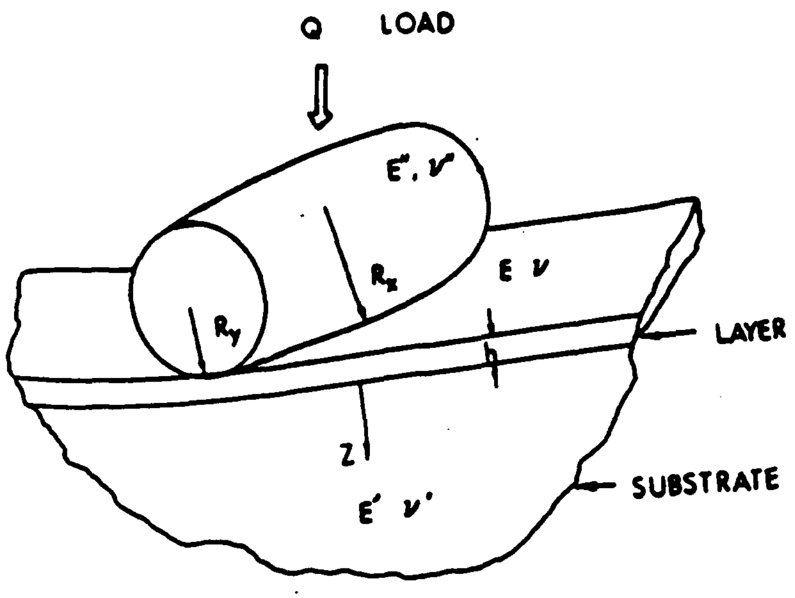

Fig.1 The layered solid contact of second-order surfaces with principal radii of curvatures Rx and Ry. The lower solid is a layered half space of uniform layer thickness h.

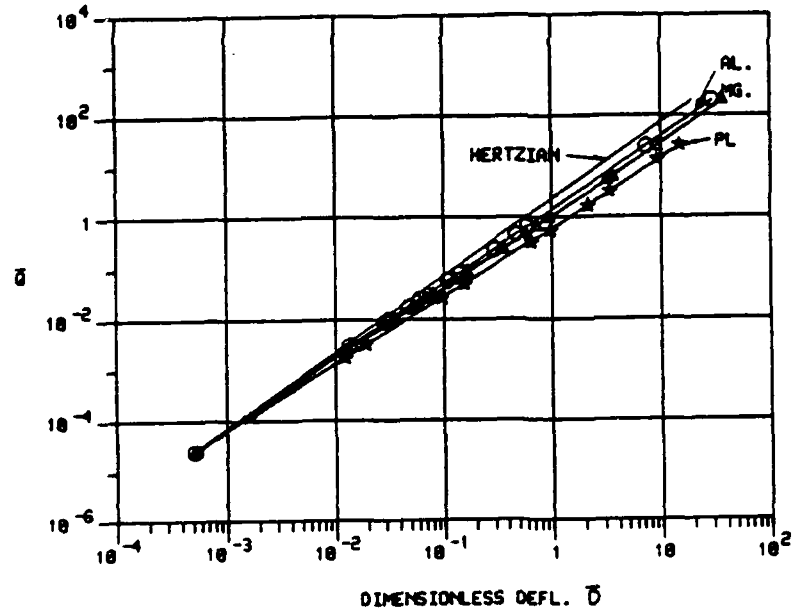

Fig.2 The variation of dimensionless approach $\bar{D} = DR_y/h^2$ with the dimensionless load $\bar{Q} = QR_y/Eh^3$ for three different layer/substrate combinations.

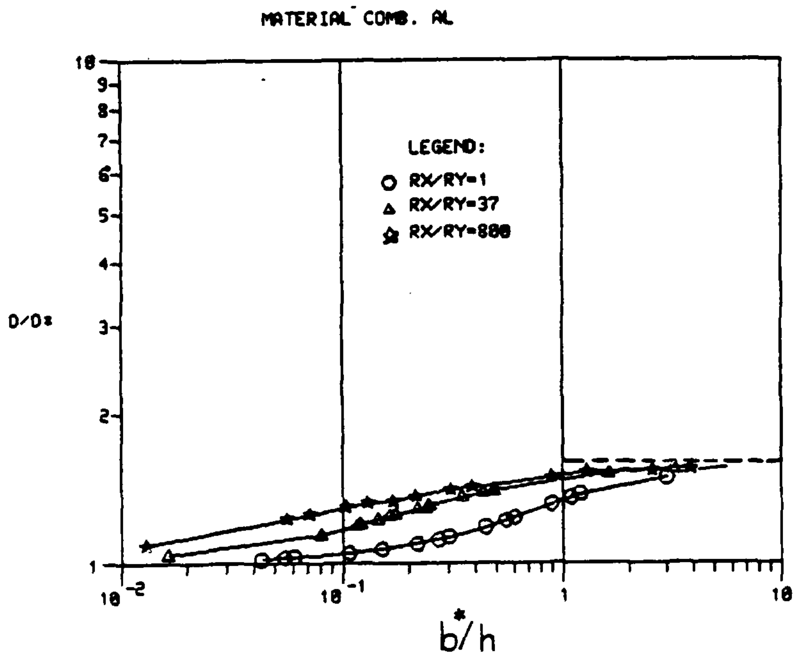

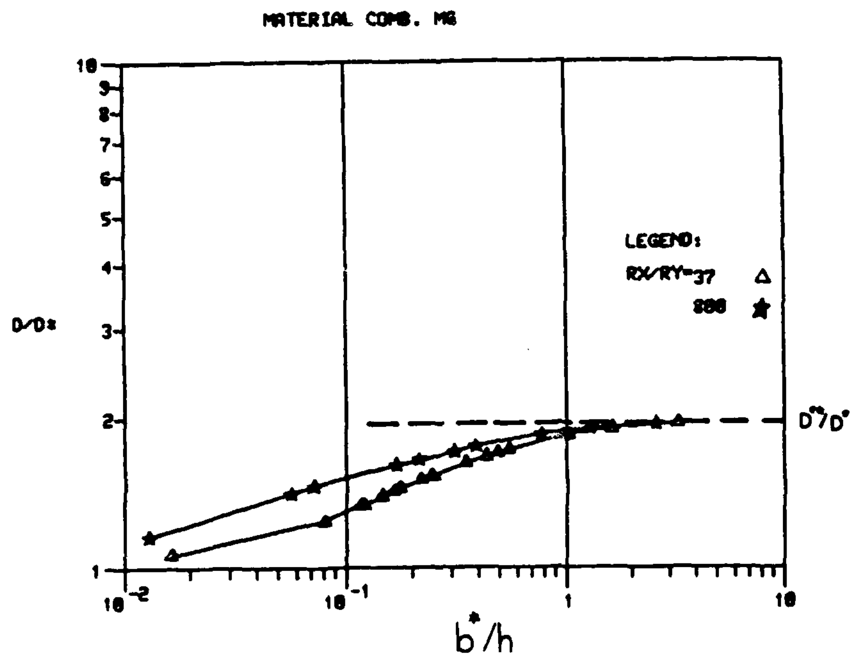

Fig.3 The relative approach (D/D*) as a functions of the ratio b*/h for material combinations AL (in Fig.3a) and MG (in Fig.3b)

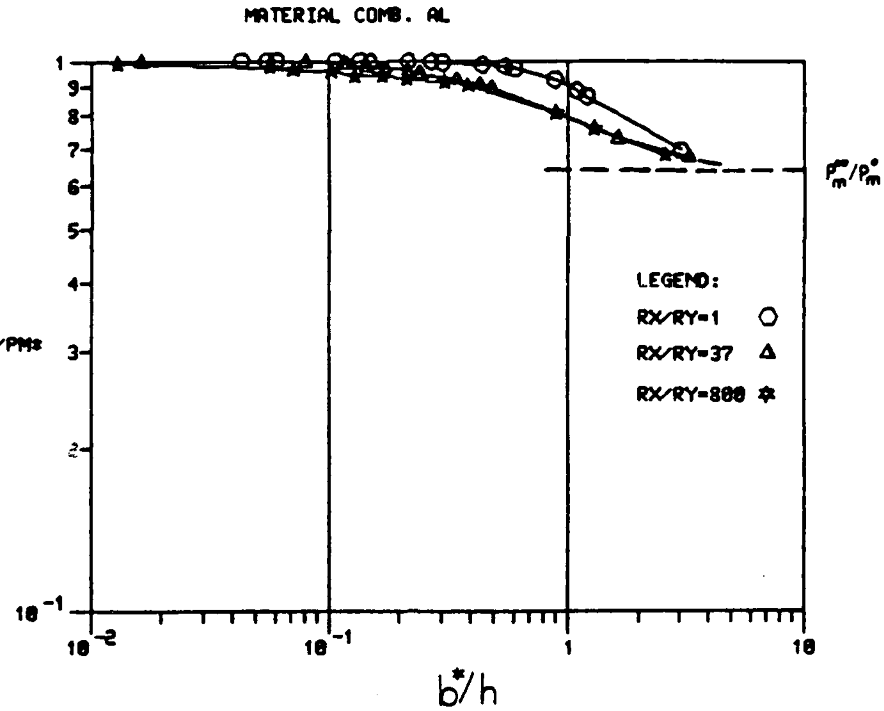

Fig.4 The relative maximum pressure (pm/pm*) as a function of the ratio b*/h for material combination AL

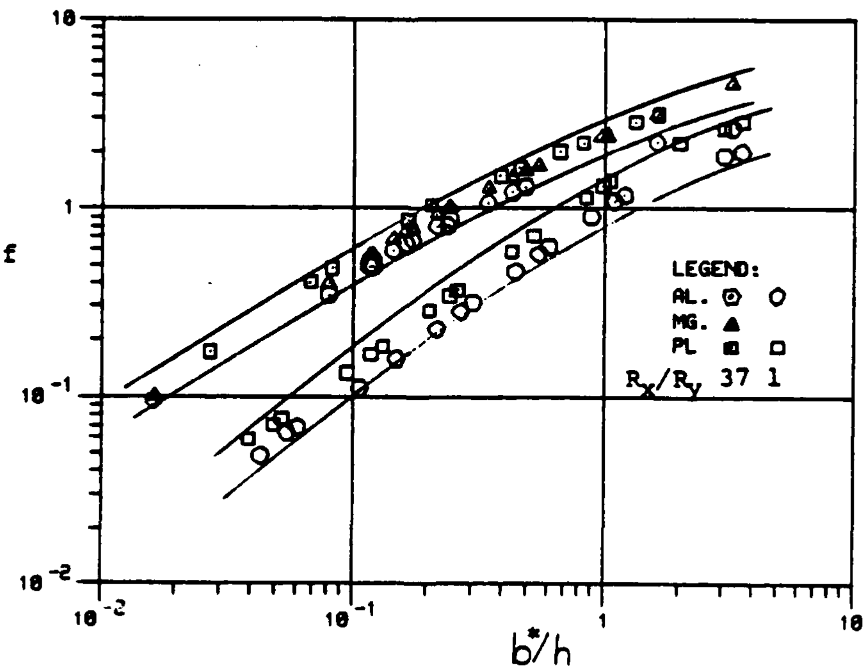

Fig.5 Values of function f as a function of b*/h for two values of Rx/Ry and different material combinations.

COMPRESSION-INDUCED VOID COLLAPSE AND TENSILE CRACKING
IN DUCTILE SINGLE AND POLYCRYSTALS

by

S. Nemat-Nasser and S.-N. Chang

University of California, San Diego
La Jolla, California 92093

ABSTRACT

Recently Nemat-Nasser and Hori (1987) have presented an analytic study of dynamic void collapse and void growth in single crystals which deform plastically by slip on crystallographic slip systems, accompanied by elastic lattice distortion. The study includes the effects of the loading rate, the initial void geometry, and the stress state on void collapse (in compression) and void growth (in tension). In addition, it was suggested that a crack which has been formed under a compressive pulse, by void collapse, may grow in its own plane, normal to the direction of compression, during unloading. The analysis shows that the extent of crack growth depends on the initial void size, the rate of loading, and the fracture toughness of the material. The tendency for crack growth increases with an increasing loading rate and initial void size. In addition, the resistance to void collapse into a crack increases with an increasing loading rate.

In this paper we report the results of a series of experiments performed on single and poly-crystal copper specimens, as well as mild steel (AISI 1018 steel) and pure iron, containing pre-existing cavities. The experiments are done in compression at various strain rates. It is found that void collapse, even in single crystal copper, occurring under purely compressive axial loading, can and does lead to tensile cracking in the general direction normal to the applied compression. The crack growth process appears to be very fast, involving extensive crack branching whose intensity and extent increase as the applied compressive strain rate is increased until the recrystallization occurs at the crack tip. The cracking directions of many branches coincide with appropriate crystallographic planes of maximum atomic density, but at the same time, cracks do also grow essentially normal to the direction of the compression. These and related results are discussed in light of the theoretical observations.

REFERENCE

S. Nemat-Nasser and M. Hori (1987), "Void Collapse and Void Growth in Crystalline Solids", J. Appl. Phys. 62, No. 7, 2746-2757.

ACKNOWLEDGEMENT

This work has been supported by the U.S. Army Research Office under Contract No. DAAL-03-86-K-0169 to the University of California, San Diego.

DYNAMIC TESTING OF LIGHTWEIGHT CERMETS

W.R. BLUMENTHAL

Materials Science and Technology Division, Los Alamos National Laboratory, Los Alamos, New Mexico 87545.

Dynamic and quasi-static compression testing was conducted on a series of boron carbide - aluminum (B_4C-Al) cermets fabricated under the direction of Professor Ilhan A. Aksay of the University of Washington. The material is fabricated by dispersing B_4C powder into an aqueous slurry and slip casting 50%-60% dense green bodies. Partial sintering is performed at 2150 C in a helium/argon atmosphere to produce a 65% to 80% dense skeletal structure. This stage removes much of the internal oxygen and oxide surface layers on the B_4C particles making them less reactive during subsequent metal infiltration. Metal infiltration is the final processing step. Liquid aluminum forms a low contact angle with B_4C substrates above about 1200 C. In order to achieve wetting of the B_4C and minimize the formation of deleterious reaction phases, aluminum is vacuum-infiltrated into the B_4C skeletal structure at 1175 C. The resulting microstructure consists of two finely interconnected phases with less than 2% porosity in 1 cm of thickness.

A partial matrix of microstructural variables has been investigated which include: phase volume fraction, phase size, and metal phase composition. Nominal B_4C volume fractions of 65% and 80% were studied. One 65% B_4C composition used a low cost, abrasive-grade B_4C starting powder with an average particle size of 5 microns. The remaining compositions used high purity sintering grade B_4C powder with a particle size of 1 micron. One 65% B_4C cermet was infiltrated with 7075 aluminum alloy to determine the effects of metal phase strengthening. All remaining compositions were infiltrated with pure aluminium.

These materials are novel due to their low specific gravity, high fracture toughness, high flexure strength, and their broad range of fabricability. The specific gravity of these cermets is between 2.54 and 2.58 g/cc which is only 1%-2% greater than pure B_4C. Fracture toughness values of up to 9.9 $MPa \cdot m^{1/2}$ have been measured compared to a typical value of 4 $MPa \cdot m^{1/2}$ for pure B_4C. Finally, average flexure strengths of up to 670 MPa have been measured compared to a typical B_4C value of 350 MPa.

Dynamic compression testing was performed with a Hopkinson split pressure bar (HSPB) using a small version of the dumb-bell-shaped specimen recently advanced by the Army Materials Technology Laboratory. Quasi-static compression was performed using the same specimen geometry with a constant load rate testing machine. Quasi-static testing with a right circular cylinder geometry (L/D = 1.27) produced failure at less than half the stress and strain achieved with the dumb-bell-shaped specimen.

Under quasi-static loading conditions most ceramics respond elastically and subsequently fail at a critical stress intensity factor with little or no macroscopic yielding. Hence, the mechanical response is not controlled, as it is in most metals, by the deformation behavior generated by dislocations, twins, or point defects, but by the propagation of one or a small number of "critical" microstructural flaws. Inferring that fracture is a serious limitation to the impact performance of pure ceramics, then the development of high fracture toughness cermets which retain much of the strength benefits of the parent ceramics is of considerable interest.

Uniaxial compression testing was performed on the four cermet compositions at nominal strain rates of 10^{-3} and 10^3 1/s. Dynamic loading was provided by a 12.7 mm diameter Hopkinson split pressure bar. Tungsten carbide load rams were used between the bar and the specimen for the 80% B_4C-Al material due to its high strength. Specimen stress was determined from the transmitted bar strain gages for dynamic loading and from a load cell during quasi-static loading. Specimen strain was determined directly by two or three independent strain gages attached to opposing sides of the specimen gage section. The incident pressure bar strain gage record measures the incident and reflected stress waves and also provides a measure of the specimen strain and strain rate. However, this record can only be used after calibration with the specimen strain gages since the specimen geometry is relatively complex . Calibration tests were performed by striking the bar so that specimen simply loads and unloads elastically without failure. Under these conditions the peak strain calculated from integrating the reflected wave is set equal to the maximum strain measured directly on the specimen gage section and an effective specimen length is calculated. Strain and strain rate calculated from the incident pressure bar can then be used as a verification of the specimen strain gage record.

The 65% B_4C compositions displayed varying strain rate sensitivity and yielding prior to failure. The strengths of these materials were all close to 2000 MPa; However, the composition with a fine (1 micron) B_4C grain size infiltrated with pure Al showed a 24% increase in strength at the higher strain rate. None of the other 65% B_4C compositions displayed a strain rate sensitivity outside the 5% standard deviation of the strength measurements. The low-cost large B_4C grain size composition yielded at about 1% total strain which is well before the 1.2% to 1.3% yield of the other materials. There did not appear to be any rate dependence on the yield stress. The large B_4C grain size material also failed sooner at a total strain of about 1.2% quasi-statically and 1.6% dynamically. The remaining 65% compositions all failed at about 1.6% total strain quasi-statically and between 2% to 2.5% strain dynamically.

The 80% B_4C-Al cermet was approximately twice as strong and stiff as the 65% B_4C compositions. Quasi-statically, very little yielding was observed before failure at a total strain of 1.35% and a stress of 4100 MPa. Dynamically, failure occurs at a total strain of about 2% and a stress of 4600 MPa ($\pm$ 500 MPa).

Fractography was performed on selected Hopkinson bar failure specimens to characterize the origin of failure and the mode of crack propagation through the interconnected phases. One to three fracture surfaces developed in the center of the gage sections with orientations between 24 to 63 degrees from the load axis. Fracture orientations of 45 degrees predominated indicating failure on planes of maximum shear stress. SEM micrographs show broad sliding damage on several planes which suggests multiple sources of failure initiation. These surfaces also show the development and arrest of numerous microcracks intersecting the fracture surface. A single critical flaw responsible for failure was not observed.

Dynamic Behavior of Ceramic Composites:
Experiments and Observations

G. Ravichandran
Center of Excellence for Advanced Materials
Department of Applied Mechanics and
Engineering Sciences, R-011
University of California, San Diego
La Jolla, California 92093

ABSTRACT

Ceramic composites such as cermets are finding increasing applications, and there is a need to design them for resistance against impact loading. Ceramic composites are hard and brittle, and hence their failure occurs at small strains. An understanding of damage initiation and evolution, under dynamic loading conditions, is important in the analysis of such brittle materials. A coordinated experimental program to study and characterize the mechanical response, fracture, and failure modes of ceramics, cermets, and related composites under high loading rates, and to relate the overall material properties to the microstructure, and hence, to the associated processing techniques is described. The experimental research is being carried out at the University of California, San Diego's Center of Excellence for Advanced Materials, as a part of the Center's research on Dynamic Performance of Materials. Some preliminary results from this program on a boron carbide-aluminum cermet [1] and recent developments in understanding the failure modes and compressive failure mechanisms in ceramic composites will be presented.

The main objective of this research is the systematic characterization of the mechanical behavior of ceramic composites under high strain rate loading conditions and the effect of processing and microstructure on mechanical properties. The objectives of the tests are (a) to identify the effects of processing on the dynamic failure modes, (b) to identify the role of grain size, initial defects such as porosity, and secondary phases in microcrack initiation and growth, (c) to develop standard reliable high strain rate testing techniques for ceramic composites, and (d) to explore the role of processing techniques in improving the toughness of the materials.

A new experimental technique [2] for high strain rate testing of ceramic composites, using the split Hopkinson bar, is described. The conventional split Hopkinson bar is modified for application to testing very hard materials (see Fig. 1). This new technique involves two essential changes to the conventional compression Hopkinson bar: (a) a thin copper plate is glued to the impact end of the incident bar and (b) the strain is measured directly by attaching strain gauges to the sample. The presence of the copper plate introduces a ramp-like stress pulse (see Fig. 2) in the incident bar. While this limits the strain rates at which the test can be performed, it does preclude the sudden straining of the sample, as in the conventional split Hopkinson bar. The stress in the sample is measured from the transmitted pulse. Thus, reliable stress-strain curves for hard ceramic based materials can be obtained at moderately high strain rates of about 100-300 s^{-1}. This technique is used to study the mechanical response and failure modes of a boron carbide-aluminum cermet. The effects of processing and heat treatment on the dynamic response of this cermet are examined. Fig. 3 shows the stress-strain curve for the heat treated boron carbide-aluminum cermet which has disintegrated at failure. Microscopic observations of fractured materials reveal failure modes corresponding to high strain rate behavior of these ceramic composites.

To understand the mechanisms of microcracking for the boron carbide-aluminum cermet, a normal plate impact recovery technique [3] is used. The experiment is schematically shown in Fig. 4. A thin flyer plate impacts the specimen at a known velocity. The momentum trap and the flyer have nearly the same acoustic impedance as the material under investigation and remain elastic during the entire experiment. Upon impact, compressive waves travel through the specimen and the flyer plate. The compressive pulse that propagates through the specimen, also propagates through the momentum trap and reflects from the rear free surface as a tensile pulse. When this pulse reaches the interface between the specimen and the momentum trap, the interface fails, causing the momentum trap to separate. The thickness of the momentum trap is chosen such that the entire pulse is trapped. Thus, the specimen can be recovered having been subjected to single compressive pulse of known duration and amplitude. During the experiment, the rear surface motion of the momentum trap is monitored using a laser interferometer. By limiting the pulse duration (less than a μs), the available energy is limited and therefore, while loading and unloading with high stress amplitude stress amplitudes can initiate microcracking, the overall damage remains limited. Hence, the samples can be recovered and evaluated, using microscopy, ultrasonics, and other characterization techniques. The interferometric measurement may provide the means for assessing the level of damage in the specimen and relate it with the observed damage. Some preliminary results are presented for the boron carbide-aluminum cermet and the implications of the observed damage and the interferometric velocity measurement (see Fig. 5) are discussed.

Acknowledgement

The support of the U. S. Army Research Office is gratefully acknowledged.

References

[1] D. C. Halverson, A. J. Pyzik, I. A. Aksay, and W. E. Snowden, "Processing of Boron carbide-Aluminum Composites," *Lawrence Livermore Laboratory, Technical Report*, UCRL-93862, 1986.

[2] G. Ravichandran and S. Nemat-Nasser, "Micromechanics of Dynamic Fracturing of Ceramic Composites," *Proceedings of the ICF-7*, Houston, Texas, 1989 (in press).

[3] P. Kumar and R. J. Clifton, "Dislocation Motion and Generation in LiF Single Crystals Subjected to Plate Impact," *Journal of Applied Physics*, 50, p. 4747.

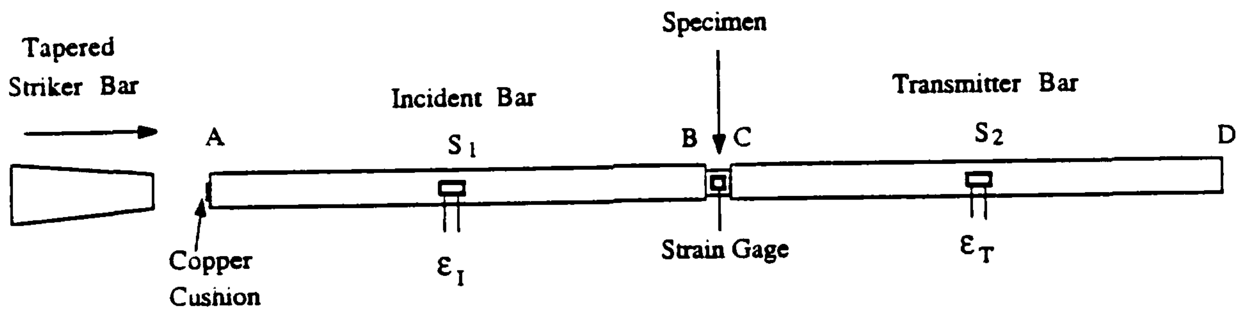

Fig. 1 The schematic of a modified split Hopkinson bar for testing of ceramics and ceramic composites.

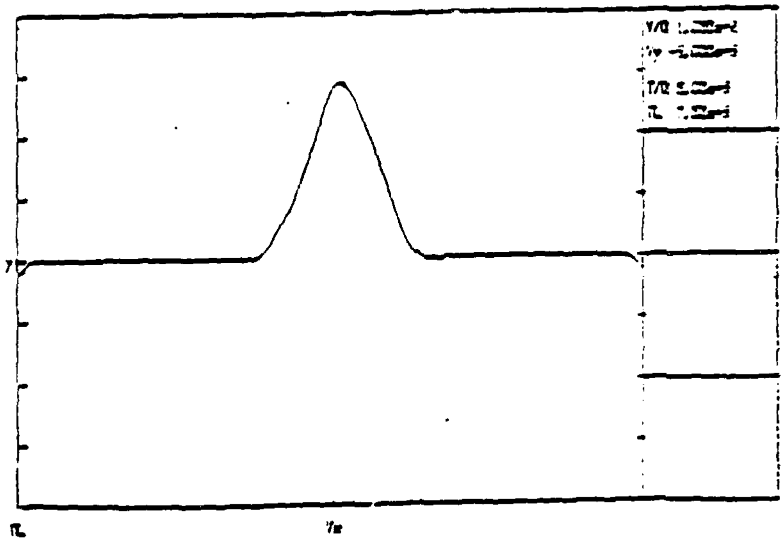

Fig. 2 Ramped pulse produced by a tapered striker bar and a 1/4" copper cushion piece.

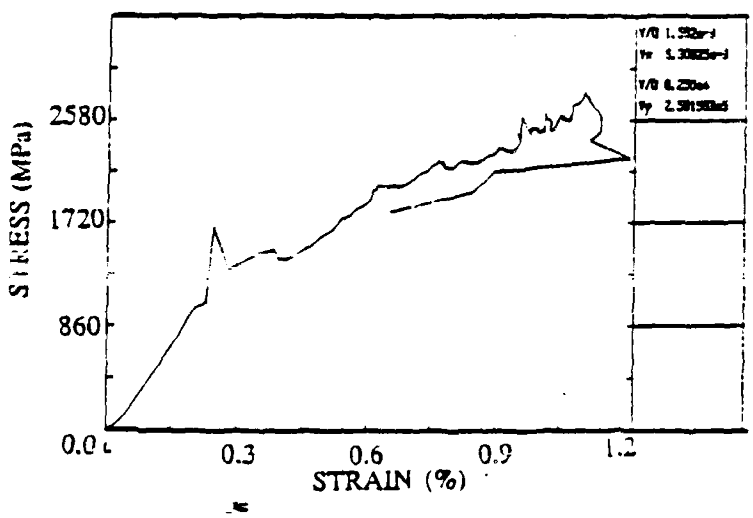

Fig. 3 Stress-strain curve for heat treated B_4C-Al cermet.

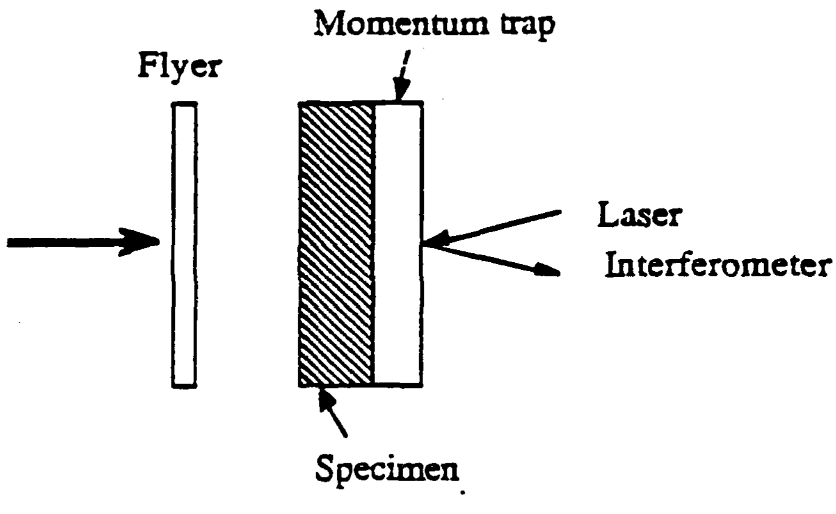

Fig. 4 Normal plate impact recovery experiment.

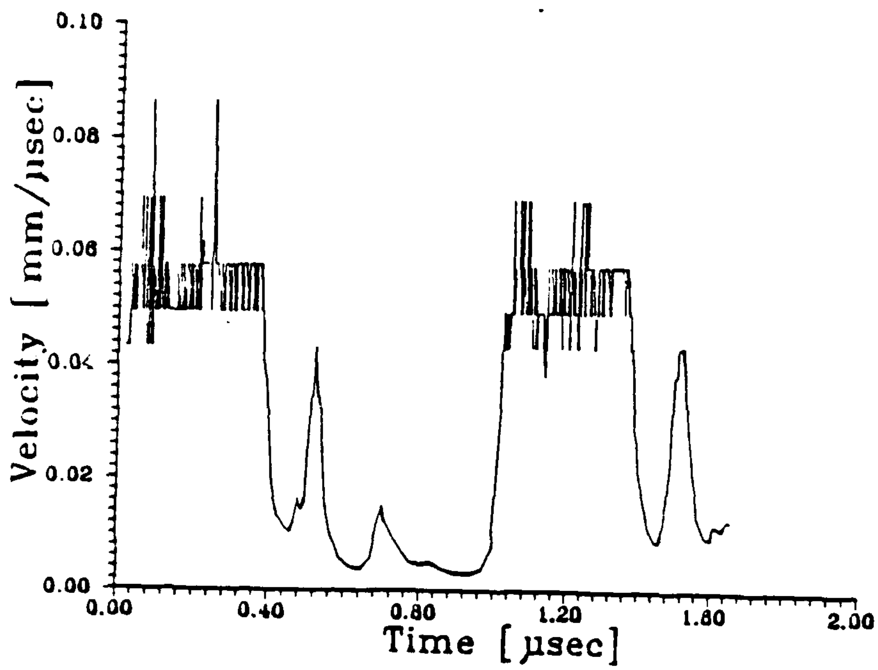

Fig. 5 Measured velocity profile at the free surface of the momentum trap.

DEFORMATION OF A POLYVINYLCHLORIDE BASED ELASTOMER AT HIGH STRAIN RATES

by

D. P. Dandekar and J. L. Green

U.S. Army Materials Technology Laboratory
Watertown, Massachusetts 02172-0001

Abstract

Elastomers, as a class, because of their frequency dependent mechanical properties present some unique problems in determining their responses to impact loadings. As a result, there is paucity of information pertaining to deformations of elastomers under dynamic loading, i.e. at high strain rates and high pressures. The results of the work to be presented here is a part of a comprehensive investigation initiated to determine deformation of a polyvinylchloride based elastomer, commercially known as Isodamp, under dynamic loading and to clarify the roles of complex modulus in the propagation of stress waves through the elastomer. This work deals with the response of Isodamp at high strain rates both under unconfined and confined stress state conditions using the Hopkinson Bar apparatus. The strain rates of deformation ranged between 1250 and 9250 S^{-1}. The maximum strains achieved under unconfined and confined stress states were 40 and 6 percent, respectively. The observed significant stiffening of Isodamp as a function of increasing strain rates and confining stress state points out the inadequacy of static tests in determining deformation of an elastomer under impact loading. This work, in addition, describes some experimental difficulties faced in conducting high strain rate experiments in rubber like elastomers.

A REVIEW OF THE BTI PROGRAM ON ADVANCED A/AA MATERIALS AND ADVANCED COMPUTATIONAL METHODS

by

John F. Mescall

U.S. Army Materials Technology Laboratory
Watertown, Massachusetts. 02172-0001

A multi-year, multiple organization effort is being sponsored by DARPA under the Balanced Technology Initiative auspices of ODD R&E, the Pentagon. A review of the program, as presently constituted, was held recently. A brief presentation of the principal elements of this program is believed to be useful to attendees at this Mechanics Symposium and will be given. The advanced materials referred to include simple and composite ceramics, refined processing techniques and cost-efficient products for armor systems. The attempts to refine computational methods and to incorporate advanced macro-and-microscopic based failure models into such simulations forms the basis for the mechanics aspects of this presentation.

PROCESSING OF POLYMERIC MATRIX COMPOSITES

by

John W. Gillespie, Jr. and Tsu-Wei Chou

University of Delaware
Newark, Delaware 19716

Abstract

The development of residual stresses is strongly influenced by processing history. Residual stresses can have a significant effect on the mechanics and performance of composite structures by inducing warpage or initiating matrix cracks and delaminations. An investigation into the two-dimensional cure simulation of thick thermosetting composites is presented to quantify thermal history and predict processing-induced stresses. These predictions are based upon a non-isothermal kinetic viscoelastic constitutive model for the composite.

Temperature and degree of cure distributions within the arbitrary cross-sectional geometries are predicted as a function of the autoclave temperature history. The boundary-fitted coordinate system (BFCS) transformation technique is combined with the Alternating Direction Explicit (ADE) method of finite difference solution to solve the governing equations for the geometries shown below:

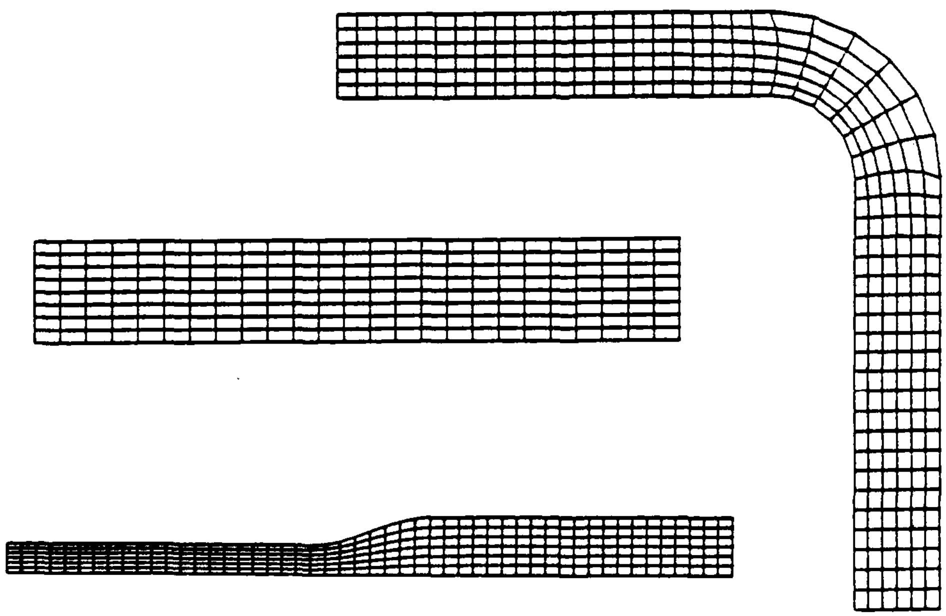

Cure Simulation Mesh Geometries Investigated.

A generalized boundary condition formulation is used so that Dirichlet, Neumann or mixed conditions can be enforced on domain boundaries straightforwardly. The heat conduction equation for two-dimensional, transient anisotropic heat transfer is coupled to the cure kinetics of the thermosetting composite material. A heat generation term is introduced to account for the heat liberated due to the chemical reaction occurring during the curing process. The heat generation term is expressed as a function of cure rate and the total heat of reaction.

The cure simulation of the geometries shown above is investigated for graphite/epoxy and glass/polyester material systems. Cure rate expressions are based on experimental procedures utilizing Differential Scanning Calorimetry. The reaction rate expression for the glass/polyester system was second order overall. Isothermal cure simulations show that the glass/polyester system is extremely sensitive to process temperature.

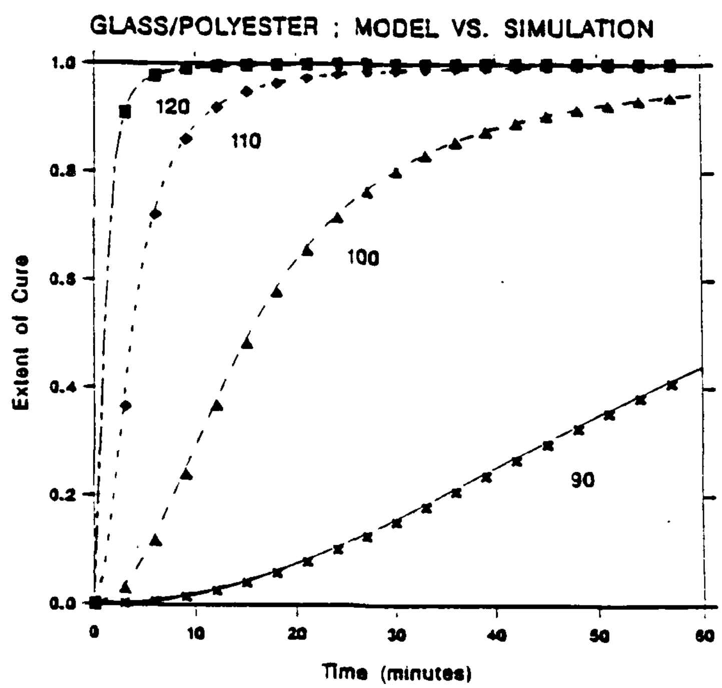

Verification of the Degree of Cure Model

The influence of the tool and bagging materials on the curing process in thick sections is investigated by defining effective heat transfer coefficients $(h/k)_{eff}$ at the specimen surface. The surface and centerline temperature profiles shown for the flat plate geometry indicates that tooling strongly influence thermal history.

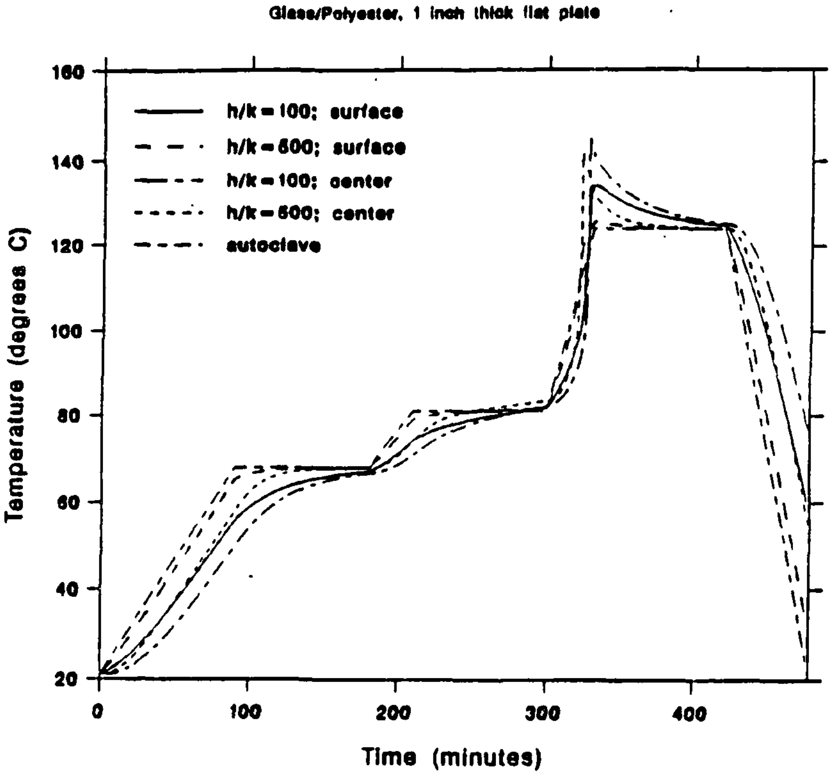

Influence of Effective Heat Transfer Coefficient on Thermal History

Experimental transient temperature profiles are in good agreement with model predictions.

Spatial gradients in degree of cure are shown to be strongly dependent on specimen geometry, material anisotropy, cure kinetics and the proscribed cure cycle. In glass/polyester structures, increasing the te.nperature ramp during processing dramatically increases the rate of the reaction at the surface which is undesirable because volatiles may be trapped within the part during processing. Complex gradients in temperature and degree of cure are predicted in the glass/polyester ply drop geometry shown:

Temperature (°C)

Degree of Cure

At this point in time, significant gradients in the degree of cure are predicted in the thick section while the thin section has cured completely.

The development of residual stresses are strongly influenced by processing history. Residual stresses can have a significant effect on the performance of composite structures by initiating matrix cracks and delaminations. Previous research has experimentally investigated thermosetting matrices using layer removal methods and photoelasticity. Some experiments have been conducted on cross-ply laminates to determine the stress-temperature using the bimetallic strip equation. Other work has focused on modelling residual stresses in isotropic viscoelastic materials. These approaches have been used successfully to predict residual stresses in fully cured epoxy plates subjected to non-isothermal cooling.

The present investigation is extending previous work by predicting residual stress in a viscoelastic material undergoing a chemical reaction. The constitutive relationship is based upon a non-isothermal kinetic viscoelasticity model for the matrix material. Micromechanics are employed to estimate the process history dependent material properties of the composite. In this approach, residual stresses due to thermal and chemical shrinkage are evaluated during the cure as well as subsequent cooling. It is anticipated that the significant gradients in degree of cure noted in thick sections may represent an important source of residual stress not previously considered. Preliminary findings for the one-dimensional cure of thick graphite/epoxy laminates will be reported.

STRUCTURAL STABILITY AND CRACK GROWTH IN THICK SECTION COMPOSITE LAMINATES WITH DELAMINATION

by

S. S. Wang

University of Illinois
Urbana, Illinois

Abstract was not available at time of publication.

METHODOLOGY FOR DETERMINING THE THREE-DIMENSIONAL ELASTIC PROPERTIES OF CONTINUOUS FIBER COMPOSITE MATERIALS

JOHN C. FISH
ADVANCED STRUCTURES SECTION
STRUCTURES DEPARTMENT
MCDONNELL DOUGLAS HELICOPTER CO.
MESA, ARIZONA

EXTENDED ABSTRACT

The elastic behavior of composite structures is inherently complex, introducing sources of interlaminar stress in most designs. Interlaminar stress analyses require data on the out-of-plane elastic properties, as well as the in-plane elastic properties of the composite material. However, due to the lack of out-of-plane elastic constant data, most authors assume a simplified material model. This simplified model assumes equality of all extensional moduli, shear moduli and Poisson's ratios. Griffin [1] examined residual curing effects in cross-ply graphite/epoxy laminates using this assumption and a more appropriate assumption of transverse isotropy. He found that the assumption of a simplified material model leads to significant errors of up to 25% in interlaminar shear stress calculations.

Experimental determination of the complete three-dimensional (3D) set of elastic constants is both tedious and costly. Very thick laminates on the order of 200 plies must be fabricated. Specimens must be carefully cut from the thick laminates. Furthermore, during the cure there is difficulty in maintaining uniform ply thicknesses. This may result in differences in the material properties of the test specimens. Finally, instrumentation of the specimens may also prove to be tedious.

As a result of these difficulties only a sparse amount of test data exists on the 3D elastic properties of composite materials [2,3]. However, these data show significant differences between some of the in-plane and out-of-plane properties of graphite/epoxy. The out-of-plane Poisson's ratios were as much as 76% greater than the major Poisson's ratios, while the out-of-plane shear moduli were about 40% less than the in-plane shear moduli.

In addition to experimental determination of the composite properties, some micromechanics relationships exist which provide estimates of the properties [4,5]. However, these relationships require knowledge of the 3D elastic properties of the constituents. Experimental measurement of the fiber elastic properties (other than the longitudinal modulus) is not possible with current experimental techniques.

This paper presents a methodology for determining the 3D elastic properties of composite materials. The methodology incorporates innovative numerical procedures and easily determined experimental data. A 3D finite element model of a composite unit cell is used and structural optimization techniques are applied to numerically determine elastic behavior. The numerical results are then matched with measured ply properties to determine the unknown fiber and composite properties.

A 3D micromechanical finite element model has been developed to simulate the axial and transverse extensions of a portion of a composite unit cell. The evolution of the model is presented in Figure 1. A composite ply is assumed to be transversely isotropic and composed of a large number of composite unit cells. Each unit cell consists of one fiber surrounded by matrix. By imposing symmetry conditions, only one-eigth of the basic unit cell needs to be modeled. The finite element model itself consists of one fiber element and two matrix elements. The finite elements are eight-noded hexahedral elements based on an assumed stress hybrid formulation [6]. These hybrid elements perform better than standard displacement based elements.

Since the finite element model is heterogeneous, the intersecting sides of the model do not remain perpendicular to one another as the model deforms under uniaxial extension. Thus, the micromechanical deformations incorrectly represent the overall behavior of a composite ply. To ensure proper micromechanical behavior two steps are taken:

1. displacement constraints are applied to the model to keep the intersecting sides of the model perpendicular to one another under uniaxial extension and

2. the conjugate direction method of structural optimization [7] is applied to minimize the strain energy of the model.

This optimization process determines the proper deformation of the model for the assumed set of constituent elastic properties. A strain energy density contour plot for glass/epoxy under a uniaxial extension in the Y direction is given in Figure 2. The optimization steps taken to minimize the strain energy are shown by the broken lines in the figure. The finite element model deformations using no displacement constraints and using the optimization process are shown in Figure 3.

This methodology also incorporates a limited amount of easily measured unidirectional coupon data to establish numerical behavior that is consistent with the macromechanical behavior of the composite material. The required properties are:

1. the longitudinal Young's modulus, E_L,

2. the transverse Young's modulus, E_T and

3. the major Poisson's ratio, ν_{LT}.

The numerically determined elastic behavior of the 3D micromechanical finite element model can then be matched with the known ply properties to determine unknown constituent properties. For example, Figure 4 shows the numerically determined relationship between the longitudinal strain energy, U_l, and the longitudinal fiber modulus, E_{lf}, for glass/epoxy. The results are for a uniaxial strain of 0.01 in the X (or 1) direction. The known value of E_L determines the desired strain energy (350 in-lb/in^3), from which the appropriate fiber modulus (12.5 x 10^6 psi) can be determined.

By establishing all of the required fiber properties in this manner, the unknown composite properties can then be extracted from the elastic behavior of the finite element model. Table 1 compares the experimentally measured (reference 3) transverse Poisson's ratios, ν_{23}, and transverse shear moduli, G_{23}, for graphite/epoxy with values calculated using the present method. The comparison appears to be quite good, with the present method predicting a slightly higher Poisson's ratio (+11%) and a slightly lower shear modulus (-6.9%).

An illustration of this 3D elastic property solution methodology is shown in Figure 5. By combining the numerical procedures and a limited amount of easily determined experimental data, it is possible to calculate 3D elastic properties of the fibers and of the composite material. These calculated elastic properties are difficult, if not impossible, to measure experimentally. Furthermore, the micromechanical basis of the model can yield valuable insight into the relationships between constituent properties and composite behavior.

REFERENCES

1. Griffin, O. Hayden, "The Use of Proper Shear Moduli in the Analysis of Laminated Composites," *Composites Technology Review*, Vol. 6, No. 1, Spring 1984, pp. 22-24.
2. Knight, M., "Three-Dimensional Elastic Moduli of Graphite/Epoxy Composites," *Journal of Composite Materials*, Vol. 16, March 1982, pp. 153-159.
3. Kim, R.Y., Abrams, Frances and Knight, Marvin, "Mechanical Characterization of a Thick Composite Laminate," *Proceedings of the American Society for Composites Third Technical Conference*, September 25-29, Seattle, WA, pp. 711-718.
4. Hashin, Z., "Analysis of Properties of Fiber Composites With Anisotropic Constituents," *Journal of Applied Mechanics*, September, 1979, Vol. 46, pp. 543-550.
5. Chamis, Christos C., "Simplified Composite Micromechanics Equations for Hygral, Thermal, and Mechanical Properties," *SAMPE Quarterly*, April, 1984, pp. 14-23.
6. Loikkanen, M.J. and Irons, B.M., "An 8-Node Brick Finite Element," *International Journal for Numerical Methods in Engineering*, Vol. 20, 1984, pp. 523-528.
7. Vanderplaats, Garret N., Numerical Optimization Techniques for Engineering Design: With Applications, McGraw Hill Book Company, 1984.

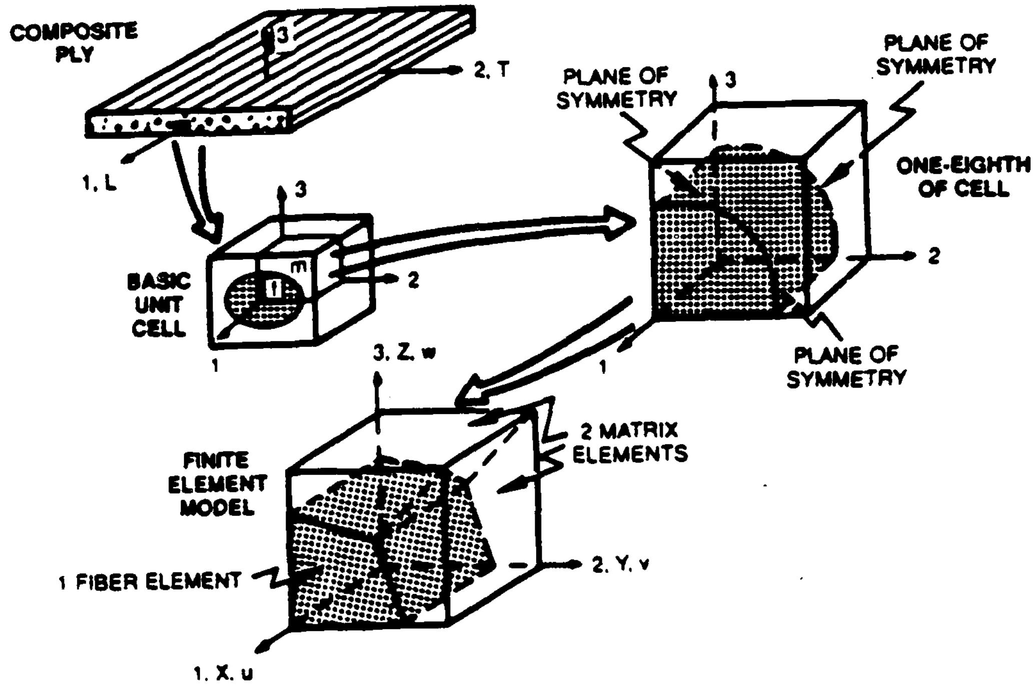

Figure 1 - Micromechanical Modeling Scheme

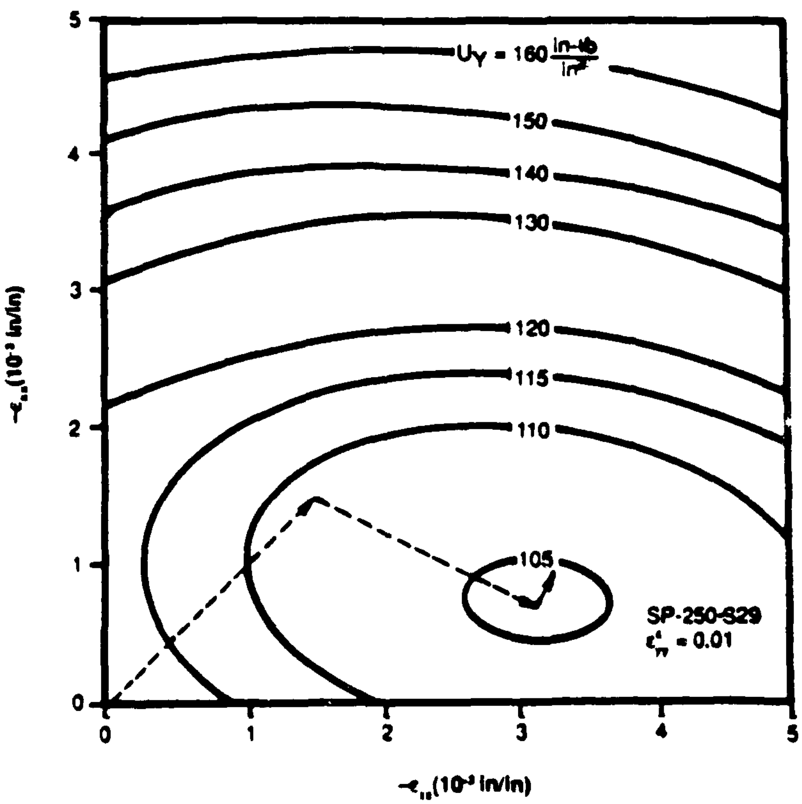

Figure 2 - Strain Energy Density Contour Plot

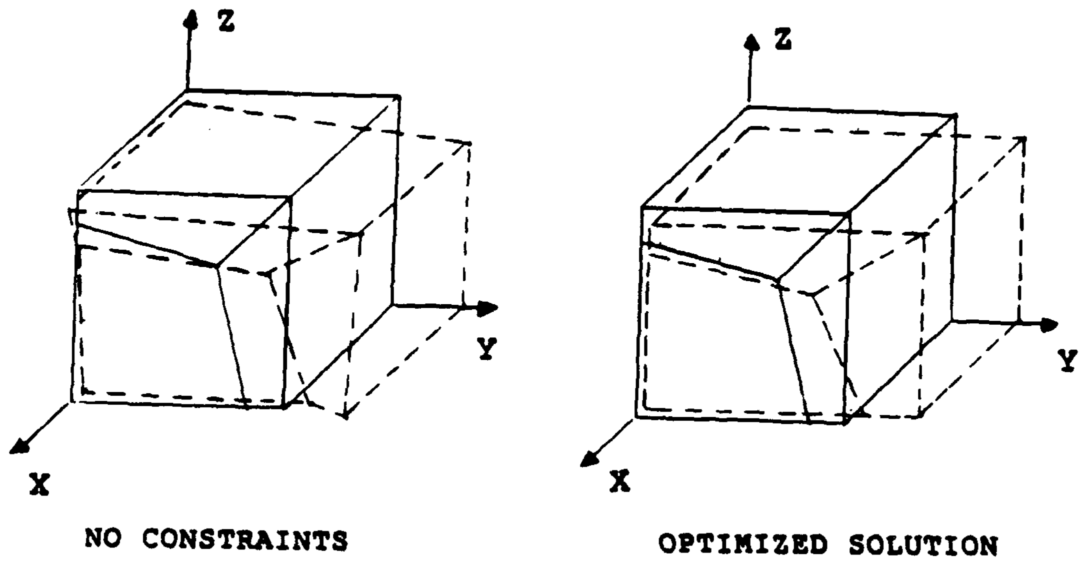

Figure 3 - Finite Element Model Deformations

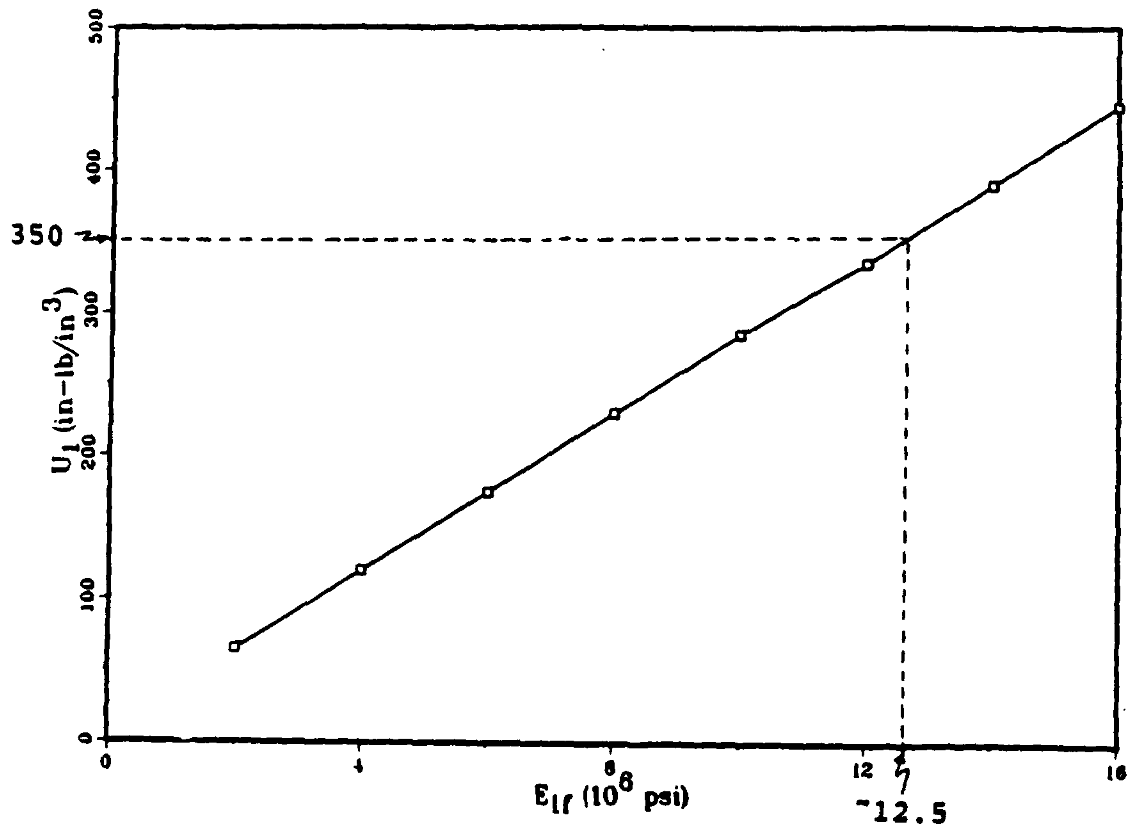

Figure 4 - Longitudinal Strain Energy Versus Longitudinal Fiber Modulus

TABLE 1 - Comparison of Elastic Constants

	REF. 3	PRESENT	%DIFFERENCE
ν_{23}	0.520	0.577	+11
G_{23} (MSI)	0.439	0.409	-6.9

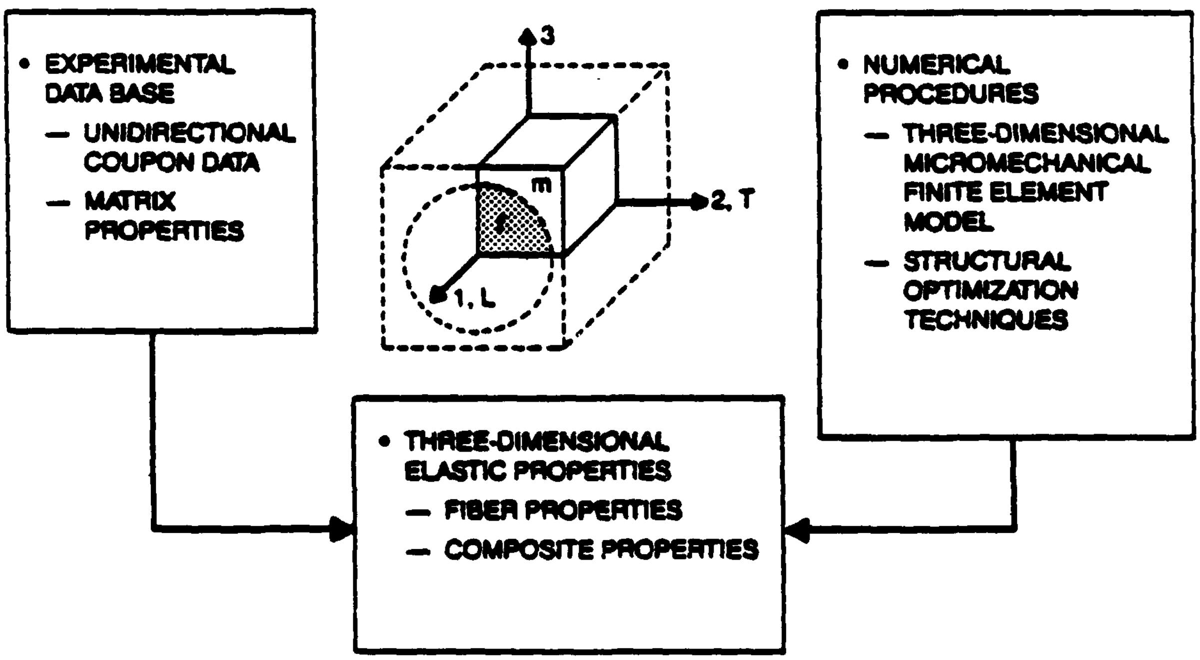

Figure 5 - Composite Three-Dimensional Elastic Property Methodology

ORTHOTROPIC ELASTIC-PLASTIC BEHAVIOR OF
AS4/APC-2 THERMOPLASTIC COMPOSITE IN COMPRESSION

by

C. T. Sun and Y. Rui

School of Aeronautics and Astronautics
Purdue University
West Lafayette, Indiana 47907

APC-2 PEEK is a promising thermoplastic system with good mechanical properties for forming fiber composite. It has better toughness than most existing epoxy systems. It exhibits more pronounced plasticity especially at elevated temperature environments. Thus, modeling the orthotropic elastic-plastic behavior and temperature effects in thermoplastic composite is an important task.

In this paper, a plastic potential of the form

$$2f = \sigma_{22}^2 + 2a_{66}\,\sigma_{12}^2 \tag{1}$$

is used. The plastic strain increments are given by

$$d\varepsilon_{ij}^p = d\lambda \frac{\partial f}{\partial \sigma_{ij}} \tag{2}$$

Inherent in the assumed plastic potential is

$$d\varepsilon_{11}^p = 0 \tag{3}$$

i.e., no plastic strain exists in the fiber-direction. In Equation (2), the proportionality factor $d\lambda$ is given by

$$d\lambda = \frac{3}{2}\,\frac{d\bar{\varepsilon}^p}{\bar{\sigma}} \tag{4}$$

where $\bar{\sigma}$ is the effective stress defined by

$$\bar{\sigma} = \sqrt{3f}$$

and $d\bar{\varepsilon}^p$ is the effective plastic strain increment which satisfies the plastic work increment

$$dW^p = \bar{\sigma} d\bar{\varepsilon}^p = 2f d\lambda \tag{5}$$

The parameter a_{66} and the effective stress-effective plastic strain relation are determined using off-axis composite coupon specimens. For the AS4/APC-2 thermoplastic composite, $a_{66} = 1.7$ is valid for a temperature range up to 250°F.

In the relation

$$\bar{\varepsilon}^p = A(\bar{\sigma})^n \tag{6}$$

it is found that $n = 5.0$ is valid for temperatures up to 250°F and the factor A is related to temperature as

$$\ln (A) = 0.0089T - 17$$

where T is temperature (°F).

Figure 1 shows the effective stress-effective plastic strain curve for the thermoplastic composite at 150°F with $a_{66} = 1.7$. It is evident that all the stress-strain curves obtained from various off-axis specimens collapse into a master curve in the $\bar{\sigma} - \bar{\varepsilon}^p$ plane. From this master curve the complete constitutive orthotropic elastic-plastic relations can be obtained.

Also included in this paper is a simple compression failure criterion which has the same form as the plastic potential function

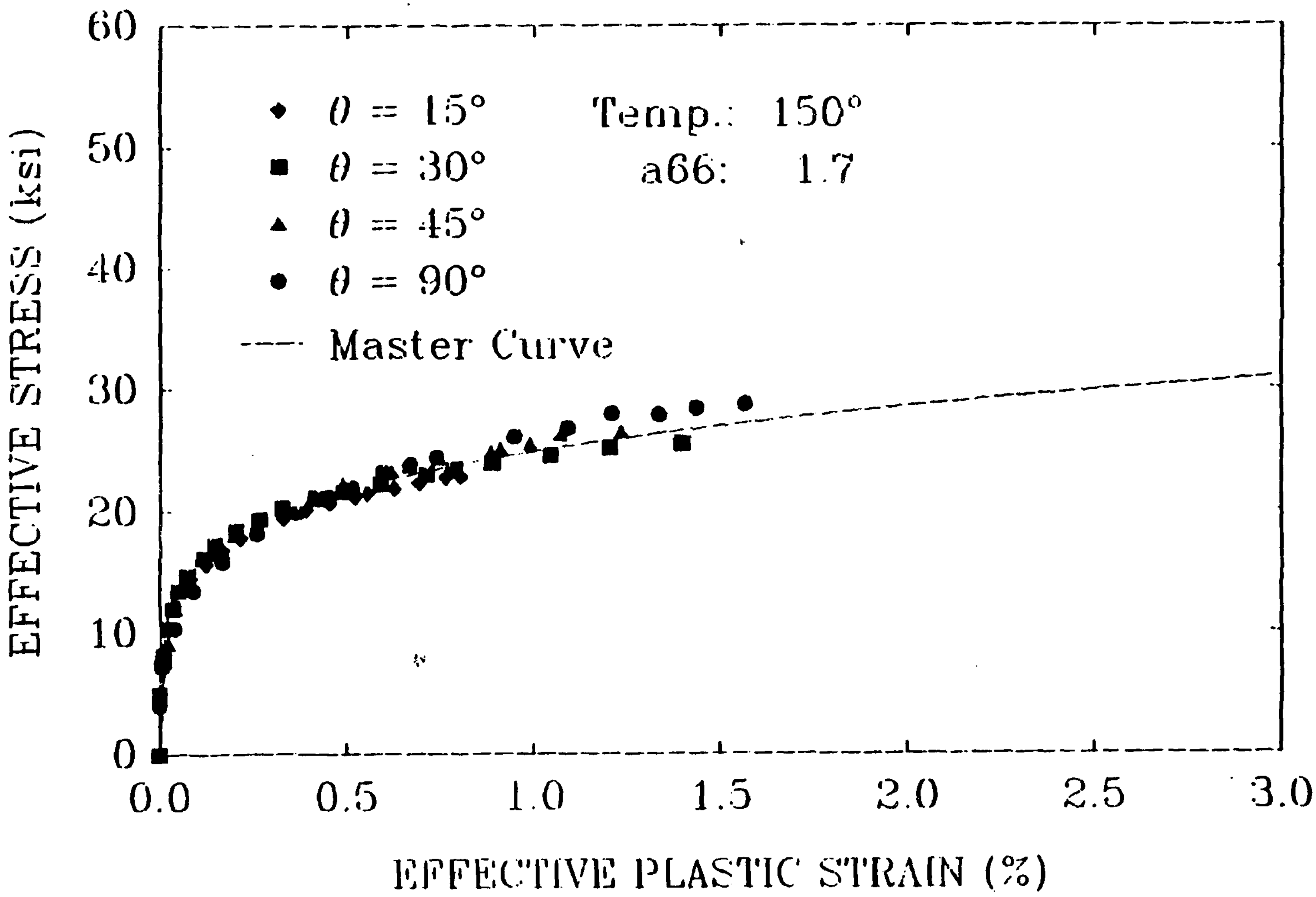

Fig. 1 Effective stress-effective plastic strain curves with $a_{66} = 1.7$ at 150°F.

STATISTICALLY BASED MATERIAL PROPERTIES:

A MILITARY HANDBOOK-17 PERSPECTIVE

by

Donald M. Neal and Mark G. Vangel

U.S. Army Materials Technology Laboratory
Watertown, Massachusetts 02172-0001

This paper describes the statistical procedures and their importance in obtaining composite material property values for aircraft and military combat system applications. The property value is a stress measurement such that strength exceeds this value with a prescribed probability and 95% confidence in the assertion. The survival probabilities are in the 99th percentile and 90th percentile for the A and B basis values respectively. The basis values for strain to failure measurements are defined in a similar manner.

The procedures presented in this paper required substantial research efforts in order to solve the statistical problems associated with obtaining basis values. Some of the procedures include: Determination of outliers, selection of statistical models, tests for batch to batch variation, single and multi-batch models for obtaining basis values including nonparametric methods. In Figure 1, a flow chart is shown outlining the computation methods. The authors have written the statistics chapter for the Military Handbook-17 which includes a more detailed description of the methods and a carefully chosen set of example problems (Reference 1).

The primary concern of this paper is to provide an appreciation for the need of statistics in obtaining composite material property values. Unlike most traditional structural materials, which are homogeneous and isotropic, composite materials have extensive intrinsic statistical variability in many material properties. This variability, particularly important to strength properties, is due not only to inhomogeniety and anisotropy, but also to the basic brittleness of many matrices and most fibers and to the potential for property mismatch between the components. Because of this inherent statistical variability, careful statistical analysis of composite material properties is not only more important but is also more complex than for traditional structures.

A plot of normal distribution data with mean zero and variance one is shown in Figures 2 and 3 for 25 simulations. The points are $(X_i, i/(N + 1))$, where X_i is the i th ordered value, and N equals the number of specimens tested. An estimate of the probability that X_i is less than some X is $P = i/(N + 1)$. When $P = .1$ and $N = 50$, the spread in the simulated data is .7. The corresponding spread for $N = 10$ is 2.1. This difference in spread identifies the potential uncertainties that exist when a limited amount of data is available and an accurate estimate of strength corresponding to a high level of reliability is required. Methods are shown in the text for obtaining protection against this situation by providing a tolerance limit estimate on the stress corresponding to high reliability.

An important application of the basis value is in the design of composite aircraft structures. In the design process it is required that a margin of safety (MS) be greater than one. The basis value divided by the applied stress or strain defines MS. The basis value is also used in qualifying new composite material systems to be used in the manufacturing of aircraft. In addition, the value provides guidance in the selection of material for specific design requirements. In designing with composites it is important to obtain basis values for various environmental conditions (hot-wet, cold-dry, etc.) in addition to loading requirements (tension, compression, shear).

In conclusion, the research outlined in this paper represents a unique and comprehensive development of statistical methodology for evaluating composite material strength data for application in structural design.

References

(1) Military Handbook-17B, "Polymer Matrix Composites", Guidelines, 29 February 1988, Naval Publications and Forms Center, 5801 Tabor Avenue, Philadelphia, Pennsylvania 19120.

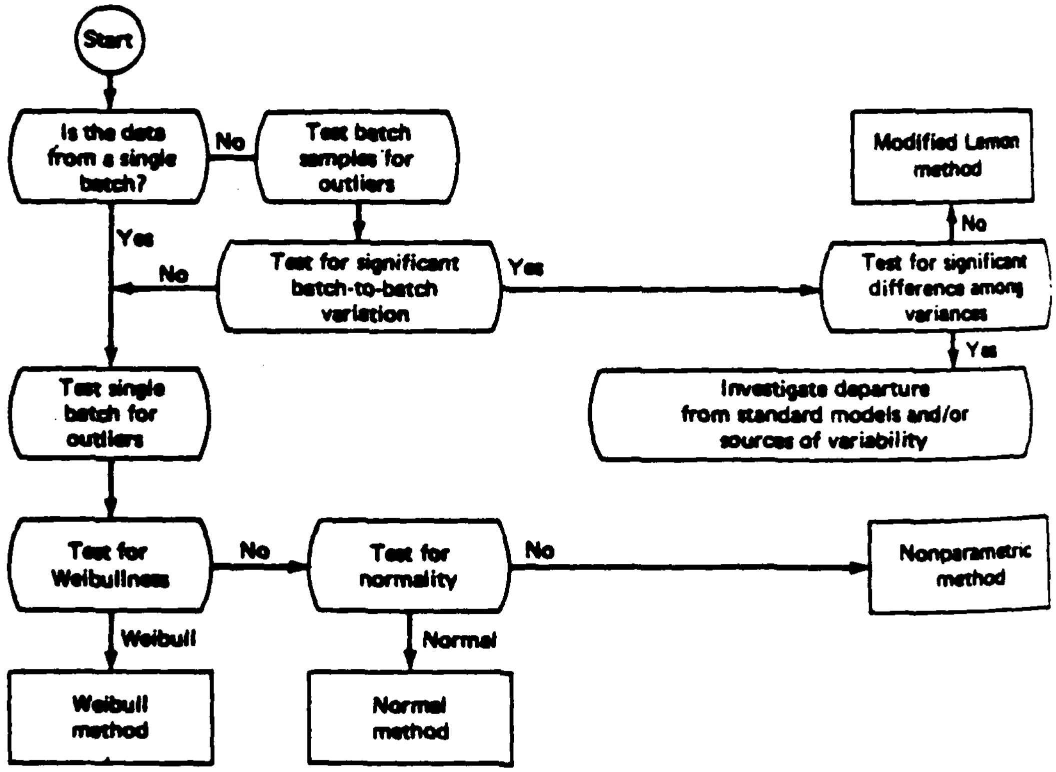

FIGURE 1 COMPUTATIONAL PROCEDURES FOR STATISTICALLY BASED MATERIAL PROPERTIES

NORMAL CUMULATIVE DISTRIBUTION FUNCTION

MEAN = 0   STANDARD DEVIATON = 1

25 SIMULATIONS

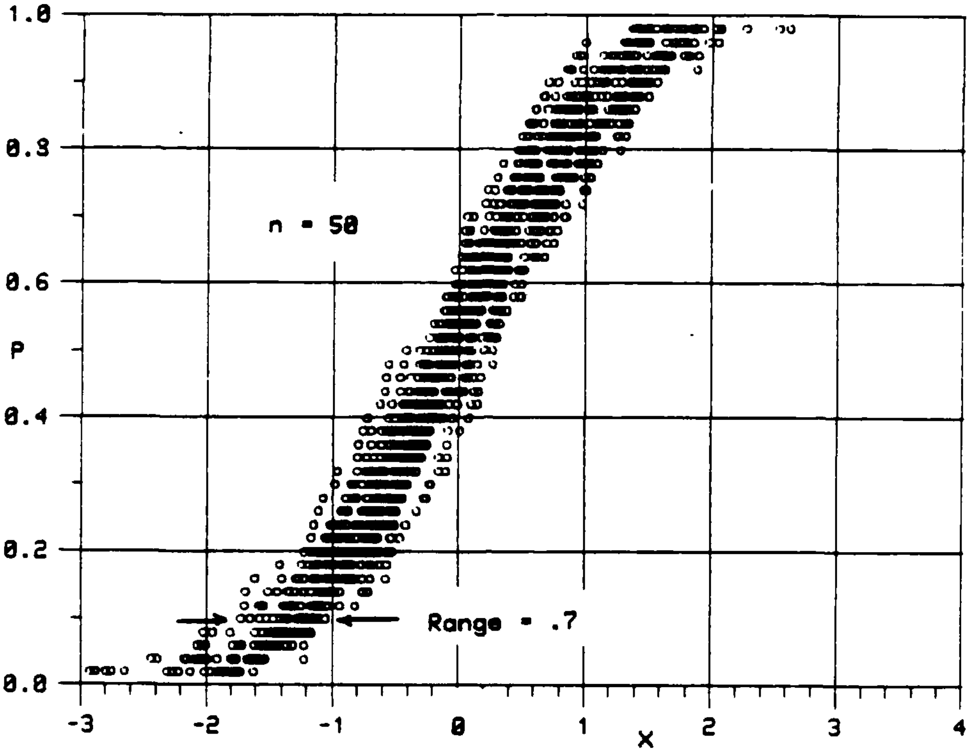

FIGURE 2

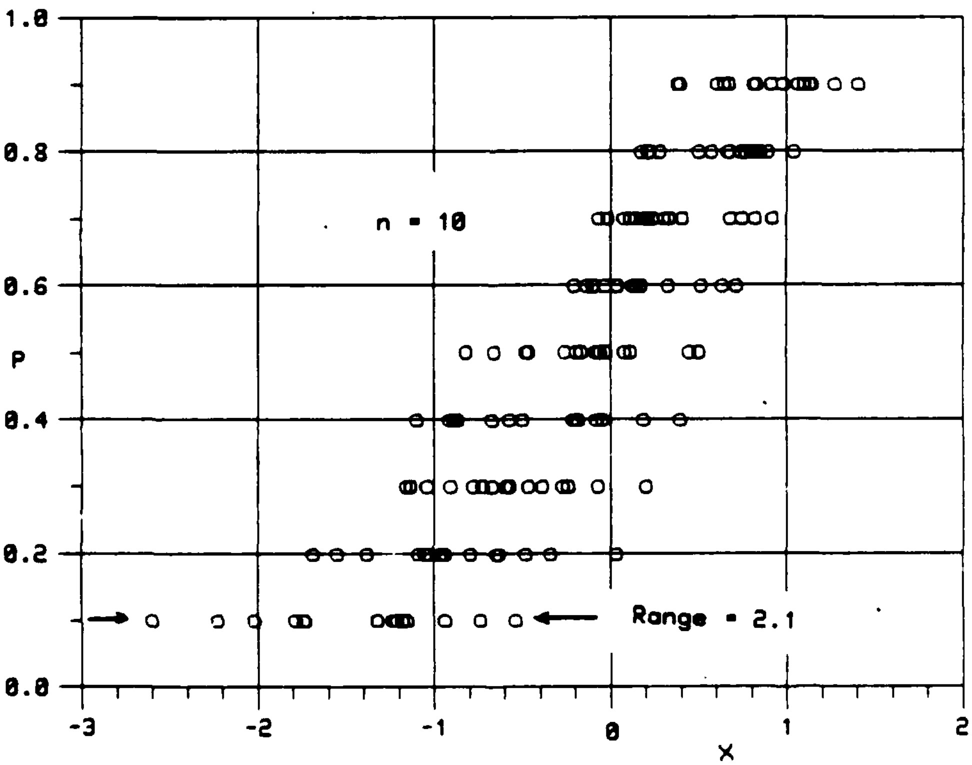

FIGURE 3

Orthotropic Theory of Viscoplasticity with Applications to Laminated Composite Analyses

Erhard Krempl
Mechanics of Materials Laboratory
Rensselaer Polytechnic Institute
Troy, N.Y. 12180-3590

An infinitesimal, orthotropic theory of viscoplasticity based on overstress (VBO) is presented. The theory is of the unified type and does not separately account for creep and plasticity. Yield surfaces and loading and unloading conditions are not used in the theory where the total strain rate is the sum of elastic and inelastic strain rates. The rate form of the orthotropic Hooke's law is used as a constitutive assumption for the elastic strain rate. The inelastic strain rate is an orthotropic, nonlinear function of the overstress, the difference between the stress and the equilibrium stress. The equilibrium stress is a state variable of the theory. The first order nonlinear differential growth law for the equilibrium stress is formulated in terms of stress rate and overstress. Asymptotic solutions for constant strain rate loading are admitted by the theory and the stress strain diagrams in uniaxial tests can have positive, zero or negative slopes at the maximum strain of interest. In uniaxial tests, the theory permits the modeling of almost linear behavior in one direction while the other directions behave in a viscoplastic manner. Orthotropic creep, relaxation and strain rate sensitivity are part of the theory as is the modeling of tension/compression asymmetry.

In an extension of simple laminate theory, VBO is used to replace the orthotropic elasticity law. The geometric assumptions of the classical theory are maintained. It is now possible to characterize the rate dependent ply behavior including creep and relaxation of metal matrix plies. The in-plane and bending behavior of laminates of arbitrary lay-up can now be computed. To this end, the set of first order nonlinear differential equations are numerically integrated for the specified boundary conditions. Computer programs have been written for this purpose.

The approach is illustrated by showing that the on-axis and off-axis stress-strain curves of metal matrix plies published in the literature can be matched by the theory. Then the behavior of symmetric laminates is computed under in-plane, monotonic and cyclic loading with periods of creep or relaxation. Stress redistribution in the plies during creep or relaxation is obtained from the calculations and is discussed.

THERMAL ASPECTS OF SHEAR LOCALIZATION IN VISCOPLASTIC SOLIDS

L. Anand, A. M. Lush, and K. H. Kim

Department of Mechanical Engineering
Massachusetts Institute of Technology
Cambridge, Massachusetts

ABSTRACT

Anand, Kim and Shawki [J.M.P.S. Vol. 35, 1987, pp. 407-429] have recently carried out a linear perturbation stability analysis for the initiation of shear bands in thermo-viscoplastic solids undergoing plane motions. This analysis accounts fully for strain hardening, thermal softening, rate sensitivity, heat conduction and inertial effects. We briefly review the results of this analysis. It is well known that an *inherent limitation* of this (and all other) linear perturbation analyses is that it provides information only about the conditions at the ***initiation*** of shear bands. It does not provide any information regarding the more interesting stages of localization when the strain rate, temperature, and strain in the shear bands becomes much larger than elsewhere. Accordingly, to follow the evolution process of thermo-viscoplastic shear localization, we present full two-dimensional large deformation finite element simulations of a solid subjected to plane strain frictionless compression under (a) completely adiabatic conditions, and (b) heat conducting conditions. A small temperature perturbation is used to numerically seed the localization, and the initiation and growth of a naturally appearing band-like region of localization is followed from slow early growth to severe localization. Our numerical analysis incorporates full thermo-mechanical coupling but neglects the effect of inertia. The results of our numerical simulations are in qualitative accord with the recent experiments of Marchand and Duffy [J.M.P.S. Vol. 36, 1988, pp. 251-288] on the process of formation of adiabatic shear bands during high rate torsion testing of thin-walled, short gage-length, tubular specimens.

VERIFICATION OF THE PLASTIC SPIN CONCEPT IN VISCOPLASTICITY

Yannis F. Dafalias and Han-wook Cho
Department of Civil Engineering, University of California, Davis, CA, USA

EXTENDED SUMMARY

The basic Eulerian kinematics for small elastic but arbitrary inelastic strains yield according to the proposition of MANDEL (1971)

$$\underset{\sim}{D} = \underset{\sim}{D}^e + \underset{\sim}{D}^p \quad , \qquad \underset{\sim}{W} = \underset{\sim}{\omega} + \underset{\sim}{W}^p \tag{1}$$

with $\underset{\sim}{D}$, $\underset{\sim}{D}^e$ and $\underset{\sim}{D}^p$ the total, elastic and plastic rate of deformation tensors, respectively, and $\underset{\sim}{W}$, $\underset{\sim}{\omega}$ and $\underset{\sim}{W}^p$ the material, substructural and plastic spin tensors, respectively. Constitutive relations must be provided not only for $\underset{\sim}{D}^e$ and $\underset{\sim}{D}^p$, but also for $\underset{\sim}{W}^p$. Then, given $\underset{\sim}{W}$, one can obtain $\underset{\sim}{\omega}$ from $(1)_2$. The corotational rate $\overset{\circ}{\underset{\sim}{a}}=\dot{\underset{\sim}{a}}-\underset{\sim}{\omega}\underset{\sim}{a}+\underset{\sim}{a}\underset{\sim}{\omega}$ of a second order tensor structure variable $\underset{\sim}{a}$ must be used for its rate constitutive equation of evolution.

Within the foregoing framework, a viscoplastic model is proposed which hardens kinematically and, in addition, develops orthotropic symmetries. The plastic spin constitutive relations and the kinematic hardening rule are expressed according to the findings in DAFALIAS (1985). Then, the model is applied to the case of large simple shear γ along x_1 on the x_1-x_2 plane, and based on the work in DAFALIAS (1984, 1985) and DAFALIAS and RASHID (1989) (rigid-plastic response assumed), the following expressions are obtained

$$(d\alpha_{11}/d\gamma) = -\mathrm{sgn}(\dot{\gamma})(c_r/\sqrt{3})\alpha_{11} + (1-\rho\alpha_{11})\alpha_{12} \tag{2}$$

$$(d\alpha_{12}/d\gamma) = -\mathrm{sgn}(\dot{\gamma})(c_r/\sqrt{3})\alpha_{12} + (1-\rho\alpha_{11})\alpha_{11} + (1/3)h_\alpha \tag{3}$$

$$\alpha_{22} = -\alpha_{11} \quad , \qquad \tan 2\phi = \alpha_{12}/\alpha_{11} \tag{4}$$

$$-\frac{\sigma_{11}-\alpha_{11}}{J} = \frac{\sigma_{22}-\alpha_{22}}{J} = \mathrm{sgn}(\dot{\gamma}\cos 2\phi)\left(\frac{3\alpha}{\beta} - 1\right)\frac{\sin 2\phi}{\left[6\alpha\left(\frac{3\alpha}{\beta} + \tan^2 2\phi\right)\right]^{1/2}} \tag{5}$$

$$\frac{\sigma_{12}-\alpha_{12}}{J} = \mathrm{sgn}(\dot{\gamma})\left[\frac{1}{6\alpha}\left[1 + \left(\frac{3\alpha}{\beta} - 1\right)\cos^2 2\phi\right]\right]^{1/2} \tag{6}$$

$$J = \sqrt{2}\,k + \overline{V}(\dot{\bar{\epsilon}})^{1/n} \tag{7}$$

where σ_{ij} and α_{ij} are the stress and back-stress components, respectively, sgn(*) = sign of *, h_α and c_r are the kinematic hardening parameters, α and β the orthotropic parameters for cubical symmetries, $\overline{V}$ and n the viscoplastic parameters (rate dependence), k the size of the static yield condition, $\dot{\bar{\epsilon}} = |\dot{\gamma}|/\sqrt{3}$ and ρ the plastic spin parameter. The α and β are assumed to evolve exponentially with $\bar{\epsilon}$ from their initial values 1 and 3 to their saturation value α_s and β_s, respectively.

Figures 1-3 illustrate the application of the theory to the experimental data from fixed-end torsion at different rates for iron α-Fe at 800° C, for a proper set of model constants. Figure 1 shows the experimental data as reported in MONTHEILLET, et al. (1984), for 3 rates $\dot{\bar{\varepsilon}} = |\dot{\gamma}|/\sqrt{3} = 0.5, 0.05, 0.007\ \text{sec}^{-1}$, indicated by thick dots, solid squares and thin dots, respectively (the σ_{12}-γ curve is given for the highest rate only). Figure 2 shows the model simulation for all 3 rates according to equations (2)-(7) and Figure 3 the superposition of simulation and data for the highest rate. Remarkable is the predicted change of sign of σ_{22} from negative to positive for all rates in the proper order, a result of the synergetic effect of kinematic hardening, developing orthotropic symmetries and rate sensitivity.

Acknowledgement

The support by the NSF Grant No. MSM-8619229 is gratefully acknowledged. This presentation is an abbreviated version of a paper with the same title to appear in the Symposium Proceeding of Plasticity 89, July 1989, Mie University, Tsu, Japan.

REFERENCES

1971 MANDEL, J., Courses and Lectures No <u>97</u>, ICMS, Udine, Springer.
1984 DAFALIAS, Y.F., Mechanics of Materials, <u>3</u>, 223.
1984 MONTHEILLET, F., COHEN, M., and JONAS, J.J., Acta metall. <u>32</u>, 2077.
1985 DAFALIAS, Y.F., ASME J. Appl. Mech., <u>52</u>, 865.
1989 DAFALIAS, Y.F. and RASHID, M.M., Int. J. Plasticity, in press.

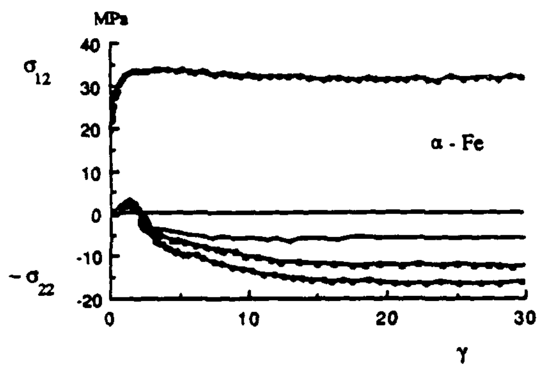

Fig. 1. Experimental data after MONTHEILLET, et al. (1984).

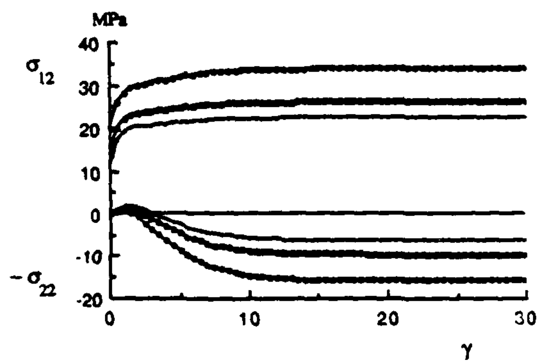

Fig. 2. Model simulation for three strain rates.

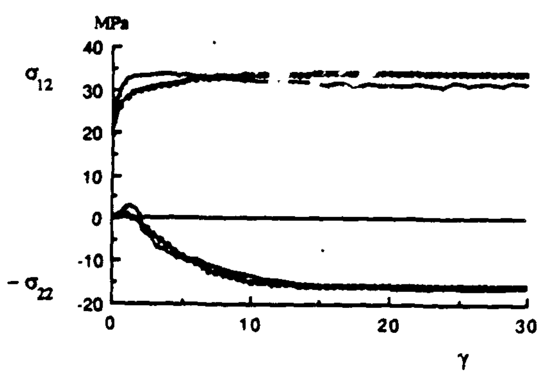

Fig. 3. Experimental data and superposed model simulation for the highest rate.

CHRONORHEOLOGICAL CHARACTERIZATION OF ELASTOMERS

William W. Feng
University of California
Lawrence Livermore National Laboratory
Livermore, California 94550, USA

Introduction

Elastomers have been used in many structures for years. But the mechanical properties of elastomers, other than the elastic properties, are still unknown; hence, studies of these structures are generally based upon their elastic properties only. In reality, elastomers often exhibit chronorheological (rheological and aging) behavior. The magnitudes of the property change with time, and are often large enough that they cannot be neglected. To date, very few analytical and experimental studies for determining these time-dependent properties have been attempted. This is because the study of mechanics for elastomers must consider both geometric and material non-linearities. The additional chronorheological effects make the analytical and experimental studies very difficult.

In this article, the chronorheological effects of elastomers are studied theoretically and experimentally. The viscoelastic constitutive equation developed by Christensen [1] is used. With two more material property functions, the constitutive equation is extended to include chronorheological effects.

Formulation

The viscoelastic phenomena for elastomers, subjected to biaxial stress states, are obtained theoretically. The formulation centers on the determination of the deformed configuration of a plane circular membrane under an inflating pressure. The stretch ratios are λ_1 and λ_2 in the meridian and circumferential directions respectively. For incompressible materials, and based on the assumption that for a thin membrane the stress in the normal direction is small, the relationship between the normal Cauchy stress in the meridian direction (σ_1) and the stretch ratios is

$$\sigma_1(t) = g_0\left(\lambda_1^2 - \frac{1}{\lambda_1^2\lambda_2^2}\right) + \frac{\lambda_1^2}{2}\int_0^t g_1(t-T)\,\frac{\partial\lambda_1^2(T)}{\partial T}\,dT - \frac{1}{2\lambda_1^2\lambda_2^2}\int_0^t g_1(t-T)\,\frac{\partial}{\partial T}\left(\frac{1}{\lambda_1^2(T)\lambda_2^2(T)}\right)dT \qquad (1)$$

A similar relationship obtains for σ_2, the normal Cauchy stress in the circumferential direction. There are two material property functions, g_0 and g_1. The g_0 term is the long-term elastic material constant, and $g_1(t)$ is a viscoelastic relaxation function. The stretch ratios are unknown functions of the inflating pressure (P). These unknown functions can be determined from the force equilibrium equations in the tangential and normal directions. The equilibrium equations can be reduced to a set of nonlinear differential-integral equations. In order to simplify the numerical procedures for solving these equations, two steps are taken. First, the governing equations are written in terms of three variables: λ_1, λ_2, and θ. The value θ is the angle between a vector normal to the midsurface of a deformed membrane and the axis of symmetry. Second, a recurrence formula, developed by Feng [2], is used. With the recurrence formula, the governing equations are reduced to three first-order ordinary differential equations for each time step. With specified boundary and initial conditions, the solutions to these equations can be obtained by numerical integration.

The relaxation function, written in terms of the exponential law, is used here:

$$g_1 = \sum_{i=1}^{N} c_i \, e^{-t/\tau_i} \tag{2}$$

where c_i and τ_i are material constants.

It is postulated that the elastomer is a chronorheologically simple material. The constitutive equation for chronorheologically simple materials preserves the form as Equation (1). Two new material functions $\bar{g}_0(t_a)$ and $\bar{g}_1(t_a,t)$ replace g_0 and $g_1(t)$. The aging time is denoted by t_a. The constitutive Equation (1) is extended to

$$\bar{\sigma}_1(t_a,t) = \bar{g}_0(t_a)\left(\lambda_1^2 - \frac{1}{\lambda_1^2\lambda_2^2}\right) + \frac{\lambda_1^2}{2}\int_0^t \bar{g}_1(t_a,t-T)\,\frac{\partial\lambda_1^2(T)}{\partial T}\,dT \tag{3}$$

$$- \frac{1}{2\lambda_1^2\lambda_2^2}\int_0^t \bar{g}_1(t_a,t-T)\,\frac{\partial}{\partial T}\left(\frac{1}{\lambda_1^2(T)\lambda_2^2(T)}\right) dT$$

These four functions are related by

$$\bar{g}_0(t_a) = \alpha(t_a)g_0 \quad \bar{g}_1(t_a,t) = \alpha(t_a)\sum_{i=1}^{N} c_i \, e^{-\beta(t_a)t/\tau_i} \tag{4}$$

where $\alpha(t_a)$ and $\beta(t_a)$ are two new material properties that are functions of the aging time t_a. The material property functions $\alpha(t_a)$ and $\beta(t_a)$ can be determined with the experimental results.

For determination of $\alpha(t_a)$ and $\beta(t_a)$, Equation (3) can be written in the following form

$$\log \bar{\sigma}_1(t_a,\xi) = \log \alpha(t_a) + \log \sigma_1(\xi) \tag{5}$$

where

$$\log \xi = \log \beta(t_a) + \log t \tag{6}$$

Therefore, if we plot the stress versus time on the log-log plots, with the vertical axis being the stress and the horizontal axis being the time t, then the stress-relaxation curve for any aged time history can be obtained directly from the stress-relaxation curve at $t_a = 0$ by imposing a vertical shift and a horizontal shift on the stress-relaxation curves. The vertical shift and the horizontal shift are $\log \alpha(t_a)$ and $\log \beta(ta)$, respectively.

Experiments and Results

In order to show the chronorheological effect on an elastomeric membrane, an experiment is performed. In the experiment, a circular plane latex rubber membrane is clamped between two plates. The thickness of the membrane is 0.0762 cm. The radius of the membrane is 5.08 cm. The membrane is inflated and the height of the deformed membrane at the pole is fixed at 6 cm which corresponds to the stretch ratios at the pole of 2.0. An infrared photosensor, connected to a solenoid air intake valve, is used to maintain the maximum height of the deformed membrane at the pole. The pressure-time histories for biaxial extension of unaged and aged specimens are shown in Figure 1. The specimens are aged under stress-free condition and at 50°C for a period of t_a. The specimens are removed from the oven and cooled to room temperature before the relaxation tests. From the pressure-time histories of an unaged specimen ($t_a = 0$), the material properties g_0 and $g_1(t)$ can be determined. From the pressure-time histories of the aged specimens ($t_a \neq 0$), the horizontal and vertical shifts of the relaxation curves are observed. The values of log α and log β versus the aging time t_a, are shown in Figure 2. From the figure, one observes that there is a moderate change of α during aging; however, the values of β changed significantly.

Conclusions

The interpretation of chronorheological properties of an elastomer has been obtained. The constitutive equations and a method for determining these material properties are also presented. In the formulation, the geometric nonlinearity as well as the material nonlinearity are included. The theoretical value for the strains can be as large as needed; for practical applications, however, these values are limited by the fracture strength and are usually less than a few hundred percent. The method described in this article is for the temperature aging; however, the constitutive equations and the method for obtaining the material properties can be extended readily to other types of aging.

References

1. Christensen, R. M., "A Nonlinear Theory of Viscoelasticity for Application to Elastomers," Journal of Applied Mechanics, 47, 1980, pp. 762-768.

2. Feng, W. W., "A Recurrence Formula for Viscoelastic Constitutive Equations," Proceedings of International Conference on Computation Mechanics, II, May 25-29, 1986, Tokyo, Japan, pp. 77-82.

List of Figures

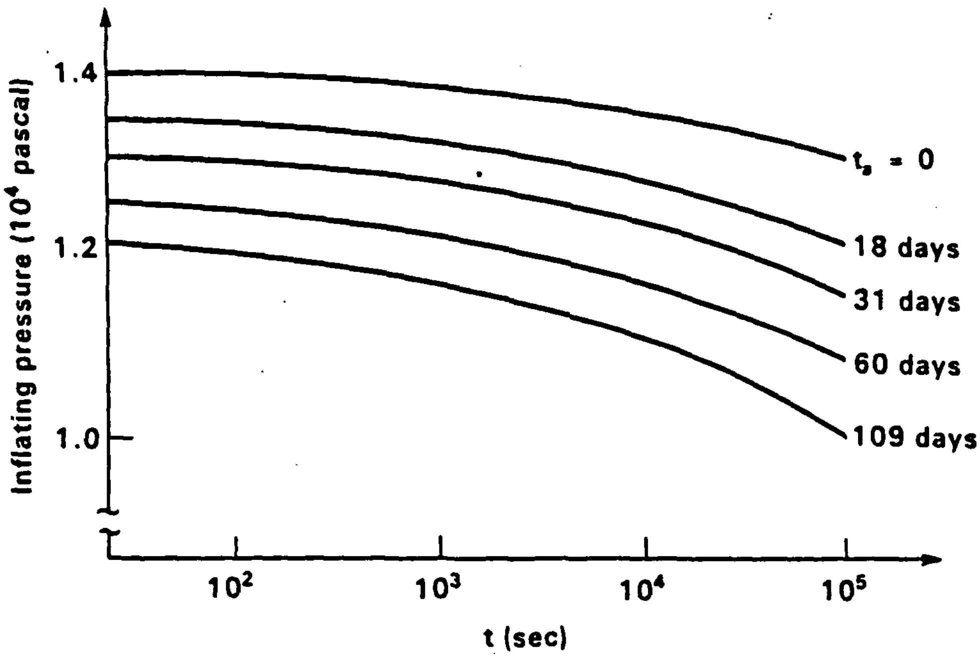

1.4
1.2
1.0
Inflating pressure (10⁴ pascal)
t_a = 0
18 days
31 days
60 days
109 days
10^2
10^3
10^4
10^5
t (sec)

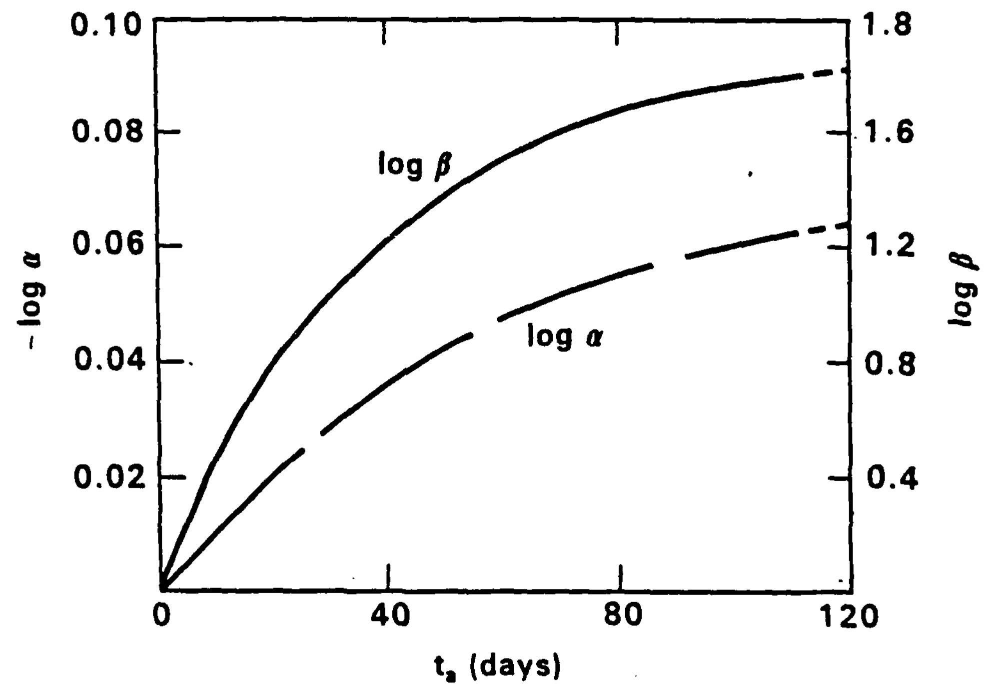

0.10
0.08
0.06
0.04
0.02
- log α
1.8
1.6
1.2
0.8
0.4
log β
log β
log α
0
40
80
120
t_a (days)

A Finite Element Method for an Incremental Viscoplasticity Theory Based on Overstress*

T.-L. Sham
Department of Mechanical Engineering, Aeronautical Engineering & Mechanics,
Rensselaer Polytechnic Institute, Troy, New York 12180-3590, U.S.A.

Abstract

This work is concerned with the development of a time integration method and its finite element implementation for a viscoplasticity theory based on overstress (VBO), developed by Krempl and his co-workers [1-3]. VBO is a *unified* theory. It does not distinguish, for example, plastic deformation from creep. All nonlinear responses are modeled in their totality as inelastic deformation. Also, no yield surface nor loading/unloading conditions are employed in VBO. However, VBO reproduces the observed responses of loading, unloading, and reloading under strain control in a realistic manner. For the purpose of this abstract, we present the constitutive relations for VBO in the following one dimensional form:

$$\dot{\varepsilon} = \dot{\varepsilon}^{el} + \dot{\varepsilon}^{in} = \frac{\dot{\sigma}}{E} + \frac{\sigma - G}{C} ,$$

$$\dot{G} = \psi\, \dot{\varepsilon} - \frac{|G - F|}{b}\, \dot{\varepsilon}^{in} , \qquad b = \frac{A}{\psi - E_t} \frac{E - E_t}{E}$$

$$\dot{F} = \frac{E_t}{1 - E_t / E}\, \dot{\varepsilon}^{in} ,$$

$$\dot{A} = (B_1 - B_2 A)\, |\dot{\varepsilon}^{in}| , \qquad A(t = 0) = A_0$$

where ε is the axial strain, σ the axial stress, and superimposed dots the material rates. The state variables of VBO are G the equilibrium stress, F the kinematic stress, and A. The functions C and ψ are material functions and they are assumed to depend on $\sigma - G$ which is sometimes referred to as the *overstress*. The material constants are E, E_t, A_0, B_1, and B_2. We

* This work was supported by the Army Research Office under Contract No. DAAL03-88-K-0041.

note that σ, G, and F can be represented schematically as a function of ε as shown in Fig. 1. The state variable A allows the modeling of cyclic hardening/neutral/softening behaviors in metals.

The time integration of the constitutive equations for VBO follows the procedure of Peirce, Shih and Needleman [4] which represents a particular variant of a general class of explicit one-step algorithms, the so-called forward gradient methods. This leads to explicit tangent operators suitable for finite element implementation and results in a symmetric stiffness matrix. Due to the strong nonlinear response of the material function ψ in the evolution equation of the equilibrium stress G, we have found that an automatic sub-increment procedure is required for the update of G in the rapidly decaying region of ψ. Drifting of the stress/strain curves can then be avoided by this sub-increment procedure. An adaptive time-stepping procedure is also developed. The adaptivity is based on a measure of the absolute truncation error of the accumulated inelastic equivalent strain. In addition, a measure which restricts the maximum allowable increase in the inelastic equivalent strain within a time step, as suggested by Anand, Lush, Briceno and Parks [5], is also employed.

Finite element calculations which simulate plane strain homogeneous deformations in 304 stainless steel and 6061 T6 aluminum alloy at room temperature and under various strain and stress rate histories, e.g., monotonic, strain-rate change, strain control cyclic loading, and stress control cyclic loading, have been performed. The finite element results compared very well with the solutions obtained from the stiff differential equation solver. The numerical experiments also showed that the use of these relatively simple one-step explicit integration formulas together with adaptive time-stepping procedure provide a satisfactory strategy for general finite element stress analysis in viscoplastic solids.

References

[1] Yao, D. and Krempl, E., *Viscoplasticity theory based on overstress: the prediction of monotonic and cyclic proportional and nonproportional loading paths of an aluminum alloy*, Int. J. Plast., Vol. 1, 1985, pp. 259-274.

[2] Krempl, E., McMahon, J.J. and Yao, D., *Viscoplasticity based on overstress with a differential growth law for the equilibrium stress*, Mech. Mater., Vol. 5, 1986, pp. 35-48.

[3] Krempl, E. and Yao, D., *The viscoplasticity theory based on overstress applied to ratchetting and cyclic hardening*, In: Low cycle fatigue and elasto-plastic behavior of materials, Rie, K.T. Ed., Elsevier Science Publishing Company, New York, 1987, pp. 137-148.

[4] Peirce, D., Shih, C.F. and Needleman, A., *A tangent modulus method for rate dependent solids*, Comput. Struct. Vol. 18, 1984, pp. 875-887.

[5] Anand, L., Lush, A., Briceno, M.F. and Parks, D.M., *A time-integration procedure for a set of internal variable type elasto-viscoplastic constitutive equations*, Reports of research in mechanics of materials, Massachusetts Institute of Technology, Cambridge, 1985.

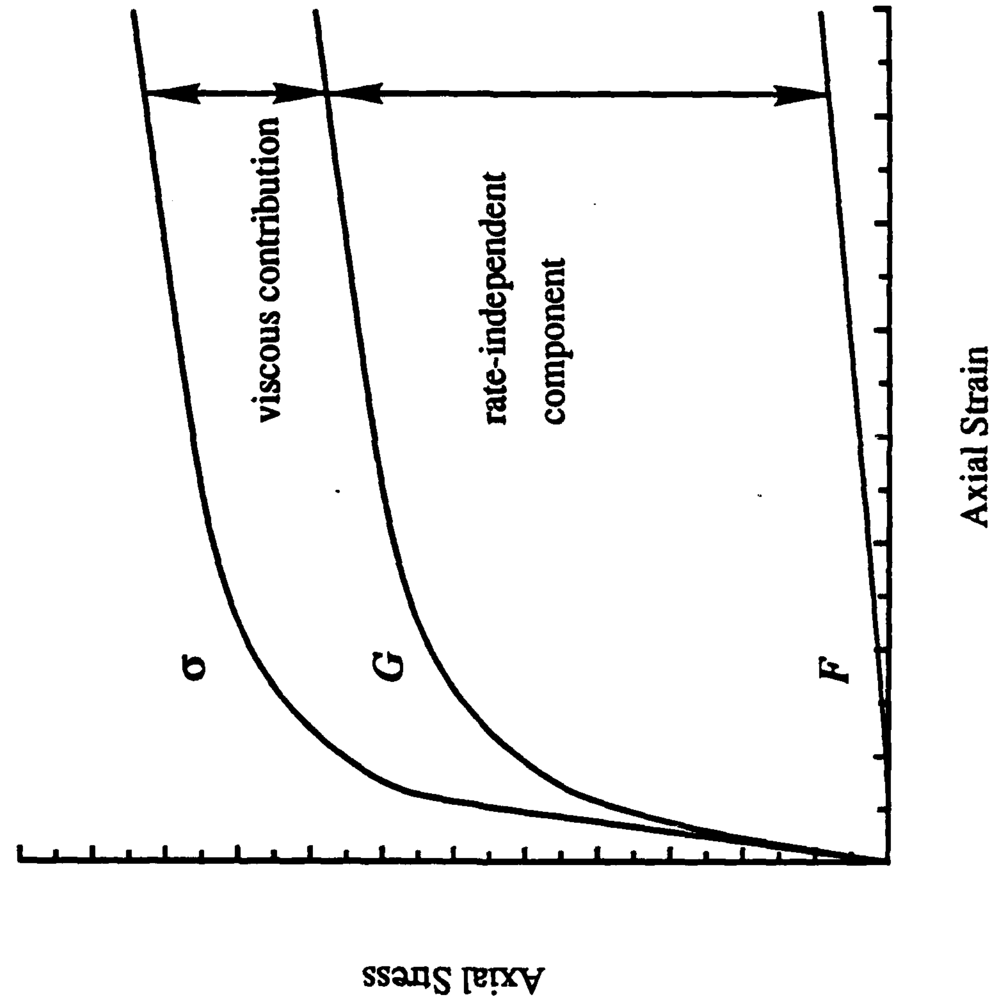
σ
G
F
viscous contribution
rate-independent component
Axial Strain
Axial Stress

Fig. 1

STUDY ON IMPACT DAMAGE IN LAMINATED COMPOSITES

Fu-Kuo Chang and Hyung Yun Choi

Department of Aeronautics and Astronautics
Stanford University
Stanford, California 94305

An investigation was performed to study impact damage in laminated composites caused by a low-velocity foreign object. The major focus of the study was to fundamentally understand the failure mechanisms in composites caused by impact, and to evaluate the effects of velocity, mass, and size of the impactor on the failure modes and the extent of damage in composites. Matrix cracks and delaminations were primary concerns for the failure modes.

A special impact test facility was designed, in which an impactor travels in a rectangular barrel and strikes the target without leaving the barrel. Impactors with different types of noses and various impact velocities were selected for the impact study. T300/976 Graphite/Epoxy prepregs were used to fabricate specimens with different thicknesses and ply orientations. All specimens were x-rayed and c-scanned before and after impact to examine the damage caused by impact. Strain gauges were also mounted on specimens to record the strain history during impact.

An analytical model was developed to evaluate the response of the laminates during impact and to determine the effects of the impactor's velocity and mass on the impact damage in the laminated composites. The model consists of a stress analysis and a failure analysis. Stresses, strains, and deformations in the laminates were calculated by a proposed transient dynamic finite element method. Failure modes and the location of damage were predicted by appropriately selected failure criteria. The results of the calculations from the model were compared with the test data. An excellent agreement was found between the predictions and the experiments.

Based on the extensive study, it was concluded that 1). matrix cracks initiate delamination during impact, 2). laminates with inherent cracks, resulting from manufacturing, are much more susceptible to impact than laminates without, 3). impact damage strongly depends on the thickness and ply orientation of the specimens, and 4). the size of the impactor's head significantly affects the failure mode and the extent of impact damage.

EROSION OF TUNGSTEN CYLINDERS: A TWO PART PHYSICAL STUDY

by

Noel C. Calkins* and William Gooch**

*Los Alamos National Laboratory
Los Alamos, New Mexico 87545

**US Army Ballistic Research Laboratory
Aberdeen Proving Ground, MD 21005-5066

Abstract

Part I -- Ballistic Testing of Particulated Targets

In an effort to evaluate erosion as a penetrator defeat mechanism, long-rod penetrators were ballistically tested against tightly confined ceramic particulates. Ceramic target cells in which the particulates were confined were identical to those prepared for the US Army Materials Technology Laboratory for their 1/4-scale testing and development. The ceramic was confined on all sides by a welded cell. The TiB_2 ceramic was then particulated by the use of shock waves to prevent dilation.

A 1/4-scale long-rod penetrator was shot at the confined ceramic targets to get V_{50} comparison. The V_{50} testing, using identical cell construction for monolithic and particulated ceramic, yielded exciting results, indicating that erosion plays a major role in defeating the penetrator. Although more work needs to be done, indications are that erosion is a major contributor in defeating a penetrator when it is shot into tightly confined ceramic armor.

Part II -- Comparison of Penetrator Erosion Rates Using Various Ceramics

This study compares erosion rates attained from using selected particulated ceramic armor materials and driving them against tungsten long-rod penetrators. Using abrasive particles, this simulation gives an effect similar to reverse ballistics. A method was developed to achieve a Gaussian distribution of screened ceramic particles striking a 97%W penetrator at an appropriate velocity. Relative rates of penetrator weight loss were accurately measured, and a loss curve was generated on the basis of the weight of abrasive used. This testing is structured to simulate as closely as possible the erosion effect of broken up ceramic and tungsten particles as they impact the nose of a penetrator after an initial shockwave reflection occurs in confined armor. This testing may apply to monolithic, monolithic-layered, and epoxy particulate armor only if the armor is completely confined. This erosion rate comparison study is expected to become more important as emphasis on confined ceramic armor gains favor. The various physical properties of ceramic that are typically identified by high cost are not necessarily those with the best erosion qualities.

CONSTITUTIVE EQUATIONS FOR LIQUID CRYSTALLINE BASED POLYMERIC MATERIALS UNDER BALLISTIC IMPACT

Philip Cunniff

U. S. Army Natick Research, Development and Engineering Center
Individual Protection Directorate
Natick MA 01760

INTRODUCTION

The response of polymers to ballistic impact is exceedingly complex, and unsolvable in closed analytical form for all but the most simple of systems. Research to determine the constitutive equations of body armor materials under ballistic impact conditions is motivated by the need to provide guidance to fiber manufacturers concerning the needs of body armor users, and by the need to better predict the performance of woven fabric body armor systems. The experimentalist in the field of ballistic impact has the challenge of determining the stress-strain equations and failure criteria of materials that are generally nonlinear, time dependent, may exhibit significant stress relaxation, and are loaded to large strains in microseconds. The work in progress at this Center has combined available numerical models with experimental techniques using high speed photography to determine equations to define the material behavior of single yarns of body armor materials. The resulting constitutive equations may be used in other numerical models to predict the system performance of woven fabric armor. This methodology has allowed us to estimate the ballistic performance of new materials that are not currently available in sufficient quantities to perform large scale ballistic testing on.

SINGLE YARN IMPACT MECHANICS

The salient features of the response of rate independent materials to transverse ballistic impact before reflections of the traveling waves can be summarized with reference to figure 1. Upon impact, a series of strain wavelettes propagate away from the impact point in both directions with velocity $c(\in) = \sqrt{kE(\in)}$, where c is the velocity of the strain wave, and is a function of strain $\in$, E is the dynamic modulus of elasticity in textile units, and k is a numerical constant (k=88254). In the wake of the final wavelette of this longitudinal wave, material flows inward toward the point of impact with constant velocity, strain, and tension. In the region between the two longitudinal wave fronts, a V shaped transverse deflection is formed from the inwardly flowing material, with the projectile at the vertex of the V. At the edge of the transverse wave, the inward material flow ceases abruptly, and is replaced by a transverse particle velocity, equal to that of the projectile; the strain and tension are unchanged across this wave front. Behind the transverse wave front, the yarn configuration is a straight line with constant inclination to the undeformed yarn axis. In a finite length system the outwardly propagating waves eventually reflect from the clamps of the system, and complicate the motion of the yarn. The response of long textile yarns to ballistic impact has been studied quite

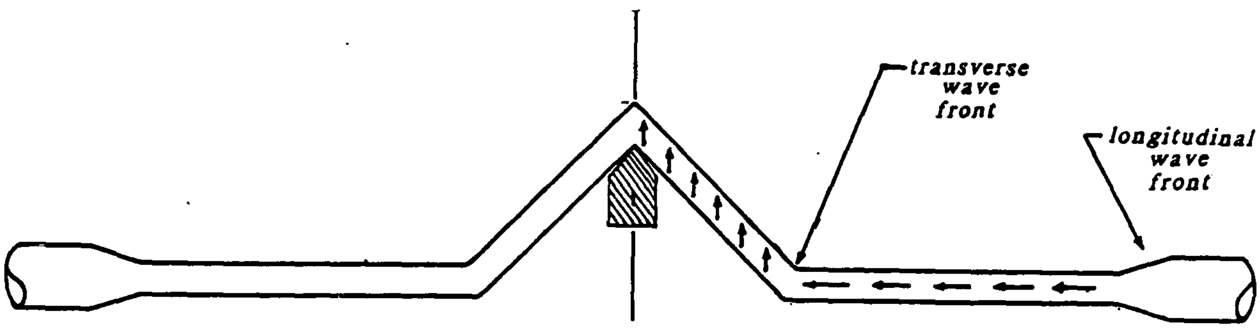

Figure 1. Idealized single yarn under ballistic impact illustrating wave propagation, and transport mechanisms.

extensively by Smith et.al. [1]. Lynch [2] applied a "direct analysis" method developed by by Koeing [3] to the transverse ballistic impact of yarns, and outlined a linear viscoelastic model for use with the direct analysis method. The direct analysis method is applicable to the motion of a constrained yarn both before and after reflections of the traveling waves. Roylance [4], extended that work, which had assumed a rate independent response of the materials, to include the viscoelastic response of transversely impacted fibers.

DIRECT ANALYSIS METHOD

The basic algorithm for the direct analysis simulation of transverse impact of a single yarn may be stated as follows:

1. The yarn is assumed to be one-dimensional; shear is assumed to be negligible.
2. The following system variables are known prior to execution of the routine:
   a. Projectile striking velocity, and mass,
   b. Yarn constitutive equation, failure criteria, length (l), and linear density.
3. The yarn is idealized as a series of lumped masses such that in the undeformed state, the distance (h) between each lumped mass is:

$$h = ct_1 \qquad \text{(Eq. 1)}$$

where t_1 is the time the longitudinal wave would take to propagate one element length in a linearly elastic material, and c is the wave speed. In practice, the element length is determined from the selection of the number of elements (n) desired for the simulation ($h = l/n$). Equation 1 is solved for t_1, and this time is selected for the time increment of the simulation.

4. For each time increment:
   a. The velocity of the first lumped mass is set equal to the current projectile velocity.
   b. The velocity of each element mass is found from the tension and position of the element and it's neighboring elements at the previous time increment.
   c. Element strain is found from the velocity of the neighboring lumped masses

necessary to iteratively execute the computer model, changing the assumed value of the constitutive properties until the predicted values matched the experimental ones. The criteria selected for comparison of the model predictions to the experimental data was the best match of the overall shape of the predictions to the experimental data. Figure 2 is an example of a photograph of a Kevlar yarn under ballistic impact at 290 m/s, and the plot of experimental results and model predictions. The time spacing between microflashes in the photograph is somewhat uneven and is due to variation in frequency of the flash unit trigger circuit. The microflash times in Figure 2 are about 15 microseconds apart; the first flash with significant yarn deflection is 22 microseconds after impact, and the last one before break is 172 microseconds after impact.

[redacted]

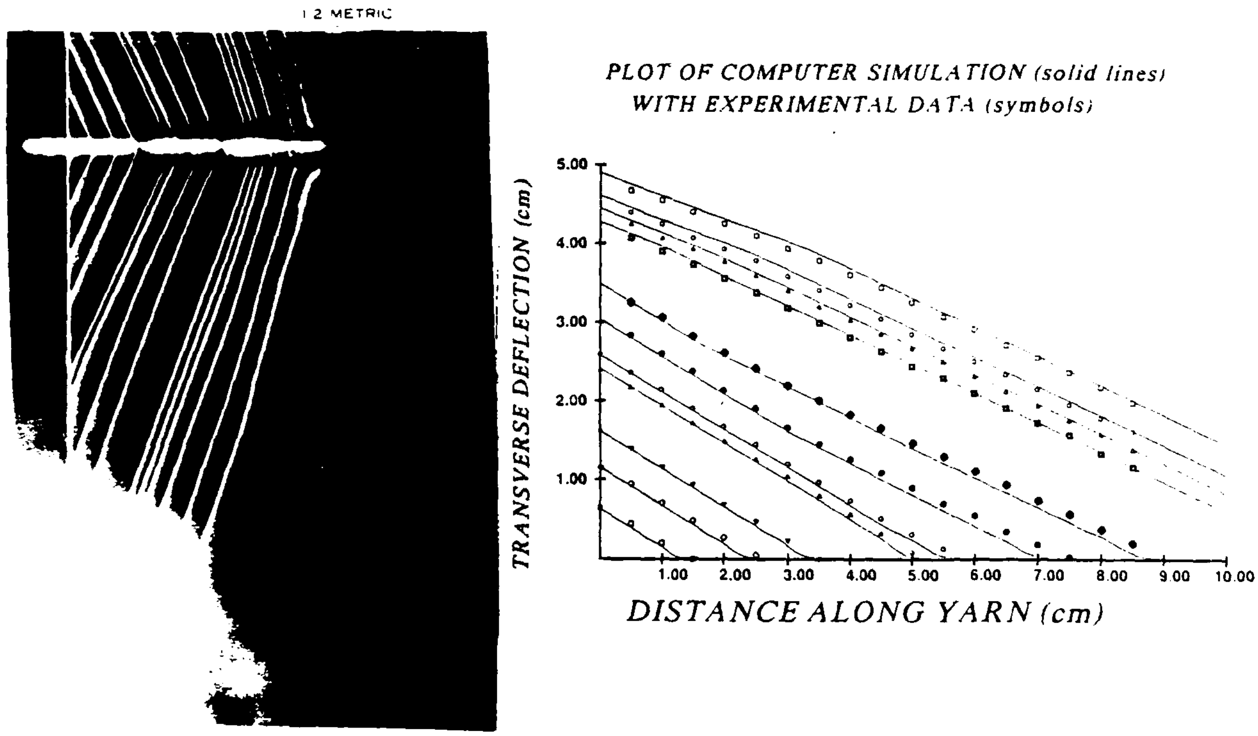

(a) (b)

Figure 2. (a) Multiflash Photograph of Kevlar Yarn Under Ballistic Impact at 290 m/s (b) Direct Analysis Model Prediction of Yarn Deflection (Lines) and Experimentally Measured Deflections (Symbols) at Various Times After Impact.

PRELIMINARY RESULTS

Preliminary analysis has been completed on each of the yarns to be discussed in this paper. This analysis indicates that the stress-strain relationship for Kevlar exhibits rate dependency and relaxation at ballistic strain rates. The nominal initial modulus of Kevlar at ballistic rates appears to be somewhat higher than the static initial modulus. The modulus of PBO and PBZT appears to decrease over the static value at ballistic strain rates; insufficient data is available at this point to speculate on the rate dependency or relaxation of PBO or PBZT at ballistic rates.

calculated during the current time increment, and their positions calculated from the previous time increment.

d. Element tension is calculated from element strain and the assumed material constitutive equation.

e. The position of each lumped mass is calculated from the velocity calculated during the current time increment, and position from the previous time increment.

f. The projectile velocity is determined from tension and position of the first element.

5. Step 4 is repeated until the failure criteria is met.

EXPERIMENTAL MATERIALS

Three types of fibers representing two different molecular configurations are reported on in this paper. Included in the analysis is the current standard body armor material, Kevlar 29, which is an extended-chain poly(1,4 phenylene terephthalamide), commercially available from E.I. du Pont de Nemours & Company, Inc. The study also includes two high performance experimental rigid-rod fibers, poly(p-phenylene benzbisoxazole) (PBO) and poly(p-phenylene benzobisthiazole) (PBZT), developed under the U.S. Air Force Ordered Polymers Program. All the fibers discussed in this paper are considered to be liquid crystalline based. Both the PBO and PBZT fibers were evaluated in the as-spun and heat-treated state.

EXPERIMENTAL METHOD

Transverse ballistic impact tests were carried out on Kevlar, PBZT, and PBO yarns at velocities ranging from approximately 190 m/s to 460 m/s. The test specimens were mounted between two rigidly supported steel clamps and impacted in the center by a 1.1-g steel fragment simulator. The projectile striking and residual velocities were measured using light screens and 10-MHz counter timers.

A multiple exposure photograph of each specimen was taken duri[illegible] 'mpact event with a Polaroid camera. A ½-mm graded ruler was placed in the projectile [illegible]h and recorded on each piece of film prior to the ballistic tests. Illumination for the photographs was provided by an EG&G model 502A multiple microflash unit. The time of each microflash was determined from an oscilloscope recording of an induced voltage in a coil of wire wrapped around the microflash unit power cable. Each photograph was enlarged with an opaque projector to approximately 0.5 m and traced on paper. Yarn deflections were measured at 0.5-cm intervals from the projectile line of flight. The resulting time-displacement data was tabulated and later used for comparison with predictions from the direct analysis method.

NUMERICAL METHOD

The numerical method used in this investigation is similar to the one used by Morrison [5], who used the direct analysis method and experimental data to find the stress strain curves of Kevlar 29 and Kevlar 49. Morrison compared the gross extension of yarns subjected to ballistic impact at velocities ranging from 40 to 140 m/s to the predictions of the direct analysis method to determine the tensile modulus of the material. In this investigation the tabulated experimental results were compared to the predictions of the direct analysis method by plotting the data and visually inspecting the results. The materials were assumed to be linearly viscoelastic, and rate dependent; hence it was only

REFERENCES

1. Smith J.C., Fenstermaker C.A., and Shouse P.J. Stress-Strain Relationships in Yarns Subjected to Rapid Impact Loading, Part X: Stress-Strain Curves Obtained by Impacts With Rifle Bullets, TRJ, pp. 919-934, Nov 1965

2. Lynch DeS. .F., Dynamic Response of a Constrained Fibrous System Subjected to Transverse Impact - Part II: A Mechanical Model, Army Materials and Mechanics Research Center, Watertown MA, AMMRC TR-70-16, July 1970

3. Koeing H.A. and Davis N., Dynamical Finite Element Analysis for Elastic Waves in Beams and Plates Int J Solids and Struct., V4 pp 643-660, 1968.

4. Roylance D, Wave Propagation in a Viscoelastic Fiber Subjected to Transverse Impact, J. Appl Mech, pp. 143-148, March 1973

5. Morrison C.E., Bader M.G., Behavior of Single Aramid Fiber Yarns Under Ballistic Impact, Fifth Inter Conf Comp Mater, Aug 1985

Perforation of Aluminum Armor Plates with Conical-Nose Projectiles

M. J. Forrestal and V. K. Luk

Sandia National Laboratories
Albuquerque, New Mexico 87185

N. S. Brar

University of Dayton Research Institute
Dayton, Ohio 45469

ABSTRACT

Backman and Goldsmith (1978) show eight possible perforation mechanisms that depend on the geometry and material of the targets and projectiles. Because many mechanisms are possible, observations from terminal-ballistic experiments usually guide engineering models. We limited this study to tungsten conical-nose projectiles that perforated aluminum armor plates at normal incidence. The 5083-H131 aluminum armor plates experienced ductile hole growth with cavity diameters nearly equal to the shank diameter of the projectile. In addition, post-perforation x-ray photographs showed that the tungsten projectiles remained undeformed to impact velocities of about 1,200 m/s. At about 1,400 m/s, the projectiles either deformed or fractured.

In a recent paper, Rosenberg and Forrestal (1988) presented equations that predicted residual velocity and ballistic limit for rigid conical-nose rods that perforated elastic, perfectly plastic targets. In this study, we used the techniques developed by Kawahara (1986) to obtain compression, stress-strain data to 100 percent true strain for the target material. We then approximated the post-yield, stress-strain curve with a power-law data-fit. Figure 1 shows the stress-strain data and the power-law approximation for a strain rate of 10^0 s^{-1}. Data from the large-strain compression test and the power-law, strain-hardening model provided a more realistic material description for the target material than was previously available.

In this study, we developed engineering models that predicted residual velocity and ballistic limit for rigid conical-nose projectiles that perforated rate-independent, strain-hardening target plates. The cylindrical cavity-expansion approximation simplified the target analysis, so we obtained closed-form perforation equations. To verify our models, we conducted terminal-ballistic experiments at normal incidence with 0.026-kg, 8.31-mm-diameter tungsten projectiles and armor plates of 5083-H131 aluminum. Figure 2 compares predicted and measured residual velocity V_r versus impact velocity V_i ($200 < V_i < 1{,}200$ m/s) for the 12.7-, 50.8-, and 76.2-mm-thick targets. In Fig. 2, μ is the sliding-interface friction coefficient. As shown in Fig. 2, model predictions are in generally good agreement with measurements.

REFERENCES

Backman, M. E., and Goldsmith, W., 1978, "The Mechanics of Penetration of Projectiles into Targets," International Journal of Engineering Science, Vol. 16, pp. 1-99.

Rosenberg, Z., and Forrestal, M. J., 1988, "Perforation of Aluminum Plates with Conical-Nosed Rods - Additional Data and Discussion," Journal of Applied Mechanics, Vol. 55, No. 1, pp. 236-238.

Kawahara, W. A., 1986, "Compression Materials Testing at Low to Medium Strain Rates," Paper No. 86-WA-Mats-15, Presented at the Winter Annual Meeting, ASME, Anaheim, CA, Dec. 7-12, 1986.

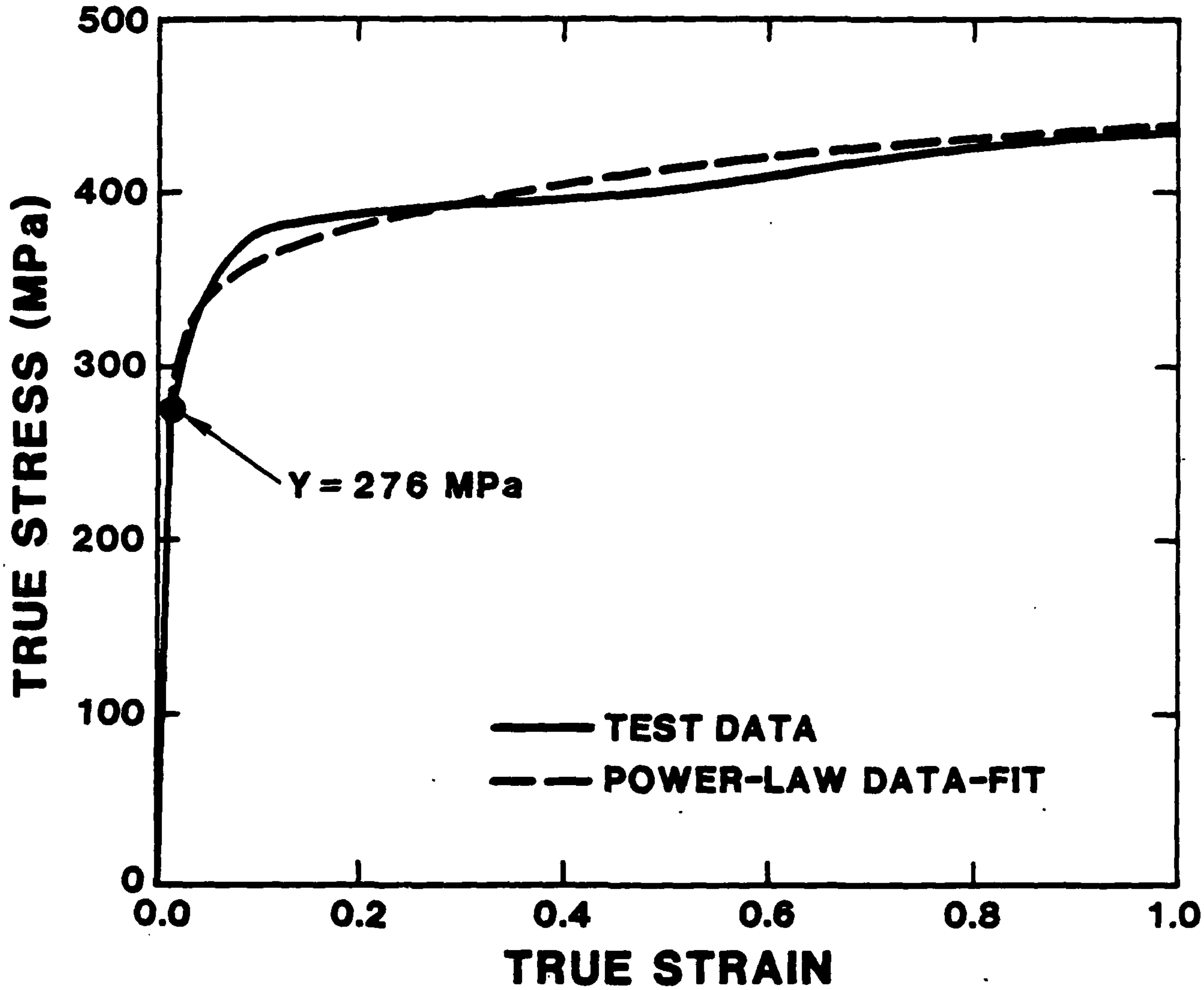

Fig. 1. Stress-strain data for the 5083-H131 aluminum target plates and the power-law data-fit with Young's modulus E = 70.3 GPa, Poisson's ratio ν = 0.3, yield stress Y = 276 MPa, and strain-hardening exponent n = 0.084.

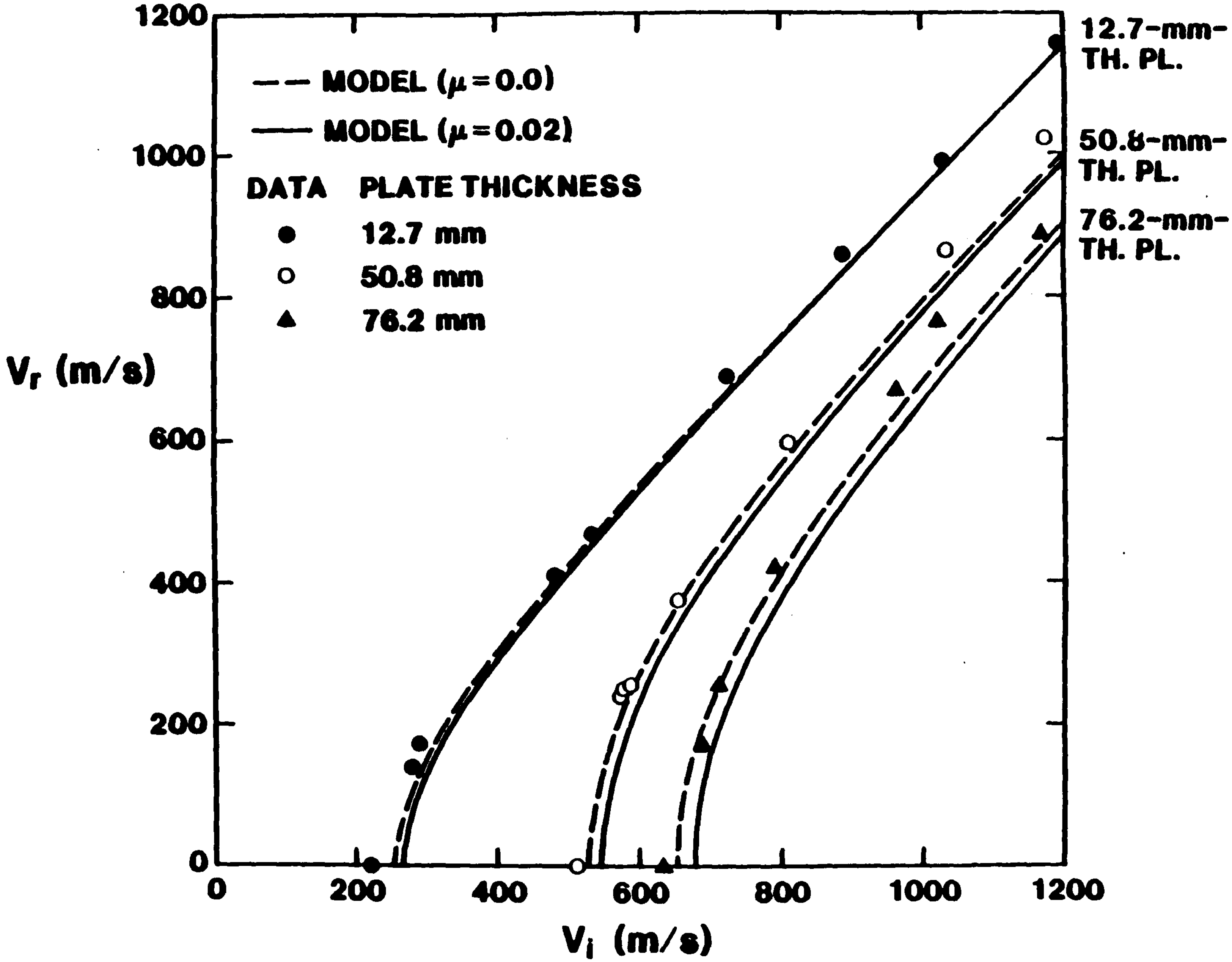

Fig. 2. Comparison of predicted and measured residual velocity.

FINITE ELEMENT SIMULATION OF PERFORATION AND PENETRATION OF ALUMINUM TARGETS BY CONICAL-NOSED STEEL RODS[1]

E. P. Chen
Sandia National Laboratories
Albuquerque, New Mexico 87185

ABSTRACT

Numerical simulations of perforation and penetration of targets by projectiles have been sub·· .cts of interest for many years. The work of Anderson and Bodner (1988). ''ilkins (1978), and Zukas, et al. (1982), provide comprehensive reviews to the sub ect matters. A series of articles, Chen (1987), Johnson and Stryk (1987), and Schwer, Rosinsky and Day (1988) has appeared recently in the literature using the finite element method to treat perforation and penetration problems involving geological targets. A unique feature of these problems is the low impact velocity (less than 1 km/s) involved which leaves the projectiles essentially undeformed (Forrestal et al. (1986)). One of the problems associated with geological media relates to the difficulty in characterizing their material properties. Although good results have been obtained by the finite element method in the above papers, the validity of the calculations remains clouded by the issue of material property characterization.

Recently, a series of laboratory scale experiments on perforation and penetration of aluminum targets by conical-nosed steel penetrators was conducted by Forrestal, Rosenberg, Luk, and Bless (1987), Rosenberg and Forrestal (1988), and Forrestal, Okajima, and Luk (1988a). Along with these experiments, thorough laboratory tests have been conducted to obtain accurate material properties for the 6061-T6 aluminum target. The observations and measurements from the experiments are an excellent set of data to verify the validity of Lagrangian computer code calculations. The purpose of the current investigation is to simulate numerically the configurations of the aforementioned experiments in an attempt to establish the validity of the Lagrangian finite element numerical technique. The finite element code PRONTO 2D (Taylor and Flanagan (1987)) was used for numerical simulation purposes. Both the perforation problems corresponding to the experiments in Forrestal et al. (1987) and Rosenberg and Forrestal (1988), and the penetration problems corresponding to Forrestal et al. (1988a) have been considered.

The numerical procedures used are similar to those reported in Chen (1987, 1988a, 1988b). Both the steel projectile and the aluminum target are treated as

[1]This work performed at Sandia National Laboratories supported by the U.S. Department of Energy under contract number DE-AC04-76DP00789.

elastic/plastic materials with isotropic hardening. Large deformation behaviors are also included. Slide-lines are used to transfer momentums between the projectile and the target. Comparisons between calculated and experimentally measured data show very good agreements. See Figure 1 and 2, respectively, for perforation and penetration results. This lends support to the validity of applying the finite element method to obtain solutions for this class of perforation and penetration problems.

REFERENCES

Anderson, C. E. and Bodner, S. R., 1988, Ballistic Impact: The Status of Analytical and Numerical Modeling, *International Journal of Impact Engineering*, 7, pp. 9-35.

Chen, E. P., 1987, Finite Element Simulation of Penetration Into Geological Targets, *Theoretical and Applied Fracture Mechanics*, 8, pp. 125-135.

Chen, E. P., 1988a, Finite Element Simulation of Perforation of Aluminum Plates, COMPUTATIONAL MECHANICS '88, Volume 1, S. N. Atluri and G. Yagawa, editors, pp. 21.iii.1-10, Springer-Verlag, New York.

Chen, E. P., 1988b, Penetration Into Dry Porous Rock: A Numerical Study on Sliding Friction Simulation, *Sandia National Laboratories Report*, SAND88-2485, Sandia National Laboratories, Albuquerque, NM, to be published.

Forrestal, M. J., Lee, L. M. and Jenrette, B. D., 1986, Laboratory-Scale Penetration Experiments into Geological Targets to Impact Velocities of 2.1 km/s, *Journal of Applied Mechanics*, 53, pp. 317-320.

Forrestal, M. J., Rosenberg, Z., Luk, V. K. and Bless, S. J., 1987, Perforation of Aluminum Plates with Conical-Nosed Rods, *Journal of Applied Mechanics*, 54, pp. 230-232.

Forrestal, M. J., Okajima, K. and Luk, V. K., 1988a, Penetration of 6061-T651 Aluminum Targets With Rigid Long Rods, *Journal of Applied Mechanics*, accepted for publication.

Forrestal, M. J., Brar, S. N. and Luk, V. K., 1988b, Penetration of Strain-Hardening Targets with Rigid Spherical Nose Rods, submitted for publication.

Johnson, G. R. and Stryk, R. A., 1987, Two- and Three-Dimensional Computational Approaches for Steel Projectiles Impacting Concrete Targets, Preprint of a paper presented at the Post-SMIRT Seminar on Impact, Lausanne, Switzerland.

Rosenberg, Z. and Forrestal, M. J., 1988, Perforation of Aluminum Plates with Conical-Nosed Rods - Additional Data and Discussion, *Journal of Applied Mechanics*, 55, pp. 236-238.

Schwer, L. E., Rosinsky, R. and Day, J., 1988, An Axisymmetric Lagrangian Technique for Predicting Earth Penetration Including Penetrator Response, *International Journal for Numerical and Analytical Methods in Geomechanics*, 12, pp. 235-262.

Taylor, L. M. and Flanagan, D. P., 1987, PRONTO 2D - A Two-Dimensional Transient Solid Dynamics Program, *Sandia National Laboratories Report*, SAND86-0594, Sandia National Laboratories, Albuquerque, NM.

Wilkins, M. L., 1978, Mechanics of Penetration and Perforation, *International Journal of Engineering Science*, 16, pp. 793-807.

Zukas, J. A., Nicholas, T., Swift, H. F., Greszczuk, L. B. and Curran, D. R., 1982, IMPACT DYNAMICS, John Wiley & Sons, New York.

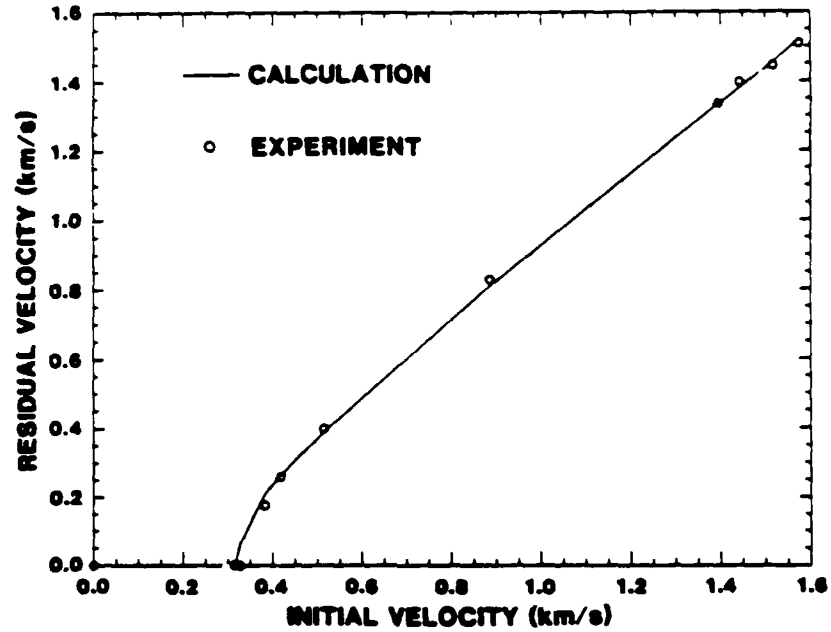

Figure 1. Comparison of Calculated and Measured Results for Perforation Problems

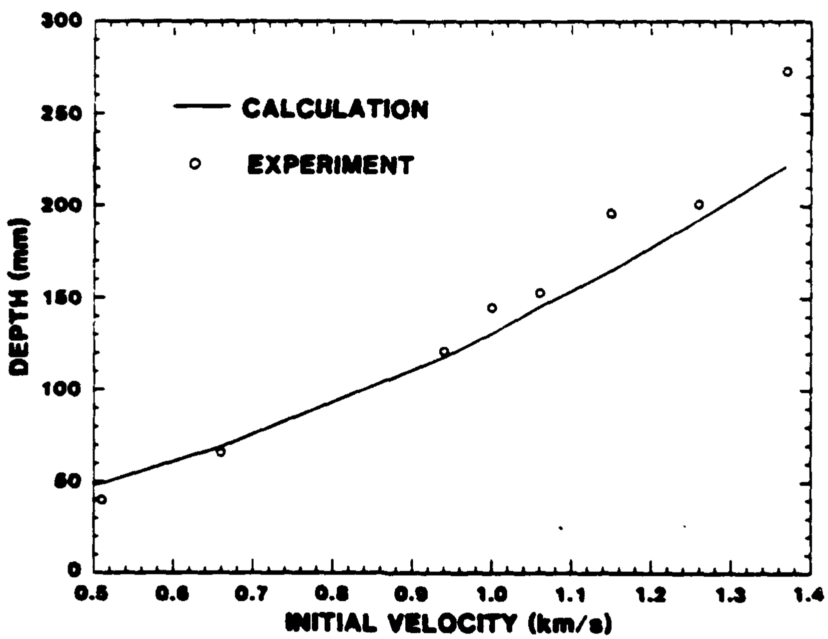

Figure 2. Comparison of Calculated and Measured Results for Penetration Problems

A DYNAMIC STUDY OF ENERGY LOSS DURING HIGH VELOCITY PROJECTILE IMPACT

R.H. Zee, C.J. Wang, A. Mount and B.Z. Jang
Materials Engineering Curriculum
Department of Mechanical Engineering
Auburn University
Auburn, Alabama 36849
(205) 826-4575

Abstract

Fabric and fibrous composites are finding increasing use in ballistic protection. Understanding the impact response of these materials, particularly in composites, has become an area of great academic and practical importance. However, our grasp of the impact response in composites and other ballistic materials is still quite limited, possible because of the complex energy loss phenomenon and the high projectile velocity involved. In order the properly design the appropriate materials for impact applications, it is essential to first determine the energy dissipation processes involved. It is only then that the appropriate materials can be designed and fabricated for specific applications. The purpose of this research is the develop a new method to monitor the energy loss of a projectile during impact so that the real-time impact response of the materials can be determined.

An air gun and an innovative microvelocity sensor unit were developed. This system is capable of providing a real time velocity profile of the projectile during the slowing down process. An air gun based on helium propulsion was designed, constructed and tested at Auburn University's Materials Engineering. A high pressure helium storage tank (up to 6000 psi) was used to supply the helium gas required for propulsion. When the proper conditions have been attained, a fast acting valve was activated and the pressure burst accelerated the projectile through the barrel to hypervelocities. The gun itself is consisted of a 36" long liner with a 1/4" diameter hole through the center. During the flight of the projectile, it was accelerated to the desired velocity through the barrel and then passed through the microvelocity sensor unit (to be described), impacted on the target and then exited into the catcher at the end.

The projectiles used in the preliminary study were all 1.75" in length and 1/4" in diameter. A small magnet was inserted into the end of each projectile. The purpose of this magnet will be discussed in the next section. The magnets were cylindrical in shape and each measured 1/8" in diameter and 1/8" in length. Muzzle velocities were measured as a function of helium gas pressure used. Results are shown in figure 1. The velocities were measured using the microvelocity sensor to be described below.

The thrust of this research is based on this newly developed innovative sensor unit. The prefix "micro" refers to the superior spatial resolution of this device. In this system, a magnet was attached to the projectile rod. A detector made of a series of coils on an electrically insulating tube was

placed in front of the materials of interest. During the impact and the penetration of the projectile through the protective material, the magnet in the projectile triggered the coils in succession as a result of the rapidly changing magnetic flux the individual coils experienced. The proper timing of the triggering will therefore provide the needed information on the real time, real space velocity mapping. To determine the dynamic energy loss process, spatial resolution in the order of 0.1" is required. To overcome the signal overlap problem at less than 0.1" separations, a special digital electronic circuitry was developed. The final signals were displayed and stored on a Tektronics digital storage oscilloscope as shown in figure 2. The eleven pulses represent the passing of the magnet in the projectile through the eleven coils. A separate secondary coil unit was used to measure the exit velocity of the projectile. Therefore by monitoring the spreading out of the pulses, direction information on the slowing down of the projectile can be determined.

Energy loss profiles for aluminum projectiles into various materials, such as polyester composites and PE fabrics, were determined. An example is shown in figure 3 where a composite material with three 10-layer plates (a total of 30 plies) of polyester stacked together. Here the energy loss process began near the point of impact indicating the rigidity of the materials compared to the single layer material. Furthermore, the energy loss process occurred over a 1 inch distance whereas the material was only 0.4" thick. Since the material is rather rigid, this suggests the final energy loss is most likely due to the generation of frictional heat between the projectile and the material after the formation of the hole. A second experiment was conducted on the same type of material but with only two 1^-layer plates of polyester stacked together. Result shows that the energy loss phenomenon is similar to that found in the thicker material. However, the amount of energy loss did not scale linearly with material thickness. The 30-ply polyester absorbed a 65 joules of energy compared to 54 joules in the 20-ply material, giving a ratio of 1.2 instead of 1.5. When a single 10-layer polyester composite was used. The projectile lost 30% of its energy during the entire process, as shown in figure 4. The composite was 1/8 inch thick. It was observed using the detector unit that during the first 1/4" of the penetration, no energy was lost. All the 30% energy loss occurred within a 0.1 inch interval after the composite was penetrated by 1/4". This implies that little energy loss occurs through the generation of frictional heat, elastic deformation of the materials and fiber breakage since these phenomena would have given either a continuous energy loss spectrum or an energy loss upon initial impact. Upon examination of the failed composites, it was found that extensive delamination has occurred. This means that the 30% energy loss is most likely due to the generation of these delaminated layers, which is consistent with the very discrete energy loss in a short interval.

Results on other materials will also be presented.

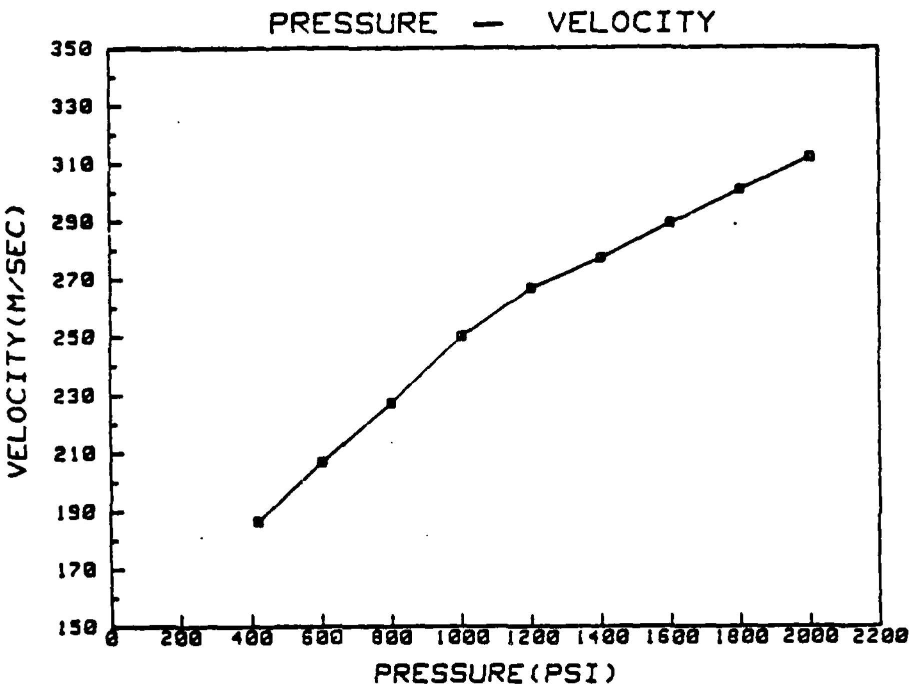

Figure 1. Velocity versus helium pressure for the air gun.

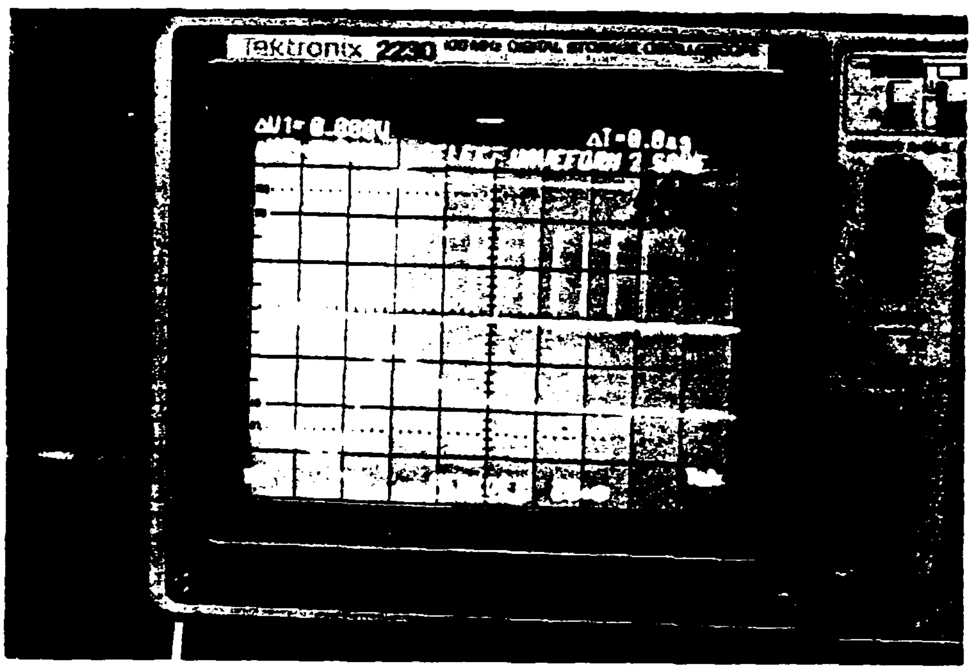

Figure 2. Digital pulses from the microvelocity sensor for a projectile through air (no slowing down). The constant spacing between pulses is a result of constant velocity. The bottom trace shows the raw signal from the first coil.

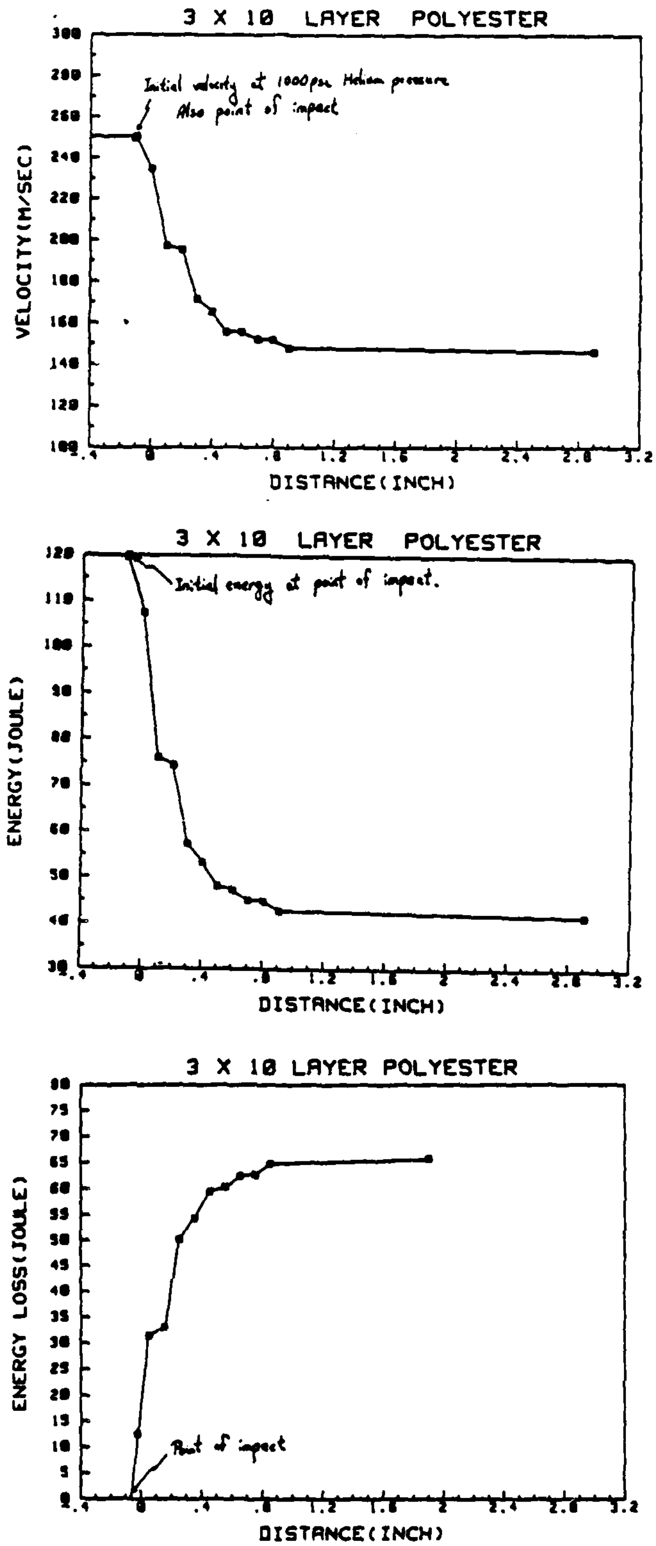

Figure 3. Velocity, energy and energy loss profiles for the slowing down of the projectile in three 10-layer polyester.

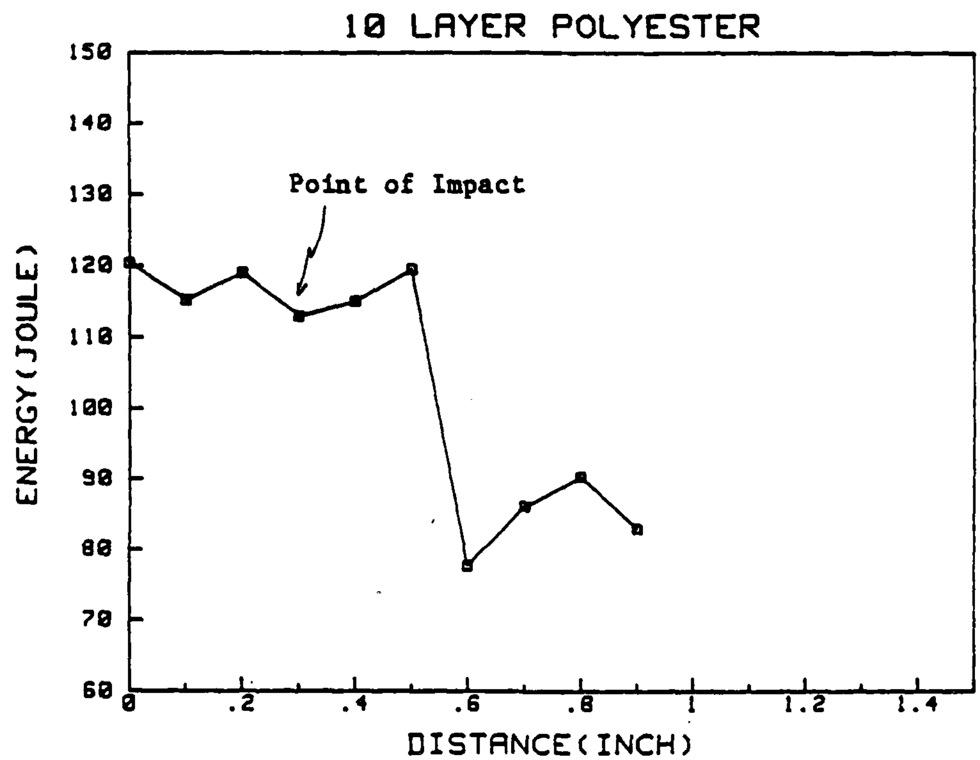

Figure 4. Energy profile for the slowing down of the projectile in a single 10-layer polyester.